Mathematical modelling of Centrosomin incorporation in *Drosophila* centrosomes

Suruchi Bakshi

Linacre College

University of Oxford

A thesis submitted for the degree of

Doctor of Philosophy

Trinity 2013

Acknowledgements

I would like to express my deep sense of gratitude to my D.Phil. supervisors Prof. Philip Maini, Dr. Eammon Gaffney, Dr. Ruth Baker and Dr. Alex Fletcher for their guidance, support, patience and constant encouragement. As I came from a biological background the guidance provided by my supervisors was crucial for the successful completion of my D.Phil. work. I am grateful to them for providing the opportunities for me to develop as a researcher during the course of my D.Phil.

This D.Phil. project was of an interdisciplinary nature and its progress would not have been possible without the very productive collaboration with Prof. Jordan Raff's group at the Sir William Dunn School of Pathology (University of Oxford). In particular, I would like to thank Dr. Paul Conduit for performing the necessary experiments. I would also like to thank Dr. Omer Dushek for guidance with the mathematical analysis of FRAP data as well as the numerous discussions that helped to shape this research.

This research was funded by a Clarendon Scholarship. I am indebted to Linacre College and especially to my college advisor, Prof Shonil Bhagwat, for all the support that has been extended to me during the course of study. I would like to thank the European Society for Mathematical and Theoretical Biology, the Society for Mathematical Biology, Linacre College and the Mathematical Institute (University of Oxford) for providing financial support for attending conferences.

Taught courses during the first year of my D.Phil. were very valuable and I would like to thank all the course instructors, demonstrators and the doctoral training centre (DTC) staff. I acknowledge the current and former DTC programme directors Profs. David Gavaghan, Charlotte Dean, Elspeth Garman and Dr. James Wakefield for designing the courses and

supporting progress during my D.Phil. My short project was completed under the supervision of Dr. Radek Erban and I am grateful to him for his invaluable guidance during and after the completion of the project.

I would like to acknowledge Dr. Ruth Baker, Prof. Philip Maini and Dr. Gail Preston for giving me the opportunity to demonstrate in undergraduate as well as DTC courses.

It has been a pleasure working at the Centre for Mathematical Biology (CMB) and I thank all the academic staff and colleagues in the group for an excellent research environment. I would like to thank my collegues Louise Dyson, Gabriel Rosser, Thomas Woolley and Kit Yates whose expertise in mathematical techniques I have benifitted from during my studies. I am also grateful to my office-mates Louise, Aaron, Gabriel and Jessica for several useful discussions and a very lively lab atmosphere. I am thankful to the administrative assistants from the DTC, CMB as well as Linacre College for making my stay in Oxford run smoothly.

My stay in Oxford was made most enjoyable by my husband Dr. Prashant Potnis. His constant support and encouragement throughout my D.Phil. has been invaluable. I cannot thank my parents enough for providing me with a good education as well as the mental and financial support which allowed me to secure a place at Oxford. Their faith in me has helped me persevere through the D.Phil. My brother, Aditya, has also been very supportive and ensured that I stay updated with any interesting movies and books. I am grateful to my parents-in-law, my sister-in-law and her family for being kind and understanding through the course of my D.Phil. I would also like to take this opportunity to thank all my friends in and out of Oxford who supported and encouraged me from time to time.

Abstract

Centrosomin (Cnn) is an integral centrosomal protein in *Drosophila* with orthologues in several species, including humans. The human orthologue of Cnn is required for brain development with Cnn hypothesised to play a similar role in *Drosophila*. Control of Cnn incorporation into centrosomes is crucial for controlling asymmetric division in certain types of *Drosophila* stem cells. FRAP experiments on Cnn show that Cnn recovers in a peculiar fashion, which suggest that Cnn may be incorporated closest to the centrioles and then spread radially outward, either diffusively or advectively. The aim of this thesis is to understand the mechanism of Cnn incorporation into the *Drosophila* centrosomes, to determine the mode of transport of the incorporated Cnn, and to obtain parameter estimates for transport and biochemical reactions.

A crucial unknown in the modelling process is the distribution of Cnn receptors. We begin by constructing coupled partial differential equation models with either diffusion or advection as the mechanism for incorporated Cnn transport. The simplest receptor distribution we begin with involves a spherical, infinitesimally thick, impermeable shell. We refine the diffusion models using the insights gained from comparing the model output with data (gathered during mitosis) and through careful assessment of the behaviour of the data. We show that a Gaussian receptor distribution is necessary to explain the Cnn FRAP data and that the data cannot be explained by other simpler receptor distributions. We predict the exact form of the receptor distribution through data fitting and present preliminary experimental results from our collaborators that suggest that a protein called DSpd2 may show a matching distribution. Not only does this provide strong experimental support for a key prediction from our model, but it also suggests that DSpd2 acts as a Cnn receptor.

We also show using the mitosis FRAP data that Cnn does not exhibit

appreciable radial movement during mitosis, which precludes the use of these data to distinguish between diffusive and advective transport of Cnn. We use long time Cnn FRAP data gathered during S-phase for this purpose. We fit the S-phase FRAP data using the DSpd2 profiles gathered for time points corresponding to the Cnn FRAP experiments. We also use data from FRAP experiments where colchicine is injected into the embryos to destroy microtubules (since microtubules are suspected to play a role in advective transport of Cnn). From the analysis of all these data we show that Cnn is transported in part by advection and in part by diffusion. Thus, we are able to provide the first mechanistic description of the Cnn incorporation process. Further, we estimate parameters from the model fitting and predict how some of the parameters may be altered as nuclei progress from S-phase to mitosis. We also generate testable predictions regarding the control of the Cnn incorporation process. We believe that this work will be useful to understand the role of Cnn incorporation in centrosome function, particularly in asymmetrically dividing stem cells.

Contents

List of Figures

Table 1: Abbreviations used throughout this text and their meaning.

Abbreviation	**Explanation**
Cnn	Centrosomin
GFP	Green fluorescent protein
RFP	Red fluorescent protein
MTOC	Microtubule organising centre
FRAP	Fluorescence recovery after photobleaching
PCM	Pericentriolar matrix
TACC	Transforming acidic coiled coil
NEBD	Nuclear envelope break-down
Asl	Asterless
MSPS	Microtubule-associated protein minispindles
DSpd2	*Drosophila* spindle defective protein 2
CENPJ	Centromere associated protein J
MCPH1	Microcephalin-1
ASPM	Abnormal spindle-like microcephaly-associated
CDK5	Cyclin-dependent kinase 5
CDK5RAP2	Cyclin-dependent kinase 5 regulatory associated protein 2
NuMA	Nuclear mitotic apparatus protein
mGSC	Male germline stem cell
AU	Arbitrary units
PDE	Partial differential equation
ODE	Ordinary differential equation
FTCS	Forward time central space
FEM	Finite element method
BDF	Backward differentiation formula
NDF	Numerical difference formula
DAE	Differential algebraic equation
CFL	Courant Freidrich Lewy
LASER	Light amplified by stimulated emission of radiation

Chapter 1

Introduction

Faithful cell division and precise segregation of genetic information into the resulting daughter cells is the bedrock of life. Several molecular machineries work in tandem to ensure the fidelity of cell division. The centrosomal machinery is a notable example. Centrosomes are responsible for forming the bipolar spindle during cell division. A bipolar spindle is crucial to ensure the faithful segregation of chromosomes into the two daughter cells. Centrosomes are ubiquitous in all eukaryotes with the exceptions of higher plants and yeasts (Marshall, 2009). Components of this machinery have been shown to play a role in cell division, establishing cell polarity and locomotion (Nigg and Raff, 2009). Centrosomes were first described by Theodor Boveri in 1888. They are located at the mitotic spindle poles, a location in dividing cells to which sister chromosomes migrate during mitosis. Like DNA, centrosomes duplicate only once per cell division cycle and show dynamic features throughout the cell cycle (Alberts et al., 2002). Understanding their structure and maturation dynamics is important in understanding the control of cell division. In this chapter we describe the structure and function of centrosomes (Sections 1.1-1.2), with a focus on an integral centrosomal protein called Centrosomin (Cnn). The functional importance of Cnn in centrosome function is described in Section 1.3. In Section 1.4 we describe the

experiments performed with Cnn and the peculiar results of these experiments which have prompted this mathematical study. In Section 1.5 we proceed to describe the previous mathematical analyses of similar experiments. Lastly, in Section 1.6 we state the biological questions that we aim to address with this work and the approaches we will take to address them.

1.1 Structure of centrosomes

Centrosomes are important cellular organelles. They are amorphous, i.e., they are formless and are not bound by a membrane. They have at their core one or two centrioles, depending upon the stage of the cell cycle. Centrioles are complex, cylindrical, microtubule-based structures. Figure 1.1 shows an electron micrograph of a pair of human centrioles. The side view (left panel) shows the cylindrical structure and a near-orthogonal arrangement. The two centrioles are connected by electron-dense filamentous structures at their base (not visible in this micrograph). The older of the two centrioles, the mother centriole, harbours appendages at its distal end. These appendages aid in anchoring the centriole to the plasma membrane during the formation of cilia or flagella (Gönczy, 2012). The cross section (right panel) shows the microtubule triplets arranged in ninefold radial symmetry. In early *Drosophila* embryos, the centrioles are roughly 200 nm in diameter and 200 nm in length, and have microtubule doublets (in contrast to human centrioles) (Martins et al., 2010). Apart from forming the core of the centrosomes, centrioles also serve as basal bodies during the formation of cilia and flagella. In a centrosome, the centrioles are surrounded by a matrix of proteins called the pericentriolar matrix (PCM) (Debec et al., 1999). The PCM consists of several hundred proteins such as Asterless (Asl), Centrosomin (Cnn), Spd2, AuroraA, γ-tubulin, transforming acidic coiled coil (TACC) protein and Msps (Bettencourt-Dias and Glover, 2007; Nigg and Stearns). Centrosomes organise

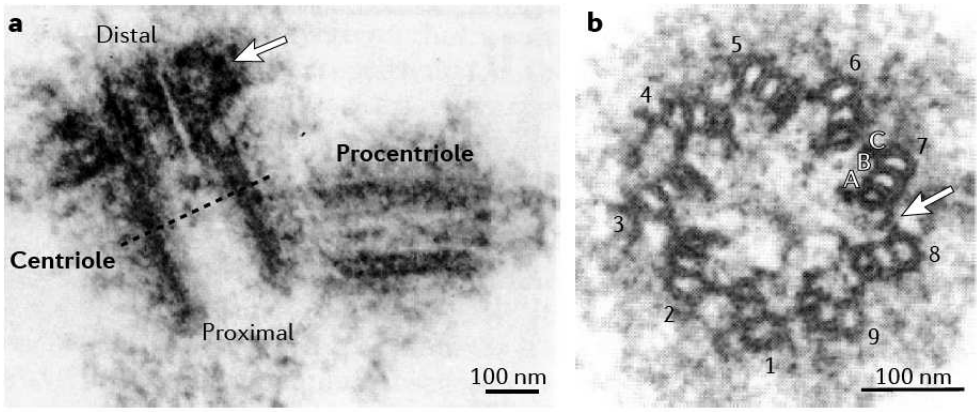

Figure 1.1: (a) *Side view of a centriole pair embedded in resin. A mature mother centriole with the distal appendages (indicated by the arrow) and a developing daughter centriole, also known as the procentriole, can be seen. When the centriole serves to form a cilium or a flagellum, the appendages help anchor the centriole to the plasma membrane. The black dashed line denotes the rough position at which a cross section of the centriole is viewed in part b.* (b) *The cross sectional view of the centriole exhibits the classic ninefold radial symmetry with nine microtubule triplets (numbered). Each microtubule filament of a triplet is identified as A, B and C. The A microtubule from one triplet is connected to the C microtubule of the next via the A-C linker, indicated by the arrow. Reprinted with permission from Macmillan Publishers Ltd: [Nature Reviews. Molecular Cell Biology] (Gönczy, 2012), Copyright (2012).*

astral as well as spindle microtubules in animal cells and are a major microtubule organising centre (MTOC) (Alberts et al., 2002). An MTOC is an assembly site for microtubules and contains proteins, such as γ-tubulins, that nucleate microtubule arrays (Pereira and Schiebel, 1997). Figure 1.2 shows a schematic representation of a centrosome.

1.1.1 Centrosome cycle

As a cell progresses through the cell cycle, the centrosomes duplicate exactly once. A dividing cell has two centrosomes during mitosis, each of which has a pair of centrioles at its core. As the two daughter cells separate, each daughter inherits one of the centrosomes with its pair of centrioles. During the G1 phase of the cell cycle, the

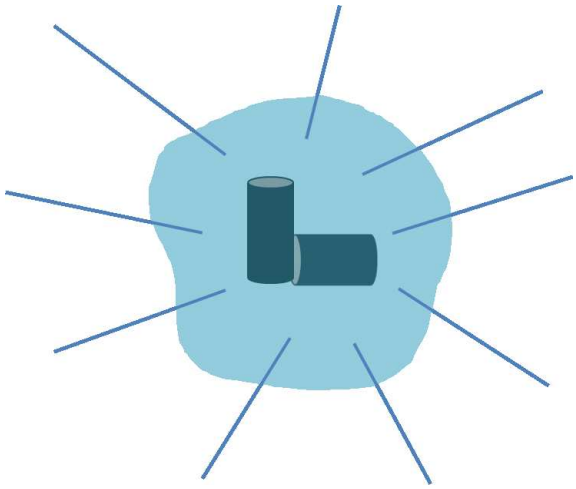

Figure 1.2: *Schematic representation of a centrosome. The cylinders in the middle indicate a pair of centrioles. The centrioles are always positioned roughly orthogonally to each other (Gönczy, 2012). The amorphous blue matrix around the centrioles represents the matrix of proteins called the pericentriolar matrix (PCM). During the cell cycle, only one of the centrioles, namely the mother centriole, actively recruits PCM* (Conduit et al., 2010). *The straight lines emanating from the PCM denote the filamentous microtubules.*

two centrioles in a centrosome separate from each other, in a process called 'disengaging'. During S-phase, the separated centrioles each help in assembling a daughter centriole. These processes of centriole duplication, length control and maturation are tightly regulated. Proteins involved in these processes are conserved across diverse species (Azimzadeh and Marshall, 2010). The daughter centrioles continue to elongate throughout the G2 phase. Towards the beginning of mitosis the resulting two pairs of centrioles begin to move to opposite poles of the nucleus and organise the PCM. This process is called centrosome maturation. At the end of mitosis, the two centrosomes are located at the two poles of the dividing cell, ready to be inherited by the resulting daughters. Figure 1.3 shows a schematic of the centrosome cycle with respect to the cell cycle stages (Nigg and Raff, 2009).

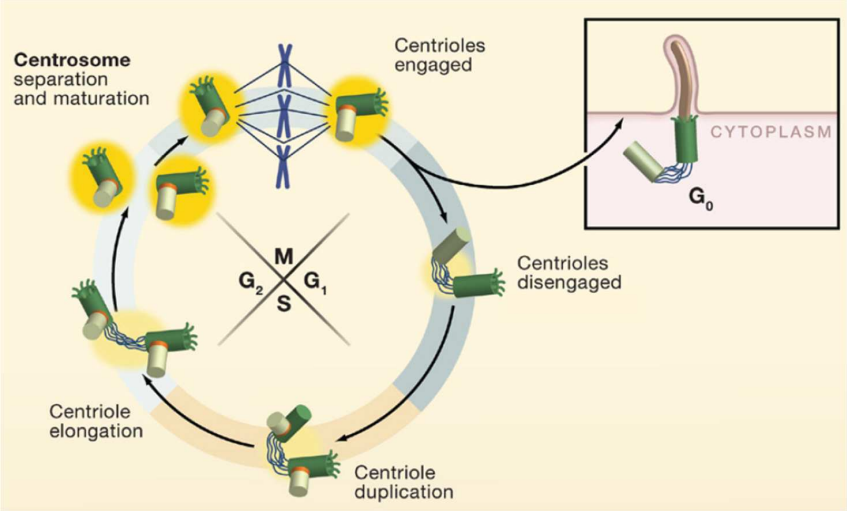

Figure 1.3: *Schematic representation of the centrosome cycle with respect to the cell cycle. When the two daughter cells separate after mitosis, each daughter inherits a centrosome with its pair of centrioles. If the daughter cell enters G0-phase (i.e. the resting phase), the centriole may form a basal body and participate in the formation of a flagellum or a cilium (as shown in the box). If the daughter enters G1-phase, the centriole pair disengages and biogenesis of two new centrioles begins. The daughter centrioles grow through S-phase. Towards the end of G2-phase the filamentous structure holding the original pair of centrioles together breaks and the two centriole pairs separate. Each centriole pair begins to accumulate PCM to form mature centrosomes. The two centrosomes move towards the two spindle poles during M-phase and organise spindle microtubules. Reprinted from Cell, 139(4), E. A. Nigg and J. W. Raff, Centrioles, centrosomes, and cilia in health and disease, 663-678, Copyright (2009), with permission from Elsevier.*

1.2 Function of centrosomes

Centrosomes are responsible for the formation of a bipolar spindle during cell division. A bipolar spindle assembly is required to ensure correct segregation of chromosomes into two daughter cells. Centrosomes have been shown to be essential for embryonic cell division in *Xenopus* and *C. elegans*, as well as in *Drosophila* (Nigg and Raff, 2009). However, centrosomes are not essential in several cell types. For example, plants and yeasts do not have centrosomes. An adult *Drosophila* without centrosomes can survive, provided the centrosomes were functional (and maternally

provided) during development (Basto et al., 2006). Cells in these systems are capable of organising the bipolar spindles in a centrosome-independent manner (Kalab and Heald, 2008). Even though centrosomes are dispensable for bipolar spindle assembly, they are required when orientation of spindle apparatus is important for faithful division. This is observed in asymmetrically dividing stem cells such as *Drosophila* neuroblasts and male germline stem cells (mGSCs) in *Drosophila* and *C. elegans* (Gonczy, 2008; Yamashita et al., 2007). In the absence of functional centrosomes, about 30% of *Drosophila* neuroblasts and about 35% mGSCs exhibit faulty asymmetric division, as judged by factors such as the orientation of spindle and segregation of cell-fate determinants (Basto et al., 2006; Yamashita et al., 2003). The function provided by the centrosomes appears to be two-fold. Firstly, the astral microtubules organised by the centrosomes are crucial in determining the polarity of division which, in turn, allows for proper segregation of cell-fate determinants into the two daughter cells. Secondly, the centrosomes themselves are organised asymmetrically in these cells. One of the centrosomes organises more PCM than the other and thereby generates a more robust microtubule aster than the other (Nigg and Raff, 2009; Nigg and Stearns). Apart from these, functional centrioles – a core component of centrosomes – are required for assembly of cilia and flagella in differentiated cells. These cellular appendages have functions in motility and sensory perception (Bettencourt-Dias and Glover, 2007; Nigg and Raff, 2009). Centrosomal function has also been shown to be important in meiosis in male spermatogonia in *Drosophila* (Yamashita et al., 2007).

1.2.1 Centrosomes and human diseases

Due to the role of centrosomes in formation of the bipolar spindles, it was believed that the centrosomes may be essential for maintaining genomic stability. This view was further strengthened by observations of various cancers. Cancers such as liposarcoma, cervical, prostate, breast, adrenocortical, bladder carcinomas, as well as

several lymphomas and leukemias, show genomic instability. These cells also show centrosome amplification, which can potentially form multipolar spindles (Zyss and Gergely, 2009; Harrison et al., 2011). However, no direct evidence has been found for this claim (Nigg and Stearns). Castellanos et al (2008) have shown that *Drosophila* larval brains with dysfunctional centrosomes develop tumours. They have further shown that these tumours are not due to a genome instability but may arise due to the failure of asymmetric division of neuroblasts (Castellanos et al., 2008).

Another human disease where function of centrosomes appears to be crucial is 'autosomal recessive primary microcephaly' (MCPH). This is a genetic condition where the brain is structurally normal, but shows a reduction in size due to a reduction in the number of brain cells. All proteins that are mutated in MCPH have centrosomal functions (Bond and Woods, 2006; Megraw et al., 2011). *Drosophila* neuroblasts divide to produce a larger daughter that retains stemness and a smaller daughter called the 'ganglion mother cell' that differentiates to generate neurons. This asymmetric division is impaired in a small proportion of neuroblasts in the absence of functional centrosomes. It is possible that dysregulation of neuroblast asymmetric division may result in fewer neurons, a condition similar to microcephaly, even though the effects are not as pronounced as in humans (Gonzalez, 2008).

1.3 Centrosomin (Cnn)

Cnn was first described in 1995 by Heuer et al. (1995). Li et al (1996) showed that Cnn is an essential component of the centrosomes. Cnn is shown to be incorporated in centrosomes throughout the cell cycle in the syncytial blastoderm stage (Li and Kaufman, 1996) that is, the first fourteen nuclear division cycles in *Drosophila* embryogenesis. Observing Cnn incorporation in centrosomes during this stage has re-

vealed the dynamic features of centrosomes. Centrosomes appear to extrude chunks of PCM proteins that may completely break away from the PCM around the centrioles. These extrusions are called 'flares'. The flare particles are believed to travel along the astral microtubules (Megraw et al., 2002). After this stage, Cnn incorporation into the centrosomes is only observed during mitosis. In adult *Drosophila* Cnn has been shown to be expressed in various tissues, such as the testes and the ovaries, in a cell-cycle-dependent manner (Li and Kaufman, 1996).

Cnn is important for embryonic development. Products of the Cnn gene are supplied to the embryos maternally in *Drosophila*. Several Cnn mutants are available in which mutant Cnn protein is expressed but fails to be incorporated in the centrosomes. If both copies of the Cnn gene in a female fly are mutated, the fly lays eggs which are fertilised but do not develop beyond the first fourteen nuclear division cycles. Thus, female flies homozygous for Cnn mutation are sterile (Megraw et al., 1999; Vaizel-Ohayon and Schejter, 1999). The spindles in these embryos appear irregular. The spindle poles lack key proteins such as CP60, CP190 and γ-tubulins. These are integral proteins in the wild type centrosomes that form the poles of the spindle apparatus. For example, γ-tubulins act as nucleating centres for microtubules (Pereira and Schiebel, 1997). Consistent with this, no astral microtubules can be detected. This shows that centrosomes that are devoid of functional Cnn cannot nucleate spindle fibres (Megraw et al., 1999). During the first fourteen nuclear divisions in the embryo nuclei migrate with respect to each other in an orderly manner such that by the tenth division cycle most of the nuclei have migrated to the periphery of the embryo. This process is called cortical migration. Adjacent centrosomal apparati have to be separated from each other in order to ensure fidelity of this process. Cnn mutations give rise to disruption of cortical migration resulting in disordered nuclear arrangement (Vaizel-Ohayon and Schejter, 1999; Megraw et al., 1999). Mutant embryos exhibit

multipolar spindles (in contrast to the usual bipolar spindles) forming rosettes or chains and spindles with excess amounts of DNA. Thus it is hypothesised that Cnn may be required to maintain the correct spacing between the adjacent spindle apparatus through astral microtubules (Vaizel-Ohayon and Schejter, 1999). It has been further hypothesised that the PCM flares may achieve this function by organising the actin cytoskeleton during the syncytial stage (Megraw et al., 2002).

As such, Cnn function in centrosomes appears to be essential for rapid, high fidelity divisions such as in the syncytium and during spermatogenesis. However, no lethal mutant of Cnn in adult *Drosophila* has been described. This suggests that Cnn may be dispensable for most somatic divisions (Vaizel-Ohayon and Schejter, 1999). However, Cnn mutations have been shown to reduce the fidelity of asymmetric stem cell divisions in *Drosophila* neuroblasts as well as mGSCs (Gonzalez, 2008; Yamashita et al., 2007). Thus, Cnn may control neurogenesis by controlling the balance between asymmetric and symmetric divisions of neuronal progenitors (Bond and Woods, 2006). This hypothesis is based on the observation that *Drosophila* Cnn is an orthologue of one of the proteins mutated in human microcephalies, called cyclin-dependent kinase 5 regulatory associated protein 2 (CDK5RAP2) (Bond and Woods, 2006). Understanding Cnn dynamics may, therefore, provide insights into the control of asymmetric stem cell division.

1.4 Previous experiments with Cnn

Our experimental collaborators, Prof. Jordan Raff and Dr. Paul Conduit (Dunn School of Pathology, University of Oxford), have been studying how Cnn is incorporated into the PCM and its role in PCM organisation. They use Cnn fluorescently labelled with either green fluorescent protein (GFP) or red fluorescent protein (RFP)

in the background of Cnn null mutant *Drosophila* and observe how it is recruited to the centrosomes. Using the Cnn null background is important so as to ensure that the native (i.e. non-fluorescent) Cnn does not interefere with the results. They use various *Drosophila* systems, such as the syncytial blastoderm, as well as neuroblasts, for their observations. In this section we explain the biology of the syncytial blastoderm of *Drosophila* and the advantages of using it as a model system. We then explain the various experiments performed with Cnn and how the results of these experiments raise interesting questions about the mechanism of Cnn incorporation into the PCM.

After a *Drosophila* egg is laid, the nucleus undergoes several rounds of division. In the first fourteen divisions, cell division is not complete, as the cell envelope never forms around the divided nuclei. Therefore, during these stages the egg is called the syncytium, meaning a multinucleate cell. By the end of the eighth nuclear division, all the nuclei migrate towards the periphery of the ellipsoidal egg. The tenth to fourteenth nuclear division cycles are together called the syncytial blastoderm stage (Gilbert, 2000). Figure 1.4 shows the various nuclear division cycle stages. Studying nuclear divisions in this stage offers several advantages. Firstly, all the nuclei divide synchronously. Thus, while an experiment is being performed on one of the nuclei, the others serve to identify the cell cycle stage. Secondly, many nuclei can come into focus simultaneously under a microscope as they are all peripherally positioned. Lastly, eggs in the syncytial blastoderm stage are much easier to obtain than, say, neuroblasts. Our collaborators have shown that the amount of Cnn in the centrosomes of the syncytial blastoderm increases throughout interphase and remains steady during mitosis. Figure 1.5(a) shows how the total amount of Cnn in the centrosomes changes during the cell cycle. Our collaborators have also measured the fluorescence intensities along a diameter through the centrosomes of *Drosophila* embryos expressing GFP-Cnn and have shown that Cnn forms a gradient through the centrosomes

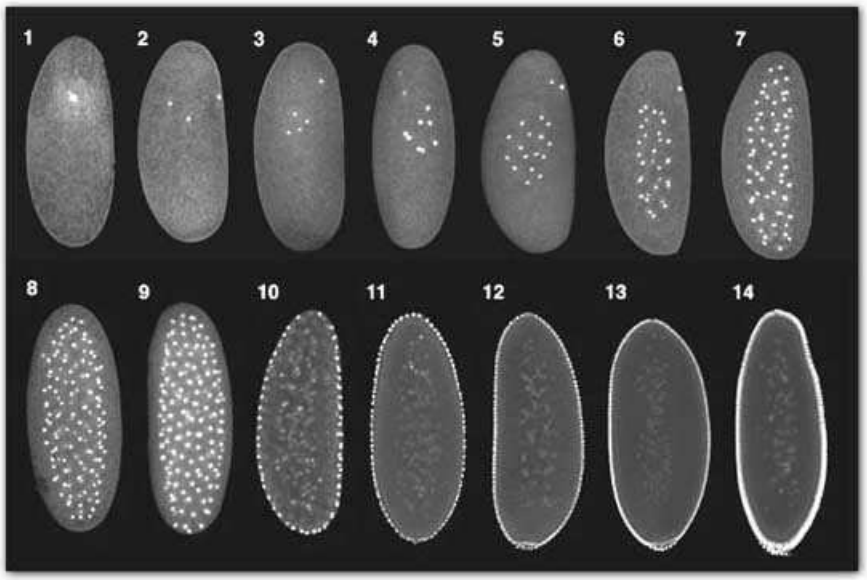

Figure 1.4: *Stages in early development of Drosophila. The numbers identify the nuclear division cycles. The nuclei, seen as fluorescent spots, complete their migration to the periphery by the tenth division and further nuclear divisions occur at the periphery of the embryo. Reproduced with permission from Prof. William Sullivan* (Sullivan, 2002).

(Figure 1.5(b)). Thus, Cnn concentration peaks at the centre of the centrosome and it decreases radially outwards.

Lastly, our collaborators have used fluorescence recovery after photobleaching (FRAP) experiments to study the incorporation of Cnn into the *Drosophila* centrosomes. Figure 1.6 schematically describes the idea behind the FRAP experiment. The FRAP technique was initially developed for studying the two-dimensional diffusion of proteins (Axelrod et al., 1976) in, for example, a cell membrane. However, it is now widely applied to study the diffusion (or transport) of various cellular or extracellular proteins. When FRAP experiments are performed on embryos with fluorescent Cnn, the peculiar recovery kinetics shown by Cnn can be observed. Figure 1.7 shows the recovery kinetics exhibited by a different centrosomal protein TACC and by Cnn during S-phase. The protein TACC is also recruited to the centrosomes and is responsible

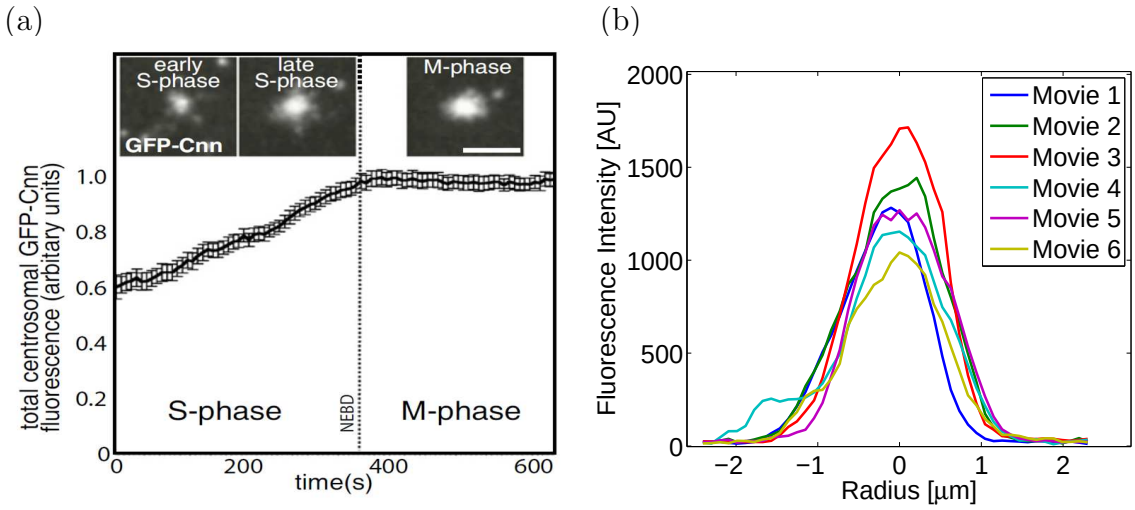

Figure 1.5: (a) *Total Cnn fluorescence in the centrosomes increases throughout S-phase and remains constant during mitosis. Fluorescence is measured in arbitrary units and is normalised by dividing with the maximum intensity. NEBD denotes the time point at which the nuclear envelope breaks down. Reprinted from Current Biology, 20, P. C. Conduit, K. Brunk, J. Dobbelaere, C. I. Dix, E. P. Lucas and J. W. Raff, Centrioles regulate centrosome size by controlling the rate of Cnn incorporation into the PCM, 2178-2186, Copyright (2010), with permission from Elsevier.* (b) *From the data obtained by our collaborators, we gather the fluorescence intensities along a diameter through centrosomes of various Drosophila embryos expressing GFP-Cnn. Zero µm indicates the centre of the centrosome. The inset box identifies the results from the various embryos studied.*

for stabilising microtubules during mitosis. Both of these proteins localise at the centrosome. When a centrosome containing GFP- and RFP-tagged TACC is bleached, TACC begins to recover everywhere in the centrosome simultaneously and evenly. However, when a centrosome containing GFP- and RFP-tagged Cnn is bleached, Cnn recovers initially only in the centre of the centrosome and slowly spreads outwards. Embryos expressing only GFP-Cnn (and not both RFP- and GFP-Cnn) are usually used for FRAP experiments. Both the fluorescent molecules were used in the experiment described above in order to have a template of the centrosomes against which the recovery of Cnn can be compared (Conduit et al., 2010). Figure 1.8 shows the relative recovery of Cnn (and TACC) in the centre of the centrosome versus in

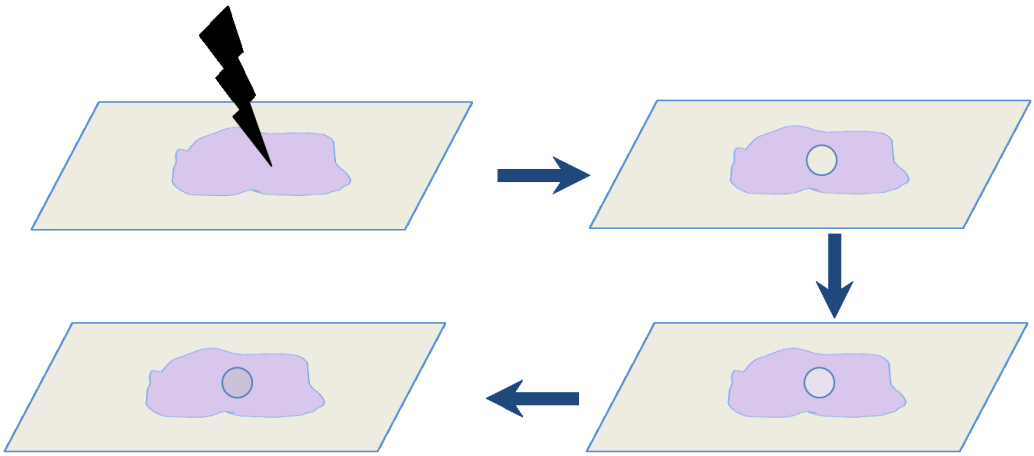

Figure 1.6: *Schematic representation of the FRAP experiment. A high intensity light amplified by stimulated emission of radiation (LASER) is shone on a region of a fluorescent sample on a glass slide. This 'bleaches' the region, i.e., destroys the fluorescence in that region (denoted in the diagram by an uncoloured circular region). If the fluorescent species is diffusible (or is transported by some means) then the fluorescence in the bleached region recovers with time. Observing the kinetics of this recovery helps one study the rate of diffusion (or transport) and any binding-unbinding reactions that may be taking place in the bleached region.*

the flares during S-phase. It can be seen that Cnn only recovers in the centrosomes and not in the flares, whereas TACC recovers both in the centrosomes as well as the flares (Conduit et al., 2010). As shown in Figure 1.7, Cnn fluorescence begins recovery in the centre of the PCM and slowly spreads radially outwards. Another way to understand this is to plot the recovery of Cnn in the central PCM region versus peripheral PCM regions. Conduit et al. (2010) have studied such recovery for Cnn as well as several other PCM proteins. Figure 1.9 shows how Cnn recovery during S-phase starkly differs from the other PCM components. Cnn recovers initially only in the centre of the PCM whereas other PCM components recover everywhere in the PCM.

It should be noted that the component proteins in the PCM are not synthesised in the centrosome and that these component proteins are present in the cytoplasm

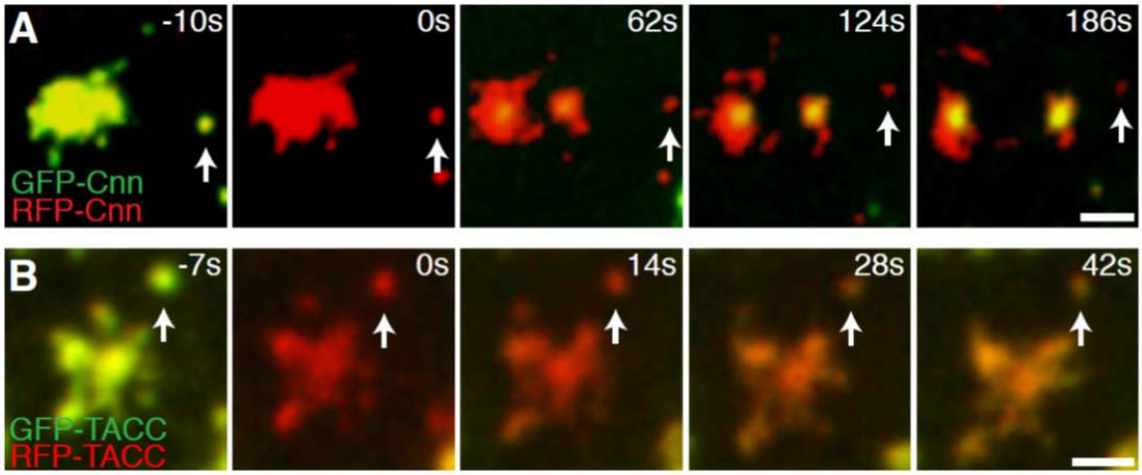

Figure 1.7: *Fluorescence recovery shown by Cnn (upper panel) and another centrosomal protein TACC (lower panel). Both GFP- and RFP- tagged Cnn (or TACC) are expressed in the Drosophila embryo. Only the GFP-tagged protein is bleached using LASER. The bleached area includes the whole centrosome. The RFP-tagged protein provides a template against which the recovery of the GFP-tagged protein is observed over time. Notice that, in the case of the TACC protein, the recovery of green fluorescence occurs uniformly everywhere in the PCM. However, in the case of Cnn, recovery begins at the centre of the PCM and the fluorescence then appears to spread radially outwards. In the case of Cnn, the images show a dividing centrosome, whereas in the case of TACC only one centrosome with flares is shown. White arrows point to the PCM flares. Notice also that Cnn never recovers in the flares, whereas TACC does. Scale bar indicates* 3 μm. *Reprinted from Current Biology, 20, P. C. Conduit, K. Brunk, J. Dobbelaere, C. I. Dix, E. P. Lucas and J. W. Raff, Centrioles regulate centrosome size by controlling the rate of Cnn incorporation into the PCM, 2178-2186, Copyright (2010), with permission from Elsevier.*

at much smaller concentrations. Therefore, the accumulation of these proteins in the centrosome implies that they may bind to the PCM. The recovery dynamics of PCM components other than Cnn suggest that these proteins may recover uniformly by binding uniformly to an underlying PCM matrix. The peculiar Cnn recovery dynamics, which is in contrast to these other PCM components, suggests that Cnn recovery (and indeed incorporation) must be governed by some unique, and as yet unidentified, mechanisms.

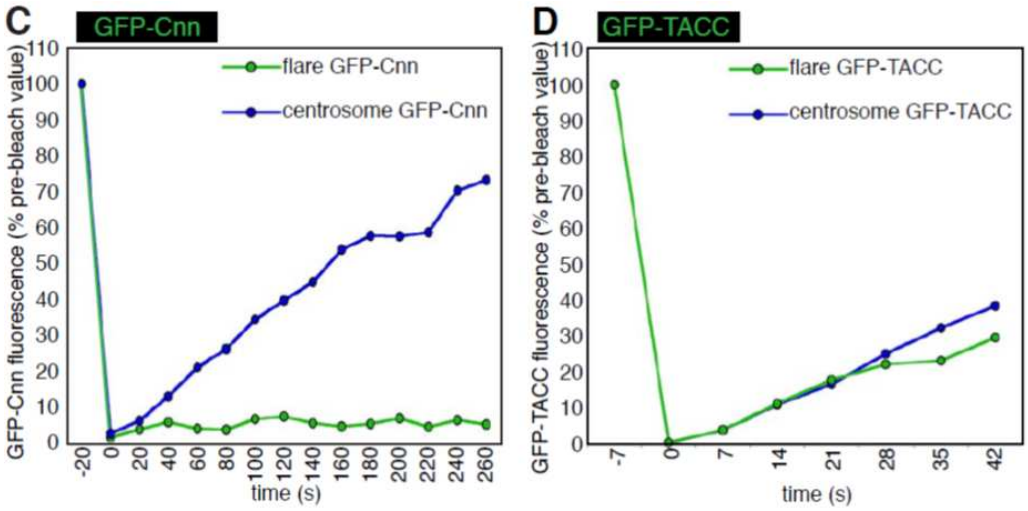

Figure 1.8: *Average GFP fluorescence intensity relative to the pre-bleached intensity of the four central pixels at the centrosome (blue lines) and at PCM flares (green lines) is shown for both Cnn (left panel) and TACC (right panel). Notice that in the case of Cnn, GFP fluorescence recovers in the centrosomes but not in the flares, whereas for TACC it recovers everywhere. Reprinted from Current Biology, 20, P. C. Conduit, K. Brunk, J. Dobbelaere, C. I. Dix, E. P. Lucas and J. W. Raff, Centrioles regulate centrosome size by controlling the rate of Cnn incorporation into the PCM, 2178-2186, Copyright (2010), with permission from Elsevier.*

1.5 Mathematical modelling background

To our knowledge, this thesis represents the first mathematical study of Cnn incorporation dynamics. However, the FRAP technique has been used widely for studying various reaction-transport systems. In this section we describe various mathematical approaches used to analyse FRAP data. The FRAP technique was initially described by Peters et al. (1974). They called it fluorescence photobleaching recovery (FPR). Their method was greatly modified via the use of a circular (axisymmetric) bleach spot to allow rigorous analysis of the data generated by the technique (Axelrod et al., 1976). They used a solution of a fluorescent dye (rhodamine 6G) on a glass slide. In their theoretical analysis, they considered both diffusive and advective transport

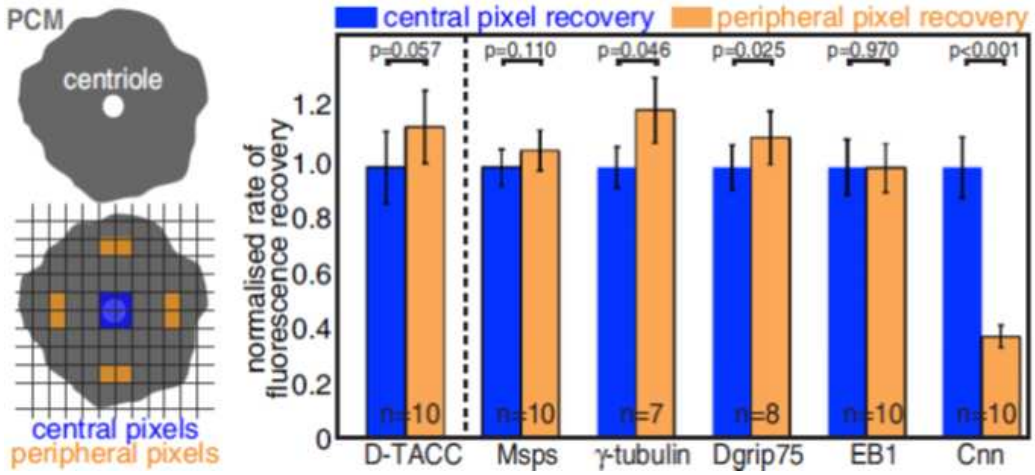

Figure 1.9: *The left panel is a schematic diagram of central (blue) and peripheral (orange) pixels used to study recovery of various PCM components. The right panel shows the rates of initial fluorescence recovery for various PCM components in the centre of the PCM and in the peripheral regions of the PCM. It can be seen that initially most PCM components show slightly greater recovery rates in the peripheral regions, whereas Cnn shows much greater recovery in the central region than in the peripheral regions. Reprinted from Current Biology, 20, P. C. Conduit, K. Brunk, J. Dobbelaere, C. I. Dix, E. P. Lucas and J. W. Raff, Centrioles regulate centrosome size by controlling the rate of Cnn incorporation into the PCM, 2178-2186, Copyright (2010), with permission from Elsevier.*

mechanisms. Thus, they considered an equation of the form

$$\frac{\partial u(x,y,t)}{\partial t} = D\nabla^2 u(x,y,t) - a\frac{\partial u(x,y,t)}{\partial x}, \tag{1.5.1}$$

where $u(x,y,t)$ denotes concentration of the fluorescent species at position (x,y) and time t, D denotes the diffusion coefficient. The authors only considered advection in the x-direction and a denotes the advection velocity in that direction. They worked with a system that was homogeneous before the FRAP experiment. In the FRAP set up used by the authors, the bleached area was the same as the observation area. Since the observation (or bleached) area was much smaller than the glass slide, the boundary conditions were of inhomogeneous Dirichlet form, $u(x \to \infty, y \to \infty, t) = u_0$. The

fluorescence was assumed to be proportional to the concentration, u, i.e. the possibility of quenching was not considered. Different initial conditions were used depending upon whether the bleaching was uniform circular or whether it had a Gaussian profile. Fluorescence in the bleached region was integrated over the bleached area to obtain a single fluorescence value for each time. The time series of this total fluorescence was plotted and is known as the FRAP curve. Equation (1.5.1) was solved (either analytically or numerically, depending upon the profile of the bleaching beam) for three separate cases of (a) $D \neq 0,\ a = 0$, (b) $D = 0,\ a \neq 0$ and (c) $D \neq 0,\ a \neq 0$. This pioneering work provided initial guidelines for both theoretical as well as practical aspects of FRAP measurements and methods of distinguishing between different transport mechanisms.

Early FRAP analysis revolved around studying the diffusion of proteins in the cell membrane, where chemical fluorescent dyes, such as fluorescein or rhodamine, were used (Axelrod et al., 1976). The bleaching beam used was circular with either Gaussian intensity profile or uniform intensity profile. Because of these factors the models could be written in plane polar coordinates. The discovery and subsequent adaptation of GFP allowed individual cellular proteins to be tagged and monitored. The optical properties of GFP made it a popular fluorescent tag for FRAP studies (Lippincott-Schwartz et al., 2001). Observations of cell-internal structures in live cells was made possible by the advent of confocal LASER scanning microscopes. Even the three-dimensional reconstruction of cellular structures was possible through the optical sectioning ability of confocal microscopes (Phair and Misteli, 2001). The LASER scanning beam allowed for non-circular bleach regions to be used. Also, the new microscopy technique allowed the bleached region to be smaller than the observation region (Kang et al., 2009).

These technological advances necessitated construction of more and more complex mathematical models. A number of research groups have tackled various cellular systems and different aspects of FRAP modelling. For example, the kinetic properties of various nuclear proteins were studied by a number of groups (Phair and Misteli, 2000; Carrero et al., 2003; Mueller et al., 2010). The diffusion coefficients of proteins depend upon the mass of the proteins as well as the viscosity of the medium in which they diffuse. The retardation in recovery of proteins may not be because of the additional mass of the protein, since the recovery times scale extremely weakly with mass (Sprague and McNally, 2005). In cellular environments, it has been found that the estimated diffusion coefficients of various proteins are often much smaller than those expected from their molecular masses (Carrero et al., 2003; Sprague and McNally, 2005; Mueller et al., 2010). Thus, fluorescence recovery in cells is often dominated by specific or non-specific binding reactions, and the estimated diffusion coefficients denote the "effective" diffusion coefficients. Carrero et al (2003) have explored the effect of the nuclear membrane and a nuclear geometry with finite dimensions on the estimation of diffusion coefficients. Further work from their group incorporated the effect of nonspecific binding to an underlying homogeneous immobile structure, using both a reaction-diffusion model, as well as a compartmental model. The compartments in the compartmental model denoted the bleached and the unbleached regions of the nucleus (Carrero et al., 2004). Much of this analysis, however, was focused on special cases and involved making qualitative predictions. Sprague et al. (2004) provided a comprehensive analysis of a reaction-diffusion system, which can involve a single (or multiple) binding state(s). They identified regimes in which the recovery can be said to be diffusion-uncoupled (i.e. binding-dominated) or diffusion-coupled (i.e. diffusion and binding are both important). This analysis focused on a spatially homogeneous system, with a homogeneous distribution of binding sites. Further work from their group considered a system with localised binding site cluster and showed

the importance of including the spatial localisation of binding sites in estimating parameters (Sprague et al., 2006).

FRAP experiments on complex sub-cellular geometries and heterogeneous environments are often not amenable to mathematical analysis. Some studies make use of numerical solutions of the corresponding reaction-diffusion systems or even use computational approaches such as cellular automata to model their systems. For example, Müller et al. (2012) estimated the diffusion coefficients of two proteins namely, Nodal and Lefty, in Zebrafish embryos using FRAP. They used finite element methods (FEMs) to simulate the production, degradation and diffusion of these proteins in a three-dimensional domain with embryo-like geometry. Elsner et al. (2003) have studied the binding kinetics of coat proteins to Golgi membranes. They used a grid-based description of a cell, with a proportion of connected grid points representing Golgi membrane. The diffusion and binding of the coat proteins was simulated using a cellular automaton approach and the results of the simulation were compared qualitatively with experimentally obtained FRAP measurements to assess whether the coat proteins showed diffusion-limited dynamics (Elsner et al., 2003).

Most of the research mentioned above has focused on the canonical "FRAP curve", i.e. the time evolution of the total fluorescence in the bleached region. Thus, these analyses have not made explicit use of the spatial information within the bleach spot. Coarse-grained spatial information from within the bleach spot has been used, however, by some studies focusing on complex cellular structures, such as the endoplasmic reticulum (Siggia et al., 2000; Klonis, 2002). Association of various proteins with centrosomes has been studied using FRAP by some research groups (Stenoien et al., 2003; Thompson et al., 2008). However, much of this analysis has been qualitative. For example, Stenoien et al. (2003) made a comparative study of time required for half

the total recovery ($t_{1/2}$) of various proteins such as Aurora A, nuclear mitotic apparatus protein (NuMA), γ-tubulin and α-tubulin. Sprague et al. (2006), while working with transcription factor binding within a nucleus, allowed spatial heterogeneity by letting the binding rates differ between the bleached region and the surrounding region. Hallen and Layton (2010) extended this approach in the case of centrosomes, where they allowed the binding rates to vary within two concentric zones inside the bleached region. However, they do not allow for continuous variation of binding rates within the bleached region.

FRAP analysis has been performed on various biological systems ranging from membranes to nuclei to endoplasmic reticulum. It is clear from the existing research in this field that in order to obtain reliable parameter estimates the following aspects need to be considered: (a) it is important to tailor the FRAP experimental protocol to the system of interest; (b) it is crucial to consider the effect of the bleach profile, bleaching time and fluorescence loss during the course of experiment, and lastly; (c) correctly simulating the geometry and the reactions of the system of interest will improve the process of parameter estimation.

1.6 Motivation and aims

As discussed, Cnn is an integral centrosomal protein. It is responsible for recruiting other PCM components and is indispensable for functional centrosomes in *Drosophila*. The orthologue of Cnn in humans, namely CDK5RAP2, has been shown to be important for brain development as its mutation causes microcephaly (Bond and Woods, 2006). The absence of Cnn during embryonic development is fatal. In adult *Drosophila*, Cnn has been shown to be important for ensuring the asymmetric division of neuroblasts and mGSCs (Gonzalez, 2008; Yamashita et al., 2007). The differential

incorporation of Cnn in the dividing neuroblast centrosomes has been shown to determine the resulting asymmetry of centrosome sizes (Conduit and Raff, 2010). Thus, understanding the mechanism of Cnn incorporation in centrosomes may provide clues about the mechanisms of centrosome size determination.

The peculiar fluorescence recovery profile shown by Cnn raises the possibility that Cnn is incorporated in the centre of the centrosomes and spreads outwards. From their experiments our collaborators have hypothesised that Cnn may exist in two different forms, a cytoplasmic form and a centrosome-incorporated form, the latter of which moves radially outwards in the centrosome. The cytoplasmic form diffuses quickly and is present at very low concentrations throughout the syncytium, whereas the centrosome-incorporated form may exist only within the centrosomes and accummulate to large concentrations within the centrosomes. The Cnn form incorporated into the centrosomes moves much slower as compared to the cytoplasmic form (Conduit et al., 2010). The experiments of Conduit et al. (2010) have been similarly interpreted by Gomez-Ferreria and Pelletier (2010). It is not clear, however, whether this radial spread occurs by a process of diffusion or by some form of active transport. In this work we aim to understand the mechanism of Cnn incorporation and the transport process by which the Cnn gradient is established in the centrosome. Moreover, we would like to obtain parameter estimates for various reactions and transport processes in which Cnn participates within the centrosome. Parameter estimation and sensitivity analysis may help us explore how Cnn incorporation may be controlled (by suggesting the parameters to which the Cnn incorporation process is most sensitive), so that we can study how the neuroblasts differentially modulate the levels of Cnn in their centrosomes.

We begin Chapter 2 by describing the experimental process used by our collaborators

to generate the Cnn FRAP data. We have worked closely with them to develop this experimental protocol. We then describe the steps undertaken for data processing and describe various mathematical methods used throughout this work. In Chapter 3 we propose two mechanistically different models of Cnn incorporation, namely the diffusion model and the advection model. We present an analysis of these models and the results of fitting these models to Cnn data. We then document a modification of the diffusion model and the results of data fitting with this model. We conclude by summarising the insights gained from these models. In Chapter 4 we propose a further modification of the diffusion model, which involves a receptor gradient, with a justification for this modification, together with the analysis and results of data fitting for this model, followed by preliminary experimental data supporting our model. Further, we consider a reduced version of the receptor gradient model and conclude by discussing the implications of parameter estimates from the reduced model. In Chapter 5 we show how the reduced model could be used to further understand the biology of the Cnn system. We conclude, in Chapter 6, by highlighting the insights gained from this study and suggest future avenues for research into centrosomal biology.

Chapter 2

Experimental and mathematical methods

As discussed in Chapter 1, centrosomes are an important cellular organelle and Cnn is an integral centrosomal protein required for forming functional centrosomes. Cnn shows peculiar incorporation dynamics in the centrosomes that can be studied using fluorescence microscopy. In order to distinguish between the various Cnn incorporation models and to find the best-fitting model, we (together with our collaborators) refined the Cnn FRAP experiment protocol and obtained new Cnn recovery data. We worked closely with our collaborators in devising experiments that would generate data for fitting to our models. These data were gathered by our collaborator Dr. Paul Conduit (Dunn School of Pathology, University of Oxford). We describe the data generation process in Section 2.1. We processed the data further in order to make them suitable for model-fitting. We describe the data processing in Section 2.2. In Sections 2.3 and 2.4 we describe the various mathematical techniques we used for simulating and fitting models and for comparison of the various model fits.

2.1 Data collection

A number of studies have reported the use of FRAP analysis to study the dynamics of particular proteins of interest. Most of these studies have one common aspect, that the system under study is believed to be in a steady state before bleaching, and continues to remain in a steady state during the FRAP experiment (Sprague et al., 2004, 2006; Carrero et al., 2003, 2004). This ensures the subsequent recovery appropriately reflects the kinetics of diffusion (or transport) and turnover of binding-unbinding reactions, thereby simplifying the FRAP analysis process.

For this reason we decided to conduct our FRAP experiments during the cell cycle stage when the Cnn concentration reaches a steady state. As shown in Figure 1.5, the Cnn concentration in the PCM increases throughout interphase and then stays constant during mitosis. We anticipate that Cnn incorporation reaching a steady state during mitosis may be biologically meaningful. At the end of mitosis, the two centrioles disengage, the daughter centriole begins to accumulate its own PCM, and the cycle repeats again (Conduit et al., 2010). This allows a window of time, on the order of a few minutes, in which to observe the system at steady state.

If we could arrest syncytial nuclei in mitosis, we could observe the Cnn steady state for longer. Whilst it is possible to arrest cells in mitosis by adding drugs such as colchicine, the latter inhibits microtubule polymerisation and this appears to affect some aspects of Cnn incorporation. Colchicine-inhibited centrosomes accumulate Cnn for a very long time, without reaching a steady state. Thus, microtubules appear to play a role in the Cnn incorporation process. Therefore, the observation that microtubule destabilisation results in the absence of a steady state for Cnn is not surprising. However, this also means that we cannot study arrested embryos and we need to observe embryos during mitosis, while it lasts, in embryos undergoing rapid

nuclear divisions.

Drosophila syncytial embryos in stage 11 or 12 were selected for the experiments. In these stages, the nuclei are located peripherally and divide synchronously. Selecting embryos at roughly the same stage ensures that we minimise inter-embryo variation. All the data are collected on the same day, so as to ensure that there is minimal variation introduced from slightly different fly-raising conditions and differences in the LASER source used for microscopy.

A confocal fluorescence microscope is used for observing Cnn incorporation. Seven Z-images are taken through each embryo, with a vertical spacing of 400 nm between the Z-images. The pinhole diameter of the microscope used is 50 μm, which means that the thickness of each Z-image is greater than 400 nm. This ensures that there is no loss of data in-between the two consecutive Z-slices. It is known that the mother centrioles are oriented perpendicular to the embryonic membrane (Callaini and Riparbelli, 1990). Thus, the mother centriole, which is the PCM organising centriole of the pair (Conduit et al., 2010), is oriented perpendicular to the focal plane of the microscope (see Figure 2.1 for a schematic representation). A Z-image may, therefore, capture a transverse optical section through the centre of the PCM. Since centrosomes can move in the X, Y as well as Z directions, taking several Z-images increases the probability that at least one of the images captures the fluorescence through the centriole, i.e., through the centre of the centrosome. For the FRAP experiment, a centrosome from an embryo that has just gone into mitosis is chosen, and a bleaching radius of 2.5 μm is empirically selected. This ensures that the bleach spot is larger than the distance over which the Cnn fluorescence falls to cytoplasmic levels. Images are captured every 10 seconds until the centrioles begin to disengage and separate at the end of mitosis.

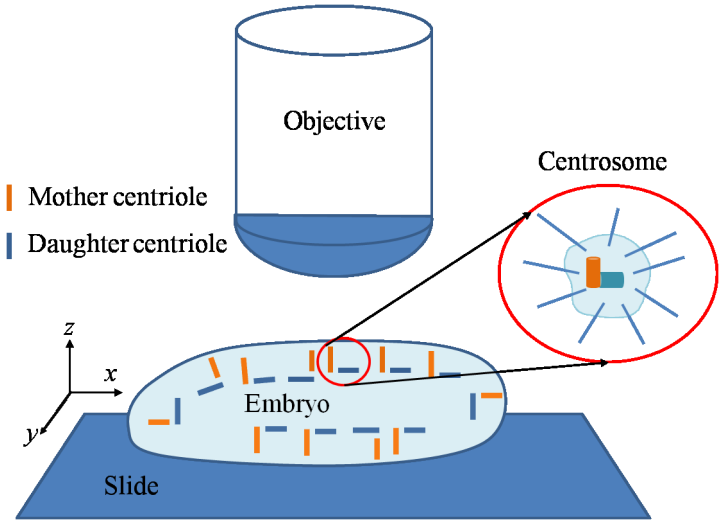

Figure 2.1: *Schematic representation of orientation of centrioles with respect to the embryonic membrane and focal plane of the microscope. During the syncytial blastoderm stages selected for observation, all the nuclei and their corresponding centrosomes are located towards the periphery of the embryo. The mother centrioles, i.e. the ones which accumulate PCM are oriented perpendicular to the embryonic membrane. Since the focal plane is parallel (due to the objective of the microscope being perpendicular) to the embryonic membrane, the mother centrioles are perpendicular to the focal plane. (Note that curvature of the embryo has a greater length scale than the area under focus, and hence, for practical purposes the centrioles can be considered perpendicular to the focal plane. Note also that the figure is not to scale).*

The above process generates four-dimensional data (i.e. data in the X, Y, Z and time dimensions). The pixel size of the images in the (X, Y) plane is 0.1046 μm. Note that the resolution obtained by observing the point spread function is $0.35\mu m$. Once all the images are captured, we select the maximum intensity projection from all the Z-images. This is done for the following reason: since centrosomes can move around during the experiment, the Z-image that goes through the centriole will not be the same at all time points. But since Cnn fluorescence peaks at the centre of the centriole, it is reasonable to assume that any Z-image that shows maximum intensity

at a given time point may have passed through the centriole. A maximum intensity projection thus converts the data to three dimensions, i.e. the X, Y and time dimensions. Figure 2.2(a) shows the maximum intensity projection through one centriole before and after bleaching. The centrosome that is bleached is identified and line of

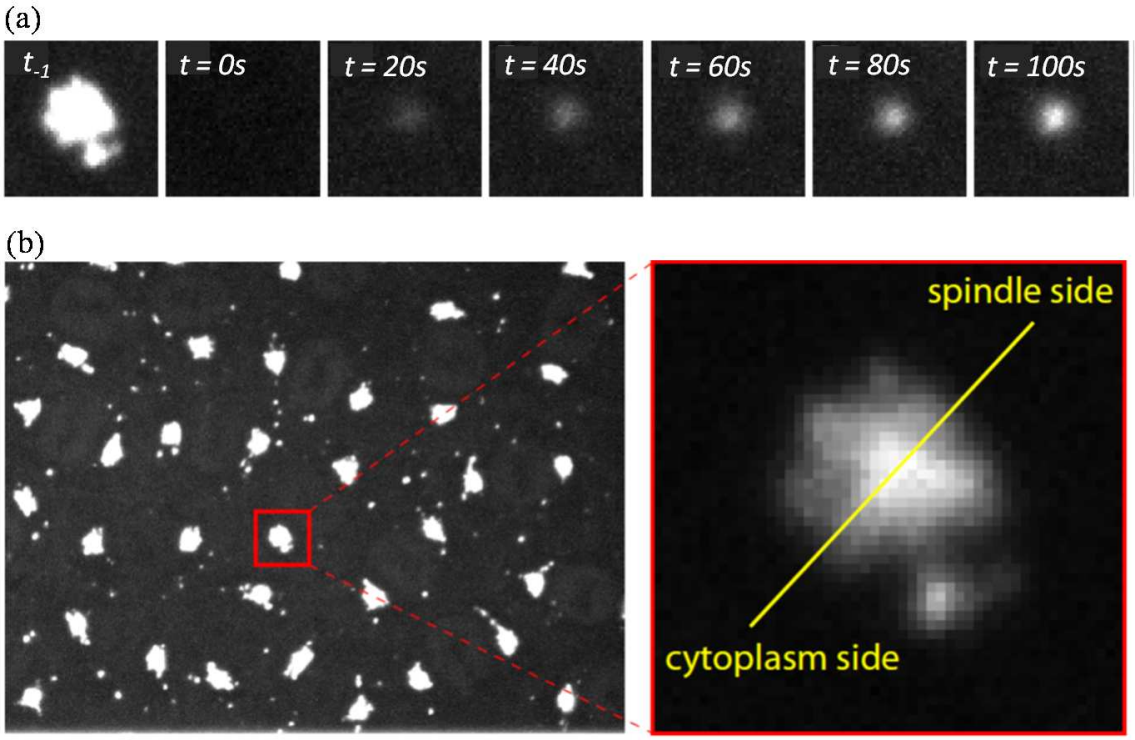

Figure 2.2: (a) *Maximum intensity projection through one of the centrioles showing the fluorescence intensities before bleaching* (t_{-1}) *and select time points after bleaching. Figure courtesy of Dr. Paul Conduit.* (b) *Left panel shows a maximum intensity projection through the* $Z-$*images at a pre-bleach time point. Out of several centrosomes, the one that would be subsequently bleached is chosen. The spindle orientation can be determined by observing the partner of the centrosome to be bleached. (The partner of the centrosome is identified through temporal observation of the behaviour of centrosomes). A line is drawn through the centrosome, such that it is parallel to the spindle direction as indicated in the right panel. Intensities along this line are stored for each time point. Figure courtesy of Dr. Paul Conduit.*

length 4.7μm is drawn through it, such that it passes through the centre and is in the direction parallel to the spindle. (Note that only one centrosome per embryo is bleached). The length of the line is chosen such that it is longer than the distance

over which the Cnn fluorescence falls to cytoplasmic levels. The line is drawn such that half of the line lies on either side of the centriole (see Figure 2.2(b)). One of the sides is called the spindle side, since the spindle apparatus lies on this side. The other side is called the cytoplasm side, since this side faces away from the spindle and towards the cytoplasm. Fluorescence intensities along this line are measured. The process is repeated at each time point after bleaching, and for all of the six datasets. This process converts the three-dimensional data into two-dimensional data in X, along the above line, and time. Figure 2.2(b) shows the process of gathering the two-dimensional data from the maximum intensity projection images.

We are interested in the levels of Cnn, as measured by the fluorescence intensity of GFP-Cnn. However, several other molecules in the cells also show some fluorescence. This background fluorescence of cells needs to be subtracted from the GFP-Cnn fluorescence so as to obtain the correct levels of changes in GFP-Cnn fluorescence. To do this, our collaborators use the fluorescence microscope to observe *Drosophila* embryos that do not have GFP-Cnn. The background fluorescence of these embryos is measured and used as a benchmark.

2.2 Data processing

Having thus obtained the time series data in the $X-$dimension, our collaborators send the data to us for further analysis, including data-fitting. Figure 2.3 shows the steps taken in data processing. We begin processing these data by subtracting the background fluorescence from all the fluorescence intensities at all time points. This ensures that the remaining fluorescence intensities in the data only correspond to the fluorescence from GFP-Cnn. As mentioned before, even though GFP-Cnn concentrates into the centrosomes, it is also present at very low levels throughout the

cytoplasm. This can be seen from Figure 2.3 (top right panel). We then go through data from each individual embryo and identify the cytoplasmic Cnn levels from pre-bleached centrosomes. (Note that cytoplasmic Cnn fluorescence is different from the background fluorescence. The latter is given by all the non-GFP-Cnn molecules in the cells that show native fluorescence). Next, we normalise all the data points using the corresponding cytoplasmic Cnn levels, so as to make normalised cytoplasmic Cnn levels in all data series equal to unity. The normalised fluorescence intensities are dimensionless. We then subtract unity from all the data points from different embryos. This is done to ensure that we are only left with fluorescence from the Cnn incorporated into the centrosomes. We justify this step in the following text.

We make a simplifying assumption that the levels of cytoplasmic Cnn remain roughly at cytoplasmic levels even in the centrosomes. Our collaborators anticipate that the cytoplasmic Cnn recovers fast as compared to the time scale of the FRAP experiment, which can be motivated as follows. On the length scale of the bleaching radius, $r_{bl} = 2.5\mu m$, the associated diffusive time scale is $r_{bl}^2/4D_L$ (where D_L is the diffusion coefficient of cytoplasmic Cnn) and is anticipated to be an order of magnitude faster than the time scale of the FRAP experiment. For instance, with the parameter estimates discussed later in Table 4.1 one finds $r_{bl}^2/4D_L \sim 1$ second, which is much faster than the 10 second scale of measurement for the FRAP experiments. Hence, the parameter estimates indicate that the rapid initial transients cannot be resolved experimentally and thus they are discarded when performing data fitting and when seeking model simplifications.

An additional indication of rapid diffusion on the scales of the FRAP experiment also emerges when considering FRAP experiments in general: cellular proteins that undergo very little binding recover completely in under a second, owing to the diffu-

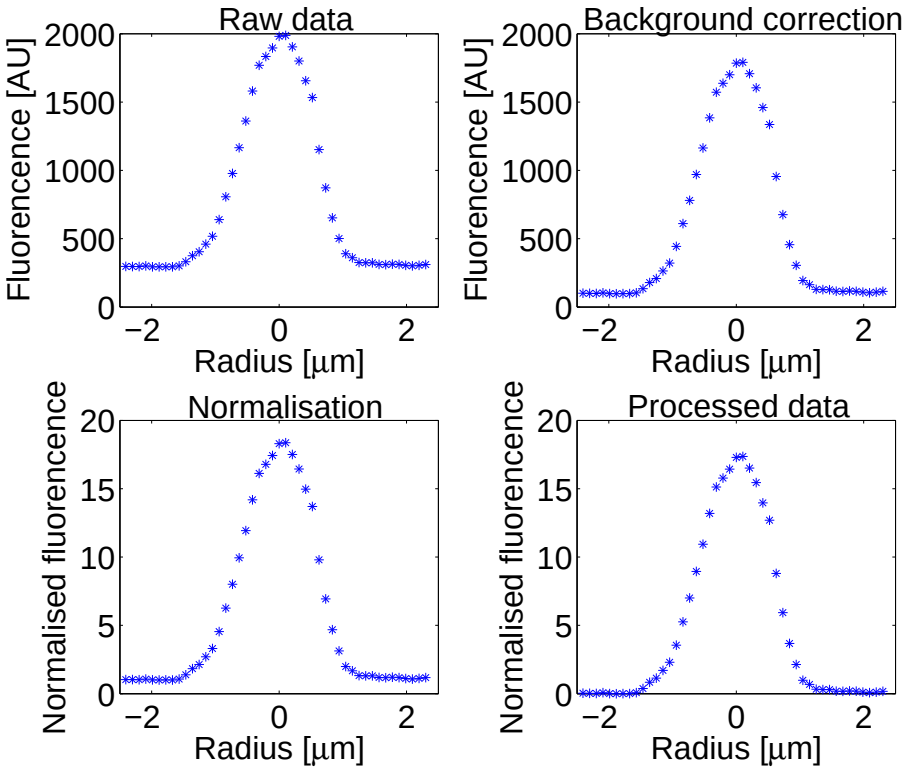

Figure 2.3: *Data processing method indicated using a sample data set, identified as 'movie'. Top left panel shows the data obtained from our collaborators. Top right panel shows the data corrected for background fluorescence. Bottom left panel shows data normalised with the cytoplasmic Cnn levels and the bottom right panel shows the data in final form where cytoplasmic fluorescence is subtracted from the normalised data, in order to obtain the fluorescence from only the incorporated Cnn. The fluorescence intensities along the negative distance from the centre correspond to the cytoplasmic side data and those along the positive radius correspond to the spindle side data. The origin denotes the tentative position of the centriole.*

sive process being rapid (Sprague and McNally, 2005). Proteins that recover much slower than one second (say, over several seconds or even minutes, as in the case of Cnn) may exhibit either effective diffusion or reaction-dominated recovery, where 'reaction' refers to binding and unbinding of fluorescent molecules to their receptors.

Effective diffusion is said to occur when the reaction process is much faster than

diffusion, whereas reaction-dominated recovery occurs when diffusion is very fast compared to the reactions and the time scale of the FRAP experiment. Changes in bleaching radius affect the dynamics of effective diffusion, but not those of the reaction-dominated system (Sprague et al., 2004; Sprague and McNally, 2005). In particular, the smaller the bleaching radius, the faster the recovery for the case of effective diffusion. Thus, if Cnn was undergoing effective diffusion, we would expect the rate of Cnn fluorescence increase in the case of the FRAP experiment to be much slower relative to the case of an unperturbed system (i.e., when one simply observes the fluorescence over time, without bleaching. This can be said to mimic an infinitesimal bleaching radius). Figure 1.8 (left panel) shows Cnn recovery in the central pixels in a FRAP experiment, while Figure 1.5(a) shows the Cnn fluorescence increase in the case of an unperturbed system. (Note that the fluorescence recovery is presented as a fraction of the pre-bleach value in Figure 1.5(a), while it is presented as a percentage of the pre-bleach value in Figure 1.8). It can be seen that counter to our expectation (assuming effective diffusion for Cnn) the rate of Cnn incorporation is greater in the case of the FRAP experiment, suggesting that Cnn may not be undergoing effective diffusion. Thus, we argue that Cnn undergoes a reaction-dominated recovery (i.e., the recovery kinetics of Cnn is dominated by binding-unbinding events rather than being limited by the diffusion of cytoplasmic Cnn into the centrosomes). In the case of reaction-dominated recovery, free molecules (cytoplasmic Cnn in this case) quickly equilibrate, so that their diffusion is not detected in the FRAP experiment. Therefore, we believe that the assumption that the levels of unbleached cytoplasmic Cnn remain roughly at cytoplasmic levels in the centrosomes following bleaching is justified.

Table 2.1 summarises the different data sets provided by our collaborators. The fluorescence intensities are measured in arbitrary units [AU]. Having thus obtained

six processed data sets we calculate the mean fluorescence at each time point by averaging over the six data sets. Note from Table 2.1 that fewer than six data sets are available for later time points. Figure 2.4(a) shows processed pre-bleach fluorescence data from six different embryos and 2.4(b) shows the average fluorescence along with standard deviation. Since the centrosome appears radially symmetric, we could further combine the data along the positive and negative radii (i.e. data corresponding to the cytoplasm side and the spindle side). However, we notice that the data are not symmetric on either side of the centriole. Figure 2.5 shows the average pre-bleach cytoplasm side data overlaid with the average pre-bleach spindle side data. When comparing our Cnn incorporation models with the data, we consider the cytoplasm side and spindle side data separately.

Figure 2.6(a) shows the mean fluorescence recovery curves at select time points and

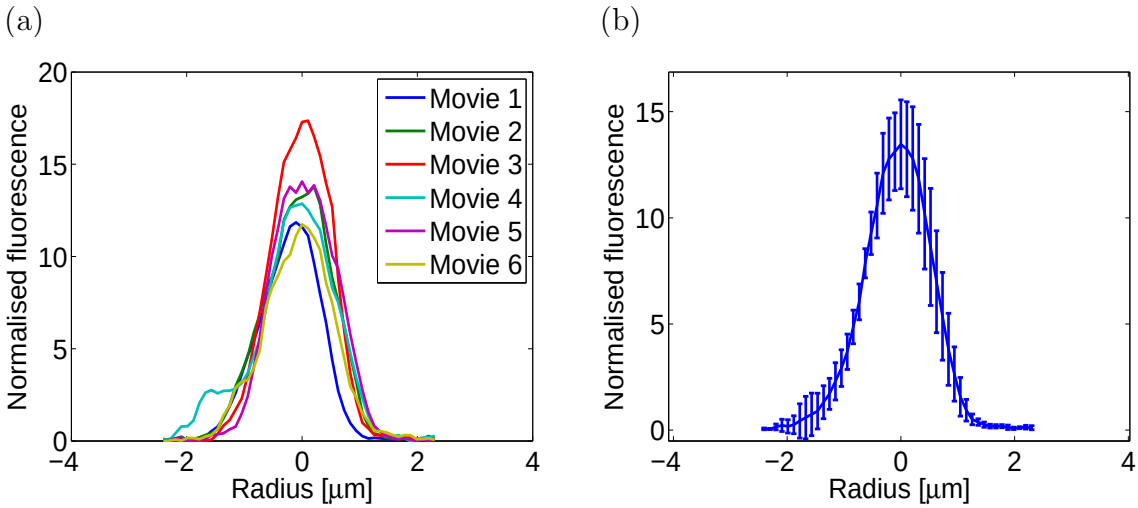

Figure 2.4: (a) *Normalised fluorescence intensities of Cnn at a pre-bleach time point from different embryos. The box denotes the various movies from which these data are obtained. Even though the data are discrete, they are plotted using continuous curves for better visualisation.* (b) *Average normalised fluorescence intensities, along with the standard deviation.*

the pre-bleach profile. It can be seen that recovery is faster close to the origin (i.e.

Table 2.1: Summary of the data obtained from our collaborators. The first column labels the various movies of FRAP experiments from which the data were extracted. Each movie corresponds to a different embryo. The second column lists the number of time points for which data were gathered. The first time point is the pre-bleach time point (t_{-1}). The second time point captures the data immediately post-bleaching and is, therefore, called the zeroth time point (t_0). The time for which each embryo could be observed post-bleaching varies and is indicated in the third column. The fourth column lists the different cytoplasmic Cnn levels in each of the movies in arbitrary units (AU). The difference in these levels could be due to the inter-embryo variation or due to variation in the stage of embryonic division at which the data are captured.

Data	**Number of time points**	**Latest post-bleach time point [sec]**	**Cytoplasmic Cnn levels [AU]**
Movie 1	18	158.5	107.2
Movie 2	18	158.5	103.6
Movie 3	15	128.5	97.5
Movie 4	12	98.5	88.9
Movie 5	18	158.5	88.9
Movie 6	16	138.5	87.5

close to the centriole) than towards the periphery. It is customary to plot the total recovery in the bleached region as a function of time. The resultant graph is called the FRAP curve. Considering the spherical geometry of the Cnn fluorescence in the centrosomes, the total Cnn recovery in the bleached region can be obtained by using the formula for the surface area of a sphere as

$$R_{total}(t) = \sum_{r=0}^{r_{bl}} 4\pi r^2 f(r,t),$$

where $R_{total}(t)$ denotes the total Cnn recovery as a function of time, $f(r,t)$ denotes the fluorescence data along the radius at each time point and r_{bl} denotes the radius of the bleaching region. Both radius and time are discrete since the data gathered are discrete. The FRAP curve thus obtained is plotted in Figure 2.6(b). It can be

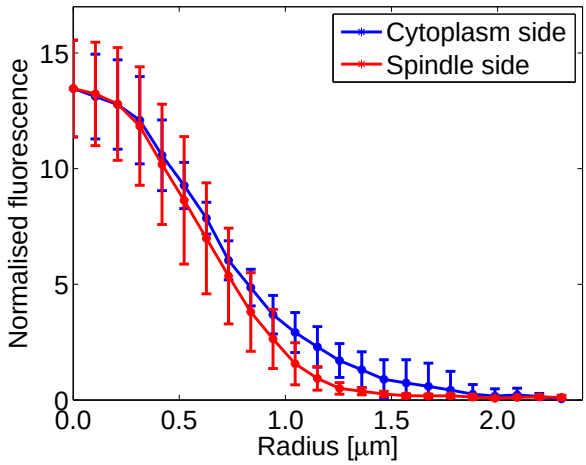

Figure 2.5: *Average pre-bleach data from the cytoplasm side and the spindle side are overlaid for comparison. Error bars denote the standard deviation. It can be seen that Cnn forms a wider distribution on the cytoplasm side as compared to the spindle side.*

seen from the FRAP curve that over the course of the FRAP experiment, the total fluorescence does not begin to plateau. The implications of this for model fitting will be discussed in the subsequent chapters.

2.3 Mathematical methods of model analysis

We have used several mathematical methods for the analysis of our models of Cnn incorporation. We have used various numerical methods for the solution of the partial differential equations (PDEs) arising from our models and various data-fitting algorithms for fitting our models to the experimental data (which are gathered and processed as described in Section 2.1 and Section 2.2). In this section we describe briefly these numerical methods.

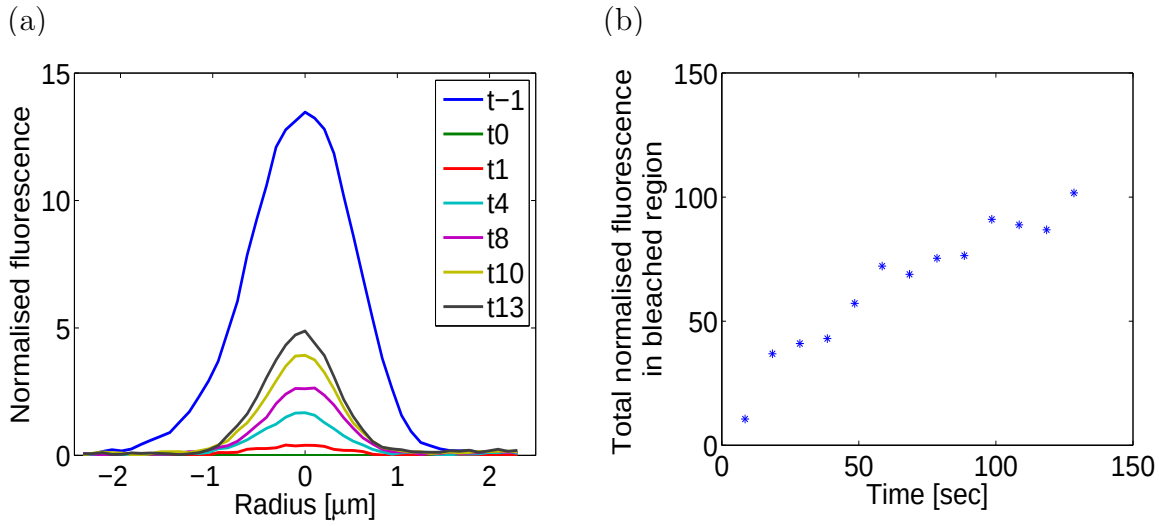

Figure 2.6: (a) *Mean fluorescence recovery profiles are plotted at select time points. t-1 denotes the pre-bleach profile. t0 denotes the profile just after bleaching. It can be seen that bleaching has completely obliterated the fluorescence in the centrosome. t1 to t13 denote post-bleach recovery profiles.* (b) *Total normalised fluorescence intensities of the average Cnn fluorescence with respect to time are plotted for up to 128.5 seconds. The final three time points are not included in the FRAP curve since we have fewer data points for these later time points.*

2.3.1 Numerical methods for solution of PDEs

The models proposed in this work are described by systems of parabolic or hyperbolic PDEs. Various numerical methods exist for their approximation. We have used some of these methods to solve the systems of PDEs arising from our models. In this section we describe these methods briefly.

2.3.1.1 The MATLAB PDE solver `pdepe`

The MATLAB solver `pdepe` can be used to solve equations of the form

$$\mathbf{C}(x,t,\boldsymbol{u},\boldsymbol{u}_x)\boldsymbol{u}_t = x^{-m}\left[x^m \boldsymbol{s}(x,t,\boldsymbol{u},\boldsymbol{u}_x)\right]_x + \boldsymbol{f}(x,t,\boldsymbol{u},\boldsymbol{u}_x), \tag{2.3.1}$$

where m can be 0, 1 or 2, and defines the geometry of the problem (i.e. Cartesian, cylindrical or spherical). $\boldsymbol{u}$ denotes the vector of dependent variables in the system of

PDEs and $\boldsymbol{u}_t$ and $\boldsymbol{u}_x$ denote the derivatives of $\boldsymbol{u}$ with respect to time and space (radial coordinate only, in the case of $m > 0$), respectively. $\boldsymbol{s}(x, t, \boldsymbol{u}, \boldsymbol{u}_x)$ denotes the flux term and $\boldsymbol{f}(x, t, \boldsymbol{u}, \boldsymbol{u}_x)$ denotes the source term. The diagonal values of the diagonal matrix $\boldsymbol{C}$ can be zero or positive. If all values are zero then the PDE is elliptic, while positive values correspond to a parabolic PDE. The boundary conditions need to be provided in the form

$$\boldsymbol{\gamma}(x, t, \boldsymbol{u}) + \boldsymbol{\eta}(x, t)\boldsymbol{s}(x, t, \boldsymbol{u}, \boldsymbol{u}_x) = 0 \quad \text{at} \quad x = \alpha, \beta, \tag{2.3.2}$$

where $[\alpha, \beta]$ denotes the spatial domain over which the problem is solved. For problems with spherical or cylindrical geometry, α cannot be negative. $\boldsymbol{\gamma}$ and $\boldsymbol{\eta}$ denote vectors of coefficients that satisfy the boundary conditions. For example, in the case of homogenous Neumann boundary condition for u_i at $x = \alpha$, $\gamma_i = 0$ and $\eta_i = 1$. `pdepe` uses the method of lines for solving a PDE problem, which is a general method where the PDEs are discretized in all dimensions but one and the resulting system of ODEs is solved using algorithms for the solution of ODEs. `pdepe` discretizes the PDEs in the spatial dimension and uses MATLAB's `ode15s` for the solution of the resulting ODEs in the time dimension. The spatial discretization is carried out using the method suggested by Skeel and Berzins (1990). This method is based on the Petrov-Galerkin method and is second-order accurate in space. The accuracy (and computational cost) of the `pdepe` solution depends upon the mesh that is provided. The optimal time steps are selected by the `ode15s` algorithm.

2.3.1.2 The MATLAB ODE solver `ode15s`

The MATLAB solver `ode15s` can be used to solve initial value problems of the form

$$\boldsymbol{z}' = \boldsymbol{q}(t, \boldsymbol{z}), \quad t_0 \leq t \leq t_{end}, \quad \boldsymbol{z}(t_0) = \boldsymbol{z}_0, \tag{2.3.3}$$

where $'$ denotes the derivative with respect to t. `ode15s` is a linear multistep solver, i.e., it uses information from several previous time points to evaluate the solution at the next time point. The method used by `ode15s` is based on numerical difference formulae (NDFs), which are based on the backward differentiation formula (BDF) (Shampine and Reichelt, 1997). The general k-step BDF for a step from $(t_n, \boldsymbol{z}_n)$ to $(t_{n+1}, \boldsymbol{z}_{n+1})$ can be written as

$$\sum_{m=1}^{k} \frac{1}{m} \bigtriangledown^m \boldsymbol{z}_{n+1} - \triangle t \boldsymbol{q}(t_{n+1}, \boldsymbol{z}_{n+1}) = 0, \tag{2.3.4}$$

where $\triangle t$ denotes the time step $(t_{n+1} - t_n)$, (where $t_n = n\triangle t$), $\bigtriangledown$ denotes a backward difference operator $\bigtriangledown \boldsymbol{z}_{n+1} = \boldsymbol{z}_{n+1} - \boldsymbol{z}_n$ and m is the order of the difference operator. Equation (2.3.4), which is implicit in $\boldsymbol{z}_{n+1}$, is solved iteratively using Newton's interpolation formula. The iteration is started with the predicted value

$$\boldsymbol{z}_{n+1}^0 = \sum_{m=0}^{k} \bigtriangledown^m \boldsymbol{z}_n.$$

The NDF method makes use of the fact that the above predicted value uses information from one more time point in the past than the BDF (2.3.4). The NDF achieves higher accuracy than the BDF for the same step size $\triangle t$ (Shampine and Reichelt, 1997).

2.3.1.3 Explicit finite difference schemes

One of our models, namely the advection model (Section 3.7), is a system of coupled diffusion-advection PDEs. MATLAB's `pdepe` solver cannot be used for solving such a system since the solver is unable to handle hyperbolic PDEs. Therefore we use an explicit finite difference scheme, namely the upwind scheme, for solving the hyperbolic equation (Morton and Mayers, 2005). The coupled parabolic equation is approximated using a forward-time, central-space (FTCS) explicit scheme as de-

scribed below.

Upwind scheme

Consider a first order hyperbolic equation on a spatial domain $x \in (\alpha, \beta)$ that is to be solved for $t \in (0, t_{end})$,

$$\frac{\partial u}{\partial t} + a\frac{\partial u}{\partial x} = 0, \tag{2.3.5}$$

where a is constant and denotes the advection velocity. The initial condition is given by $u(x,0) = u_0(x)$ and the boundary condition by $u(\alpha, t) = g(t)$ for $a > 0$ or $u(\beta, t) = g(t)$ for $a < 0$. Consider the case $a > 0$. The exact solution of this equation can be obtained using the method of characteristics and is given by $u(x,t) = u_0(x-at)$ for $x - at \geq \alpha$ and $u(x,t) = u(\alpha, t) = g(t)$ for $x - at < \alpha$ and $x \geq \alpha$. The numerical solution of equation (2.3.5) can be obtained using the upwind scheme given by,

$$\begin{aligned} &\frac{u_j^{n+1} - u_j^n}{\triangle t} + a\frac{u_j^n - u_{j-1}^n}{\triangle x} = 0, \quad \text{for} \quad a > 0, \\ &\frac{u_j^{n+1} - u_j^n}{\triangle t} + a\frac{u_{j+1}^n - u_j^n}{\triangle x} = 0, \quad \text{for} \quad a < 0, \end{aligned} \tag{2.3.6}$$

where u_j^n denotes the approximation to the solution u at time point n and spatial point j. $\triangle t$ denotes the time step, given by $t^{n+1} - t^n$, and $\triangle x$ denotes the space step, given by $x_{j+1} - x_j$. Thus, $j = 1, 2, 3, \ldots, (\beta/\triangle x + 1)$, and $n = 1, 2, 3, \ldots, (t_{end}/\triangle t + 1)$. The choice of a backward difference scheme in the space variable for $a > 0$ (and of a forward difference scheme for $a < 0$) ensures that the characteristics lie within the domain of dependence of the numerical scheme. The upwinding naturally takes care of the boundary conditions. The Courant-Friedrich-Lewy (CFL) condition also requires that

$$|a|\triangle t/\triangle x \leq 1,$$

for the stability of this numerical scheme (Courant et al., 1967). This method is first order accurate in space as well as time (Morton and Mayers, 2005).

The forward-time, central-space (FTCS) scheme

The FTCS is an explicit finite difference scheme for numerical approximation of parabolic PDEs. The time derivative is approximated using the forward difference method while the spatial derivative is approximated using the central difference method. Consider a classic parabolic equation, the diffusion equation in one-dimensional Cartesian coordinates,

$$\frac{\partial u}{\partial t} = D\frac{\partial^2 u}{\partial x^2}, \tag{2.3.7}$$

where D is the diffusion coefficient. The solution is sought for the spatial domain $x \in (\alpha, \beta)$ and for time $t \in (0, t_{end})$, the initial condition is given by $u(x, 0) = u_0(x)$ and the boundary conditions are

$$\left.\frac{\partial u}{\partial x}\right|_{x=\alpha} = 0 \quad \text{and} \quad u(\beta, t) = 0.$$

Using the FTCS scheme equation (2.3.7) is approximated as

$$\frac{u_j^{n+1} - u_j^n}{\triangle t} = D\frac{u_{j-1}^n - 2u_j^n + u_{j+1}^n}{\triangle x^2}, \tag{2.3.8}$$

where u_j^n denotes the approximation to the solution u at time point n and spatial point j. $\triangle t$ denotes the time step given by $t^{n+1} - t^n$ and $\triangle x$ denotes the space step given by $x_{j+1} - x_j$. Thus, $j = 1, 2, 3, \ldots, (\beta/\triangle x + 1)$, and $n = 1, 2, 3, \ldots, (t_{end}/\triangle t + 1)$. This scheme is second order accurate in space and first order accurate in time. It should be noted that the central differences in space variable x cannot be used at the boundaries (i.e. at $j = 1$ and $j = (\beta/\triangle x + 1)$), since the spatial points identified by $j = 0$ and $j = (\beta/\triangle x + 2)$ are outside of the domain. The boundary conditions need to be satisfied at these points. The right hand boundary condition gives that

$u^n_{(\beta/\triangle x+1)} = 0$, while the left boundary condition is satisfied by using the forward difference method and setting $u^n_1 = u^n_2$. The solver requires that

$$\triangle t/\triangle x^2 \leq 1/2,$$

for stability in one-dimensional Cartesian coordinates and it requires that

$$\triangle t/\triangle x^2 \leq 1/6,$$

for stability in spherical polar coordinates (Morton and Mayers, 2005).

2.3.1.4 COMSOL Multiphysics software

COMSOL Multiphysics uses finite element methods (FEMs) to numerically solve PDE systems arising in a variety of physics and engineering applications. The FEM is a numerical technique to approximate solutions to PDEs using a weak formulation of the problem and is particularly well-suited for problems solved over complicated geometries. In a FEM one proceeds by obtaining a weak formulation of the PDE to be solved, discretising it by replacing the continuous domain with a suitable piece-wise continuous one and choosing basis functions for the discretisation. We use the following example to demonstrate how the FEM works. Consider a two-dimensional stationary PDE problem

$$\begin{aligned} &\nabla^2 u + f(x,y) = 0 \ \text{ in } \ \Omega, \\ &u = 0 \ \text{ on } \ \partial\Omega, \end{aligned} \tag{2.3.9}$$

where $\Omega \subset \mathbb{R}^2$ with boundary $\partial\Omega$. If u solves the problem (2.3.9), then for an appropriate test function v satisfying the same boundary conditions we can write

$$\int_{\Omega} \left(\nabla^2 u + f(x,y)\right) v \mathrm{d}x\mathrm{d}y = 0. \tag{2.3.10}$$

This is the weak formulation of the problem (2.3.9). Using the derivative of a product rule and integrating on both sides and using Green's first identity, we find

$$\int_{\Omega} f(x,y) v \mathrm{d}x\mathrm{d}y = -\int_{\Omega} \nabla v.\nabla u \mathrm{d}x\mathrm{d}y. \tag{2.3.11}$$

The above problem is then solved on a finite subspace of Ω using a suitable mesh. For a problem in two spatial dimensions, the domain can be discretized (or meshed) using non-overlapping triangular or quadrilateral elements. Appropriate basis functions, which are piece-wise continuous, are chosen for each mesh element. For a stationary PDE problem, the discretization results in a system of differential algebraic equations (DAEs), whereas for a transient (non-stationary) PDE problem, it leads to a set of ODEs, which can be solved using implicit methods.

2.4 Fitting models to data

In Sections 2.1 and 2.2 we have described how experimental data on Cnn incorporation are collected and processed. We fit these data with various Cnn incorporation models in a least squares sense. In this work we focus on obtaining a 'correct' model of Cnn incorporation. During the pursuit of such a model we need to compare the fits obtained from various models, which may be non-nested or nested (see Section 2.4.3 for more description). Thus, we need methods for assessing the model fits and comparing the fits from different models. In this section we describe the least squares method, the MATLAB algorithms that we have used for minimisation of least squares,

methods for evaluating the fit and for comparing between different model fits.

2.4.1 Least squares method

The method of least squares is one of the most important classes of data fitting methods (Bates and Watts, 1988). In this method the difference between the data and model predictions is minimised in order to obtain the best-fitting model. Thus, the model parameters are adjusted in order to obtain a set of parameters that best fits the data. Let the data be denoted by $y(i)$, where $i = 1, ..., N$ corresponds to successive values of independent variable $\boldsymbol{x}$. Let $\boldsymbol{\theta}$ denote the vector of parameters. The model $m(\boldsymbol{x}, \boldsymbol{\theta})$ describes the relation between a set of independent variables, $\boldsymbol{x}$, and the dependent variables. The least squares problem requires that the sum of squared residuals

$$S = \sum_{i=1}^{N} d(i, \boldsymbol{\theta})^2,$$

be minimised, where d denotes the difference between the model prediction and the data, and is given by

$$d(i, \boldsymbol{\theta}) = y(i) - m(x(i), \boldsymbol{\theta}). \tag{2.4.1}$$

If the model that provides the relation between the independent and the dependent variables is linear with respect to all the parameters in the vector $\boldsymbol{\theta}$, then the above problem becomes a linear least squares problem, which has a closed form solution. However, if the model is nonlinear in $\boldsymbol{\theta}$, no closed form solution exists and iterative methods have to be used for the solution of the minimisation problem. Formulating a problem in the least squares sense is likely to provide optimal solutions when the following assumptions are valid (Bates and Watts, 1988):

1. the model is correct. (Usually, an incorrect model produces a poor fit. This can be diagnosed as discussed in Section 2.4.2);

2. the initial guess for the parameters is close to the true solution. (This may not be possible when no information is available about the parameters. In this case, one can use multiple different initial guesses and find the one which gives the best solution);

3. the independent variables are error-free. (In the case of the Cnn experiments, we believe that the independent variables (radius and time) can be estimated accurately);

4. the errors in the dependent variables are independently distributed, have constant variance with respect to the independent variables and zero mean. (In practice, the noise in the data increases as the signal strength increases. (See Figure 2.8 for the standard deviation in the Cnn data). In Section 2.4.2.2 we describe ways of dealing with non-constant variance in the data).

2.4.1.1 `lsqnonlin`

MATLAB's `lsqnonlin` algorithm solves nonlinear least-squares problems of the form

$$\min \sum d(\boldsymbol{\theta})^2 = \min \left(d_1(\boldsymbol{\theta})^2 + d_2(\boldsymbol{\theta})^2 + ... + d_n(\boldsymbol{\theta})^2 \right), \tag{2.4.2}$$

where $\boldsymbol{\theta}$ denotes the vector of parameter values $(\theta_1,\ \theta_2, ..., \theta_N)$ and $d_i(\boldsymbol{\theta})^2$ corresponds to the i^{th} least-squares subproblem. `lsqnonlin` uses the 'Trust region reflective' algorithm (see below). The algorithm can be constrained by providing lower and upper bounds on all the parameters.

Trust region reflective algorithm

The trust region reflective algorithm proposed by Coleman and Li (1994; 1996) can minimise a nonlinear function subject to bound constraints on the values of the min-

imisation parameters. A sample minimisation problem is

$$\min_{\boldsymbol{\theta}\in\mathbb{R}^n} S(\boldsymbol{\theta}), \quad \boldsymbol{lb} \leq \boldsymbol{\theta} \leq \boldsymbol{ub}, \tag{2.4.3}$$

where $\boldsymbol{\theta}$ denotes an array of minimisation parameters, $S(\boldsymbol{\theta})$ is the function to be minimised with $\boldsymbol{lb}$ and $\boldsymbol{ub}$ denoting the lower and upper bounds on the parameters $\boldsymbol{\theta}$, respectively. A trust region method begins by formulating a quadratic subproblem at a given iterate $\boldsymbol{\theta}_k$,

$$\min_{\boldsymbol{d\theta}\in\mathbb{R}^n} \left\{ \psi_k(\boldsymbol{d\theta}) \stackrel{def}{=} \mathbf{R}_k^T \boldsymbol{d\theta} + 0.5 \boldsymbol{d\theta}^T \mathbf{B}_k(\boldsymbol{d\theta}) \ : \ \| \mathbf{D}_k \boldsymbol{d\theta} \| \ \leq \ \triangle_k \right\}, \tag{2.4.4}$$

where $\mathbf{R}_k$ denotes the gradient $\nabla S(\boldsymbol{\theta}_k)$, $\mathbf{B}_k$ denotes the Hessian matrix $\nabla^2 S(\boldsymbol{\theta}_k)$, $\triangle_k$ is a positive scalar representing the trust region size and $\mathbf{D}_k$ is a scaling matrix. The increment $\boldsymbol{d\theta}_k = \boldsymbol{\theta}_{k+1} - \boldsymbol{\theta}_k$ is the approximate solution to the above quadratic subproblem. Depending on how significantly an iterate minimises the function $S(\boldsymbol{\theta})$, the trust region $\triangle_k$ is shrunk or expanded. In the case of bound constraints, the scaling matrix $\mathbf{D}_k$ is chosen such that the solution is strictly within the bounded region (Coleman and Li, 1996).

2.4.1.2 `fminsearch`

MATLAB's `fminsearch` algorithm is an unconstrained nonlinear minimisation algorithm based on the Nelder-Mead simplex method. The algorithm minimises the given scalar function $f(\boldsymbol{p})$ starting from an initial guess $\boldsymbol{p}_0$. This is a direct search method, i.e., it does not use numerical or analytical gradients of the function to be minimised (as in the case of the trust region reflective algorithm). It is still possible to use bound constraints with this algorithm by providing artificially high residual values if a parameter exceeds its bounds. Since the algorithm does not depend upon the gradients of the function, the artificially high residuals would not affect the further

iterative process in this algorithm.

Nelder-Mead simplex method

This is a popular direct search method that has been widely studied (Walters et al., 1991). For minimising a function with parameters $\theta_1,\ \theta_2, ..., \theta_N$, it begins by constructing a simplex with $N + 1$ vertices. The function to be minimised, $S(\boldsymbol{\theta})$, is evaluated at each vertex. The vertex with the highest function value is discarded and a new vertex is generated by the process of reflection through the remaining vertices. The function is evaluated at the reflected point. If the function takes a higher value, the simplex is contracted, whereas if the function takes a lower value then the simplex is expanded, by changing the value of the latest iterate using the remaining vertices of the simplex (Nelder and Mead, 1965; Lagarias et al., 1998). The stopping criterion is reached when the diameter of the simplex is less than the specified tolerance. The default tolerance in `fminsearch` is 10^{-6}. The algorithm may only give local minima. Therefore, care must be taken while using this algorithm. Using an initial guess closer to the solution can direct the algorithm towards the global minimum. However, when the information about an initial guess is not available, one can check whether the algorithm is stuck in a local minimum by perturbing the minimised solution and rerunning the minimisation, or by using multiple starting guesses.

We have used both `lsqnonlin` and `fminsearch` for data fitting. Figure 2.7 shows the steps taken during data fitting in the form of a flowchart. Since the models we have used throughout this work can have multiple local minima, using a perturbed solution from one round of fitting as a starting initial guess for the next round allows us to check whether the previous solution was a local minimum or a genuine solution. Using two different fitting approaches also allows a more robust search for the true minimum, rather than using a single method.

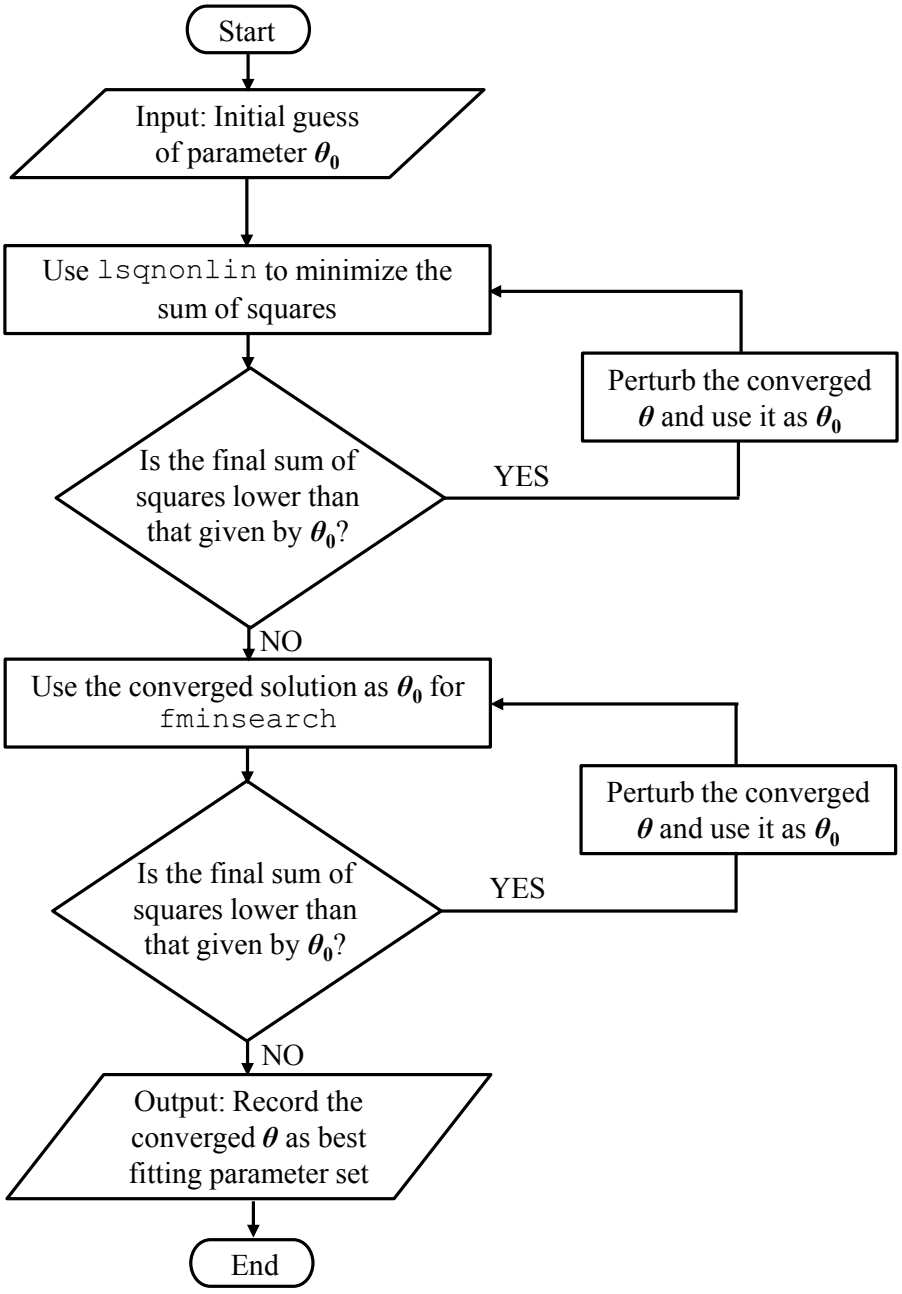

Figure 2.7: *The steps taken during data fitting are shown in the form of a flowchart.*

2.4.2 Assessing the fit

One method of deciding whether a given model fits the data is to visualise the data along with the model. A good model will produce a visibly good fit. One can also make sure that the parameter estimates produced by the fit are sensible. In the case of nonlinear least squares, it is possible to obtain suspiciously (or obviously) wrong parameter estimates (as judged by comparing them with available parameter values for closely related systems or by checking that they are not physically unrealistic, for example, negative diffusion coefficients) as the minimisation algorithm can get stuck in a local minimum. In this case, one can check if the fit improves by perturbing the solution and using that as an initial guess. Statistical measures, such as the coefficient of determination (R^2) and the distribution of residuals, can also be used for assessing the quality of the fit.

2.4.2.1 Coefficient of determination - R^2

The coefficient of determination, R^2, is a measure of how well the model approximates the experimentally observed data, in comparison to a model that assumes no relation between the independent variables and the dependent ones. Consider data-set $y(i)$, where $i = 1, \ldots, N$, corresponds to the independent variable $x(i)$. Let the best-fitting model map the independent variable onto the dependent variable using a function $m_1(x(i), \boldsymbol{\theta})$, where $\boldsymbol{\theta}$ represents the set of model parameters. To work out the R^2 coefficient, we also need a null model which assumes no relation between the independent variable and the dependent variables. Such a model would be given by a straight line parallel to the independent axis, $m_2(x(i), \boldsymbol{\theta}) = C$, where C denotes the y-intercept of this line. It is conceivable that if this model (a straight line parallel to the independent axis) is fitted to the dependent variables, the y-intercept that minimises the sum of squares would be equal to the mean of the dependent variables. Let $\overline{y}$ denote the mean of data-set $y(i)$. Let SS_{tot} denote the sum of squared residuals

with respect to the null model, and SS_{res} denote the sum of squared residuals with respect to the best-fitting model. Then the R^2 coefficient is defined as

$$R^2 = 1 - \frac{SS_{res}}{SS_{tot}}. \tag{2.4.5}$$

Thus, the value of R^2 ranges between 0 and 1. The closer the value of R^2 to unity, the better the model.

2.4.2.2 Distribution of residuals

The residuals remaining after a model fit are expected to be randomly distributed if the model has accounted for the correct functional relationships between all the independent variables. Any non-random distribution of residuals after the fitting indicates that at least one of the dependencies on the predictor variable has not been accounted for in the model. If this is the case, then the model needs to be changed in a scientifically sensible manner to account for this dependence. However, care must be taken while assessing the distribution of residuals as underlying trends in the signal strength in the data may generate non-random residual distributions. In order that the underlying trends in the signal strength reflected in the trends in variance of the data do not occlude true non-randomness in the residual distribution, we visualise the residuals differently. Rather than visualising the absolute residual values of model fits, we use the residual values normalised with the standard deviation in the data at each point. This ensures that any non-random behaviour in the residuals that we observe is only due to inadequacies in the model and not due to the underlying trends in the variance. We do the following experiment to demonstrate this method for our data set.

We first demonstrate that the residuals between a best-fitting model and data may ap-

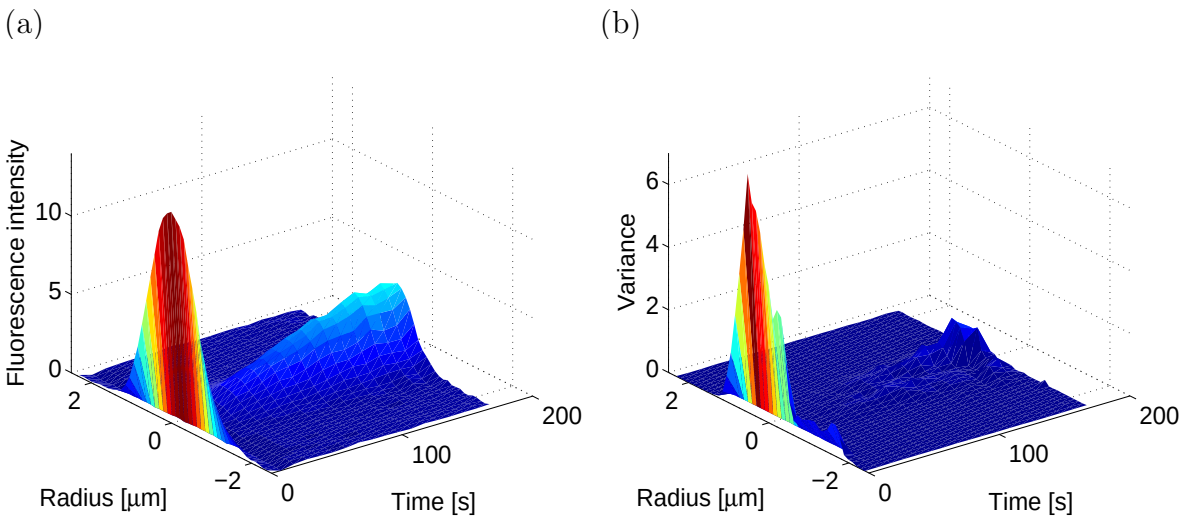

Figure 2.8: *Mean Cnn FRAP data* (a) *and the variance in the Cnn FRAP data* (b) *are plotted as a function of time and radius. The time points show the post-bleach recovery states of Cnn. Even though the data are discrete (at spatial points x spaced 0.1046 μm apart and at time points t spaced 10 seconds apart), we have plotted them using continuous surface plots for better visualisation.*

pear non-random owing to the non-random variance in the data. We begin by selecting a mean Cnn recovery profile at an arbitrarily chosen time point from our data. In order to simulate a best-fitting model, we smooth the Cnn recovery data at the chosen time point (by replacing each data point by the average over three adjacent data points in the spatial dimension. Thus, $y(x_i)$ is replaced by $(y(x_{i-1}) + y(x_i) + y(x_{i+1}))/3$.) and use the simulated data as the best-fitting model (Figure 2.9, top left panel). We evaluate the residuals between the data and the simulated model. It can be seen that these residuals appear non-random and roughly mirror the trends in the standard deviation (or variance). We then normalise the residuals using the standard deviation at the corresponding data points. The bottom right panel in Figure 2.9 shows that the normalised residuals appear to be randomly distributed as against the absolute residuals.

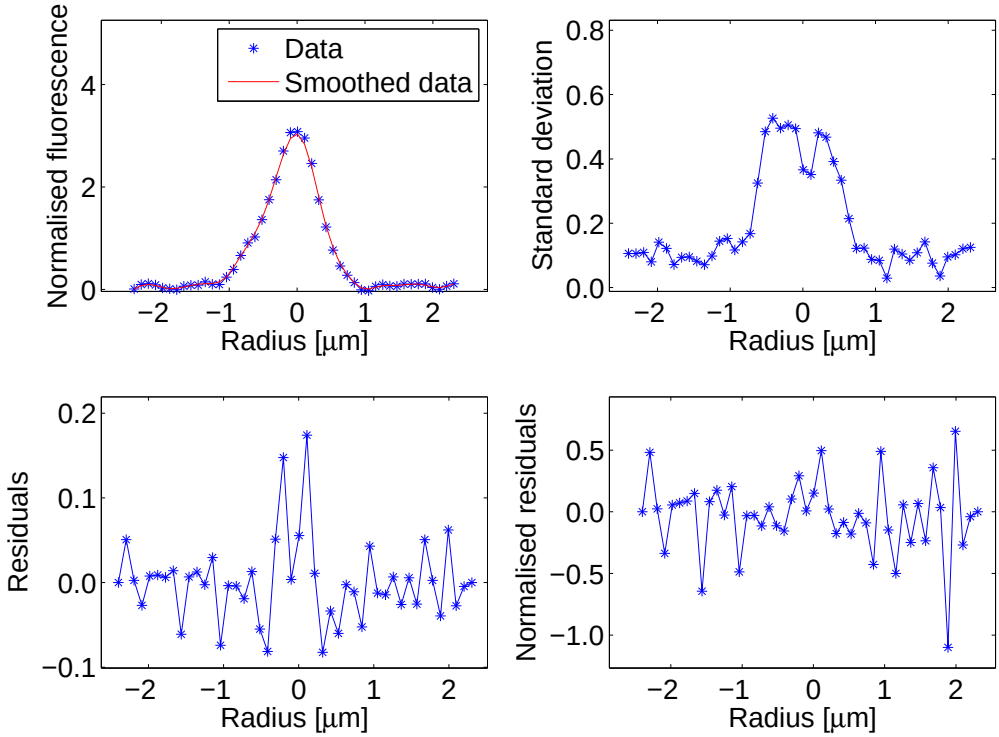

Figure 2.9: *Mean Cnn recovery profile data (blue asterisks) at an arbitrarily selected time point and a smoothed version of these data, representing the model (red curve) (top left panel). The standard deviation corresponding to these mean data (top right panel). The absolute residuals between the data and the model (the smoothed version of the data) (bottom left panel). Note that the residuals appear non-random and roughly follow the profile of the standard deviation, which roughly follow the profile of the data. Bottom right panel: the absolute residuals normalised with the standard deviation. Note that the resulting normalised residuals appear randomly distributed.*

2.4.3 Comparison of different models

Various methods exist for comparison of the fits of different models to data. The choice of comparison method depends upon whether the models are nested or non-nested. Two models are considered to be nested if reduction in the more complex model results in the simpler model. Models are considered to be non-nested when any reduction (or extension) in one model cannot generate the other model. In the case of nested models, one model invariably has fewer parameters than the other model.

2.4.3.1 Nested models

Consider that a set of data can be fitted well using a complex model with a certain number of parameters. Consider also that the same data set can be fitted, albeit less well, with a simpler model involving fewer parameters. The model with greater number of parameters will always fit the data at least as well as the model with fewer parameters. The F-test (so named in honor of Sir Ronald Fisher, who initially developed the test) is a standard statistical test used to ascertain whether the fit offered by the more complex model is significantly better than that by the simpler model. The F-test is applicable when the method of least squares is used to evaluate the fit. The null hypothesis of the F-test is that both the simpler and the complex model fit the data equally well (i.e. increasing the complexity of the simpler model does not significantly improve the fit). The F-statistic is calculated as follows (Bates and Watts, 1988). Let subscript c denote the full model and subscript p denote the partial model. Let S denote the residual sum of squares, n_θ denote the number of parameters and n_y denote the number of data points used for fitting. The F-score is given as

$$F = \frac{(S_p - S_c)/(n_{\theta c} - n_{\theta p})}{S_c/(n_y - n_{\theta c})}, \tag{2.4.6}$$

where $n_{\theta c} - n_{\theta p}$ and $n_y - n_{\theta c}$ are called the numerator and denominator degrees of freedom, respectively. If the null hypothesis holds, then the resulting F-statistic follows the F-distribution (Fisher-Snedecor distribution) with $(n_{\theta c} - n_{\theta p}, n_y - n_{\theta c})$ degrees of freedom. (The distribution of all possible values of the F-score is called the F-distribution). If the F-score thus obtained is greater than the critical value of the F-distribution for a desired rejection probability (say, $p = 0.05$) then the null hypothesis is rejected. Rejecting the null hypothesis means that the extra parameters in the more complex model are necessary to explain the data and that the improvement in the fit is not merely due to overfitting. A drawback of the F-test is that when the number

of data points is such that $n_y \gg n_{\theta c}$, the F-test tends to favour the full model, as can be seen from the formula for calculating the F-score, equation (2.4.6). In such cases, the researcher needs to decide if the model reduction does indeed lead to significant loss of fit.

2.4.3.2 Non-nested models

The best method of choosing between two (or more) rival models is to ask which model makes more sense scientifically. If both the models are plausible, and if both have the same number of parameters, then the model with the lowest root mean squared error (RMSE) and the most random distribution of residuals is chosen.

In subsequent chapters we model the incorporation of Cnn in centrosomes. We make use of the experimental data described in Sections 2.1-2.2. The mathematical methods described in this chapter are used for analysing the models and fitting them to the data. In the next chapter we begin by synthesising the biological information on Cnn incorporation and we propose two mechanistically different preliminary models of Cnn incorporation.

Chapter 3

Preliminary models of Cnn incorporation

3.1 Introduction

In Chapter 2 we saw that Cnn forms a gradient in the centrosomes and it shows a peculiar fluorescence recovery profile in the FRAP experiments. In this chapter we postulate two different mechanistic models of Cnn incorporation in the *Drosophila* centrosome, the diffusion model (Section 3.3) and the advection model (Section 3.7). We begin model development by considering various experimental details and plausible biological explanations for them. We proceed to make simplifying assumptions in order to allow the models to be analysed. We present the analysis of the diffusion model, simulations of the FRAP experiment and, finally, fitting of the diffusion model to the data. We then present the advection model and perform a similar analysis and data fitting with this model. Next we compare the outcomes of fitting the two models. Lastly, we present a further modification of the diffusion model to make it more biologically realistic and present the results of fitting this revised model to data (Section 3.12). We end the chapter by critiquing these models and discussing

the insights gained from them.

3.2 Model development

In order to explain the observed Cnn incorporation behaviour, we begin by identifying the different features of Cnn incorporation. These features have guided the development of the models we hypothesise.

1. Cnn concentrates in the centrosomes. Even though Cnn is present throughout the cytoplasm of the *Drosophila* syncytial embryo, its concentration is higher in the centrosomes than in the cytoplasm. The data (presented in Chapter 2) show that Cnn concentration at the centre of a centrosome can be around 15 times the Cnn concentration in the cytoplasm. If Cnn could be transported into the centrosomes through a molecular one-way valve, this concentration behaviour could be explained. Neurons use a similar mechanism, by way of ion channels, to selectively concentrate K^+ ions inside cells and Na^+ ions in the extracellular space. However, centrosomes are amorphous organelles, i.e. they are not bounded by a membrane. Therefore, centrosomes are permeable to two-way transport and a valve-like mechanism may not be appropriate here. Another mechanism to explain Cnn concentration involves Cnn receptors. Centrosomes may have receptors for Cnn, with the binding rate higher than the unbinding rate. Cnn has been shown to physically interact with two proteins, Asterless (Asl) and DSpd2. Both these proteins localise close to the centrioles. Thus, these proteins could act as putative receptors for Cnn (Conduit et al., 2010).

2. The second feature of Cnn incorporation is apparent from the FRAP experiments. As shown in Figure 1.7, Cnn fluorescence initially recovers at the centre of the centrosome (which coincides with the centre of the bleach spot) and then slowly spreads outwards. This indicates that any Cnn receptors present in the

centrosome must be situated at the centre of the centrosome, thereby allowing Cnn recovery to begin at the centre. If the receptors were situated throughout the centrosome, fluorescence recovery would begin at the periphery of the centrosomes and then spread inwards. As mentioned in Section 2.2, we believe that cytoplasmic Cnn recovers quickly on the time scale of the FRAP experiment, and hence the recovery is shown by the Cnn form that is incorporated into the centrosomes, rather than the cytoplasmic form. We also believe that cytoplasmic Cnn is transported by passive diffusion, like several other cellular proteins. Following the binding of Cnn to the receptors at the centre of the centrosome, the spread of Cnn fluorescence throughout the centrosome could take place either by diffusion of Cnn or by an, as yet unidentified, transport mechanism.

3. Cnn appears very quickly at the centre of the centrosome after bleaching. However, its spread throughout the centrosomes takes longer. This implies the presence of more than one diffusion (or transport) time scale. Thus, the Cnn that is coming into the centrosome from the surrounding cytoplasm should have a large diffusion coefficient as compared to the Cnn that spreads through the centrosome following recovery at the centre (if the latter is also diffusing). This suggests at least two alternate forms of Cnn: a cytoplasmic (or light) form, with a large diffusion coefficient; and a "slower" (or heavier) form, with small diffusion coefficient (or small transport velocity). Conduit et al. (2010) hypothesise that phosphorylation of Cnn may be responsible for its incorporation into the centrosomes. It is possible that phosphorylated Cnn has several non-specific binding interactions with the PCM, which result in slow apparent movement of Cnn in the centrosomes. The slower diffusing Cnn species is also necessary to explain the observed concentration of Cnn in the centrosomes. If, after unbinding from the receptors, Cnn diffused with the same diffusion coefficient as

the incoming Cnn, it would not concentrate to levels greater than cytoplasmic levels beyond the receptors.

3.2.1 Assumptions

Considering the various features of Cnn incorporation observed experimentally, we arrive at our model assumptions. We assume that Cnn exists in two forms, a cytoplasmic or a light form, with high diffusion coefficient, and an altered or a heavy form, which moves slowly as compared to the light form. As mentioned previously, the heavy form could indicate a phosphorylated form. We further assume that Cnn receptors are situated at the centre of the centrosome and binding to these receptors converts light Cnn into heavy or altered (possibly phosphorylated) Cnn. Receptors and the Cnn-receptor complex are assumed to be immobile. Thus, the reactions occurring in the centrosomes are

$$L + P \underset{k_{off}}{\overset{k_{on}}{\rightleftharpoons}} C, \qquad C \xrightarrow{k_{turn}} P + N, \qquad N \xrightarrow{k_{out}} L, \tag{3.2.1}$$

where L, P, C and N denote the concentrations of light Cnn, receptors of Cnn, molecular complex of Cnn and its receptor, and heavy Cnn, respectively. k_{on} and k_{off} denote the rates of Cnn binding to, and unbinding from, its receptor, respectively. k_{turn} denotes the rate of light Cnn modification by its receptor and k_{out} denotes the rate of heavy Cnn spontaneously converting back into light Cnn. This could be a dephosphorylation reaction. It is important to consider this reaction for biological reasons. Firstly, it is more biologically realistic to allow the heavy Cnn to either convert back into light Cnn or to be degraded. There is currently no evidence to suggest that heavy Cnn might be degraded. Therefore, we have assumed that it reconverts back into light Cnn.

The heavy Cnn may move either by diffusion or by advection. We consider both these processes separately and construct two different models, a diffusion model and an advection model. It is possible that the heavy Cnn uses both advection and diffusion mechanisms to spread in the PCM. However, to begin with, we consider the individual processes separately. Since the PCM is a protein-dense matrix, it is possible that the diffusion coefficients in the PCM are lower than the diffusion coefficients in the cytoplasm. The altered diffusion coefficients in different media would affect both light and heavy Cnn. Even though it is more biologically realistic to allow the effective diffusion coefficients to change depending upon whether one is looking at the cytoplasm or the centrosome, it is unlikely to cause a qualitative change in the predictions of our models. Thus, for simplicity, we consider the molecules to have spatially uniform diffusion coefficients, irrespective of the subcellular location.

3.2.1.1 Geometry

Conduit et al. (2010) have shown that only the mother centriole recruits Cnn in a centrosome, and the daughter centriole does not begin recruiting Cnn until it has disengaged from the mother centriole at the end of mitosis. Thus, we assume that the Cnn receptors form a spherical shell around the mother centriole. (Note that the proteinaceous matrix around the centrioles is called the PCM. Therefore, the receptor shell is a part of the PCM). We further assume that this shell has infinitesimal thickness and is impermeable to both forms of Cnn. Thus, we effectively exclude the region close to, and including, the centrioles from our analysis. Figure 3.1 shows the schematic representation of the model geometry. Assuming such geometry allows for two simplifications: 1) it makes the system spherically symmetric; and 2) it allows us to introduce receptor-binding-unbinding reactions through a boundary condition. Considering the spherical geometry (with the spherical symmetry) of the problem, the natural choice of a coordinate system is a spherical polar system. In the following

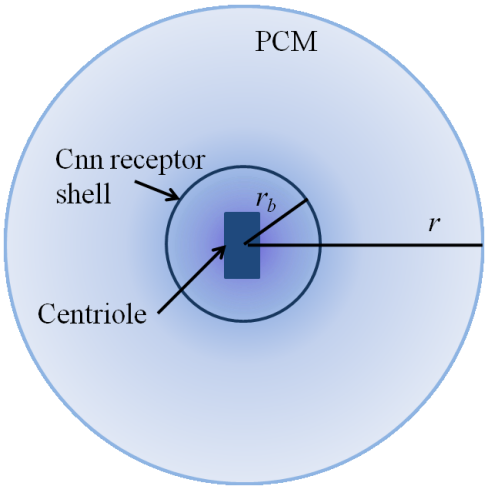

Figure 3.1: *Schematic representation of the simplified geometry used to study Cnn incorporation models. Centriole, Cnn receptor shell and the PCM are indicated. PCM surrounds the centriole. The receptor shell is a component of the PCM. r_b denotes the radius of the receptor shell and r the radial distance from the centre of the centriole. The radius of the domain R is greater than the radius over which the PCM is spread and is not indicated in the figure.*

section we present the diffusion model in detail.

3.3 Diffusion model

This model assumes that heavy Cnn moves by diffusion. The conversion of light Cnn into the heavy form may occur by the docking of light Cnn onto another molecule, thereby making it heavy, or by phosphorylation making the Cnn "sticky". Heavy Cnn may then spontaneously regenerate the light Cnn, by dissociation or by dephosphorylation. A schematic representation of the reactions involved in the diffusion model is given in Figure 3.2. With this simplified geometry we can assume spherical symmetry. The reaction-diffusion system (3.2.1) is thus described using a system of coupled PDE-ODEs,

$$\frac{\partial L}{\partial t} = \frac{D_L}{r^2}\frac{\partial}{\partial r}\left(r^2\frac{\partial L}{\partial r}\right) + k_{out}N, \quad r \in [r_b, R], \tag{3.3.1}$$

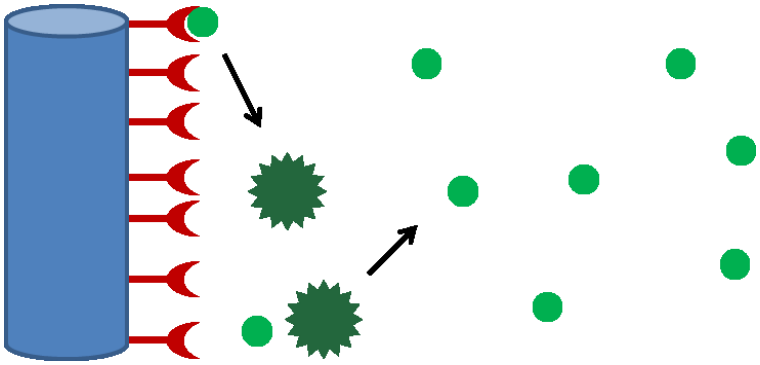

Figure 3.2: *Schematic representation of the reactions occurring in the diffusion model. The blue cylinder represents the centriole. Red objects around the centriole denote Cnn receptors. Small green circles denote light Cnn and large green star-like objects denote the slow-diffusing Cnn. Note that only one of the centrioles is shown here. This is because Conduit et al. (2010) have shown that only the mother centriole recruits Cnn in a centrosome. Even though the PCM is not explicitly shown, it exists around the centrioles as shown in Figure 3.1.*

$$\frac{\partial N}{\partial t} = \frac{D_N}{r^2}\frac{\partial}{\partial r}\left(r^2\frac{\partial N}{\partial r}\right) - k_{out}N, \quad r \in [r_b, R], \tag{3.3.2}$$

$$\frac{dP}{dt} = k_{turn}C + k_{off}C - k_{on}L(r_b, t)P, \quad r = r_b, \tag{3.3.3}$$

$$\frac{dC}{dt} = k_{on}L(r_b, t)P - k_{off}C - k_{turn}C, \quad r = r_b, \tag{3.3.4}$$

where D_L and D_N are the diffusion coefficients for light Cnn and heavy Cnn, respectively. We have hypothesised that $D_N \ll D_L$. Notice that the differential equations describing the evolution of P and C do not involve a spatial component. This is because the Cnn receptors and Cnn-receptor complex only exist on the binding shell and are immobile. We study the PDEs describing the evolution of L and N on the domain $r \in [r_b, R]$, where r_b denotes the radius of the binding shell (as shown in Figure 3.1) and R denotes the outer radius of the domain. The PDEs for L and N do not include the binding-unbinding reactions, as these are brought in via the left-hand boundary conditions. At the left-hand boundary (i.e. at the receptor shell at $r = r_b$) the complex is converted into heavy Cnn, thus leading to the production

of heavy Cnn there, and light Cnn binds to and dissociates from its receptors (see the boundary conditions in (3.3.5)). The concentration of light Cnn is considered to be constant, at cytoplasmic levels, far from the centrosomes. The concentration of heavy Cnn diminishes far from the receptor shell and therefore is considered to be zero away from the centrosomes. Thus, the boundary conditions are given by

$$\begin{aligned} D_L \frac{\partial L}{\partial r}\bigg|_{r=r_b} &= k_{on} L(r_b, t) P(t) - k_{off} C(t), \\ D_N \frac{\partial N}{\partial r}\bigg|_{r=r_b} &= -k_{turn} C(t), \\ N(R, t) = 0 \quad &\text{and} \quad L(R, t) = L_{cyt}, \end{aligned} \tag{3.3.5}$$

where L_{cyt} is the concentration of light Cnn in the cytoplasm away from the centrosomes. From equations (3.3.3) and (3.3.4) we can see that $C + P$ is conserved. Let us call this P_{tot}. This is the total receptor concentration at the receptor shell.

The average radius of a centrosome, as measured by Cnn fluorescence, is close to $1 - 1.2$ μm. The average length and width of a *Drosophila* embryo (which stay constant throughout the syncytial divisions) are 0.51 mm and 0.18 mm, respectively (Markow et al., 2009). The experiments are performed on *Drosophila* syncytial embryos, i.e., embryos in which the cells are without any cell walls. Thus, effectively, the centrosomes can be assumed to exist in a domain (the embryo), which is much larger than the individual centrosomes. Thus, it is not unrealistic to assume a domain with infinite radius. Thus, equations (3.3.1)-(3.3.2) will be analysed on the domain $r \in [r_b, \infty)$.

3.4 Analysis of the diffusion model

3.4.1 Non-dimensionalisation

To analyse our model, we non-dimensionalise it by introducing new dimensionless variables and defining non-dimensional parameters as

$$
\begin{aligned}
&u = \frac{L}{L_{cyt}}, \quad v = \frac{N}{L_{cyt}}, \quad w = \frac{C}{P_{tot}}, \quad p = \frac{P}{P_{tot}},\\
&t^* = k_{turn}t, \quad r^* = \sqrt{\frac{k_{turn}}{D_L}}r, \quad \varepsilon_1 = \frac{D_N}{D_L}, \quad \alpha = \frac{k_{on}L_{cyt}}{k_{turn}},\\
&\beta_1 = \frac{k_{off}}{k_{turn}}, \quad \beta_2 = \frac{k_{out}}{k_{turn}}, \quad \mu = \sqrt{\frac{k_{turn}}{D_L}}\frac{P_{tot}}{L_{cyt}}, \quad r_b^* = \sqrt{\frac{k_{turn}}{D_L}}r_b.
\end{aligned} \tag{3.4.1}
$$

Rearranging equations (3.3.1)-(3.3.4) and using the above substitutions, a non-dimensionalised form of our model is obtained which, on removing the asterisks for clarity, takes the form

$$\frac{\partial u}{\partial t} = \frac{1}{r^2}\frac{\partial}{\partial r}\left(r^2\frac{\partial u}{\partial r}\right) + \beta_2 v, \quad r \in [r_b, \infty), \tag{3.4.2}$$

$$\frac{\partial v}{\partial t} = \frac{\varepsilon_1}{r^2}\frac{\partial}{\partial r}\left(r^2\frac{\partial v}{\partial r}\right) - \beta_2 v, \quad r \in [r_b, \infty), \tag{3.4.3}$$

$$\frac{dp}{dt} = (\beta_1 + 1)w - \alpha u p, \quad r = r_b, \tag{3.4.4}$$

$$\frac{dw}{dt} = \alpha u p - (\beta_1 + 1)w, \quad r = r_b. \tag{3.4.5}$$

The non-dimensionalised boundary conditions are given by

$$
\begin{aligned}
&\left.\frac{\partial u}{\partial r}\right|_{r=r_b} = \alpha\mu u p - \beta_1\mu w,\\
&\left.\frac{\partial v}{\partial r}\right|_{r=r_b} = -\frac{\mu}{\varepsilon_1}w,\\
&v(\infty, t) = 0 \ \text{ and } \ u(\infty, t) = 1,
\end{aligned} \tag{3.4.6}
$$

where r_b denotes the nondimensionalised radius of the receptor shell. ε_1 is a small parameter since, according to our hypothesis, $D_N \ll D_L$. Assuming that initially no binding reaction occurs even though u and p are both present in the system, and the binding is "switched on" at time $t = 0$, the initial conditions for the model are

$$u(r,0) = H(r-\delta), \quad v(r,0) = 0, \quad p(r_b,0) = 1, \quad \text{and} \quad w(r_b,0) = 0, \tag{3.4.7}$$

where $H(x)$ denotes a Heaviside function and δ denotes an arbitrarily small distance from r_b. The Heaviside function is used so that the initial condition for u satisfies the boundary conditions for u at $t = 0$.

3.4.2 Steady states

The steady state solutions of equations (3.4.2)-(3.4.5) are given by

$$v_{eqm}(r) = v_{r_b}\frac{r_b}{r}\exp\left(-(r-r_b)\sqrt{\beta_2/\varepsilon_1}\right), \tag{3.4.8}$$

where v_{r_b} is the steady state concentration of v at $r = r_b$, and is given by

$$v_{r_b} = \frac{r_b\mu}{r_b\sqrt{\beta_2\varepsilon_1}+\varepsilon_1}w_{eqm},$$

where

$$w_{eqm} = \frac{\alpha u}{\alpha u + \beta_1 + 1}. \tag{3.4.9}$$

The steady state solution for u is given by

$$u_{eqm}(r) = 1 - \varepsilon_1 v_{eqm}, \tag{3.4.10}$$

where the subscript *eqm* denotes the steady state concentrations. Using equations (3.4.8)-(3.4.10), we have

$$v_{rb} = \frac{-b \pm \sqrt{b^2 - 4ac}}{2a}, \tag{3.4.11}$$

where

$$a = \alpha\varepsilon_1 \left(1 + r_b\sqrt{\frac{\beta_2}{\varepsilon_1}}\right),$$

$$b = -\left[\left(1 + r_b\sqrt{\frac{\beta_2}{\varepsilon_1}}\right)\varepsilon_1(\alpha + \beta_1 + 1) + \alpha\varepsilon_1\mu r_b\right],$$

and

$$c = \alpha\mu r_b.$$

Note that we only consider the smaller of the two positive solutions for v_{rb} as the greater positive solution corresponds to a negative solution for u_{r_b} which is unphysical.

3.4.3 Temporal analysis

Due to conservation of total receptor concentration we can write $p = 1 - w$. Substituting into equation (3.4.5) we obtain

$$\frac{dw}{dt} = \alpha u - (\alpha u + \beta_1 + 1)w. \tag{3.4.12}$$

Thus, the evolution of the complex concentration is given by

$$w(t) = 1 - \frac{1}{I_f(t)} - \frac{(\beta_1 + 1)}{I_f(t)}\int_0^t I_f(s)\mathrm{d}s, \tag{3.4.13}$$

where

$$I_f(t) = \exp\left(\int_0^t (\alpha u + \beta_1 + 1)\mathrm{d}\bar{t}\right). \tag{3.4.14}$$

This solution of w is implicit in u. If the explicit solution of w could be obtained, it could be used to solve for v. However, the explicit solution of u and v is complicated

due to the fact that they are a coupled PDE-ODE system which is not amenable to explicit analytical solution. The presence of a small parameter (ε_1) suggests that the system may be simplified by the use of perturbation analysis. However, we can show that our solution v possesses an essential singularity with respect to ε_1. This can be seen from the steady state solution for v given by equation (3.4.8). Notice that the solution involves a term

$$\exp\left(\frac{1}{\sqrt{\varepsilon_1}}\right).$$

Since the equation for the evolution of v (3.4.3) can be simply converted into a standard diffusion equation, it would have a solution with a Gaussian component convoluted with the boundary conditions. The Gaussian component would be of the form

$$\exp\left(\frac{x^2}{4kt}\right), \tag{3.4.15}$$

where k is the diffusion coefficient, which in this case is ε_1. Thus, once again, the evolution expression for v can also be shown to possess an essential singularity with respect to ε_1. This prevents us from using perturbation analysis to simplify the system. In the next section we use numerical methods to observe the kinetics of the system.

3.4.4 Numerical simulations

In this section we present numerical simulations of the diffusion model as well as simulations of the FRAP experiment. MATLAB's `pdepe` solver is used for the simulations. None of the parameter values in our model are known. The range into which these parameter values should fall is also not obvious. Also, the amount of Cnn is determined by measuring the fluorescence intensities in arbitrary units [AU]. It is not simple to infer the molar concentrations of Cnn using these fluorescence values. We therefore make the simplifying assumption that the fluorescence shown by Cnn is

directly proportional to the molar concentration of Cnn in the concentration ranges encountered in the experiments. As long as the LASER intensity is adjusted (as was done by our collaborators) such that the Cnn intensity peaks do not saturate the microscope camera, this assumption will hold. The parameter values chosen are given in Table 3.1. Figure 3.3 shows the numerical solution for the light and heavy Cnn at selected time points. It can be seen that the system approaches steady state as time increases. It also shows that heavy Cnn indeed forms a gradient at steady state such that its concentration peaks close to the origin.

Table 3.1: Parameter values and their units used in numerical simulations of the diffusion and advection models. The parameter values are either borrowed from the literature or chosen arbitrarily (indicated by a hyphen in the reference column).

Parameters (Dimensional)	**Value**	**Units**	**References**
k_{on}	10^{21}	$\text{mol}^{-1}\mu\text{m}^3\text{s}^{-1}$	(Schlosshauer and Baker, 2004)
k_{off}	0.1	s^{-1}	-
k_{turn}	0.1	s^{-1}	-
k_{out}	0.1	s^{-1}	-
D_L	1	$\mu\text{m}^2\ \text{s}^{-1}$	(Gregor et al., 2005, 2007)
D_N	0.01	$\mu\text{m}^2\ \text{s}^{-1}$	-
a	0.03	$\mu\text{m}\ \text{s}^{-1}$	(Barkus et al., 2008)
P_{tot}	3.15×10^{-21}	$\text{mol}\mu\text{m}^{-2}$	(Ghaemmaghami et al., 2003)
L_{cyt}	5×10^{-22}	$\text{mol}\mu\text{m}^{-3}$	(Ghaemmaghami et al., 2003)

3.4.5 Modelling the FRAP experiment

As discussed in Chapter 2, a high intensity LASER bleaches a cylindrical region through the sample during the FRAP experiment. Bleaching does not alter the underlying chemistry and therefore the system still undergoes all the reactions given by (3.2.1). Even though bleaching diminishes the local concentration of fluorescent Cnn,

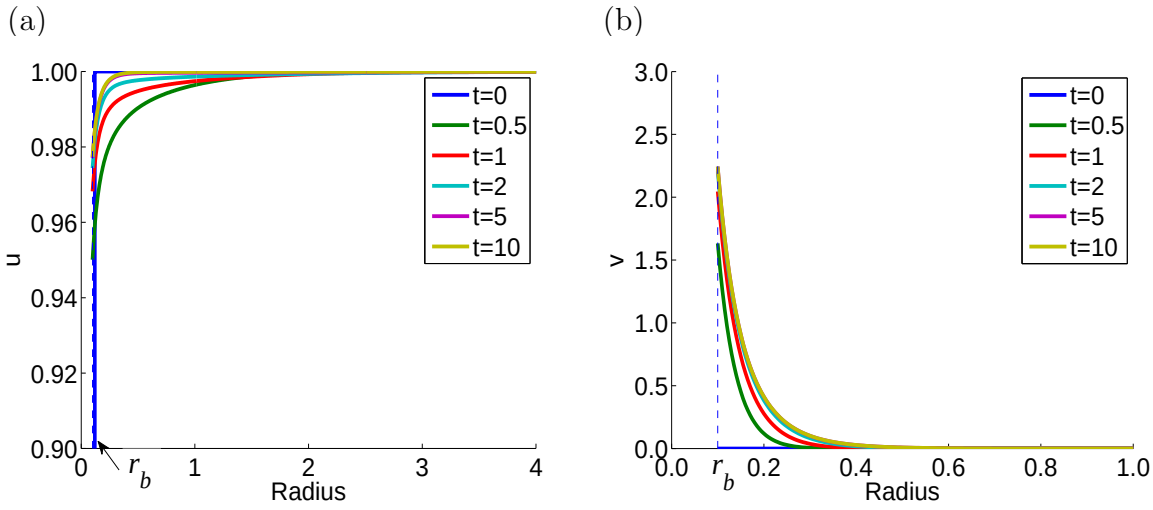

Figure 3.3: *Numerical simulation of the evolution of light Cnn* (a) *and heavy Cnn* (b) *with time given by the model* (3.4.2)-(3.4.5). MATLAB's `pdepe` *solver is used for the simulations. The parameter values from* Table 3.1 *are used. The radius of the receptor sphere,* $r_b = 0.1$*, is indicated by a dashed line. The accuracy of the solution depends upon mesh size. This was chosen to be 0.01, since refining the mesh further did not improve the solution. (Changing the mesh size from 0.01 to 0.005 did not change the solution more than the tolerance, which was 1e-4).*

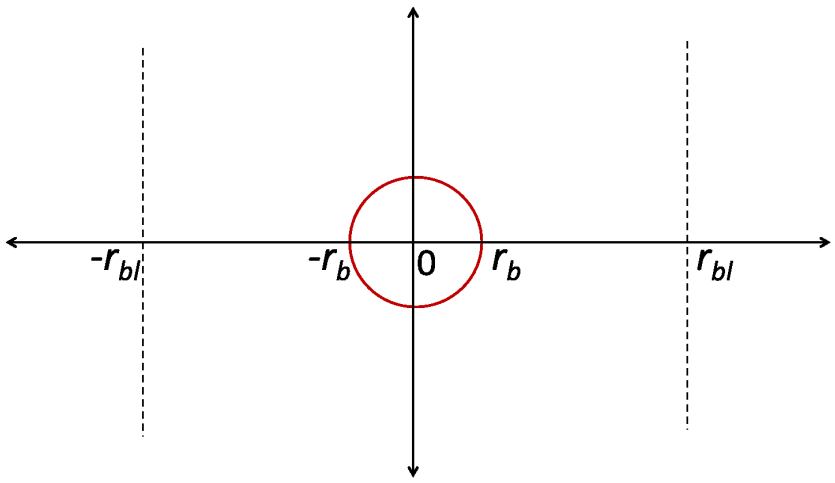

Figure 3.4: *Schematic representation of a vertical section through the bleached region. The origin coincides with the centre of the centriole,* r_b *denotes the radius of the binding sphere and* r_{bl} *denotes the bleaching radius. The domain over which the PDE system is solved is significantly larger than* r_{bl}*.*

the bleached region is much smaller than the embryo. Thus, the overall concentration of fluorescent cytoplasmic Cnn remains essentially unchanged. Bleaching creates two molecular subpopulations containing Cnn, a bleached population, which is not fluorescent, and a population that is unbleached and still fluorescent. Because of the GFP tag, all molecular species containing Cnn are fluorescent before bleaching, i.e., u, v and w are all fluorescent, but the free receptors, p, are not. Thus, the resulting evolution equations are simply two copies of the original model equations and are given as

$$\frac{\partial u_b}{\partial t} = \frac{1}{r^2}\frac{\partial}{\partial r}\left(r^2\frac{\partial u_b}{\partial r}\right) + \beta_2 v_b, \tag{3.4.16}$$

$$\frac{\partial v_b}{\partial t} = \frac{\varepsilon_1}{r^2}\frac{\partial}{\partial r}\left(r^2\frac{\partial v_b}{\partial r}\right) - \beta_2 v_b, \tag{3.4.17}$$

$$\frac{dw_b}{dt} = \alpha u_b(r_b, t)p_{eqm} - (\beta_1 + 1)w_b, \tag{3.4.18}$$

$$\frac{\partial u_f}{\partial t} = \frac{1}{r^2}\frac{\partial}{\partial r}\left(r^2\frac{\partial u_f}{\partial r}\right) u + \beta_2 v_f, \tag{3.4.19}$$

$$\frac{\partial v_f}{\partial t} = \frac{\varepsilon_1}{r^2}\frac{\partial}{\partial r}\left(r^2\frac{\partial v_f}{\partial r}\right) - \beta_2 v_f, \tag{3.4.20}$$

$$\frac{dw_f}{dt} = \alpha u_f(r_b, t)p_{eqm} - (\beta_1 + 1)w_f, \tag{3.4.21}$$

where the subscript b denotes a bleached species and subscript f denotes an unbleached species. The fluorescent species cannot be converted into bleached species spontaneously (i.e. in the absence of a bleaching LASER) and *vice versa*. Bleaching is carried out at mitosis when the Cnn incorporation is at steady state. Therefore, before bleaching all the reactions are assumed to be at steady state. Since bleaching does not change the underlying chemistry of the system, all the reactions would be at steady state even after bleaching. Thus, the rate of change of the fluorescent and non-fluorescent versions of any molecular species together is zero for all r. For

example,

$$\frac{\partial}{\partial t}(u_b(r,t)+u_f(r,t))=0,$$

even though the individual species $u_b(r,t)$ and $u_f(r,t)$ show evolution with time. Since free receptors, p, are non-fluorescent, bleaching does not create two subpopulations of p. However, the free receptors now react with two sub-populations of light Cnn but both sub-populations of complex regenerate the same free receptor by the unbinding reaction. Since the equilibrium of the system is not altered, the concentration of free receptors remains unchanged at $p=p_{eqm}$, which is the steady state concentration of free receptors. Thus,

$$\frac{dp}{dt}=(\beta_1+1)w_f+(\beta_1+1)w_b-\alpha u_f(r_b,t)p-\alpha u_b(r_b,t)p=0. \tag{3.4.22}$$

From the conservation of total receptors we have $p_{eqm}=1-w_{eqm}$, where w_{eqm} is given by (3.4.9). Boundary conditions for the different species are given by

$$\begin{aligned}
&\left.\frac{\partial u_b}{\partial r}\right|_{r=r_b}=\alpha\mu u_b(r_b,t)p(t)-\beta_1\mu w_b(t),\\
&\left.\frac{\partial v_b}{\partial r}\right|_{r=r_b}=-\frac{\mu}{\varepsilon_1}w_b(t),\\
&v_b(\infty,t)=0 \quad \text{and} \quad u_b(\infty,t)=0,\\
&\left.\frac{\partial u_f}{\partial r}\right|_{r=r_b}=\alpha\mu u_f(r_b,t)p(t)-\beta_1\mu w_f(t),\\
&\left.\frac{\partial v_f}{\partial r}\right|_{r=r_b}=-\frac{\mu}{\varepsilon_1}w_f(t),\\
&v_f(\infty,t)=0 \quad \text{and} \quad u_f(\infty,t)=1,
\end{aligned} \tag{3.4.23}$$

Notice that the right hand boundary condition for u_b is different to that for u_f. The concentration of bleached cytoplasmic Cnn, u_b, is assumed to be negligible in comparison with the total fluorescent cytoplasmic Cnn because the bleached area is

much smaller as compared to the whole domain. As the system is believed to have reached steady state before bleaching, the initial conditions are given by the steady state concentrations, denoted by subscript eqm, of the various species. Thus,

$$\begin{aligned}
&u_b(r,0) = u_{eqm}(r), \quad v_b(r,0) = v_{eqm}(r) \ \text{ and } \ w_b(r_b,0) = w_{eqm} \ \text{ for } \ r_b \leq r \leq r_{bl},\\
&u_f(r,0) = 0, \quad v_f(r,0) = 0 \ \text{ and } \ w_f(r_b,0) = 0,\\
&u_b(r,0) = 0 \ \text{ and } \ v_b(r,0) = 0, \qquad\qquad \text{for } \ r > r_{bl},\\
&u_f(r,0) = u_{eqm}(r) \ \text{ and } \ v_f(r,0) = v_{eqm}(r),
\end{aligned} \tag{3.4.24}$$

where r_{bl} denotes the radius of the bleach spot. Even though the LASER beam (and by extension the bleached region) would describe a cylinder as it passes through the specimen, we approximate the bleached region as a sphere with radius r_{bl} for simplicity. It is conceivable that this alters the dynamics of incoming cytoplasmic Cnn, which is believed to be fast. However, we are mainly interested in the dynamics of heavy Cnn. Experimentally, the bleaching radius is chosen such that it is greater than the range over which Cnn fluorescence decreases to cytoplasmic levels. Therefore, we believe that the assumption of a spherical bleached region will not affect the recovery dynamics significantly. We justify this argument as follows. Consider that the cytoplasmic Cnn diffuses into a cylindrical bleached region in the absence of binding. Due to axisymmetry, this corresponds to two-dimensional diffusion and the diffusion time scale can be given by $t = L^2/4D$, where t denotes time, L denotes the radius of the bleached region and D denotes the diffusion coefficient. If, instead, we assume the bleached region to be spherical, with the identical radius, the diffusion time scale would be given by $t = L^2/6D$. Previous work into the diffusion of various proteins has shown that the characteristic times for recovery due to diffusion are less than one second in the case of two-dimensional geometries (Sprague and McNally, 2005). Therefore, considering three-dimensional diffusion into a spherical region is likely to

increase the diffusion time scale by about 0.33 seconds and make it 1.33 seconds. The FRAP experiment we are interested in is carried out over the time scale of 100 seconds. Therefore, assuming a spherical bleached region is unlikely to affect recovery dynamics significantly. Figure 3.4 shows the position of r_{bl} with respect to the domain under consideration. The steady state concentrations $u_{eqm}(r)$, $v_{eqm}(r)$ and w_{eqm} are given analytically by equations (3.4.10), (3.4.8) and (3.4.9), respectively. We expect that, as time increases, the fluorescent species will increase in the centrosome region ($r < r_{bl}$) and the non-fluorescent species will decrease asymptotically. Figure 3.5 shows the numerical simulation of the evolution of bleached and fluorescent species. As expected, the bleached species decrease over time and the unbleached species increase over time. Furthermore, the fluorescent heavy Cnn (which we believe is responsible for showing the observed Cnn fluorescence recovery) initially recovers close to the centre and then spreads outwards, as seen in the experiments.

3.5 Fitting the diffusion model to Cnn FRAP data

In this section we fit the FRAP data with the diffusion model in order to verify the model and to generate parameter estimates from these fits. It is important to note the following considerations before we begin to fit the data.

1. We argue that the recovery due to cytoplasmic Cnn diffusing into the bleached region is not dynamically important on the time scale of the FRAP experiment (see Chapter 2, Section 2.2). The recovery is dominated by binding kinetics and the diffusion of the heavy Cnn.

2. Figure 2.6(b) in Chapter 2 shows the total fluorescence recovery of Cnn with respect to time. It can be seen that the recovery increases linearly with time. Typically, FRAP recovery data are gathered until the recovery begins to plateau. It may be possible that the recovery we observe only describes the initial lin-

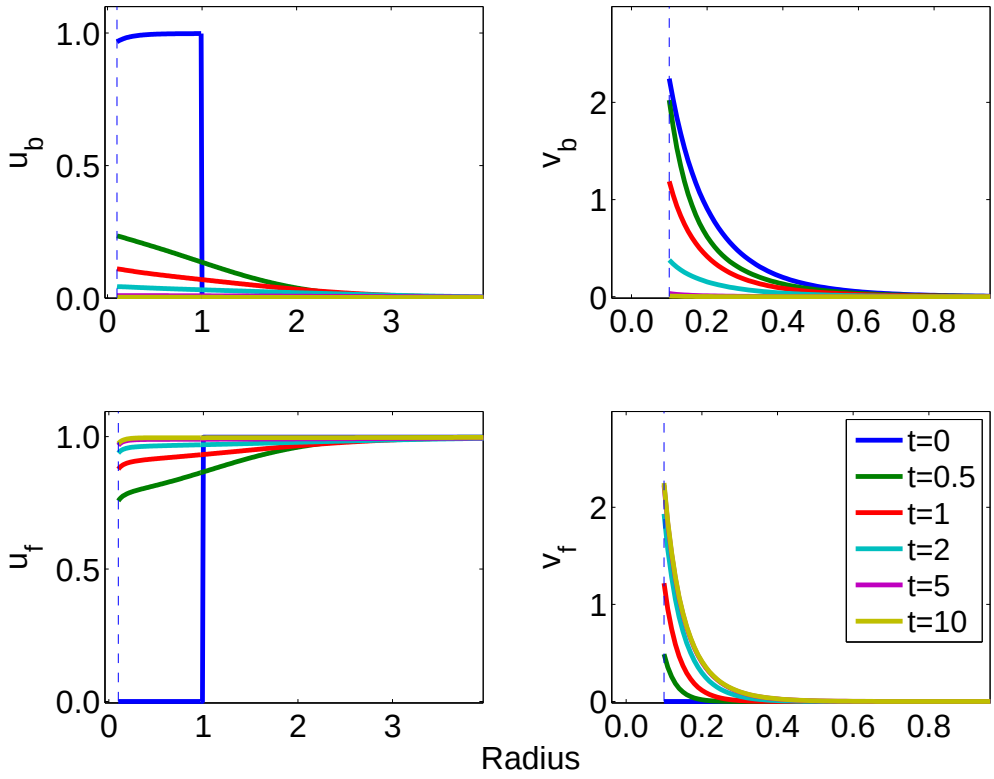

Figure 3.5: *Evolution of bleached light and heavy Cnn (top panels) and unbleached light and heavy Cnn (bottom panels) as given by the diffusion model* (3.4.16)-(3.4.24) *is shown in a simulated FRAP experiment. The bleaching radius* $r_{bl} = 1$. MATLAB's `pdepe` *solver is used for the simulations, with the parameter values from* Table 3.1. *The radius of the receptor sphere,* $r_b = 0.1$, *is indicated by a dashed line. The accuracy of the solution depends upon mesh size. This was chosen to be 0.01, since refining the mesh further did not improve the solution. (Changing the mesh size from 0.01 to 0.005 did not change the solution more than the tolerance, which was 1e-4).*

ear phase in a FRAP curve that would plateau at later times. The shape of the recovery curve can be indicative of whether the recovery is dominated by diffusion or by binding reactions or by both (Sprague et al., 2004; Sprague and McNally, 2005). However, the time for which recovery could be monitored in the case of our system is restricted by the length of mitosis in *Drosophila* syncytial embryos. Therefore, it is not possible to observe the recovery kinetics until the

FRAP curve plateaus. Secondly, not only do we wish to estimate the parameters of recovery, we also wish to study the mechanism of how Cnn recovery could begin at the centre of the centrosome and then spread outwards. Hence, along with studying the temporal evolution of total fluorescence, we are keen to explore how the fluorescence evolves spatially.

3. We have used a combination of model parameters to non-dimensionalise space (3.4.1). However, during data fitting these parameters need to be varied separately and independently in order to find the best fit. Thus, it is not possible to use the non-dimensionalised model for the purpose of fitting. However, as the fluorescence data are normalised using the cytoplasmic Cnn concentration, L_{cyt}, the dimensional model has to be similarly normalised. We denote the normalised light and heavy Cnn by u and v, respectively. FRAP data are gathered every 10 seconds after bleaching (as mentioned in Chapter 2). Since diffusion of light Cnn is unlikely to be dynamically important on the FRAP time scale, the time evolution observed in our experiments is only due to the incorporated Cnn. Therefore, effectively, the fluorescence from light Cnn, u, is subtracted from the data and the only fluorescence remaining is due to the heavy Cnn, v. Thus, we only fit heavy Cnn profiles from the model with the data. Appendix A.1 describes the normalised diffusion model.

In the sections on data fitting, we will use the normalised dimensional forms of our model.

3.5.1 Fitting steady state data

The pre-bleach Cnn fluorescence data collected during mitosis represent the biologically realistic steady state of Cnn incorporation. Figure 2.4(a) in Chapter 2 shows the normalised fluorescence intensities of heavy Cnn at a pre-bleach time point from six

different embryos. The steady state of the normalised diffusion model in dimensional form is given by

$$v_{eqm}(r) = \frac{r_b}{r} v_{r_b} \exp\left(-(r - r_b)\sqrt{\frac{k_{out}}{D_N}}\right), \tag{3.5.1}$$

where v_{eqm} denotes normalised heavy Cnn at steady state and r_b denotes the radius of the receptor sphere in dimensional form. We use MATLAB's `lsqnonlin` function to perform the nonlinear least squares fitting. Figure 3.6(a) shows the fit of the diffusion model with averaged steady state data from both the spindle side and the cytoplasm side of the centrosomes. The parameter estimates obtained from the fits are given in Table 3.2. The coefficient of determination (R^2) values are close to 1 suggesting that the model shows good fit with the data. However, visualising fits with Figure 3.6 shows that the model underpredicts v at small radii and overpredicts it at large radii, resulting in non-random distribution of residuals. In the next section we fit the FRAP recovery data with the diffusion model.

Table 3.2: Results of fitting the steady state of the diffusion model (equation (3.4.8)) with the average steady state data. Parameter estimates obtained from fitting, RMSE and the coefficient of determination, R^2, are listed.

Data	v_{r_b}	$\sqrt{\frac{k_{out}}{D_N}}$	**RMSE**	$\boldsymbol{R^2}$
Units	-	μm^{-1}	-	-
Average data (spindle side)	13.77	0.8764	0.941	0.9355
Average data (cytoplasm side)	14.24	0.5504	0.945	0.9365

3.5.2 Fitting FRAP recovery data

To simulate FRAP recovery, we only need to consider the unbleached species. Since the bleaching was carried out at the steady state, the concentration of free receptors

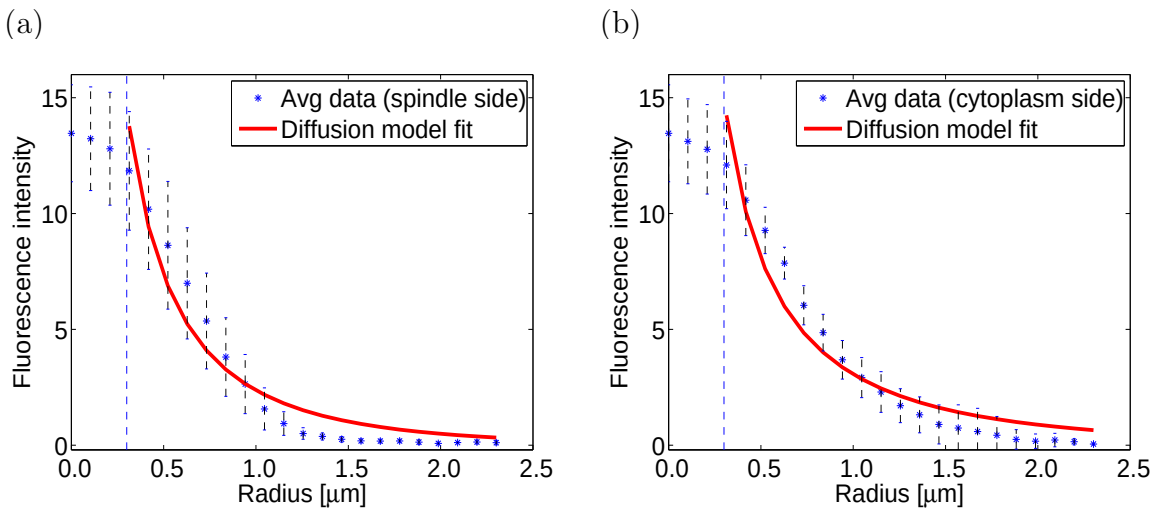

Figure 3.6: *Nonlinear least squares fit of the steady state of the diffusion model* (3.5.1) *to the normalised average steady state data from the spindle side,* (a), *and cytoplasm side,* (b). *The standard deviation of the data is indicated by the error bars. The radius of the receptor sphere,* $r_b = 0.3$ μm, *is indicated by the dashed blue line.*

p remains constant and is given by

$$p_{eqm} = \frac{P_{tot}(k_{off} + k_{turn})}{\overline{k_{on}} u_{eqm} + k_{off} + k_{turn}},$$

where $\overline{k_{on}} = k_{on} L_{cyt}$ and u_{eqm} denotes the steady state concentration of u. The pre-bleach state is fitted using the steady state solution and the post-bleach recovery is fitted using the numerical solution of v, since an analytical solution is not available. We use MATLAB's `pdepe` solver for numerical simulation of the FRAP kinetics of v for a given set of parameters. As mentioned in Chapter 2, recovery data are gathered at every 10 second intervals, starting with 8.5 seconds post-bleaching up to 158.5 seconds post-bleaching. We evaluate the numerical solution at the corresponding time points post-bleaching and at $x = r_b, r_b + 0.01, r_b + 0.02, \ldots, R$, where R denotes the right-hand boundary of the domain. The pixel size of the data is 0.1046 μm. In order to compare the data and the model solution, we interpolate the numerical solution of the model at the radial values of $(0, 0.1046, \ldots, 2.4058)$. The model values thus

obtained are used to calculate the sum of squared differences with respect to the data. We use MATLAB's `lsqnonlin` and `fminsearch` algorithms for the minimisation of sum of squares. Figure 2.7 shows the steps taken for the data fitting.

3.5.2.1 Initial guess

The success of nonlinear regression depends upon the choice of the initial parameters and how close the initial guess is to the true solution. Therefore it is necessary to choose the initial guess carefully. In the case of our model, however, no estimates are available regarding any of the parameters. We base our initial guess on values of similar reactions available from the literature. For example, consider the diffusion coefficient of light Cnn (D_L). The molecular mass of Cnn is estimated to be 130 kDa (Li et al., 1998) and the mass of GFP is around 30 kDa (Phair and Misteli, 2001). Thus, in our experiments the mass of GFP-Cnn protein would be around 160 kDa. Gregor et al. (2005) have estimated the diffusion coefficients of Dextran molecules of various sizes in *Drosophila* embryos. According to their estimates the diffusion coefficient of Dextran molecules of size 150 kDa is around 12.9 $\mu\text{m}^2\text{s}^{-1}$. However, Dextran is an inert molecule, which is not expected to interact with other cellular proteins and molecules. Therefore, this could be an overestimate for a native protein that potentially interacts with other cell components. For example, the effective diffusion coefficient of the Bicoid-GFP fusion product (molecular weight approx. 85 kDa) was estimated to be 0.3 $\mu\text{m}^2\text{s}^{-1}$ in *Drosophila* embryos (Gregor et al., 2007). Thus, in absence of a direct estimate of the diffusion coefficient of Cnn, we begin with $D_L = 1$ $\mu\text{m}^2\text{s}^{-1}$. Since our model assumes that the heavy Cnn diffuses slower than the light Cnn, we choose $D_N = 0.01$ $\mu\text{m}^2\text{s}^{-1}$. k_{on} denotes a bimolecular association rate. Typically, association rates vary widely between around $10^3 - 10^{10}$ $\text{M}^{-1}\text{s}^{-1}$ (Schlosshauer and Baker, 2004). In the normalised form of our model, however, we use the modified k_{on}, denoted as $\overline{k_{on}} = k_{on}L_{cyt}$. The value of L_{cyt} is available from

the experiments in the form of fluorescence intensity in arbitrary units. It is not clear how this fluorescence intensity relates to the molar concentration of Cnn. Therefore, it is not clear what the value of $\overline{k_{on}}$ should be. If we take $k_{on} = 10^6$ $M^{-1}s^{-1}$ and $L_{cyt} = 10^{-6}$ M, which are both realistic estimates, we obtain an estimate of $\overline{k_{on}} = 1$ s^{-1}. The value of 0.01 s^{-1} is used for the rates k_{off}, k_{turn} and k_{out}, since the recovery occurs over a time scale of 100 seconds. Since the receptors are hypothesised to only exist on a spherical surface their total concentration, P_{tot}, has units of molμm^{-2}. Since this receptor geometry is not biologically realistic, it is not clear what the initial estimate for P_{tot} should be. We begin with an estimate of 1 molμm^{-2}.

3.6 Results

Figures 3.7-3.9 show sample fits of the diffusion model with the data. Table 3.3 shows the best-fitting parameter estimates obtained from the fits. The goodness of fit estimators, namely RMSE values and R^2 coefficients, are also listed. The goodness of a fit can be evaluated using several criteria, such as the distribution of residuals and the R^2 coefficient. Values of R^2 close to unity indicate a good fit. Considering this criterion, the diffusion model appears to be a good fit with the data. As mentioned in Section 2.4.2.2, we use normalised residuals to evaluate the goodness of fit. Figure 3.10 shows the distribution of normalised residuals from the fits with the average data from the spindle side and the cytoplasm side. It can be seen that the distribution of residuals is not random. In particular, the model underpredicts the data for initial time points and overpredicts the data at later time points. This could indicate that at least one predictor variable has not been accounted for in the model or that the model does not accurately describe the system. Thus, we present another model of Cnn incorporation, namely the advection model. We then present the data fitting with this model. We defer the discussion about the comparison of the diffusion and

the advection model until Section 3.11.

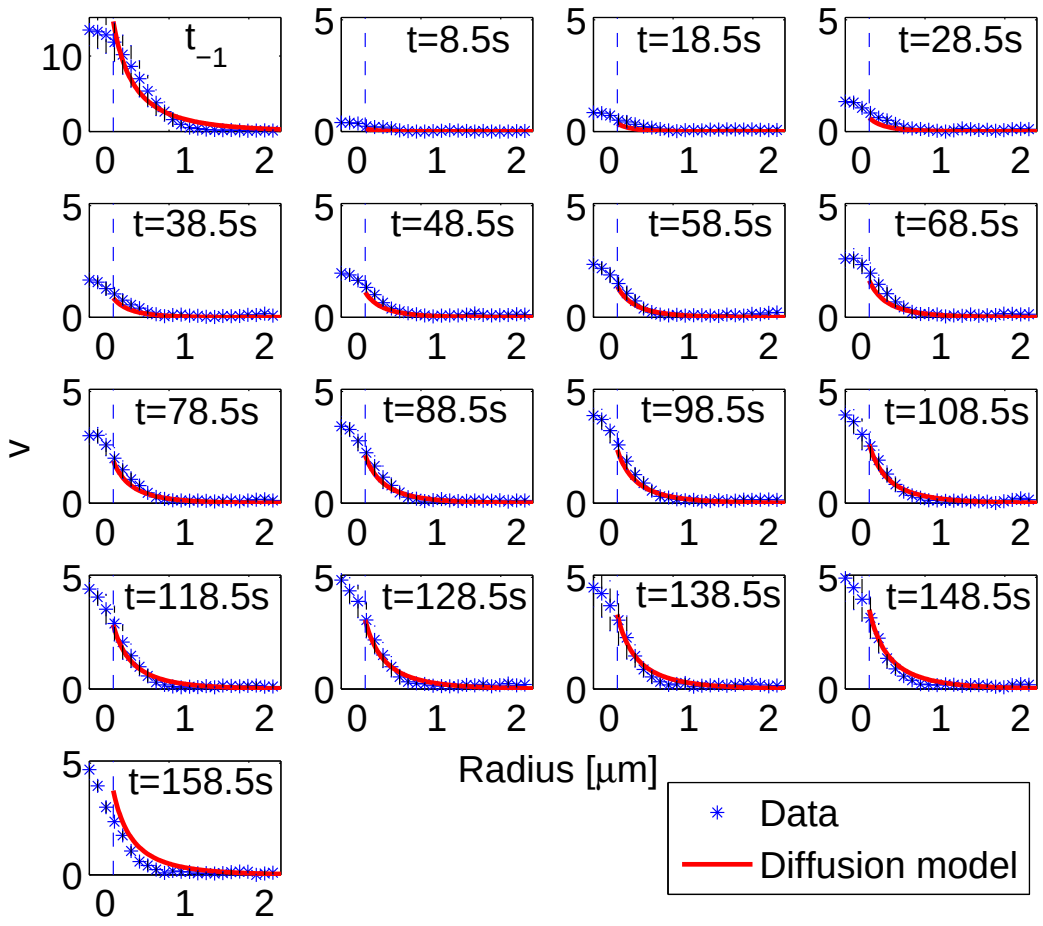

Figure 3.7: *Average spindle side FRAP kinetics data for heavy Cnn (blue asterisks) is shown with the best-fitting diffusion model solution of v (red solid lines): equations* (3.4.16)-(3.4.21). *The error bars represent the standard deviation in the data.* t_{-1} *denotes the pre-bleach time point and* $t = 8.5$ *s to* $t = 158.5$ *s denote the post-bleach recovery time points. The blue dashed lines indicate the position of* r_b.

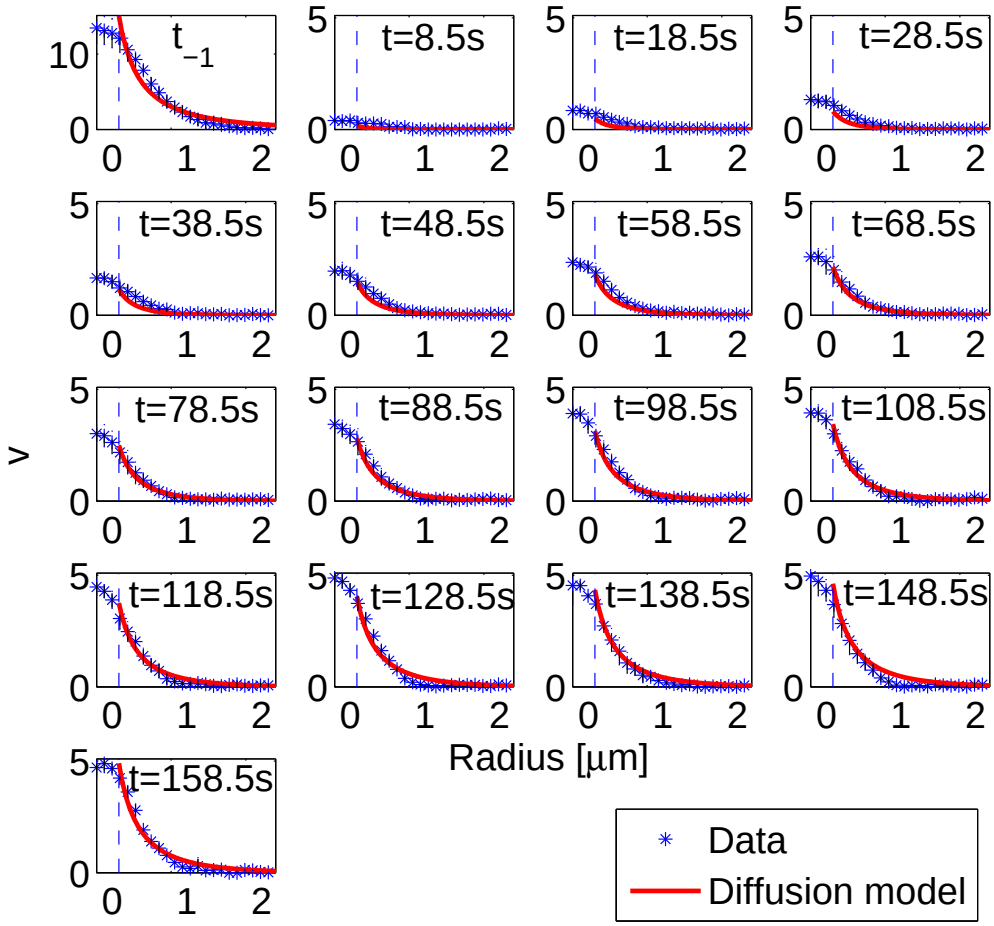

Figure 3.8: *Average cytoplasm side FRAP kinetics data for heavy Cnn (blue asterisks) is shown with the best-fitting diffusion model solution of v (red lines): equations* (3.4.16)-(3.4.21). *The error bars represent the standard deviation in the data.* t_{-1} *denotes the pre-bleach time point and* $t = 8.5$ *s to* $t = 158.5$ *s denote the post-bleach recovery time points. The blue dashed lines indicate the position of* r_b.

3.7 Advection model

In this section we present a second model of Cnn incorporation, namely the advection model. This model assumes that the altered form of Cnn is transported by the process of advection. The rationale behind this is that the reaction of light Cnn with its receptors may convert it into a form such that it is able to polymerise. The in-

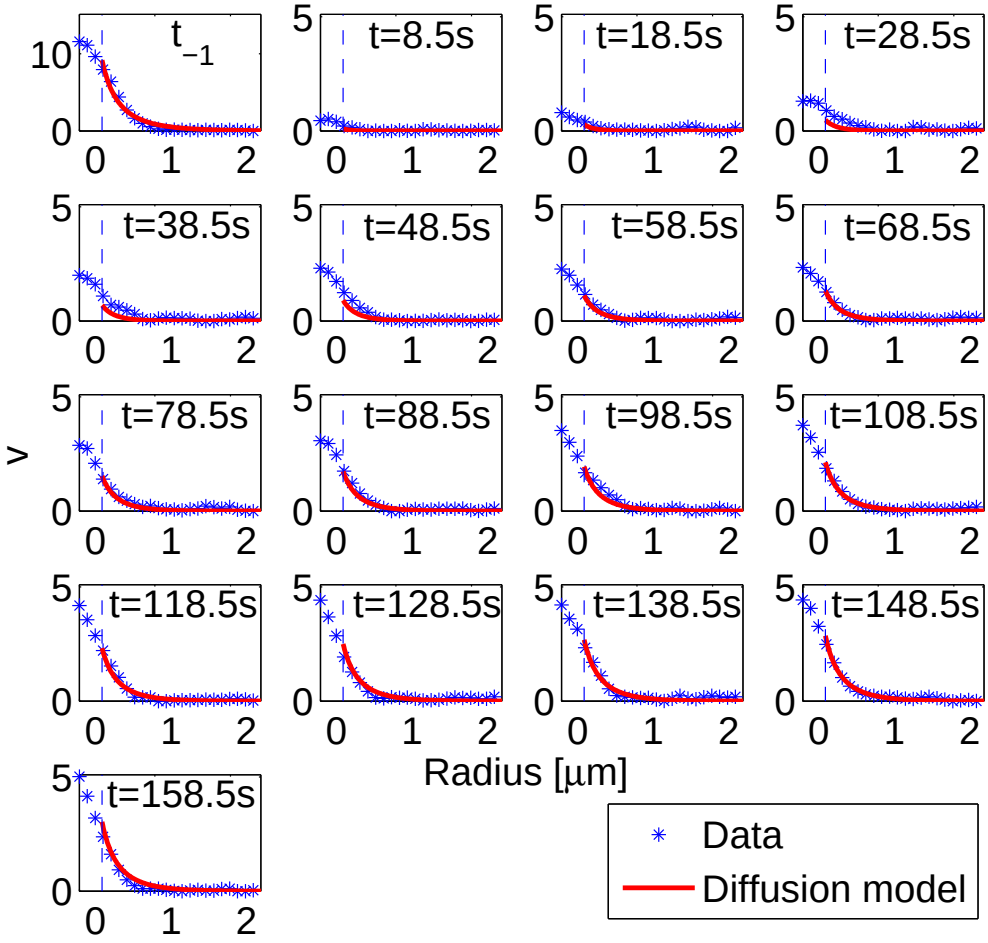

Figure 3.9: *FRAP kinetics data from a single centriole for heavy Cnn (blue asterisks) (spindle side) is shown with the best-fitting diffusion model solution of v (red solid lines): equations* (3.4.16)-(3.4.21). *t_{-1} denotes the pre-bleach time point and $t = 8.5$ s to $t = 158.5$ s denote the post-bleach recovery time points. The blue dashed lines indicate the position of r_b.*

coming light Cnn may thus push the existing Cnn polymer at the receptors outwards, thereby generating an advective velocity. The Cnn gene is known to encode for three leucine zipper motifs. These protein structural motifs are used for dimerisation in proteins (Heuer et al., 1995). Thus, it is possible that Cnn polymerises in the PCM. Alternatively, after binding to the receptors, Cnn may be transported using existing

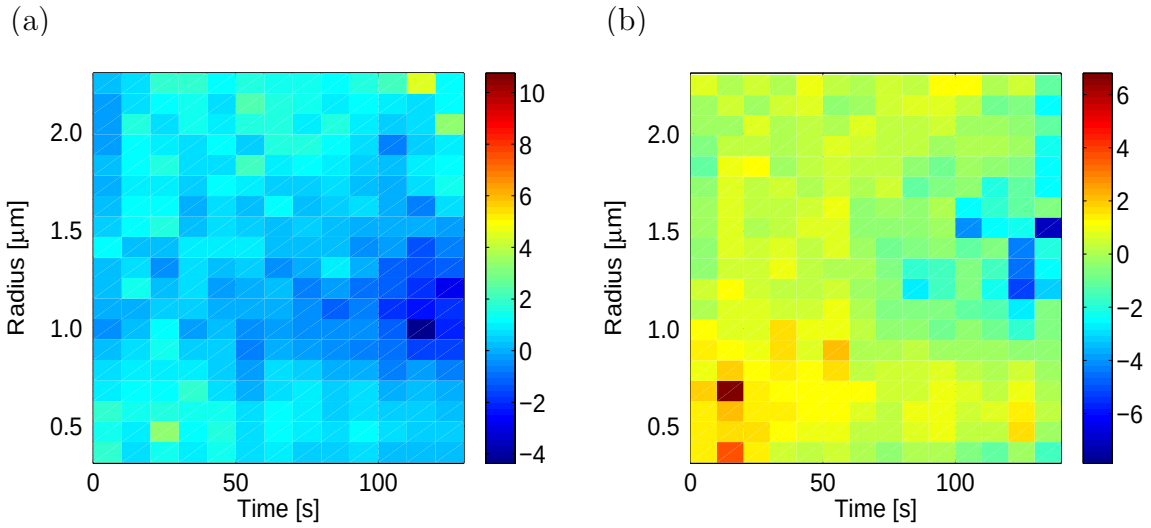

Figure 3.10: *Plots of normalised residuals between the best fitting diffusion model given by equations* (3.4.16)-(3.4.21) *and the average data (spindle side)* (a) *and (cytoplasm side)* (b).

Table 3.3: Results of fitting the FRAP kinetics of Cnn with the recovery kinetics of v given by the diffusion model, equations (3.4.16)-(3.4.21). Parameter estimates obtained from fitting, the RMSE values and the coefficients of determination R^2 are listed. N denotes the number of data points used for fitting.

	Data				
Parameters	**Avg data (spindle side)**	**Avg data (cytoplasm side)**	**Movie 5 data**	**Movie 12 data**	**Units**
$\overline{k_{on}}$	4.04	3.75	2.32	6.82	s^{-1}
k_{off}	0.0004	0.0014	7.3e-7	0.0021	s^{-1}
k_{turn}	0.0017	0.0017	0.0028	0.001	s^{-1}
k_{out}	0.0107	0.0046	0.0138	0.0021	s^{-1}
D_L	1.79	2.21	1.63	2.62	$\mu m\ s^{-1}$
D_N	0.013	0.014	0.0052	0.0049	$\mu m^2\ s^{-1}$
P_{tot}/L_{cyt}	472.57	492.86	85.05	297.16	μm
RMSE	0.2827	0.2795	0.1537	0.3971	-
N	340	340	340	340	-
R^2	0.9442	0.9577	0.9558	0.9275	-

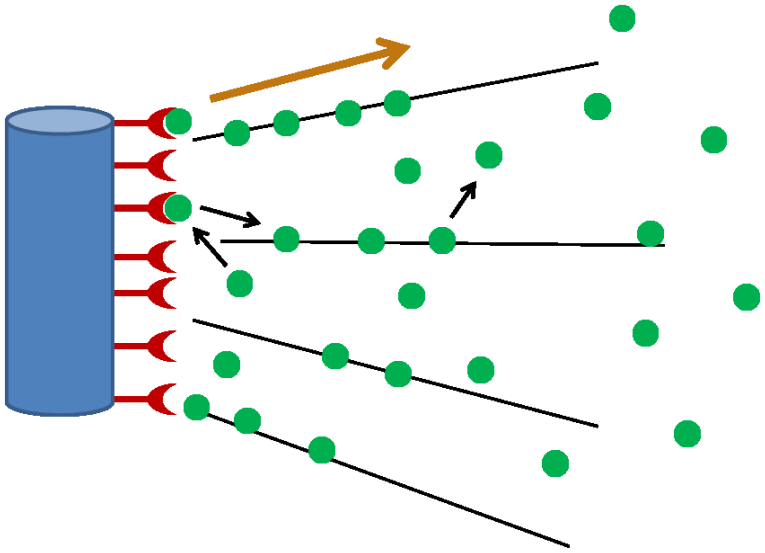

Figure 3.11: *Schematic representation of reactions occurring in the advection model. The blue cylinder represents the centriole. Red objects around the centriole denote Cnn receptors. Small green circles denote light Cnn, which can be incorporated at the centrioles and then be transported by molecular motors along the microtubules (black lines). Brown arrow denotes the direction of Cnn transport along a microtubule filament.*

polymers, such as the microtubules. It has been shown previously that flare particles ejected by PCM are associated with microtubules (Megraw et al., 2002). These flare particles contain Cnn. It is possible therefore that Cnn may move with the help of microtubules. Figure 3.11 shows one possible process which could give rise to advective transport of Cnn in the PCM. The advection model differs from the diffusion model only in the means by which altered Cnn is transported. The PDE for altered Cnn in the case of the advection model is thus given by

$$\frac{\partial N}{\partial t} = -\nabla \cdot (\bar{a}N) - k_{out}N, \tag{3.7.1}$$

where $\nabla\cdot$ denotes the divergence operator and $\bar{a} = a\hat{r}$ denotes the radially outward advection velocity (which is hypothesised to be small and constant with respect to the radius). As in the previous section, the equation for N is valid over the domain

$r \epsilon [r_b, \infty)$. As before, we use spherical polar coordinates, as this is the natural choice considering the geometry of the problem. Since we assume a simplified geometry, which makes the system spherically symmetric, only the radial component of the gradient is non-zero. Thus, the evolution of altered Cnn concentration in the advection model is given by

$$\frac{\partial N}{\partial t} = -\frac{a}{r^2}\left(\frac{\partial (r^2 N)}{\partial r}\right) - k_{out} N. \tag{3.7.2}$$

The left boundary condition for N is given by

$$N(r_b, t) = \frac{k_{turn} C(t)}{a}. \tag{3.7.3}$$

All the other differential equations and boundary conditions are exactly as given in equations (3.3.1), (3.3.3)-(3.3.5).

3.8 Analysis: Advection model

In this section we present an analysis of the advection model of Cnn incorporation and numerical simulations of it. We further discuss how the model might simulate the FRAP experiment and present some numerical simulations of a typical FRAP experiment.

3.8.1 Non-dimensionalisation

To analyse this model, we non-dimensionalise it by introducing new dimensionless variables and defining non-dimensional parameters. All parameters, except for ε_1, are exactly as given in (3.4.1). The small parameter here is denoted by ε_2 (rather than ε_1 as in the diffusion model) and is defined using the slow advection velocity a as

$$\varepsilon_2 = \frac{a}{\sqrt{D_L k_{turn}}}.$$

As the advection model differs from the diffusion model only in the means by which heavy Cnn is transported, the non-dimensionalised PDE for altered Cnn, v, in the case of the advection model is

$$\frac{\partial v}{\partial t} = -\frac{\varepsilon_2}{r^2}\left(\frac{\partial (r^2 v)}{\partial r}\right) - \beta_2 v, \tag{3.8.1}$$

where ε_2 denotes the non-dimensionalised radial component of the advection velocity. The boundary condition for v is

$$v(r_b, t) = \frac{\mu}{\varepsilon_2} w(t), \tag{3.8.2}$$

where r_b now denotes the non-dimensionalised radius of the binding shell. The non-dimensional equations and boundary conditions for u, w and p are exactly as given in equations (3.4.2), (3.4.4)-(3.4.6), respectively. The initial conditions used are also the same as those given in equation (3.4.7).

3.8.2 Steady states

The steady state solution for altered Cnn is

$$v_{eqm}(r) = \frac{r_b^2}{r^2} v_{r_b} \exp\left(-(r - r_b)\frac{\beta_2}{\varepsilon_2}\right), \tag{3.8.3}$$

where v_{r_b} at steady state is

$$v_{r_b} = \frac{\mu}{\varepsilon_2} w_{eqm},$$

and w_{eqm} is given by equation (3.4.9). The steady state solution for light Cnn is

$$u_{eqm}(r) = 1 + r_b^2 v_{r_b} \beta_2 Ei(r) - \varepsilon_2 r v_{eqm}(r), \tag{3.8.4}$$

where

$$Ei(r) = \int_{r_b}^{\infty} \frac{\exp\left(-\beta_2(\bar{r} - r_b)/\varepsilon_2\right)}{\bar{r}} \mathrm{d}\bar{r}.$$

3.8.3 Temporal analysis

Equation (3.8.1) can be solved exactly using the method of characteristics and the solution is

$$v = \frac{r_b^2}{r^2} v_{r_b}(t) \exp\left(-(r - r_b)\frac{\beta_2}{\varepsilon_2}\right), \tag{3.8.5}$$

where

$$v_{r_b}(t) = \frac{\mu}{\varepsilon_2} w(t),$$

and $w(t)$ denotes evolution of w, as given by equation (3.4.13). The solution of the equation for u (3.4.2), however, is complicated because of the Robin boundary conditions (3.4.6) at the left boundary,

$$\left.\frac{\partial u}{\partial r}\right|_{r=r_b} = \alpha\mu u(r_b, t)p(t) - \beta_1\mu w(t).$$

3.8.4 Numerical simulations

In this section we present numerical simulations of the advection model. Since equation (3.8.1) is a hyperbolic equation, we use an upwinding explicit scheme for simulation of this system. As mentioned in Chapter 2, we use backward differences in space for v and central differences in space for u. The cost of computation depends strongly upon the size of mesh (i.e. the mesh in the r-dimension). This is because the CFL condition in spherical polar coordinates requires that $\triangle t/\triangle r^2 \leq 0.166$ (Morton and Mayers, 2005). We choose mesh size $= \triangle r = 0.025$ and $\triangle t = 0.0001$. The solution of v will be first order accurate. The parameter values are as given in Table 3.1. Figure 3.12 shows the numerical solution of light and altered Cnn at selected time points, demonstrating that the system approaches a steady state as time increases.

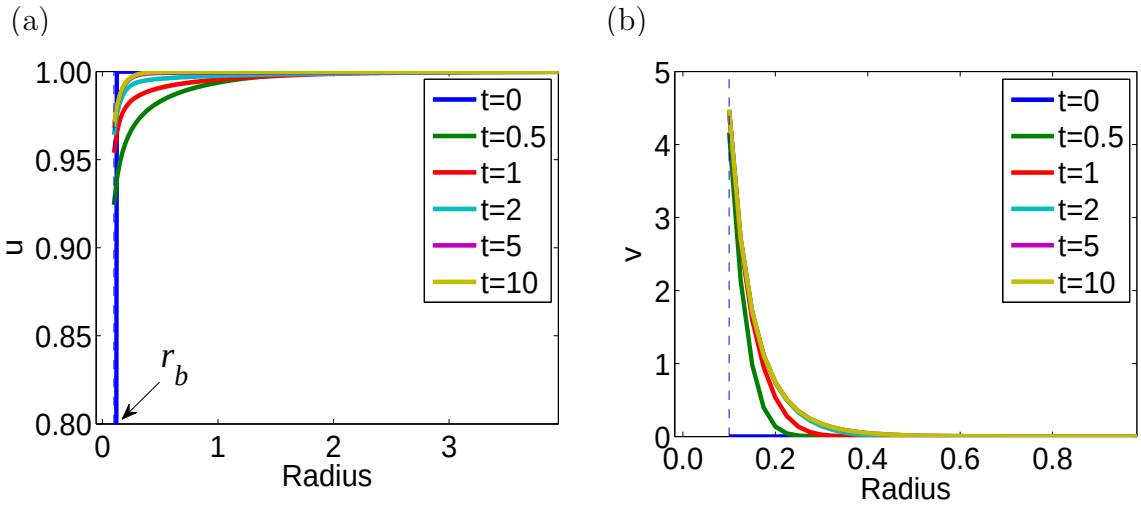

Figure 3.12: *Numerical simulation of the evolution of light Cnn* (a) *and altered Cnn* (b) *with time given by the advection model* (3.4.2), (3.4.4)-(3.4.5), (3.8.1). *The radius of the receptor sphere,* $r_b = 0.1$*, is indicated by the dashed line.*

It also shows that the altered Cnn indeed forms a gradient at steady state such that its concentration peaks close to the origin.

3.8.5 Modelling the FRAP experiment

The FRAP experiment is modelled in the same way as discussed in Section 3.4.5. The modified equations for altered Cnn are

$$\frac{\partial v_b}{\partial t} = -\frac{\varepsilon_2}{r^2}\left(\frac{\partial (r^2 v_b)}{\partial r}\right) - \beta_2 v_b, \tag{3.8.6}$$

$$\frac{\partial v_f}{\partial t} = -\frac{\varepsilon_2}{r^2}\left(\frac{\partial (r^2 v_f)}{\partial r}\right) - \beta_2 v_f, \tag{3.8.7}$$

and the boundary conditions for v_b and v_f are, respectively,

$$\begin{aligned} v_b(r_b, t) &= \frac{\mu}{\varepsilon_2} w_b(t), \\ v_f(r_b, t) &= \frac{\mu}{\varepsilon_2} w_f(t). \end{aligned} \tag{3.8.8}$$

The initial conditions are given by the steady state concentrations of light and heavy Cnn, as shown in (3.4.24). As with the diffusion model, we expect that with time the fluorescent species will recover in the centrosome region and the bleached species will diminish. In the case of the advection model, however, we can write an exact solution for v_f:

$$v_f = \frac{\mu}{\varepsilon_2} w_f(t) \frac{r_b^2}{r^2}(t) \exp\left(-(r - r_b)\frac{\beta_2}{\varepsilon_2}\right). \tag{3.8.9}$$

This solution of v_f is implicit in w_f. The full solution can only be obtained by numerical simulation. Figure 3.13 shows the results of numerical simulation of the evolution of bleached and fluorescent species, respectively. The radius of the bleach spot, r_{bl}, is chosen to be unity, without loss of generality. The figures show that the concentrations of the bleached species decrease over time and those of the unbleached species increase over time, as expected. Furthermore, fluorescent heavy Cnn (which we believe is responsible for showing the observed Cnn fluorescence recovery) initially recovers close to the centre and then spreads outwards, as seen in the experiments.

3.9 Fitting the advection model to Cnn FRAP data

3.9.1 Fitting steady state data

We use the normalised advection model, as described in Appendix A.2, for the data fitting. The pre-bleach Cnn fluorescence data collected during mitosis represents the biologically realistic steady state of Cnn incorporation. The steady state of the normalised advection model in dimensional form is given as

$$v_{eqm}(r) = \frac{r_b^2}{r^2} v_{r_b} \exp\left(-(r - r_{b)}\frac{k_{out}}{a}\right), \tag{3.9.1}$$

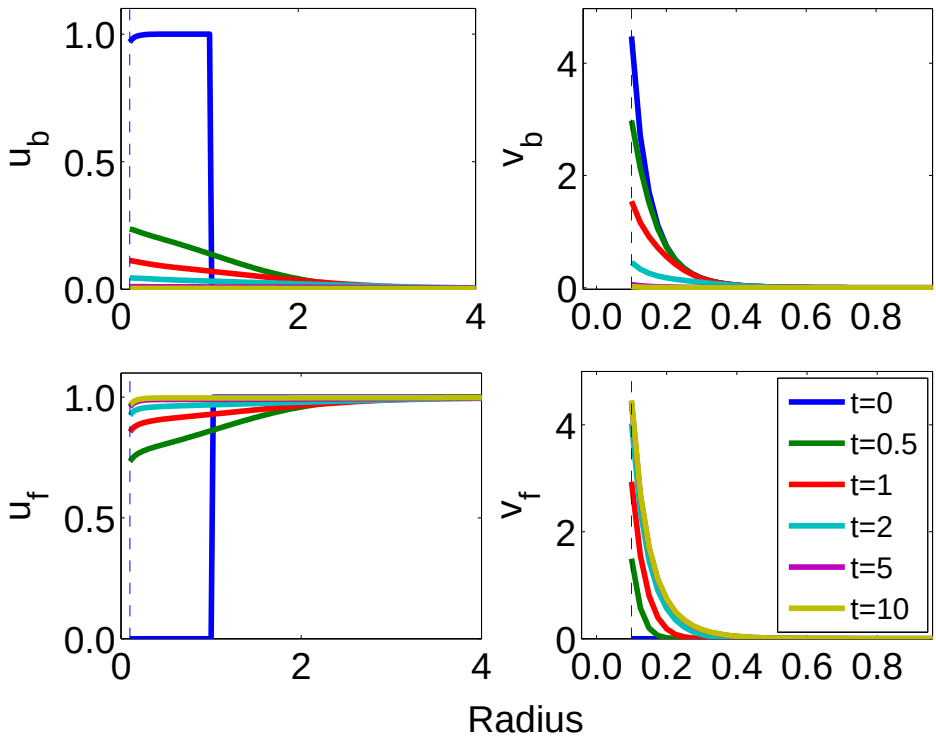

Figure 3.13: *Evolution of bleached light and heavy Cnn (top panels) and unbleached light and heavy Cnn (bottom panels) as given by the advection model in a simulated FRAP experiment. The bleaching radius, r_{bl}, is chosen to be unity. The initial conditions (blue line) for the bleached species (top panels) inside the bleaching region are given by the steady state concentrations of the respective bleached species in that region. Notice that the unbleached species (bottom panels) reach the steady state profiles at large times. An explicit upwinding scheme is used for the simulations, with the parameter values from* Table 3.1. *The radius of the receptor sphere, $r_b = 0.1$, is indicated by the dashed line.*

where v_{eqm} denotes normalised heavy Cnn at steady state and r_b denotes the radius of the receptor sphere in dimensional form. v_{r_b} is given by

$$v_{r_b} = \frac{k_{turn}}{a} w_{eqm}.$$

We use MATLAB's `lsqnonlin` function to perform the nonlinear least squares fitting. Figure 3.14(a) shows the fit of the advection model with the average steady state data from both the spindle side and the cytoplasm side of the centrosomes. We present the results from the fits with the average data. The parameter estimates obtained from the fits are given in Table 3.4. The coefficient of determination (R^2) values are poorer than those obtained from the diffusion model fits (Table 3.4). Figure 3.14 shows that the best-fitting model underpredicts v at small radii and overpredicts it at large radii. The decay rate k_{out}/a predicted by the fitting is extremely small. This suggests that the loss of v from the system via its conversion to u makes a very small contribution to the steady state of v. In the next section we fit the FRAP recovery data with the advection model.

Table 3.4: Results of fitting the steady state of the advection model (3.9.1) with the average steady state data. Parameter estimates obtained from fitting, the root mean squared error (RMSE) and the coefficient of determination, R^2, are listed.

Data	v_{r_b}	k_{out}/a	**RMSE**	$\boldsymbol{R^2}$
Units	-	μm^{-1}	-	-
Average data (spindle side)	15.31	3.7e-11	1.51	0.8336
Average data (cytoplasm side)	16.39	4.4e-11	1.86	0.7482

3.9.2 Fitting FRAP recovery data

As mentioned in Section 3.8.5, we can simulate the FRAP experiment by subdividing the various Cnn species into two subpopulations, namely bleached and unbleached. To simulate recovery, we only need to consider the unbleached species, as discussed in Section 3.4.5. Equation (3.8.9) gives the exact solution of fluorescent heavy Cnn

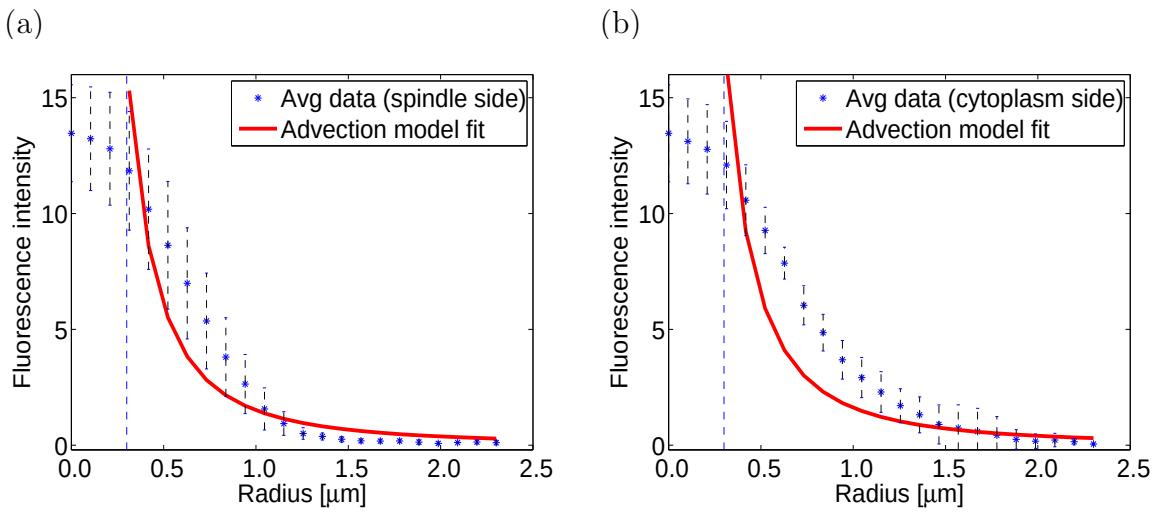

Figure 3.14: *Nonlinear least-squares fit of the steady state of the advection model* (3.5.1) *to the normalised average steady state data from the spindle side,* (a), *and cytoplasm side,* (b). *The standard deviation of the data is indicated by the error bars. The radius of the receptor sphere,* $r_b = 0.3$ μm, *is indicated by the dashed blue line.*

in non-dimensional form. The solution in normalised dimensional form is given by

$$v_f(r,t) = \frac{r_b^2}{r^2}\frac{k_{turn}}{a} w_f(t) \exp\left(-(r - r_{b)}\frac{k_{out}}{a}\right). \tag{3.9.2}$$

It can be seen that the temporal component only depends on the evolution of fluorescent complex $w_f(t)$, whereas the spatial component is given by an exponential/r^2 dependence, which is separable from the temporal component. This suggests that the spatial distribution of heavy Cnn should not change with time if the advection model is correct. We notice that if the solution of v_f is multiplied by r^2, the gradient is only exponential. The exponential gradient can be converted into a linear gradient by log-transforming it. Thus,

$$\log(r^2 v_f(t)) = \log\left(r_b^2 \frac{k_{turn}}{a} w_f(t)\right) - \frac{k_{out}}{a}(r - r_b). \tag{3.9.3}$$

The above equation is linear in space. For recovery curves in time, the y-intercept alone changes, whereas the slope remains the same. (We note that in the case of

the diffusion model, the fundamental solution has a Gaussian form given by equation (3.4.15). The spatial gradient in this form of solution is not separable from the temporal evolution. Thus, we expect that if we transformed the data suitably, we may be able to distinguish between the diffusion and advection models). We transform the FRAP recovery curves to check if they result in linear gradients with identical slopes, but different y-intercepts. We multiply the data $Y(t, r)$ by r^2 and then take the logarithm. Figure 3.15 shows the transformed data for successive time points after bleaching plotted against the radius. The figure shows that the data do not describe a linear dependence with the radius, let alone a linear dependence with constant slope. This suggests that the advection model may not be valid. However, it is also possible that the sensitivity of logarithms to small numbers may prevent us from seeing a true trend. We therefore proceed to fit the non-transformed data with the full numerical solution of the advection model.

We use an explicit upwinding scheme for the numerical simulation of the FRAP kinetics of v for a given set of parameters. We choose mesh size $= \triangle x = 0.025$ and $\triangle t = 0.0001$ for the numerical solution. The time step used for obtaining the solution is very small as compared to the time intervals used in the experiment. This allows us to obtain the solution at the time points corresponding to experimental time points. The solution at these time points is then interpolated at the radial values for which data are available. The model values thus obtained are used to evaluate the sum of squared differences with respect to the data. Figure 2.7 shows the steps taken for the data fitting.

3.9.2.1 Initial guess

The diffusion model presented in Section 3.3 differs from the advection model only in the mechanism of transport of incorporated Cnn. Since we have already obtained best-

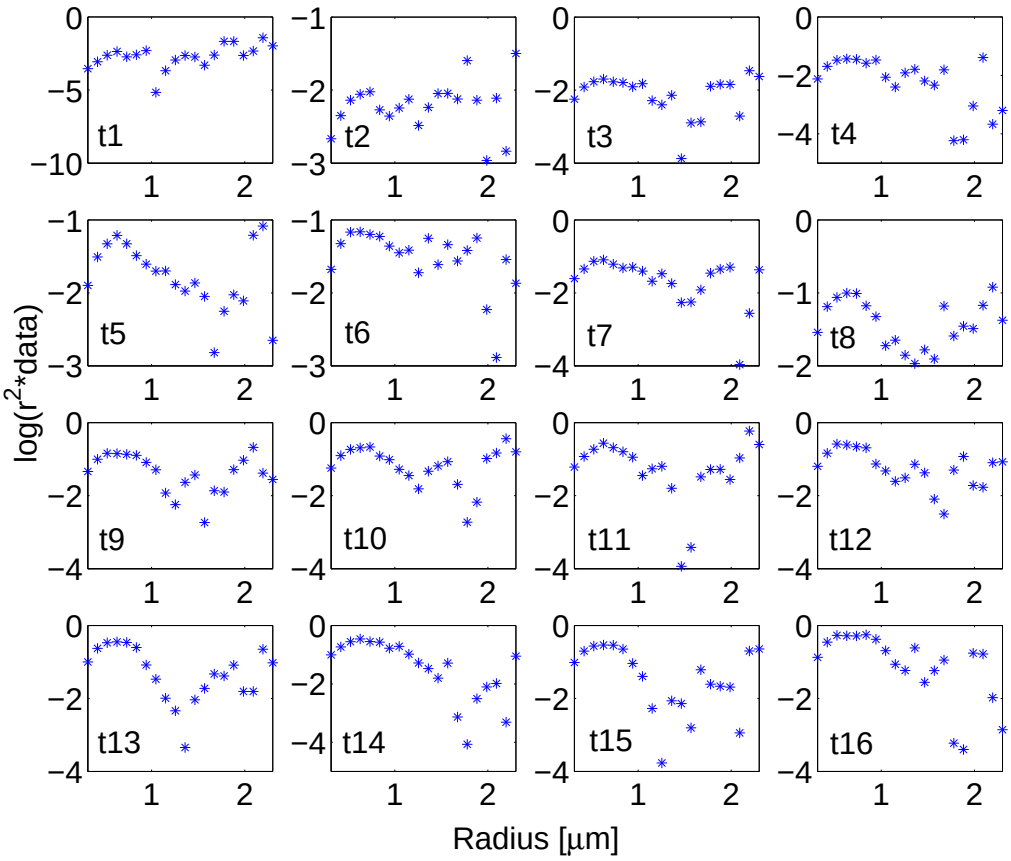

Figure 3.15: *Post-bleach data are transformed as mentioned in the text and plotted against radius at successive time points. Time points are shown in the left bottom corner of each graph. It can be seen that the treated data do not appear to describe a linear dependence on the radius.*

fit parameter estimates for the diffusion model in Section 3.5, we use these estimates as initial guesses for the parameters that are common to both the models. As for the advection velocity, a, we find from the literature that the velocity of fast microtubular motors is around 1 μm s^{-1} (Barkus et al., 2008). Since we expect the transport of incorporated Cnn to be slower, we begin with $a = 0.1$ μm s^{-1} as an initial guess.

3.10 Results

Figures 3.16-3.18 show sample best-fits of the advection model with the data. Table 3.5 shows the best-fitting parameter estimates obtained from the fits. The goodness of fit estimators, namely RMSE values and R^2 coefficients, are also listed. Figure 3.19 shows the distribution of residuals (normalised with the standard deviation at each spatial and temporal point) from the fits with the average data from the spindle side and the cytoplasm side. It can be seen that the distribution of residuals also appears to be non-random in the case of the advection model. This indicates that at least one of the predictor variables has not been accounted for. It can also be seen that the R^2 coefficient is smaller in the case of the advection fits than in the case of the diffusion fits. The estimates for k_{out} and k_{off} are very small. This suggests that these parameters are not important and that the model can be reduced by setting these parameters to zero. However, given that the fit is poor to begin with, we do not reduce the model any further. In the next section we compare the fit of the diffusion model with that of the advection model.

3.11 Comparison of models

We began this chapter with the aim of studying the incorporation of Cnn in *Drosophila* centrosomes. To our knowledge, this is the first attempt at mathematically modelling Cnn incorporation in centrosomes. Through careful consideration of the experimental data we have developed two simple models, a diffusion model, and an advection model, in order to explain the observed Cnn incorporation behaviour and FRAP recovery profile. We have assumed a simplified receptor geometry for the models, which has allowed us to gain some analytical insights into the behaviour of the two models. Steady state analysis of the diffusion model in spherical polar co-ordinates, with spherical symmetry, has shown that heavy Cnn can form a decreasing gradient

Table 3.5: Results of fitting the FRAP kinetics of Cnn with the recovery kinetics of v given by the advection model (3.8.6)-(3.8.7). Parameter estimates obtained from fitting, the RMSE values and the coefficients of determination (R^2), are listed.

	Data				
Parameters	**Avg data (spindle side)**	**Avg data (cytoplasm side)**	**Movie 5 data**	**Movie 12 data**	**Units**
$\overline{k_{on}}$	0.0043	0.0096	0.0232	0.0049	s^{-1}
k_{off}	2.4e-11	1.5e-13	1.5e-8	1.9e-11	s^{-1}
k_{turn}	0.0019	0.0023	0.0027	0.0021	s^{-1}
k_{out}	6e-15	8.2e-17	2.3e-7	5.4e-15	s^{-1}
D_L	1.47	6.7	0.46	1.45	$\mu m^2 s^{-1}$
a	0.0305	0.2228	0.0097	0.0301	$\mu m\ s^{-1}$
P_{tot}/L_{cyt}	393.87	2210.2	38.57	441.97	μm
RMSE	0.4004	0.4958	0.1964	0.5760	-
N	340	340	340	340	-
R^2	0.888	0.8668	0.9279	0.8475	-

along the radius of the centrosome. The profile of heavy Cnn is given by equation (3.4.8). The advection model also predicts a radially decreasing concentration profile of altered Cnn, which is given by equation (3.8.3).

Numerical simulations of the two models confirm that the concentration profiles indeed evolve to a steady state. We have also simulated the FRAP experiments and shown that both our models qualitatively replicate the experimentally observed Cnn fluorescence recovery behaviour. We have fitted the steady state data to each of our models and obtained parameter values. We can compare the two model fits by simply comparing the RMSE values because both the models have identical numbers of parameters. It can be seen from the RMSE values in Tables 3.2 and 3.4 that the diffusion model fits the steady state data better than the advection model. The parameter estimates from the two fits are different, as would be expected based on the

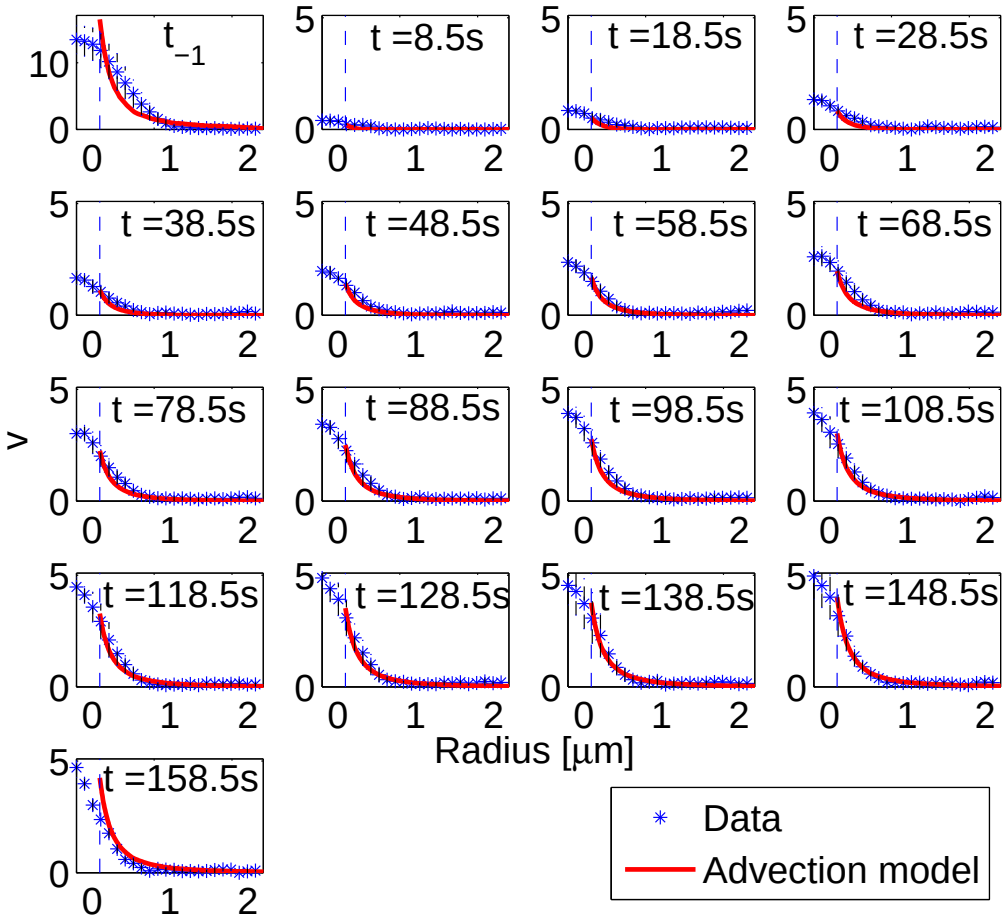

Figure 3.16: *Average spindle side FRAP kinetics data for altered Cnn (blue asterisks) is shown with the best-fitting advection model* (3.8.6)-(3.8.7) *solution of* v *(red solid lines). The error bars represent the standard deviation in the data.* t_{-1} *denotes the pre-bleach time point and* $t = 8.5$ *s to* $t = 158.5$ *s denote the post-bleach recovery time points. The blue dashed lines indicate the position of* r_b.

differences in equations (3.4.8) and (3.8.3). Fitting the FRAP data to both the models also shows that the diffusion model fits better than the advection model (Tables 3.3 and 3.5).

Both model fits with the data, however, show systematic errors. It can be seen

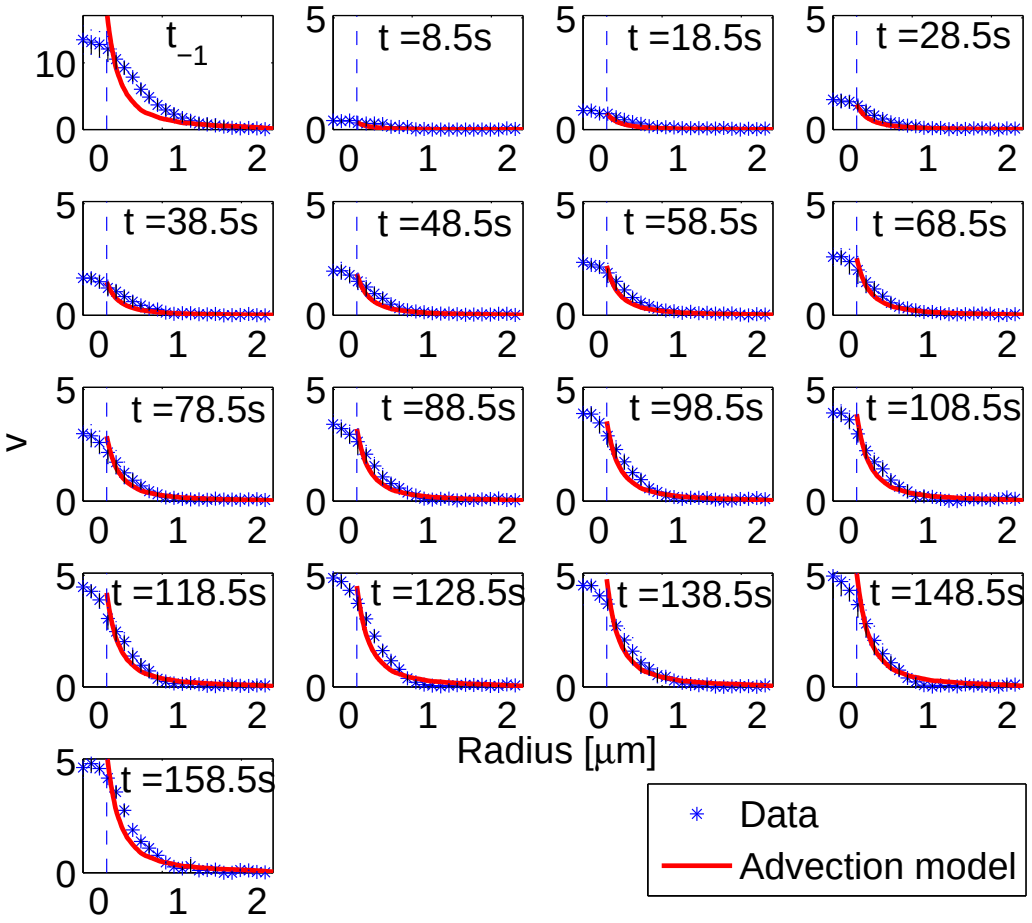

Figure 3.17: *Average cytoplasm side FRAP kinetics data for altered Cnn (blue asterisks) is shown with the best-fitting advection model* (3.8.6)-(3.8.7) *solution of* v *(red solid lines). The error bars represent the standard deviation in the data.* t_{-1} *denotes the pre-bleach time point and* $t = 8.5$ *s to* $t = 158.5$ *s denote the post-bleach recovery time points. The blue dashed lines indicate the position of* r_b.

from the diffusion model fits (Figures 3.7-3.9) that the model underpredicts the concentration at small times and overpredicts it at large times. This is also true of the advection model (Figures 3.16-3.18). Also, in the case of pre-bleach states (i.e. steady states), both the models underpredict the concentration at small radii and overpredict it at large radii. Thus, the distribution of residuals is not random, as should be

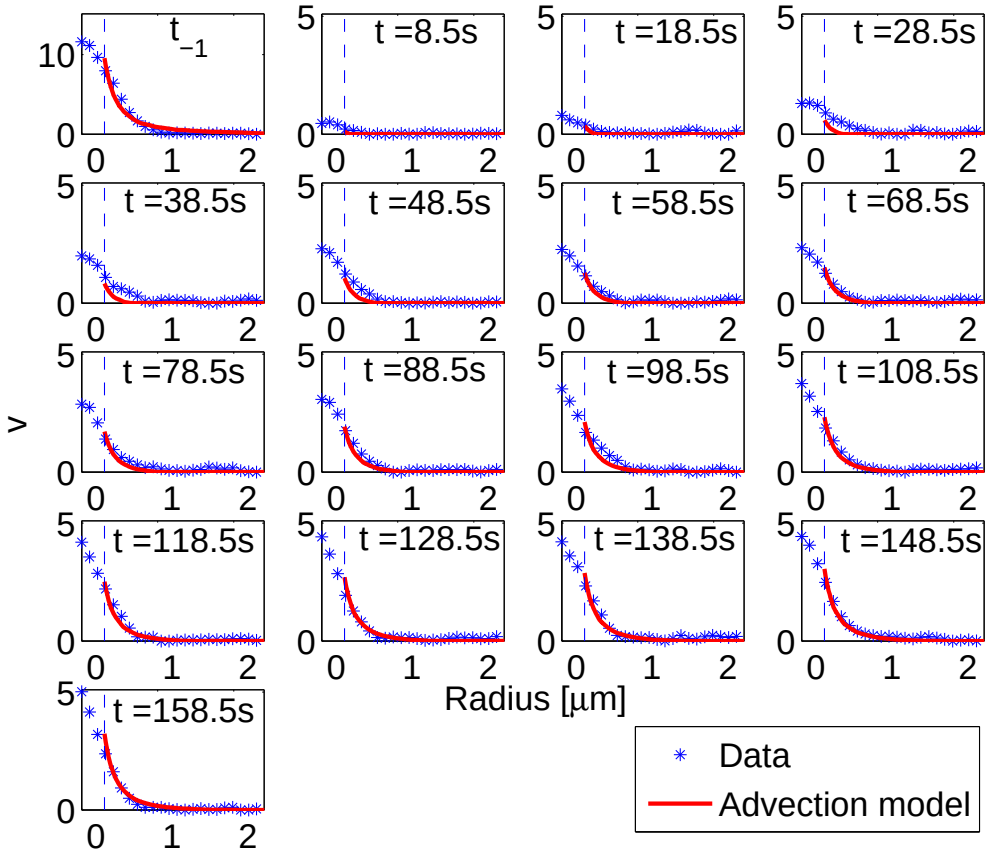

Figure 3.18: *FRAP kinetics data from a single centriole for altered Cnn (blue asterisks) (spindle side) is shown with the best-fitting advection model* (3.8.6)-(3.8.7) *solution of* v *(red solid lines).* t_{-1} *denotes the pre-bleach time point and* $t = 8.5$ *s to* $t = 158.5$ *s denote the post-bleach recovery time points. The blue dashed lines indicate the position of* r_b.

expected from a good fit (Figures 3.10 and 3.19). This implies that we may not have considered at least one predictor variable in either case. Therefore, even though the RMSE values and R^2 coefficients suggest that the diffusion model is a better fit than the advection model, we need to be cautious in choosing one model over the other based on these fits.

Because of the simple-receptor-geometry assumption, the region close to the cen-

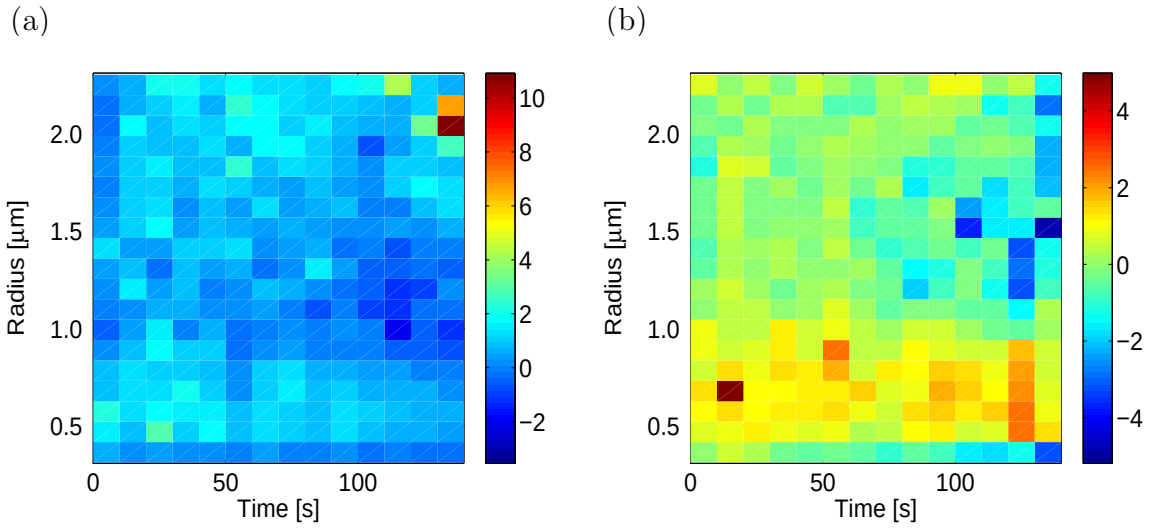

Figure 3.19: *Plots of residuals between the best fitting advection model and the average data on the spindle side,* (a), *and on the cytoplasm side,* (b).

trioles is excluded from our model. Our models cannot be simply extended to this region as the solutions are discontinuous at the origin. However, by excluding the region close to the centrioles, we are excluding the data where the fluorescence values peak. It appears from the non-random distribution of residuals that one or more of our simplifying assumptions is incorrect. In the next section we discuss a modification of one such assumption.

3.12 Diffusion model with detailed geometry

As mentioned in Section 3.11, it is not possible to fit the data near the centrioles i.e., near the origin. This is because of the assumption of a simplified receptor geometry. We have previously assumed that the Cnn receptors form an infinitesimally thin spherical shell of finite radius around the centrioles. In reality, the receptors would occupy a finite volume. Asterless (Asl) is a putative receptor for Cnn (Conduit et al., 2010). Our collaborator Prof. Jordan Raff and his laboratory have visualised Asl around the centrioles using a super-resolution microscopy technique. Figure 3.20

shows Asl coloured in green around an empty cylinder, which is the centriole. It appears that Asl forms an envelope around the centrioles in the form of a thick-walled hollow cylinder, with the width of the cylinder walls being approximately 200 nm. Using this realistic receptor geometry could improve the fit of our models near the origin. In this section we present the diffusion model which uses the more realistic receptor geometry, as shown schematically in Figure 3.21. We choose the diffusion model since it shows a better fit with the data than the advection model.

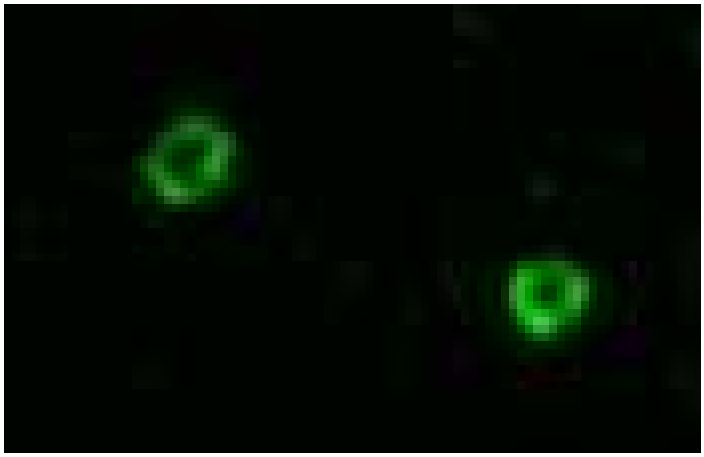

Figure 3.20: *GFP-Asl in syncytial embryos visualised using super-resolution fluorescence microscopy shows that it forms a thick-walled hollow cylinder around the centrioles. Image kindly shared by Helio Roque from Dr. Raff's laboratory.*

3.12.1 Assumptions

The centriole is modelled as a cylinder with radius $r_c = 100$ nm and height $h_c = 200$ nm. It has been shown previously that only one of the two centrioles, namely the mother centriole, recruits Asl (Conduit et al., 2010). Hence only one centriole is used for the model. The centriole is believed to be impermeable to Cnn and hence the centriolar region is excluded from the domain. Cnn receptors (and the Cnn-receptor complex) are believed to be immobile and exist in a hollow cylindrical region around the centriole, with a radius $r_b = 300$ nm and a height of 200 nm, which is the same

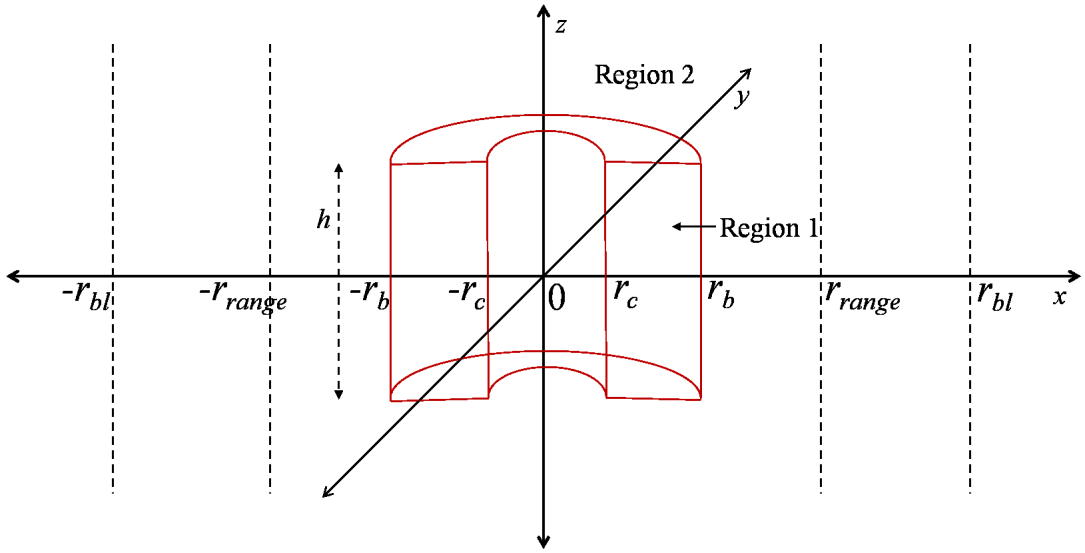

Figure 3.21: *Schematic representation of the realistic receptor geometry. A vertical cross-section through the centrosome is shown. The origin coincides with the centre of the centriole.* r_c *denotes the radius of the centriole and is* 100 nm. r_b *denotes the radius of the cylindrical binding region and is approximately* 300 nm. *Thus, the width of the binding region is about* 200 nm. *The height of the centrioles (denoted as* h*) is roughly equal to the height of the binding region.* r_{range} *denotes the range over which Cnn fluorescence drops to cytoplasmic levels and is about* 1000-1200 nm. r_{bl} *denotes the bleaching radius. Region 1 and region 2 are indicated.*

as h_c. The concentration of receptors, P_{tot}, in this cylindrical region is considered to be uniform. This receptor geometry divides the domain into two regions, namely the receptor region (region 1), where binding and unbinding reactions take place, along with heavy Cnn decay and diffusion of light and heavy Cnn, and the outer region (region 2), where the binding-unbinding reactions do not take place.

Equations for region 1

Region 1 spans $r \in (r_c, r_b)$. The reactions occurring in region 1 can be described using a coupled PDE-ODE system as

$$\frac{\partial L}{\partial t} = D_L\left(\frac{\partial^2 L}{\partial x^2} + \frac{\partial^2 L}{\partial y^2} + \frac{\partial^2 L}{\partial z^2}\right) + k_{out}N - k_{on}LP + k_{off}C, \tag{3.12.1}$$

$$\frac{\partial N}{\partial t} = D_N\left(\frac{\partial^2 N}{\partial x^2} + \frac{\partial^2 N}{\partial y^2} + \frac{\partial^2 N}{\partial z^2}\right) - k_{out}N + k_{turn}C, \tag{3.12.2}$$

$$\frac{dP}{dt} = k_{turn}C + k_{off}C - k_{on}LP, \tag{3.12.3}$$

$$\frac{dC}{dt} = k_{on}LP - k_{off}C - k_{turn}C, \tag{3.12.4}$$

$$P(r,t) + C(r,t) = \text{Constant} = P_{tot}(r) = P_{tot}.$$

The left hand boundary conditions are given by

$$D_L\frac{\partial L}{\partial r}\bigg|_{r=r_c} = 0, \qquad D_N\frac{\partial N}{\partial r}\bigg|_{r=r_c} = 0, \tag{3.12.5}$$

whereas the right hand boundary conditions are obtained by requiring continuity of the solution profiles and their gradients at $r = r_b$.

Equations for region 2

Region 2 spans $r \in (r_b, \infty)$. The reactions occurring in region 2 can be described using a system of coupled PDEs as

$$\frac{\partial L}{\partial t} = \frac{D_L}{r^2}\frac{\partial}{\partial r}\left(r^2\frac{\partial L}{\partial r}\right) + k_{out}N, \tag{3.12.6}$$

$$\frac{\partial N}{\partial t} = \frac{D_N}{r^2}\frac{\partial}{\partial r}\left(r^2\frac{\partial N}{\partial r}\right) - k_{out}N. \tag{3.12.7}$$

The right hand boundary conditions are given by

$$N(\infty, t) = 0 \;\text{ and }\; L(\infty, t) = L_{cyt}, \tag{3.12.8}$$

whereas the left boundary conditions are obtained by requiring continuity of the solution profiles and their gradients at $r = r_b$.

We note that the total receptor concentration is conserved as in the previous models. Because of the peculiar geometry, these equations cannot be solved analytically. Instead, we solve them using COMSOL Multiphysics software, which uses the FEM. Appendix B.1 shows that this model evolves to a steady state in which the heavy Cnn forms a gradient that is radially decreasing.

3.12.2 Modelling the FRAP experiment

The FRAP experiment is modelled in the same way as mentioned in Section 3.4.5. The only difference in the case of this model is that the bleaching region is modelled as a cylinder spanning the entire length of the domain, which is more physically realistic (rather than a sphere in the case of previous models, Figure 3.21). Appendix B.2 shows that the fluorescent heavy Cnn recovers initially in the binding region and then spreads radially outwards.

3.13 Fitting the detailed geometry diffusion model to Cnn FRAP data

Since we do not have an analytical expression either for the steady state or for the FRAP evolution, we use numerical solutions for the fitting. We use the normalised model (Appendix A.3) for fitting. The pre-bleach state is fitted using the steady state solution, whereas the subsequent recoveries are fitted with the solution for the fluorescent species in the FRAP set-up, as with the previous models. In the case of this model, however, there are additional complications. As mentioned before, the Cnn-receptor complex is also fluorescent. Also, the complex exists in a finite-thickness cylinder. Therefore, for fitting we need the total fluorescence from both the heavy Cnn (v) as well as the complex (w). We use MATLAB's `lsqnonlin` and `fminsearch`

algorithms for fitting according to the data-fitting protocol shown in Figure 2.7.

3.14 Results

Figures 3.22-3.24 show sample best fits of the detailed geometry diffusion model with the data. Table 3.6 shows the best-fitting parameter estimates obtained from the fits. The goodness of fit estimators, namely RMSE values and R^2 coefficients, are also listed. It can be seen that the R^2 coefficient is smaller in the case of the detailed geometry diffusion model fits than in both the previous models. Figure 3.25 shows the distribution of residuals (normalised with the standard deviation at each spatial and temporal point) from the fits with the average data from the spindle side and the cytoplasm side. It can be seen that the distribution of residuals appears non-random in the case of this model as well. Figure 3.25(a) shows that most of the residuals are positive in the case of the fit with the spindle side average data, whereas in the case of the cytoplasm side average data (Figure 3.25(b)), the residuals are large and positive for lower radii and decrease as the radius increases. This can also be seen from the respective fits (Figures 3.22 and 3.23, respectively). Thus, it appears that the detailed geometry diffusion model fits the data less well than either the simple geometry diffusion or the simple geometry advection models. We discuss the implications of this result in the next section.

3.15 Discussion and Conclusions

In this chapter we proposed two mechanistically different models of Cnn incorporation, namely the diffusion and the advection models. We began by analysing these models to see if they produce the required steady state as well as the fluorescence recovery behaviour. We found that both the diffusion and advection models are ca-

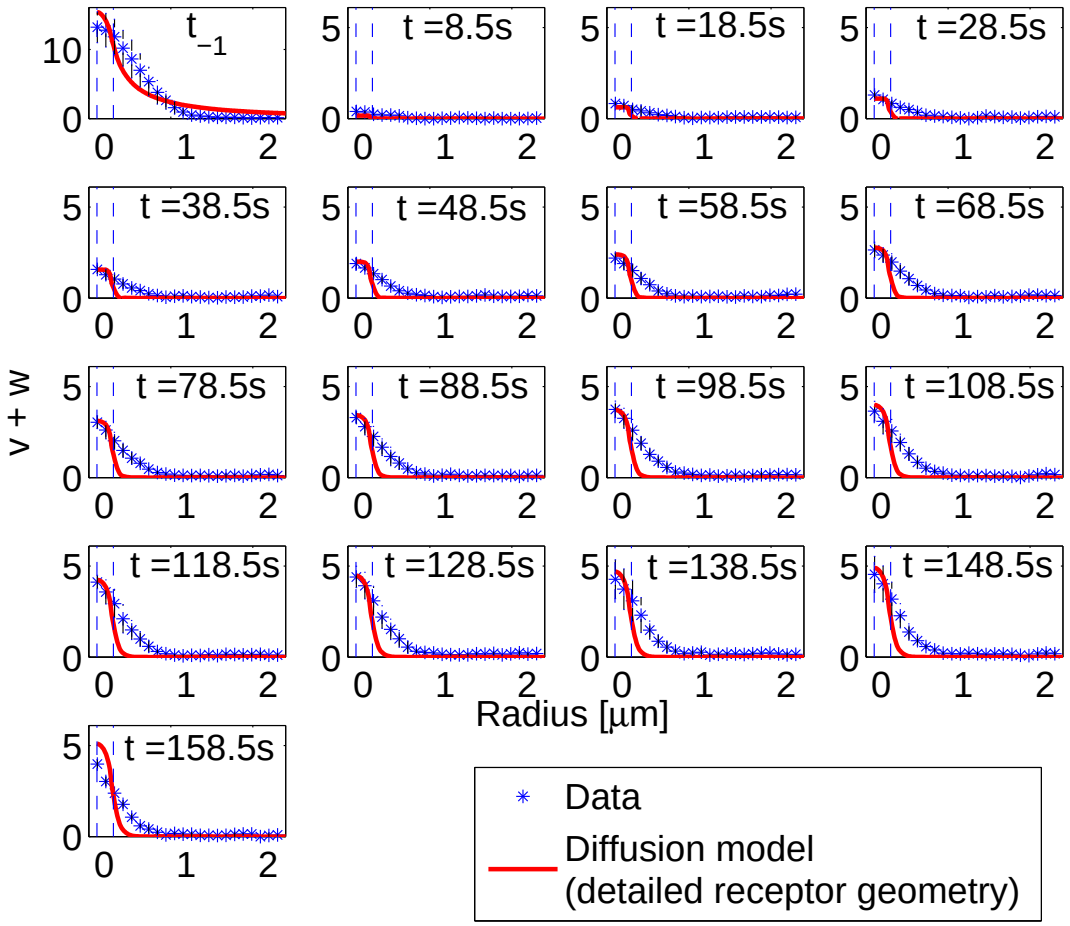

Figure 3.22: *Average spindle side FRAP kinetics data for incorporated Cnn (blue asterisks) is shown with the best-fitting detailed geometry diffusion model solution of v (red solid lines): equations* (A.3.1)-(A.3.7). *The error bars represent the standard deviation in the data. t_{-1} denotes the pre-bleach time point and $t = 8.5$ s to $t = 158.5$ s denote the post-bleach recovery time points. The boundaries of the binding region are shown by blue dashed lines.*

pable of qualitatively reproducing the experimentally observed Cnn behaviour. For example, both the models produce a Cnn concentration gradient with concentration decreasing radially outward, and both the models allow for Cnn recovery to begin at the centre and spread outwards. Fitting these models to Cnn FRAP data revealed that the diffusion model fitted better than the advection model. However, we

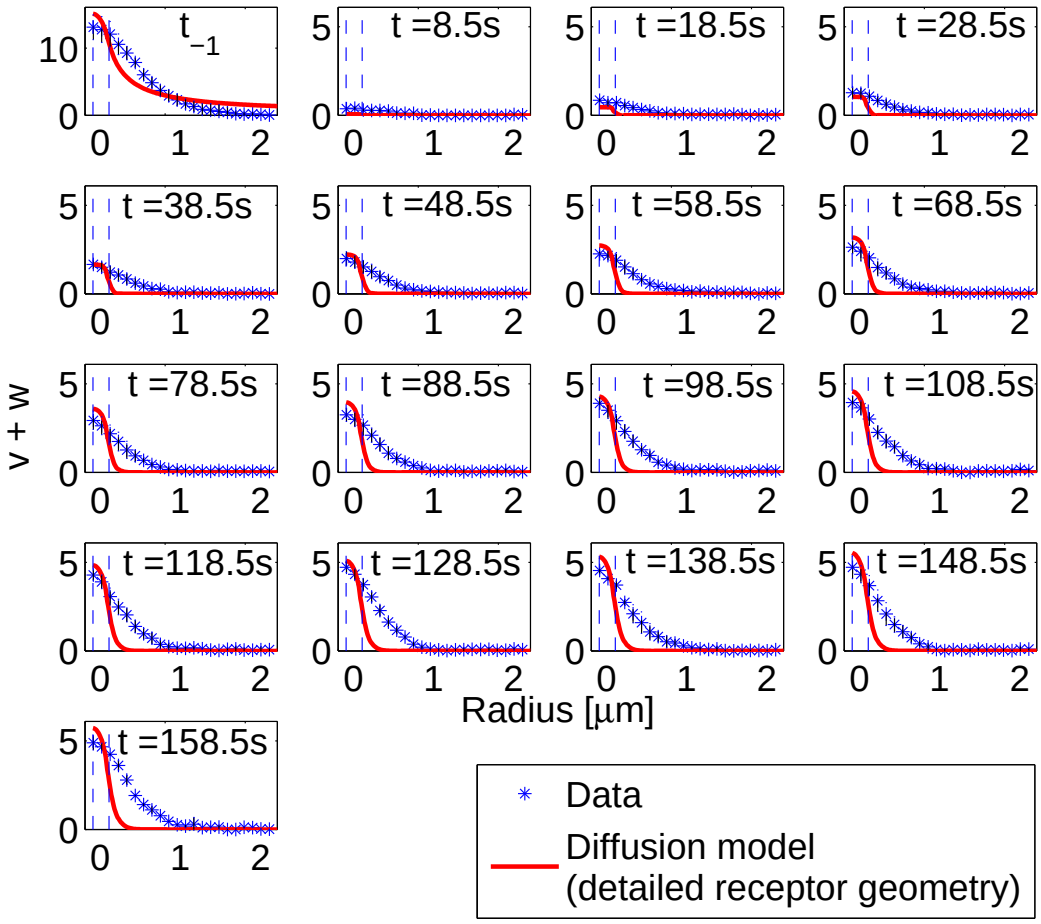

Figure 3.23: *Average cytoplasm side FRAP kinetics data for incorporated Cnn (blue asterisks) is shown with the best-fitting detailed geometry diffusion model solution of* v *(red solid lines): equations* (A.3.1)-(A.3.7). t_{-1} *denotes the pre-bleach time point and* $t = 8.5$ *s to* $t = 158.5$ *s denote the post-bleach recovery time points. The boundaries of the binding region are shown by blue dashed lines.*

cannot conclude that the diffusion model completely explains the Cnn incorporation behaviour. This is for the following reasons. Firstly, even though the RMSE values for the diffusion model fits are small and R^2 coefficients are close to unity, the distribution of residuals for the fit is not random. This suggests that we may have ignored at least one predictor variable in our model. It is not clear at this point what this predictor variable may be. Secondly, because of the simple geometry assumption in

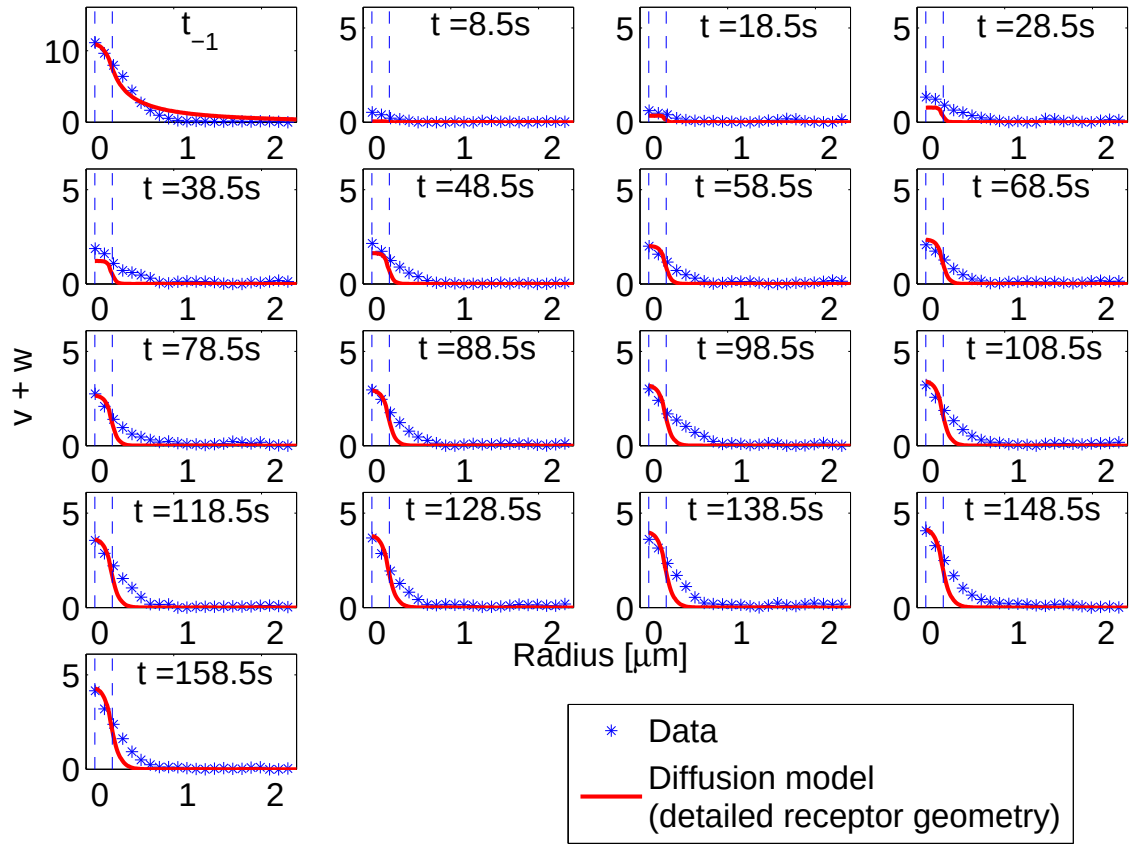

Figure 3.24: *FRAP kinetics data from a single centriole for incorporated Cnn (blue asterisks) (spindle side) is shown with the best-fitting diffusion model with detailed geometry solution of v (red solid lines): equations* (A.3.1)-(A.3.7). *t_{-1} denotes the pre-bleach time point and $t = 8.5$ s to $t = 158.5$ s denote the post-bleach recovery time points. The boundaries of the binding region are shown by blue dashed lines.*

the case of both these models, we could not fit the data near the origin. We decided to address the second concern first. We introduced a realistic receptor geometry in the diffusion model. The thick-walled hollow cylinder geometry of receptors we used is supported by biological evidence (Figure 3.20). It was plausible that the first concern could also be addressed by introducing a more realistic receptor geometry. However, we found that the detailed geometry diffusion model fitted the data less well than either of the earlier models. It can be seen that the parameter estimates from all

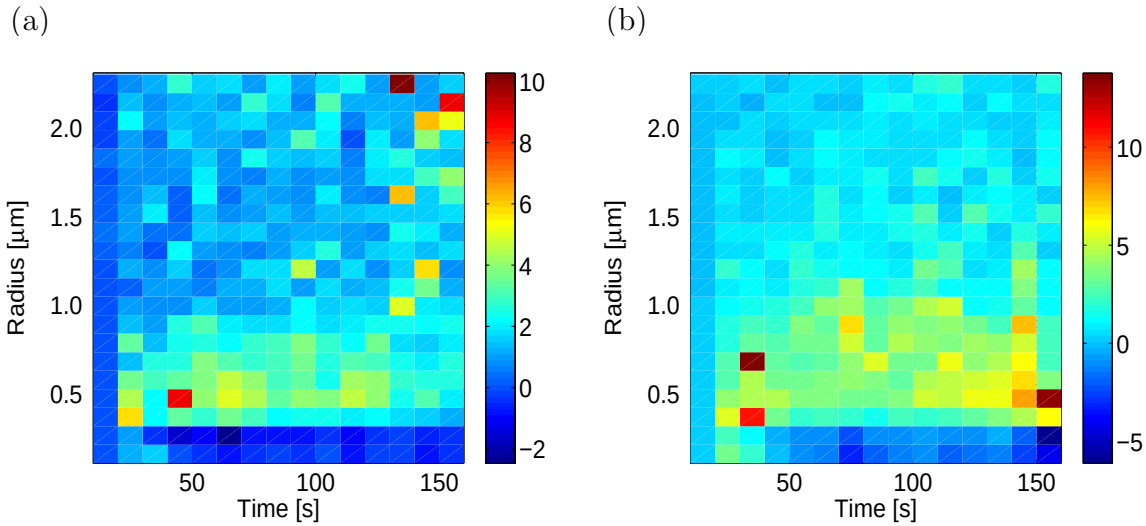

Figure 3.25: *Plots of residuals between the best fitting detailed geometry diffusion model given by equations* (A.3.1)-(A.3.7) *and the average data on the spindle side,* (a), *and on the cytoplasm side,* (b).

Table 3.6: Results of fitting the FRAP kinetics of Cnn with the recovery kinetics of $v + w$ given by the diffusion model with detailed receptor geometry (equations (A.3.1)-(A.3.7)). Parameter estimates obtained from fitting, the RMSE values and the coefficients of determination, R^2, are listed.

	Data			
Parameters	**Avg data (spindle side)**	**Avg data (cytoplasm side)**	**Movie 5 data**	Units
$\overline{k_{on}}$	1.5079	0.9509	0.3917	s^{-1}
k_{off}	8.6e-4	1.85e-4	1.9e-7	s^{-1}
k_{turn}	0.1521	0.4062	0.361	s^{-1}
k_{out}	7.7e-6	5.07e-6	1.7e-5	s^{-1}
D_L	0.7904	0.3304	0.3492	$\mu m^2 s^{-1}$
D_N	6.68e-5	1.03e-4	9.5e-5	$\mu m^2 s^{-1}$
P_{tot}/L_{cyt}	0.3593	0.254	0.27	-
RMSE	0.6205	0.77	0.3763	-
N	374	374	374	-
R^2	0.8523	0.8	0.9005	-

three models vary significantly. However, we do not comment on the parameter estimates from any of our models since none of our Cnn incorporation models adequately explain the Cnn FRAP data.

While the detailed geometry model shows a much poorer fit than the simple geometry diffusion and advection models, it still provides clues about which predictor variable we may be missing and how we may address this deficiency. We notice that in the case of the detailed geometry model fits (Figures 3.22-3.24) the fluorescence in the receptor region (region 1) recovers much more quickly than that in the region devoid of any receptors (region 2). We had assumed that the fluorescence in region 2 would recover slowly owing to the slow diffusion of heavy Cnn from region 1 into region 2. However, we note that in the data themselves, the fluorescence in region 2 recovers on the same time scale as that in region 1. This suggests that either heavy Cnn diffusion occurs on the same time scale as the binding reaction or that the location of receptors is not limited to region 1. We have attempted to fit our data with a larger initial guess of the diffusion coefficient for heavy Cnn. However we have been unable to find a fit that is better than the ones we have reported in this chapter.
In the next chapter we evaluate the possibility of receptors not being limited to region 1. We present the experimental motivation behind this modification to receptor distribution geometry. We then present the data fitting with the new model and the experimental evidence for the predictions arising from the model.

Chapter 4

Receptor gradient model of Cnn incorporation

4.1 Introduction

In Chapter 3 we argued that modifying the diffusion model of Cnn incorporation by changing the receptor geometry may result in better approximation of the data by the model. The receptor geometry may be modified in two main ways: 1) expanding the domain over which receptors exist; and 2) allowing the receptor concentration to be non-uniform throughout the domain. In this chapter we begin by presenting certain insights from the data which strengthen the case for changing the receptor geometry in the aforementioned ways. We present a discussion on why simple receptor geometries cannot explain the data. We then present the diffusion model with modified receptor geometry and show the results of fitting this model to the data. Further, we present new experimental data that corroborate the receptor geometry predicted by the model. We then simplify the model based on biological inputs and parameter estimates from the data fitting and present the results of fitting with the reduced model. Finally we present a critique of this model and the approaches to be

taken to address these criticisms.

4.2 Insights from the data

Figure 2.2 in Chapter 2 shows that Cnn fluorescence initially recovers in the centre of the centrosome and then slowly spreads outwards. This suggests that the profile of Cnn fluorescence becomes wider with time after bleaching. However, closer inspection of the experimental data reveals otherwise. Figure 4.1 shows the Cnn recovery curves at different time points. The recovery curves have all been normalised to unity by dividing the fluorescence with the peak fluorescence at each time point. This allows us to see if the width of the Cnn fluorescence distribution has changed over time. We can see from the figure that the recovered Cnn fluorescence distribution either does not change with time or, if it does change, it does so imperceptibly slowly. It should be noted that the pre-bleach Cnn distribution is wider than the post-bleach distributions. The experimental observation that recovering Cnn fluorescence spreads

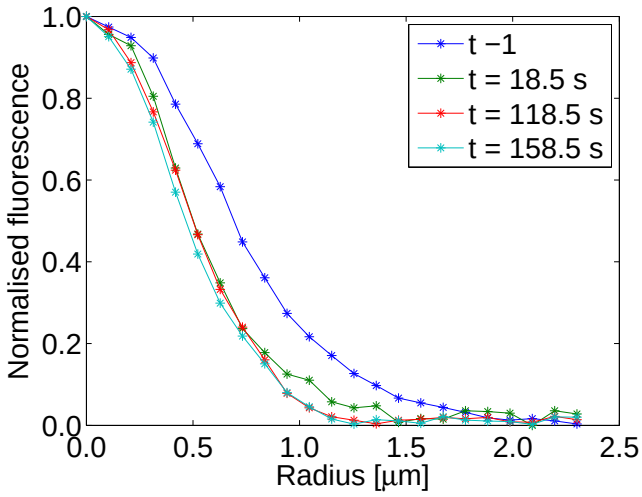

Figure 4.1: *Cnn fluorescence at a pre-bleach ($t-1$) as well as different post-bleach time points. Each recovery curve is normalised with the peak Cnn fluorescence at that time point so that the amplitude of each curve is unity. (Even though the data are discrete, they are plotted using continuous curves for better visualisation).*

radially outward in the centrosome can be explained in the following way. It is possible that the width of the Cnn gradient has reached a near-maximum value by the first time point itself. However, Cnn fluorescence is only visible at the centre of the centrosome owing to the peripheral Cnn concentration being below the detection level of the human eye. As the Cnn concentration in the centre, as well as in the peripheral regions of the centrosome, grows it gives the appearance of Cnn moving radially away from the centre. Thus, it appears that a gradient of Cnn is established early on in the recovery phase and the subsequent recovery serves to increase the concentration of Cnn on this gradient through binding interactions.

4.3 Model development

The question now is how the initial gradient of Cnn is established. One possible answer is that the initial Cnn gradient results from Cnn binding to a pre-existing Cnn-receptor gradient. This hypothesis begs the question as to how the receptor gradient was formed in the first place. However, in Section 4.4 we justify the proposition of the above hypothesis. The hypothesis of a pre-existing receptor gradient also requires us to determine what the shape of this receptor gradient should be. A possibility is suggested based on the following exercise. We fit the pre-bleach, as well as post-bleach, Cnn fluorescence profiles with separate Gaussian functions. That is, we let the peak, as well as the width of the Gaussian curves, be chosen freely at each time point. Figure 4.2 shows the results of the fit. It can be seen that the experimental data at each time point are very closely described by Gaussian curves. Since the initial time Cnn gradient can be fitted well by a Gaussian curve, and since we hypothesise that this initial gradient may result from binding to a pre-existing receptor gradient, we hypothesise that the pre-existing receptor gradient may be described by a Gaussian curve also.

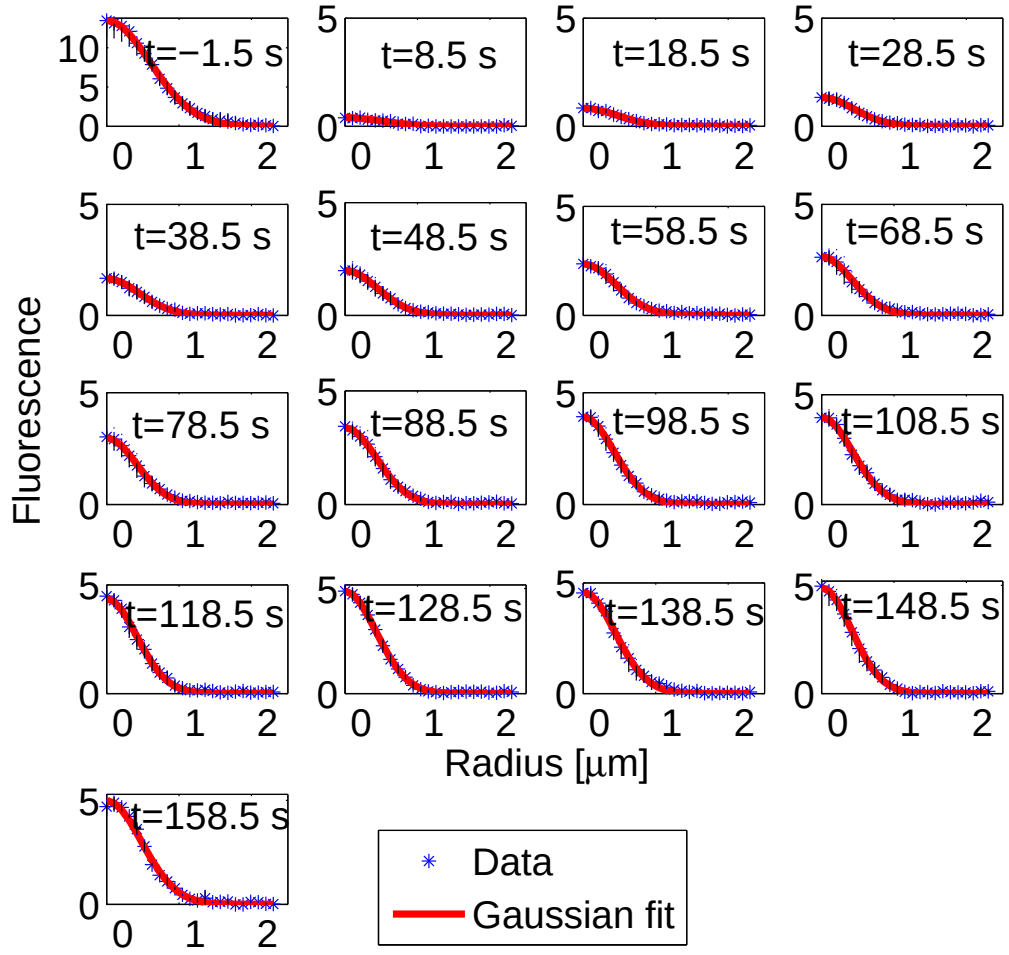

Figure 4.2: *Pre-bleach and post-bleach Cnn fluorescence profiles are fitted individually with Gaussian functions. Experimental data are denoted by blue asterisks and the Gaussian fits are denoted by red solid lines. t -1 denotes the pre-bleach time point and $t = 8.5s$ to $t = 158.5s$ denote the post-bleach recovery time points. Error bars denote standard deviation.*

4.3.1 Hypothesis

Thus, we hypothesise that the observed Cnn recovery profiles result from Cnn binding to a pre-existing Cnn receptor gradient. This receptor gradient may be described by a Gaussian function. Since the pre-bleach Cnn gradient is wider than the recovery gradients, it is possible that Cnn does move radially outwards at an imperceptibly

small rate. Thus, we continue to assume, as in the case of previous models, that binding to receptors converts cytoplasmic (fast diffusing) Cnn into heavy Cnn, which diffuses slowly. It is possible that the diffusive process results in a Cnn distribution that is different to a Gaussian distribution. The arguments presented in Section 4.6, together with Appendix C, illustrate the conditions under which the Gaussian distribution of Cnn would be maintained. We describe this receptor gradient model in Section 4.5. However, presently we argue why simpler receptor geometries are incapable of producing the observed Cnn profiles thereby justifying the need for the Gaussian-distributed receptor gradient.

4.4 Generating Gaussian distributions of diffusible molecules from simple sources

In this section we discuss how a Gaussian distribution can be generated for a diffusible molecule. We begin by assuming a simplistic source geometry, such as a point source, and examine if this source, combined with diffusion, could produce a Gaussian distribution of the molecules of interest. We then examine a more complicated source and any additional reactions which may be necessary to generate a Gaussian distribution. We will further show that obtaining a perfect Gaussian distribution at steady state from a pre-existing source requires a source gradient which is unrealistic.

4.4.1 Point source of heavy Cnn with diffusion

Our experimental collaborators have suggested that Asl may be a potential receptor for Cnn (Conduit et al., 2010). Asl is distributed very close to the centrioles. Since the centrioles are small compared to the entire centrosome, our collaborators anticipate that the Asl receptor distribution could be approximated by a point source, as described below. In order to understand what the resulting heavy Cnn distribution

may be, we simplify the model. We lump the diffusion of light Cnn and its binding to the receptors into a single source term for heavy Cnn. Thus, in this section we study whether a point source of heavy Cnn, v, without any decay, can generate a Gaussian distribution of v in three dimensions. The evolution of v in three-dimensional Cartesian coordinates[1] is

$$\frac{\partial v}{\partial t} = D_N \left(\frac{\partial^2 v}{\partial x^2} + \frac{\partial^2 v}{\partial y^2} + \frac{\partial^2 v}{\partial z^2} \right) + k\delta(x)\delta(y)\delta(z), \tag{4.4.1}$$

where v diffuses isotropically with diffusion coefficient D_N, and is produced at a constant rate k at the origin. We assume that the initial condition is given by

$$v(\boldsymbol{x}, 0) = 0, \quad \boldsymbol{x} \in (-\infty, \infty),$$

and the boundary conditions are given by

$$v(|\boldsymbol{x}| \to \pm\infty, t) \to 0, \quad \forall t,$$

where $\boldsymbol{x} = (x, y, z)$. The fundamental solution of the diffusion equation in three-dimensional Cartesian coordinates can be expressed as

$$G(x, y, z, t) = \frac{1}{(4\pi D_N t)^{3/2}} \exp\left(-\frac{x^2}{4D_N t} - \frac{y^2}{4D_N t} - \frac{z^2}{4D_N t} \right). \tag{4.4.2}$$

[1]Even though the models mentioned in this and the next chapter exhibit spherical symmetry, we use three-dimensional Cartesian coordinate description for their analysis. This is for the following reason: we wish to analyse these models using the method of Green's functions. The Green's function for the diffusion equation in the Cartesian system on a spatial domain $\boldsymbol{x} \in (-\infty, \infty)$ is simply given by equation (4.4.2). However, if we considered the diffusion equation in spherical coordinates, the domain becomes semi-infinite ($r \in (0, \infty)$), with a Neumann boundary condition at $r = 0$. This necessitates using the method of images in order to obtain Green's function that is even. This slightly complicates the form of the Green's function for the spherical system. Therefore, in order to keep the Green's function simple for the analysis, we use the Cartesian coordinate system for our models and convert the solutions to the spherical system once a suitable solution has been obtained.

Using the method of Green's functions, the solution of equation (4.4.1) is given by the convolution of G with the source of v. Thus,

$$v(x',y',z',t') = \int_{-\infty}^{\infty}\int_{-\infty}^{\infty}\int_{-\infty}^{\infty}\int_{0}^{t'} \frac{k\delta(x)\delta(y)\delta(z)}{(4\pi D_N(t'-t))^{3/2}} \exp\left(-\frac{((x-x')^2+(y-y')^2+(z-z')^2)}{4D_N(t'-t)}\right) \mathrm{d}t\mathrm{d}x\mathrm{d}y\mathrm{d}z. \tag{4.4.3}$$

Thus,

$$v(x',y',z',t') = \frac{k}{(4\pi D_N)^{3/2}}\int_0^{t'} \frac{1}{(t'-t)^{3/2}} \exp\left(-\frac{(x'^2+y'^2+z'^2)}{4D_N(t'-t)}\right) \mathrm{d}t. \tag{4.4.4}$$

We can now convert the integral to spherical polar coordinates to obtain

$$v(r',t') = \frac{k}{(4\pi D_N)^{3/2}}\int_0^{t'} \frac{1}{(t'-t)^{3/2}} \exp\left(-\frac{r'^2}{4D_N(t'-t)}\right) \mathrm{d}t. \tag{4.4.5}$$

Let $\sqrt{t'-t} = p$, then

$$v(r',t') = \frac{2k}{(4\pi D_N)^{3/2}}\int_0^{\sqrt{t'}} \frac{1}{p^2} \exp\left(-\frac{r'^2}{4D_N p^2}\right) \mathrm{d}p. \tag{4.4.6}$$

Thus,

$$v(r',t') = \frac{2k}{8\pi D_N}\left(\frac{1}{r'} - \frac{\mathrm{erf}(r'/\sqrt{4D_N t'})}{r'}\right). \tag{4.4.7}$$

We can see from equation (4.4.6) that v is undefined at $r' = 0$ for $t' > 0$. We can also see that, as $t' \to \infty$,

$$v(r') \to \frac{2k}{8\pi D_N}\frac{1}{r'}. \tag{4.4.8}$$

The reason for the blow-up at the origin stems from the source term in equation (4.4.1). The source is concentrated on a point leading to blow-up. Figure 4.3(a) shows the evolution of v as given by equation (4.4.7). It can be seen that the evolution of heavy Cnn from a point source does not resemble a Gaussian distribution; it has

algebraic radial decay at large time, for example.

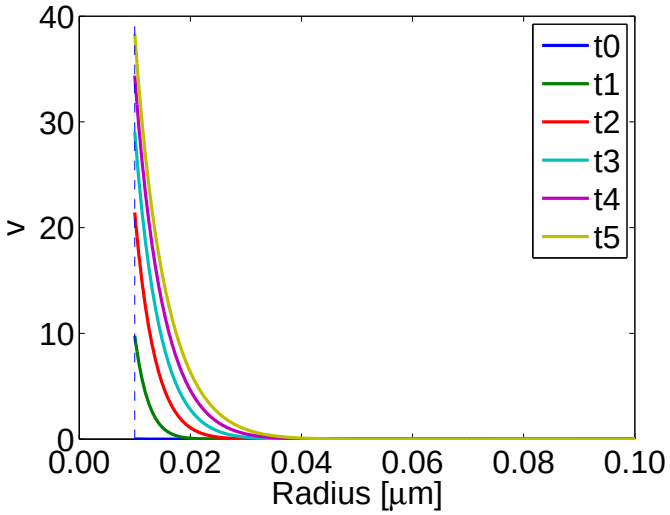

Figure 4.3: *Evolution of v as given by equation* (4.4.7). *Since the solution goes to infinity at $r = 0$, solutions are plotted for $r = [0.01, 0.1]$, and the blue dashed line indicates the $r = 0.01$ line. The parameters are $k = 0.1$ and $D_N = 0.001$.*

4.4.2 Spherical source of heavy Cnn with finite radius

In an attempt to resolve the problem of blow-up we could hypothesise that the source is a sphere of finite radius r_0, rather than a point source. The evolution equation is then given by

$$\frac{\partial v}{\partial t} = \frac{D_N}{r^2}\frac{\partial}{\partial r}\left(r^2\frac{\partial v}{\partial r}\right) + k(1 - H(r - r_0)), \tag{4.4.9}$$

where $H(r-r_0)$ is a Heaviside function in spherical polar coordinates. The boundary conditions and initial conditions are the same as in Section 4.4.1. The fundamental solution of the diffusion equation in spherical coordinates is given by

$$G(r,t) = \frac{1}{(4\pi D_N t)^{3/2}}\exp\left(-\frac{r^2}{4D_N t}\right). \tag{4.4.10}$$

The solution to equation (4.4.9) is given by the convolution of the Green's function (4.4.10) with the source of v. Thus,

$$v(r',t') = \int_0^{\infty} \int_0^{t'} \frac{k(1-H(r-r_0))}{(4\pi D_N(t'-t))^{3/2}} \exp\left(-\frac{(r-r')^2}{4D_N(t'-t)}\right) 4\pi r^2 \mathrm{d}t\mathrm{d}r. \tag{4.4.11}$$

Substituting $k(1-H(r-r_0)) = k$ for $r \leq r_0$ and zero everywhere else we get

$$v(r',t') = \int_0^{r_0} \int_0^{t'} \frac{4k\pi r^2}{(4\pi D_N(t'-t))^{3/2}} \exp\left(-\frac{(r-r')^2}{4D_N(t'-t)}\right) \mathrm{d}t\mathrm{d}r. \tag{4.4.12}$$

For $r' \gg r_0 > r$, $\exp(-(r-r')^2) \approx \exp(-r'^2)$ and equation (4.4.12) reduces to

$$v(r',t') \approx \frac{4k\pi r_0^3}{3(4\pi D_N)^{3/2}} \int_0^{t'} \frac{1}{(t'-t)^{3/2}} \exp\left(-\frac{r'^2}{4D_N(t'-t)}\right) \mathrm{d}t\mathrm{d}r, \tag{4.4.13}$$

which is a form similar to equation (4.4.5). Therefore, we can deduce that at large t', $v(r',t') \sim Constant/r'$ (see equation (4.4.8)). Thus, decay is algebraic (and not Gaussian) at large r' and t'. Since we cannot gain further insight into the behaviour of equation (4.4.12) at small or intermediate values of radius and time, we use numerical simulation to graphically present the evolution of model (4.4.9). Figure 4.4(a) shows the numerical simulation of equation (4.4.9) for arbitrary parameters. It is not clear whether or not the successive gradients generated by this process are Gaussian. To study this, we fit Gaussian curves given by

$$g(r) = a\exp(-br^2), \tag{4.4.14}$$

to the solution of v at a number of time points individually using the nonlinear least squares method. Figure 4.5 shows the numerical solution of (4.4.9) for successive time points and the best-fitting Gaussian curves at those time points. It can be seen that except for the initial time profiles, v is not well approximated by a Gaussian function.

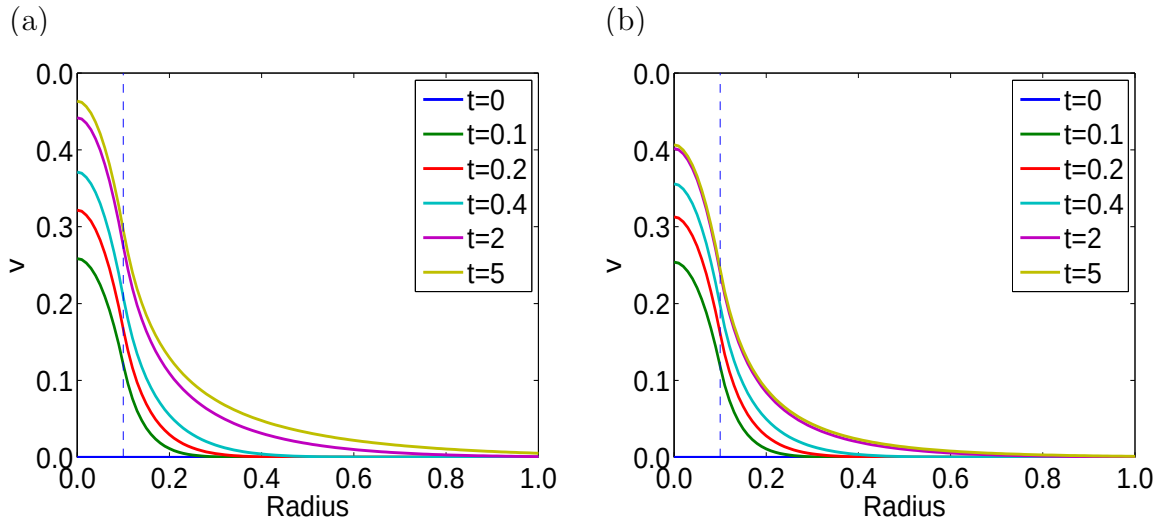

Figure 4.4: (a) *Numerical solution of equation* (4.4.9) *for parameters* $r_0 = 0.1$, $k = 5$, $D_N = 0.05$. MATLAB's `pdepe` *solver was used for the solution.* r_0 *is indicated by the dashed line.* (b) *Numerical solution of equation* (4.4.15) *for parameters* $r_0 = 0.1$, $k = 5$, $D_N = 0.05$ and $k_2 = 0.5$. MATLAB's `pdepe` *solver was used for the solution.* r_0 *is indicated by the dashed line.*

4.4.3 Spherical source of heavy Cnn with uniform decay

We have seen in the previous section that as v approaches steady state its radial profile deviates from a Gaussian curve. As described in Chapter 2, the FRAP experiments are performed when the profile of Cnn in centrosomes reaches a steady state. The pre-bleach time point, thus, corresponds to a steady state Cnn profile. It can be seen from Figure 4.2 that even the pre-bleach steady state Cnn profile is approximated well by a Gaussian function. In this section we explore whether allowing v to decay at a uniform rate can produce a Gaussian distribution of v at steady state. The evolution equation for v is given by

$$\frac{\partial v}{\partial t} = \frac{D_N}{r^2}\frac{\partial}{\partial r}\left(r^2\frac{\partial v}{\partial r}\right) + k(1 - H(r - r_0)) - k_2 v, \tag{4.4.15}$$

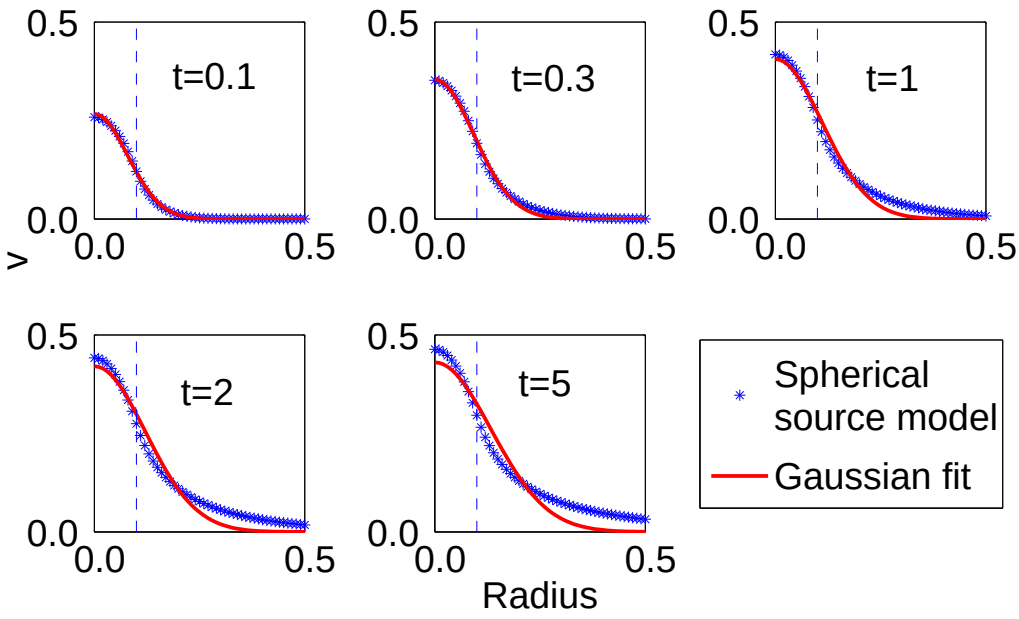

Figure 4.5: *Blue asterisks denote the numerical solution of equation* (4.4.9) *at various time points. Gaussian curves are fitted (red solid lines) individually to the evolution of* v *at various time points. The radius of the spherical source,* r_0*, is indicated by the blue dashed lines.*

where k_2 denotes a uniform decay rate for v. The boundary conditions and initial conditions are the same as in Section 4.4.1. If we multiply equation (4.4.15) with $\exp(k_2 t)$, rearrange and substitute $w = \exp(k_2 t)v$ we get

$$\frac{\partial w}{\partial t} = \frac{D_N}{r^2}\frac{\partial}{\partial r}\left(r^2\frac{\partial w}{\partial r}\right) + \exp(k_2 t)k(1 - H(r - r_0)), \tag{4.4.16}$$

which has a similar form as equation (4.4.9). Solving equation (4.4.16) by taking the convolution of the source with the Green's function (4.4.10) and substituting $v = \exp(-k_2 t)w$ gives

$$v(r', t') = \exp(-k_2 t')\int_0^{r_0}\int_0^{t'} \frac{\exp(k_2 t)k}{(4\pi D_N(t' - t))^{3/2}} \exp\left(-\frac{(r - r')^2}{4D_N(t' - t)}\right) 4\pi r^2 \mathrm{d}t\mathrm{d}r. \tag{4.4.17}$$

Once again we can make arguments similar to those in Section 4.4.2 to show that the behaviour of this model can be approximated by $Constant/r'$ for $r' \gg r_0 > r$ and for large t'. Figure 4.4(b) shows the numerical simulation of equation (4.4.15) for arbitrary parameters. As in the previous case, we fit Gaussian curves given by equation (4.4.14) to the solution v at a number of time points individually using the nonlinear least squares method. Figure 4.6 shows the numerical solution of (4.4.15) for successive time points and the best-fitting Gaussian curves at those time points. It can be seen that once again the initial time profiles of v are well approximated by a Gaussian function, but the fit becomes worse as time increases. We could continue adding complexities to our model in an attempt to obtain a steady state Gaussian distribution of v. However, in the next section, we adopt a reverse engineering approach, in order to find a source geometry that may generate a Gaussian distribution of v.

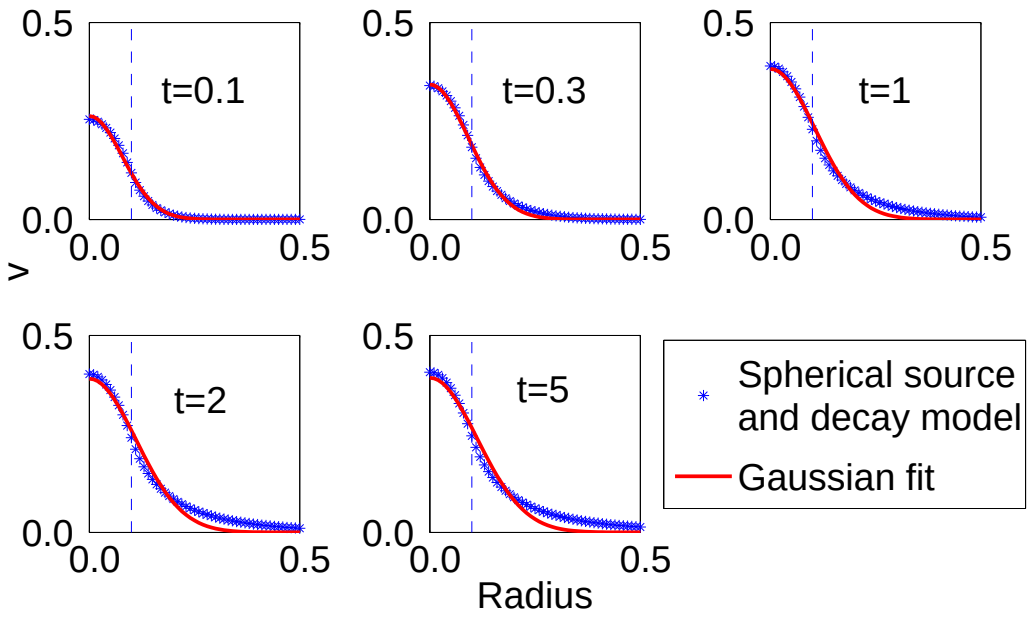

Figure 4.6: *Blue asterisks denote the numerical solution of equation* (4.4.15) *at various time points. Gaussian curves are fitted (red solid lines) individually to the evolution of* v *at various time points. The radius of the spherical source,* r_0*, is indicated by the blue dashed lines.*

4.4.4 Reverse engineering a steady state Gaussian distribution

We begin with a Gaussian distribution of v at steady state and work backwards to see what the source should look like in order to give a distribution of the form

$$v_{ss}(r) = A\exp(-Br^2).$$

Assuming that v can diffuse with diffusion coefficient D_N and is produced from a source $f(r,t)$, the evolution equation for v is given by

$$\frac{\partial v}{\partial t} = \frac{D_N}{r^2}\frac{\partial}{\partial r}\left(r^2\frac{\partial v}{\partial r}\right) + f(r,t). \tag{4.4.18}$$

We know that the steady state solution of the above equation should give a Gaussian distribution. Thus, for v_{ss},

$$\frac{D_N}{r^2}\frac{d}{dr}\left(r^2\frac{dv_{ss}}{dr}\right) = -f(r).$$

Note that the source term $f(r)$ is not time-dependent since we are concerned with a steady state scenario. Substituting the expression for v_{ss} gives

$$f(r) = \bar{A}\exp(-Br^2)\left[3 - 2Br^2\right], \tag{4.4.19}$$

where $\bar{A} = 2AB$. Thus, it appears that the source $f(r)$ should in fact be a combination of a source and a sink, wherein the source is Gaussian and the sink is a Gaussian times a quadratic. At $r = o(\varepsilon)$, where $0 < \varepsilon \ll 1$, $f(r)$ approximates a Gaussian distribution. As the radius increases, $f(r)$ goes from positive to negative, crossing the axis at $r = \sqrt{3/2B}$. As $r \to \infty$, $f(r) \to 0$. At first glance it appears that this time-invariant sink would produce negative concentration values. However, it should

be noted that, since we only considered the steady state solution in deriving $f(r)$, we have ignored the time-evolution of $f(r)$. Figure 4.7 shows the shape of the source curve that would generate a Gaussian solution for v at steady state.

Through this analysis we have shown that generating a steady state Gaussian distri-

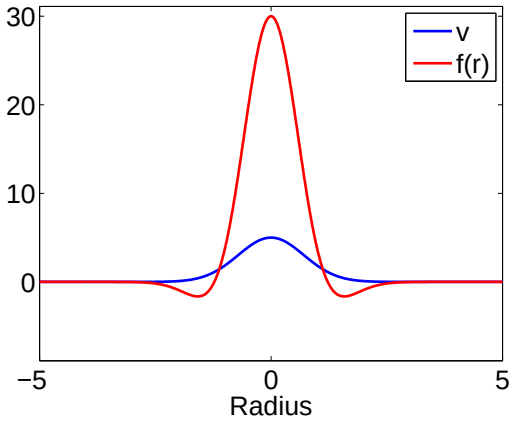

Figure 4.7: *Solid red curve shows the source term $f(r)$ at steady state, which should produce a Gaussian distribution of v, which is shown as the solid blue line.*

bution of diffusible molecules with simplistic source geometry is not a trivial problem. Even though a simple spherical source can initially produce heavy Cnn gradients that resemble a Gaussian distribution, the width of these Gaussian distributions increases with time (not shown) and they begin to deviate from the Gaussian description at large times (see Figures 4.5 and 4.6). Thus, these simplistic source models will not correctly describe the Cnn FRAP behaviour. However, it is possible that the Cnn FRAP data could be fitted by Gaussian-like curves generated from the receptor-gradient model we proposed. In the following section we present the model.

4.5 The receptor gradient model

The receptor gradient model retains the binding-unbinding reactions of light Cnn and the diffusion and decay of heavy Cnn from the previous models presented in Chapter

3. The system is described mathematically by the following set of reaction-diffusion equations:

$$\frac{\partial L}{\partial t} = \frac{D_L}{r^2}\frac{\partial}{\partial r}\left(r^2\frac{\partial L}{\partial r}\right) + k_{out}N - k_{on}LP + k_{off}C, \tag{4.5.1}$$

$$\frac{\partial N}{\partial t} = \frac{D_N}{r^2}\frac{\partial}{\partial r}\left(r^2\frac{\partial N}{\partial r}\right) - k_{out}N + k_{turn}C, \tag{4.5.2}$$

$$\frac{dP}{dt} = k_{turn}C + k_{off}C - k_{on}LP, \tag{4.5.3}$$

$$\frac{dC}{dt} = k_{on}LP - k_{off}C - k_{turn}C, \tag{4.5.4}$$

where L, N, P, C denote light Cnn, heavy Cnn, Cnn-receptor and Cnn-receptor complex, respectively. Conservation of total receptor concentration gives

$$P(r,t) + C(r,t) = P_{tot}(r) = P_{max}\underline{\exp(-p_{grad}r^2)},$$

where P_{max} is the concentration of receptors at $r = 0$ and p_{grad} is a measure of the width of receptor gradient. The underline is added to signify the difference between this model and the previous versions in Chapter 3. The boundary conditions are given by

$$D_L\frac{\partial L}{\partial r}\bigg|_{r=0} = 0, \qquad D_N\frac{\partial N}{\partial r}\bigg|_{r=0} = 0,$$
$$L(r\to\infty) = L_{cyt}, \qquad N(r\to\infty) = 0. \tag{4.5.5}$$

4.6 Analysis

To analyse the model we non-dimensionalise it by introducing new dimensionless variables and defining non-dimensional parameters as

$$
\begin{aligned}
&u = \frac{L}{L_{cyt}}, \quad v = \frac{N}{L_{cyt}}, \quad w = \frac{C}{L_{cyt}}, \quad p = \frac{P}{L_{cyt}}, \\
&t^* = k_{turn}t, \quad r^* = \sqrt{\frac{k_{turn}}{D_L}}r, \quad \varepsilon = \frac{D_N}{D_L}, \quad \alpha = \frac{k_{on}L_{cyt}}{k_{turn}}, \\
&\beta_1 = \frac{k_{off}}{k_{turn}}, \quad \beta_2 = \frac{k_{out}}{k_{turn}}, \quad \mu = \frac{P_{max}}{L_{cyt}}, \quad b = \frac{p_{grad}D_L}{k_{turn}}.
\end{aligned} \tag{4.6.1}
$$

Rearranging equations (4.5.1)-(4.5.4) and using the above substitutions, a non-dimensionalised form of our model is obtained. Removing the asterisks for clarity, we obtain

$$\frac{\partial u}{\partial t} = \frac{1}{r^2}\frac{\partial}{\partial r}\left(r^2\frac{\partial u}{\partial r}\right) + \beta_2 v - \alpha u p + \beta_1 w, \tag{4.6.2}$$

$$\frac{\partial v}{\partial t} = \frac{\varepsilon}{r^2}\frac{\partial}{\partial r}\left(r^2\frac{\partial v}{\partial r}\right) - \beta_2 v + w, \tag{4.6.3}$$

$$\frac{dp}{dt} = (\beta_1 + 1)w - \alpha u p, \tag{4.6.4}$$

$$\frac{dw}{dt} = \alpha u p - (\beta_1 + 1)w, \tag{4.6.5}$$

where

$$p(r,t) + w(r,t) = \mu \exp\left(-br^2\right).$$

The initial conditions are given by

$$u(r,0) = 1, \quad v(r,0) = 0, \quad p(r,0) = p_{tot}(r) \quad \text{and} \quad w(r,0) = 0.$$

The non-dimensionalised boundary conditions are given by,

$$\begin{aligned}
&\left.\frac{\partial u}{\partial r}\right|_{r=0} = 0, \\
&\left.\frac{\partial v}{\partial r}\right|_{r=0} = 0, \\
&v(\infty, t) = 0 \ \text{ and } \ u(\infty, t) = 1.
\end{aligned} \tag{4.6.6}$$

4.6.1 Solving for v

Multiplying equation (4.6.3) with $\exp(\beta_2 t)$, rearranging and letting $\exp(\beta_2 t)v = q$ gives

$$\frac{\partial q}{\partial t} = \frac{\varepsilon}{r^2}\frac{\partial}{\partial r}\left(r^2\frac{\partial q}{\partial r}\right) + \exp(\beta_2 t)w. \tag{4.6.7}$$

The corresponding boundary conditions for q are

$$\left.\frac{\partial q}{\partial r}\right|_{r=0} = 0, \qquad q(\infty, t) = 0. \tag{4.6.8}$$

Equation (4.6.7) can be restated using three-dimensional Cartesian coordinates as

$$\frac{\partial q}{\partial t} = \varepsilon\left(\frac{\partial^2 q}{\partial x^2} + \frac{\partial^2 q}{\partial y^2} + \frac{\partial^2 q}{\partial z^2}\right) + f(x, y, z, t), \tag{4.6.9}$$

where $f(x, y, z, t) = \exp(\beta_2 t)w$. We use the model in Cartesian coordinates only in order to simplify the solution process and we will return the model to the spherical coordinates once we have obtained a solution. The boundary conditions are now a homogeneous Dirichlet condition as $(x, y, z) \to (\pm\infty, \pm\infty, \pm\infty)$. The above equation can be solved using the method of Green's functions. The Green's function solution of the heat equation corresponding to equation (4.6.9) can be expressed as

$$G(x, y, z, t) = \frac{1}{(4\pi\varepsilon t)^{3/2}}\exp\left(-\frac{x^2}{4\varepsilon t} - \frac{y^2}{4\varepsilon t} - \frac{z^2}{4\varepsilon t}\right). \tag{4.6.10}$$

The solution of equation (4.6.9) is thus given by the convolution of the Green's function (4.6.10) with the source term $f(x, y, z, t) = \exp(\beta_2 t)w$. Thus,

$$q(x', y', z', t') = \int_{-\infty}^{\infty}\int_{-\infty}^{\infty}\int_{-\infty}^{\infty}\int_{0}^{t'} \frac{\exp(\beta_2 t)w}{(4\pi\varepsilon(t'-t))^{3/2}} \exp\left(-\frac{((x-x')^2+(y-y')^2+(z-z')^2)}{4\varepsilon(t'-t)}\right) \mathrm{d}t\mathrm{d}x\mathrm{d}y\mathrm{d}z.$$

Since $q = v\exp(\beta_2 t)$, $v(x', y', z', t')$ is given by

$$v(x', y', z', t') = \exp(-\beta_2 t') \int_{-\infty}^{\infty}\int_{-\infty}^{\infty}\int_{-\infty}^{\infty}\int_{0}^{t'} \frac{w}{(4\pi\varepsilon(t'-t))^{3/2}} \exp\left(\beta_2 t - \frac{((x-x')^2+(y-y')^2+(z-z')^2)}{4\varepsilon(t'-t)}\right) \mathrm{d}t\mathrm{d}x\mathrm{d}y\mathrm{d}z. \quad (4.6.11)$$

4.6.2 Solving for w

Due to the conservation of total receptor concentration we can write $p = p_{tot} - w = \mu\exp(-br^2) - w$. Substituting into equation (4.6.5) we obtain

$$\frac{dw}{dt} = \alpha\mu\exp(-br^2)u - (\alpha u\beta_1 + 1)w.$$

The above equation resembles equation (3.4.12) except for the radial dependence of w given by $\mu\exp(-br^2)$. This allows us to borrow the solution (3.4.13) and modify it to reflect the radial dependence to obtain

$$w(t) = \mu\exp(-br^2)\left(1 - \frac{1}{I_f(t)} - \frac{(\beta_1+1)}{I_f(t)}\int_0^t I_f(s)\mathrm{d}s\right), \quad (4.6.12)$$

where I_f is given by equation (3.4.14). Thus, it can be seen that if the light Cnn, u, is not uniformly distributed, i.e. if the concentration of the light Cnn is not constant throughout the centrosome, then the complex would not form a Gaussian distribution, whereas if u was uniformly distributed with respect to the radius, then the complex

would form a Gaussian distribution. The solution of w (4.6.12) can be substituted into equation (4.6.11) to obtain the solution for v implicit in u. In order to obtain the explicit solution of v, we will need to solve for u. (When uniform distribution of u leads to a Gaussian distribution of w, analysis similar to that given in Appendix C shows that the distribution of v would also be Gaussian at all time points).

4.6.3 Solving for u

Equation (4.6.2) is nonlinear (owing to the binding reaction with receptors, p). Therefore, the method of Green's functions is not applicable for its solution. The solution of v is thus given implicitly. Appendix B.3 shows the numerical simulation of the receptor gradient model.

4.7 Modelling the FRAP experiment and data fitting

The FRAP experiment is modelled as in the case of previous models. Appendix B.4 shows the numerical simulation of the FRAP experiment for an arbitrary set of parameters. It can be seen that the model qualitatively describes the FRAP recovery kinetics.

Since we do not have an analytical solution for the model, we use the numerical solution for data fitting. Specifically, we use the normalised model (Appendix A.4) for fitting. We have used several checks to ascertain that the numerical solutions are reliable. The numerical solutions are smooth; the change in the solution is within tolerance (1e-4) when the mesh is refined, and lastly, the numerical solution matches (not shown) with the analytical solution obtained from the reduced model (equation (C.3.6)) in the limiting case (i.e. when $k_{off} = k_{out} = 0$ and $D_L = O(1)$ or greater).

(We defer the discussion about model reduction until Section 4.10. The analytical solution of the reduced model is discussed in Appendix C). In the case of this model, the recovery is the result of the combined fluorescence from heavy Cnn as well as the Cnn-receptor complex. Thus, we use the quantity $v(r,t) + w(r,t)$ for fitting. The pre-bleach state is given by the steady state solution of the model. The post-bleach states are obtained by solving the FRAP model for the required time points. The least squares method is used for data fitting.

4.8 Results

Figures 4.8-4.9 show sample best-fits of the receptor gradient model with the Cnn FRAP data and demonstrate that the receptor gradient model fits the data well. Table 4.1 shows the best-fitting parameter estimates obtained from the fits. The goodness of fit estimators, namely RMSE values and R^2 coefficients, are also listed. The model describes the data correctly as judged by the R^2 coefficient and RMSE values. Figure 4.10 shows the distribution of residuals (normalised with the standard deviation at each spatial and temporal point) from the fits with the average data from the spindle side and the cytoplasm side. Thus, the receptor gradient model fits the Cnn FRAP data well in comparison to the previous models.

4.9 Validating the receptor gradient model

Since the receptor gradient model fits the Cnn experimental data well, it provides a plausible and ultimately testable mechanism for the Cnn incorporation process. One of the predictions of this model, however, is that Cnn receptors exist in a Gaussian distribution around the centrioles with an average width, parameterised by $p_{grad} = 3.44\ \mu\text{m}^{-2}$. (Note that the parameter p_{grad} is inversely proportional to the width of the Gaussian distribution $P_{max} \exp(-p_{grad} r^2)$, i.e., the width is larger for smaller values of

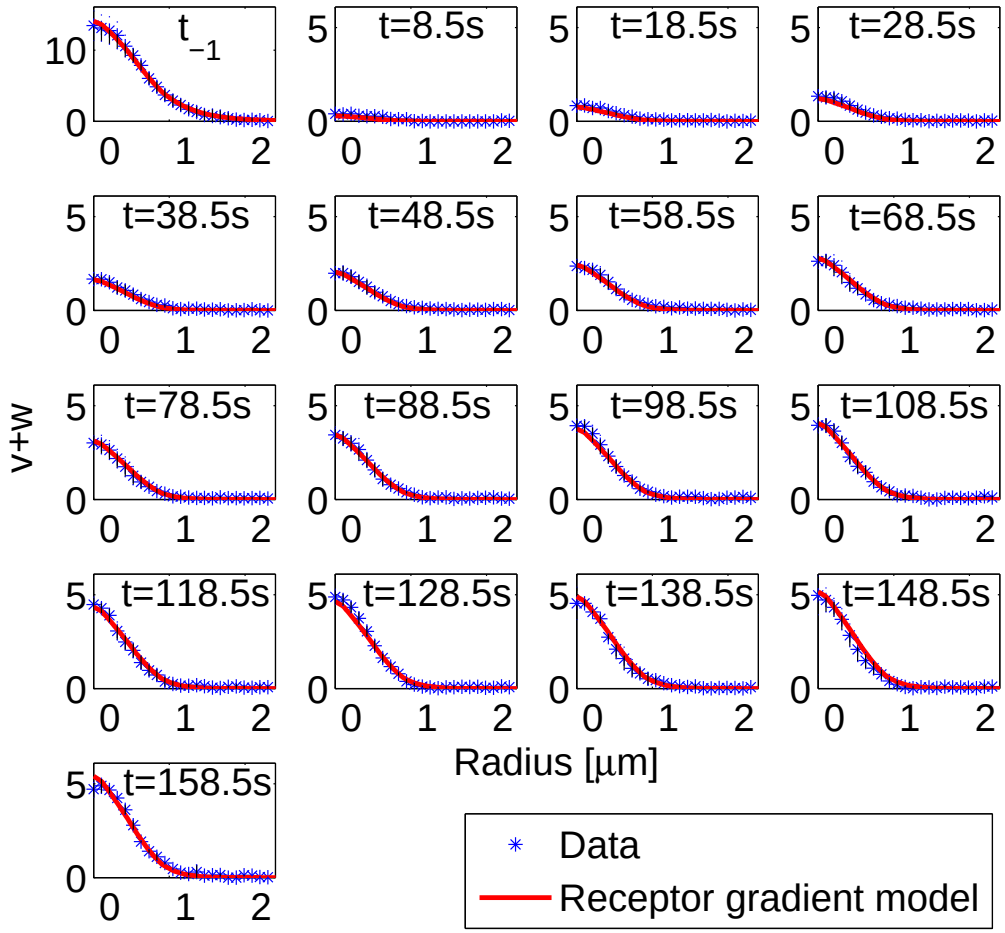

Figure 4.8: *Average cytoplasm side FRAP data for Cnn (blue asterisks) is shown with the best-fitting receptor gradient model: equations* (A.4.1)-(A.4.4) *(red solid lines).* t_{-1} *denotes the pre-bleach time point and* $t = 8.5$ *s to* $t = 158.5$ *s denote the post-bleach recovery time points.*

p_{grad} and *vice versa*). It is important that this prediction is validated experimentally. Conduit et al. (2010) have shown that Cnn associates with two other centrosomal proteins, namely Asl and DSpd2. They have also shown that blocking these proteins using antibodies reduces the incorporation of Cnn into the centrosomes. Thus, these are two potential candidates for Cnn receptors. However, it is not clear whether both proteins are involved in recruiting Cnn or whether these proteins are recruited in a

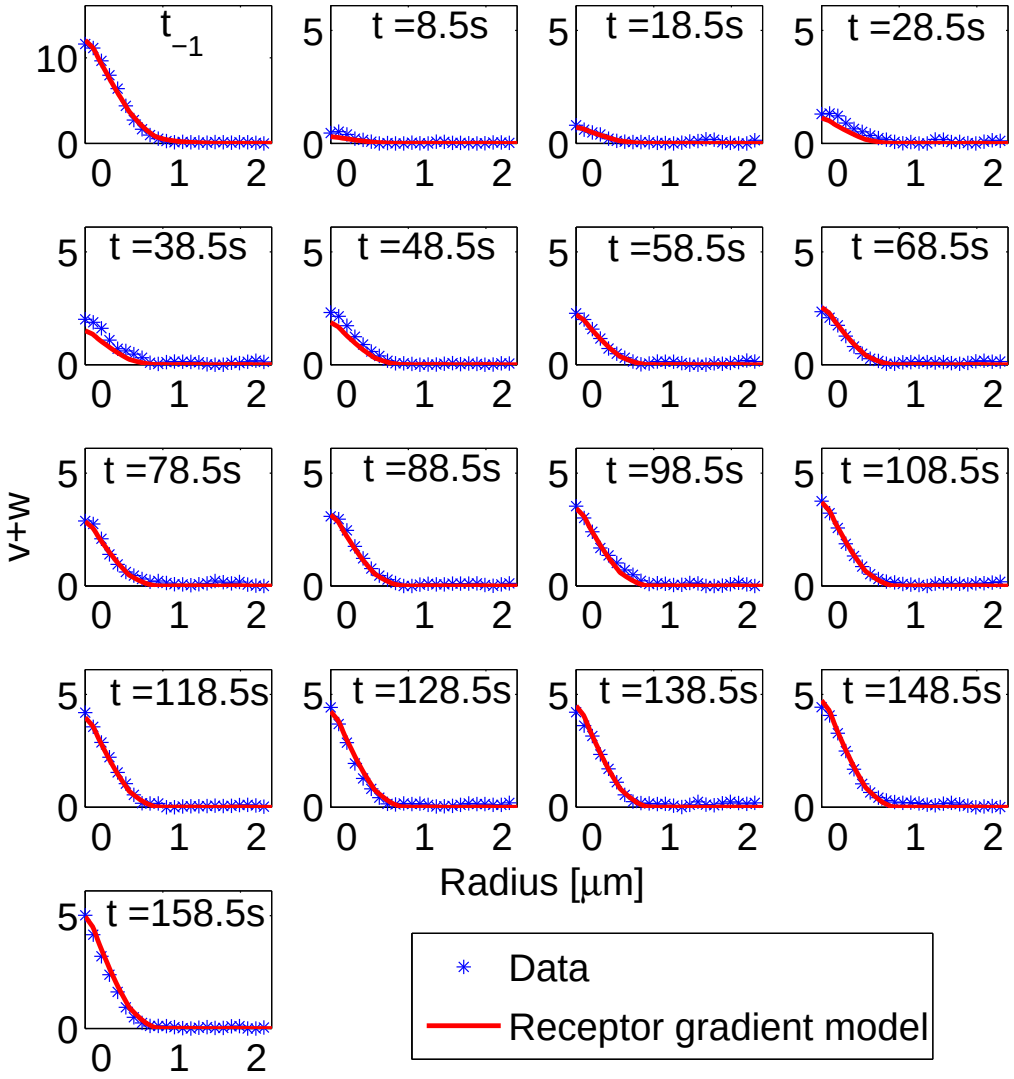

Figure 4.9: *FRAP data from a single centrosome for Cnn (blue asterisks) (spindle side) is shown with the best-fitting receptor gradient model given by equations* (A.4.1)-(A.4.4) *(red solid lines).* t_{-1} *denotes the pre-bleach time point and* $t = 8.5$ *s to* $t = 158.5$ *s denote the post-bleach recovery time points.*

sequential manner.

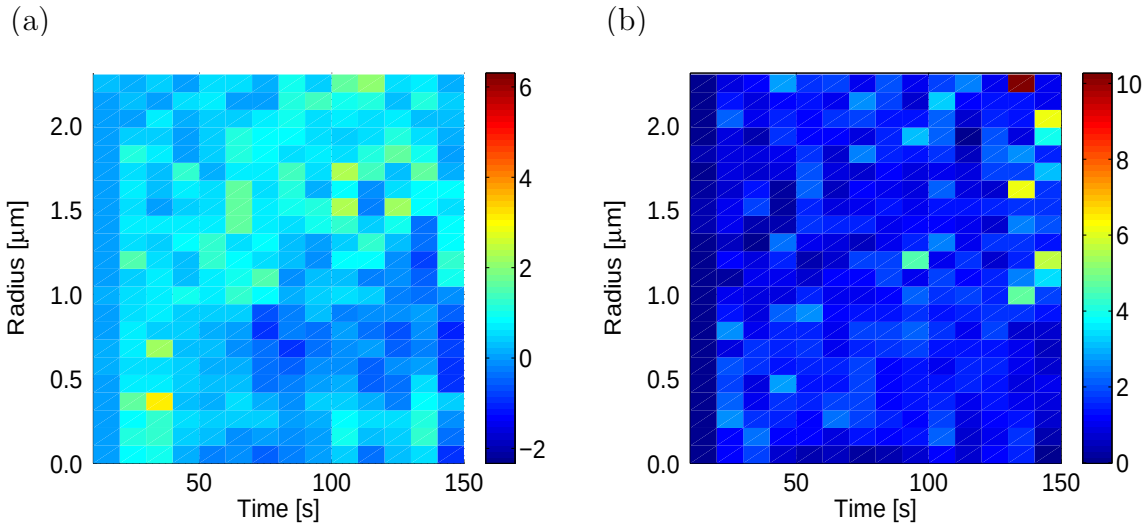

Figure 4.10: *Plots of residuals between the best fitting receptor gradient model given by equations* (A.4.1)-(A.4.4) *and the average data* (a), *and data from a single centrosome* (b).

4.9.1 Experimental evidence

Our experimental collaborators examined whether the Cnn-receptors exist in a concentration gradient in the centrosomes. They used *Drosophila* embryos expressing GFP-Asl and imaged several centrosomes from different embryos. Figure 4.11(a) shows the normalised Asl gradient observed. We carry out the normalisation in the same way as for the Cnn data (see in Chapter 2). It can be seen that Asl does appear to form a gradient in a centrosome[2]. Assuming that the observed Asl distribution is not an optical artifact, we fit the mean Asl distribution by a Gaussian. Figure 4.11(b)

[2]We mentioned in Section 3.12 in Chapter 3 that super-resolution micrographs of GFP-Asl centrosome have shown that Asl exists in an envelope around the centrioles in the form of a thick-walled hollow cylinder. The super-resolution technique requires that the specimen be fixed, whereas the current result is from live embryos imaged at a lower resolution. We anticipate that since the Cnn data were also collected at the lower resolution, the Asl profile at this resolution is more appropriate for validating the model. Moreover, we note that due to the nature of the super-resolution microscopy, the graded profile of Asl around the centrioles may not have been apparent in the earlier data. However, caution has to be exercised in the case of the new Asl data. This is because Asl is distributed over a region which is similar in size to the resolution of the microscope. Even if such small objects (i.e. Asl distribution, in this case) have sharp edges, fluorescence from them may appear Gaussian distributed due to artifacts introduced by the diffraction of the light. More experiments are required to ascertain whether the observed Asl gradient is a true gradient or an optical artifact.

Table 4.1: Results of fitting the FRAP kinetics of Cnn with the recovery kinetics of $v + w$ given by the receptor gradient model, equations (A.4.1)-(A.4.4). Parameter estimates obtained from fitting, the RMSE values and the coefficients of determination R^2, are listed.

	Data				
Parameters	**Avg data (spindle side)**	**Avg data (cytoplasm side)**	**Movie 5 data**	**Movie 12 data**	**Units**
$\overline{k_{on}}$	0.1138	0.1095	0.1111	0.17	s^{-1}
k_{off}	7.7e-6	5e-6	1.2e-7	1e-9	s^{-1}
k_{turn}	0.1242	0.122	0.0628	0.13	s^{-1}
k_{out}	5.7e-4	8.6e-4	0.0014	0.0011	s^{-1}
D_L	1.35	1.14	1.78	2.09	$\mu m^2 s^{-1}$
D_N	1.9e-4	2.6e-4	9.4e-5	3.8e-4	$\mu m\ s^{-1}$
P_{max}/L_{cyt}	0.72	0.79	0.93	0.69	-
p_{grad}	4.1	2.77	5.27	2.6	μm^{-2}
RMSE	0.21	0.1296	0.1451	0.1874	-
N	391	391	391	391	-
R^2	0.9858	0.9953	0.9893	0.9918	-

shows that a Gaussian curve fits the Asl distribution well. However, the best-fitting Gaussian curve is parameterised by $p_{grad} = 14.78\ \mu m^{-2}$. Thus, the Asl gradient is much narrower than the receptor gradient predicted by our model. Using the value of p_{grad} estimated from the Asl gradient to fit the Cnn data using the receptor gradient model results in a worse fit (not shown). Thus, it is possible that even though Asl does form a gradient, it may not be the receptor for Cnn.

Our collaborators next imaged the centrosomes from *Drosophila* embryos expressing GFP-DSpd2. Figure 4.12(a) shows the normalised DSpd2 gradient observed from preliminary experiments. We carry out the normalisation in the same way as for the Cnn data. It can be seen that DSpd2 also forms a gradient in the centrosome.

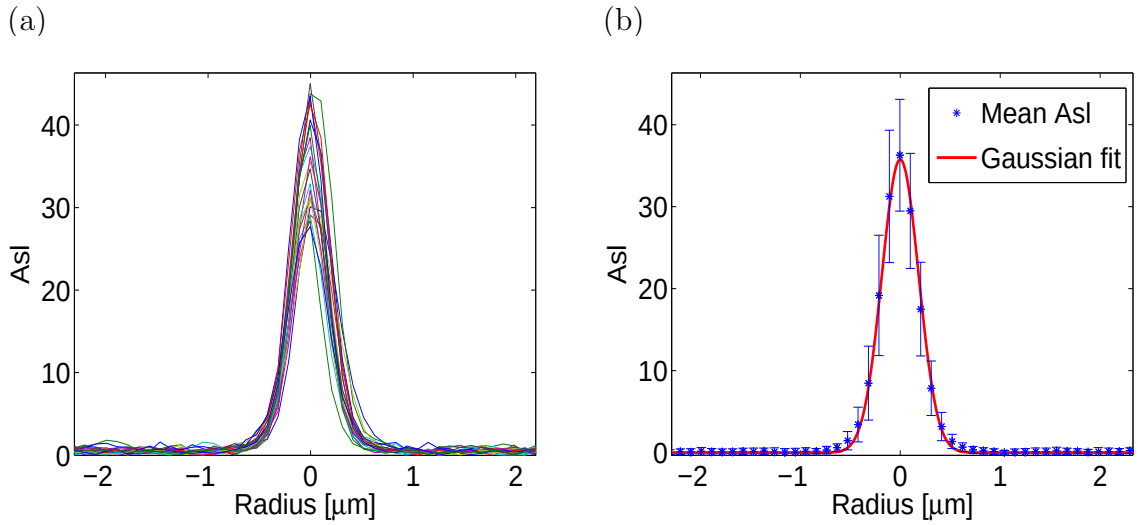

Figure 4.11: (a) *Centrosomes from embryos expressing fluorescent Asl were imaged and Asl profiles were recorded in a similar manner to that shown in Figure 2.2(b). The resulting profiles from* 24 *centrosomes are normalised (similarly to the Cnn data) and plotted as a function of radius.* (b) *The mean Asl profile (blue asterisks) is fitted with a Gaussian distribution (red solid line). Error bars indicate the standard deviation of mean Asl. Note that the fluorescence intensities are normalised and hence are dimensionless. Also note that the distribution of Asl observed here contrasts with the one observed in Figure 3.20. The previous image was gathered using a super-resolution microscopy technique, which required that the specimen be fixed. Thus, it is possible that the current image showing the Gaussian distribution may represent a true image in the absence of fixing.*

Since the DSpd2 fluorescence is spread over a wider domain as compared to the Asl fluorescence, the DSpd2 distribution is less likely to be a result of optical artifacts (however more experiments are required to ascertain that the DSpd2 gradient is not exaggerated due to optical artifacts.). The mean DSpd2 gradient can be fitted well by a Gaussian curve (Figure 4.12(b)). The best-fitting value is $p_{grad} = 4.05\ \mu\text{m}^{-2}$. This value is very close to the value of p_{grad} predicted by our model. In Figure 4.13 we show that the Gaussian distribution predicted by our model closely approximates the distribution of DSpd2 in the centrosomes. Thus, we are able to find the predicted receptor gradient with the required distribution around the centrioles.

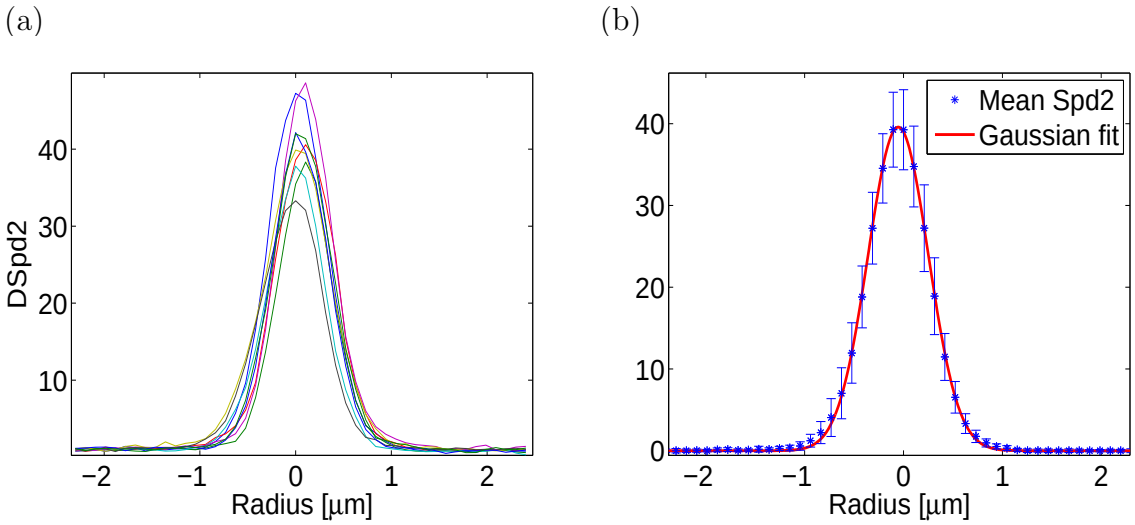

Figure 4.12: (a) *Centrosomes from embryos expressing fluorescent DSpd2 were imaged and DSpd2 profiles recorded in a similar manner to that shown in Figure 2.2(b). The resulting profiles from* 9 *centrosomes are normalised (similarly to the Cnn data) and plotted as a function of radius.* (b) *The mean DSpd2 profile (blue asterisks) is fitted with a Gaussian distribution (red solid line). Error bars indicate the standard deviation of mean DSpd2. Note that the fluorescence intensities are normalised and hence are dimensionless.*

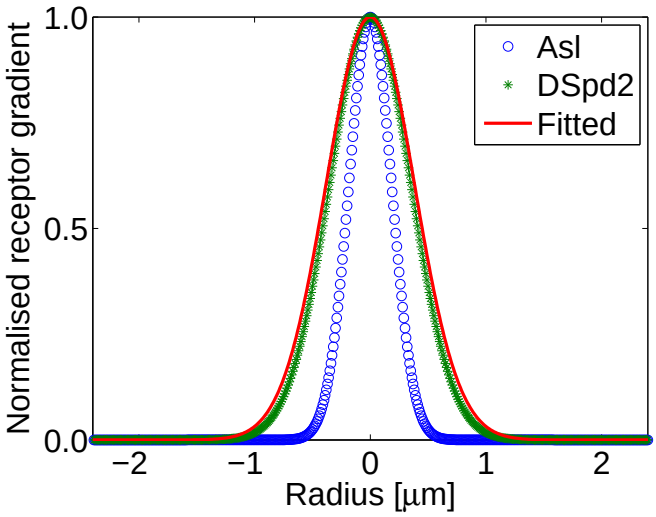

Figure 4.13: *Various Gaussian distributions are plotted with peak intensities of unity and the widths given by the best fitting Asl gradient (blue circles), best-fitting DSpd2 gradient (green asterisks) and the best-fitting receptor gradient from our model (red line).*

4.9.2 Significance of the experimental verification

With the receptor gradient model we have been able to predict the shape and size of the Cnn-receptor gradient required to generate the Cnn recovery curves. Not only have we found that the two putative Cnn receptors appear to form a Gaussian distribution in the centrosome (however, we need to be cautious in interpreting Asl distribution as a Gaussian since the previous work with the super-resolution microscopy had shown Asl to be distributed in the form of an envelope around the centriole), we have found that the size (width) of the DSpd2 gradient matches the size of the receptor gradient predicted by our model. Together with the analysis in Section 4.4 showing that the receptor distribution cannot be approximated by any simpler geometry, this experimental evidence provides strong support for the receptor gradient model. An additional result from this work (combined with previous experimental evidence (Conduit et al., 2010)) is that we are able to say with greater confidence that DSpd2 is a receptor for Cnn, even though we cannot rule out a role for Asl in binding to Cnn.

4.10 Model reduction

The receptor gradient model has eight parameters. We have been able to experimentally verify one of them, namely p_{grad}. However, even with the remaining seven parameters, there is a danger of overfitting the data. Appendix D lists the confidence intervals predicted for the parameter estimates obtained from a sample best fit. It can be seen that in the case of several parameters the confidence intervals encompass a large parameter space, often extending into the unrealistic negative parameter region. This (along with the non-dimensionalisation) suggests that various parameters in the full model may act in combination to produce the required fluorescence evolution, and the effects of each individual parameter may not be separately identified using these

data. In this section, we explore if the receptor gradient model can be reduced to have fewer parameters, while still fitting the data. We consider the following aspects for model reduction.

Firstly, we note that some parameters as estimated from the best-fits are small, for example, k_{off} and k_{out}. These parameters may not have a large effect on the model behaviour on the FRAP time scale (about 150 s). Therefore, in order to reduce the model, we set these parameters to zero. Setting k_{off} to zero means that the Cnn-receptor complex does not dissociate back to give the cytoplasmic Cnn and free receptors. Setting k_{out} to zero means that the heavy Cnn does not decay back to cytoplasmic Cnn. Secondly, we have argued in Section 2.2 that cytoplasmic Cnn diffuses fast and recovers quickly as compared to the time scale of the FRAP experiment. Our parameter estimates also suggest that the recovery of cytoplasmic Cnn would be diffusion-dominated, thereby leading to quick equilibration of fluorescent cytoplasmic Cnn in a FRAP experiment. We now make use of this argument in model reduction by setting $u(r,t) \equiv 1$ (or $L(r,t) \equiv L_{cyt}$) during recovery. Thus, the reactions in the modified model can be described by

$$P \xrightarrow{k_{on} L_{cyt}} C, \qquad\qquad C \xrightarrow{k_{turn}} P + N, \tag{4.10.1}$$

where P, C and N denote free receptors, Cnn-receptor complex and heavy Cnn, respectively. We present the reduced model and its analysis in Appendix C.

4.10.1 Results of data fitting

The reduced model can be solved for the FRAP evolution of $w(r,t)$ and $v(r,t)$ as shown in Appendix C. Since both the Cnn-receptor complex and the heavy Cnn are

fluorescent, the evolution of the total fluorescence in the centrosomes is given by

$$v_f(r',t') + w_f(r',t') = \frac{\overline{k_{on}}\mu}{\overline{k_{on}} + k_{turn}} \Bigg(\exp(-p_{grad} r'^2)\,(1 - \exp(-k_{turn} t')) + k_{turn} \int_0^{t'} \frac{(1 - \exp(-k_{turn} t))}{(4 p_{grad} D_N (t' - t) + 1)^{3/2}} \exp\left(- \frac{(r'^2)}{4 D_N (t' - t) + 1/p_{grad}} \right) \mathrm{d}t \Bigg), \quad (4.10.2)$$

where $\overline{k_{on}} = k_{on} L_{cyt}$, where L_{cyt} is the concentration of cytoplasmic Cnn, which we assume to be uniformly distributed in the reduced model. We use this solution to fit the reduced receptor gradient model to the Cnn FRAP data using the method of least squares. We evaluate the numerical integral using MATLAB's `quad` function, which uses the adaptive recursive Simpson's rule. As before, MATLAB's `lsqnonlin` is used for the fitting. Figure 4.14 shows the result of fitting average Cnn FRAP data (cytoplasmic side) to the reduced receptor gradient model. In Table 4.2 we list the estimated parameter values and various estimators of the quality of the fit. It can be seen from comparing the RMSE and R^2 coefficient values to those from the full receptor gradient model fit given in Table 4.1 that the reduced model fits the data less well as compared to the full model. This is expected as the full model uses a greater number of parameters.

4.10.1.1 F-test

We use an F-test to decide whether the full model is necessary for the fitting or whether the reduced model is adequate. Equation (2.4.6) from Chapter 2 is used for calculating the F-score. The numerator degrees of freedom, which is the difference between the number of parameters fitted in the full model and in the reduced model is $P_f - P_p = 3$. The denominator degrees of freedom are $N - P_f = 384$. The sum of squared residuals for the fit with the average data (cytoplasmic side) for the full model is $S_f = 6.58$ and that for the reduced model $S_p = 13.78$. Thus, the F-score is 140.06. Comparing this score against the F-test tables (Dinov, 2002) for the above

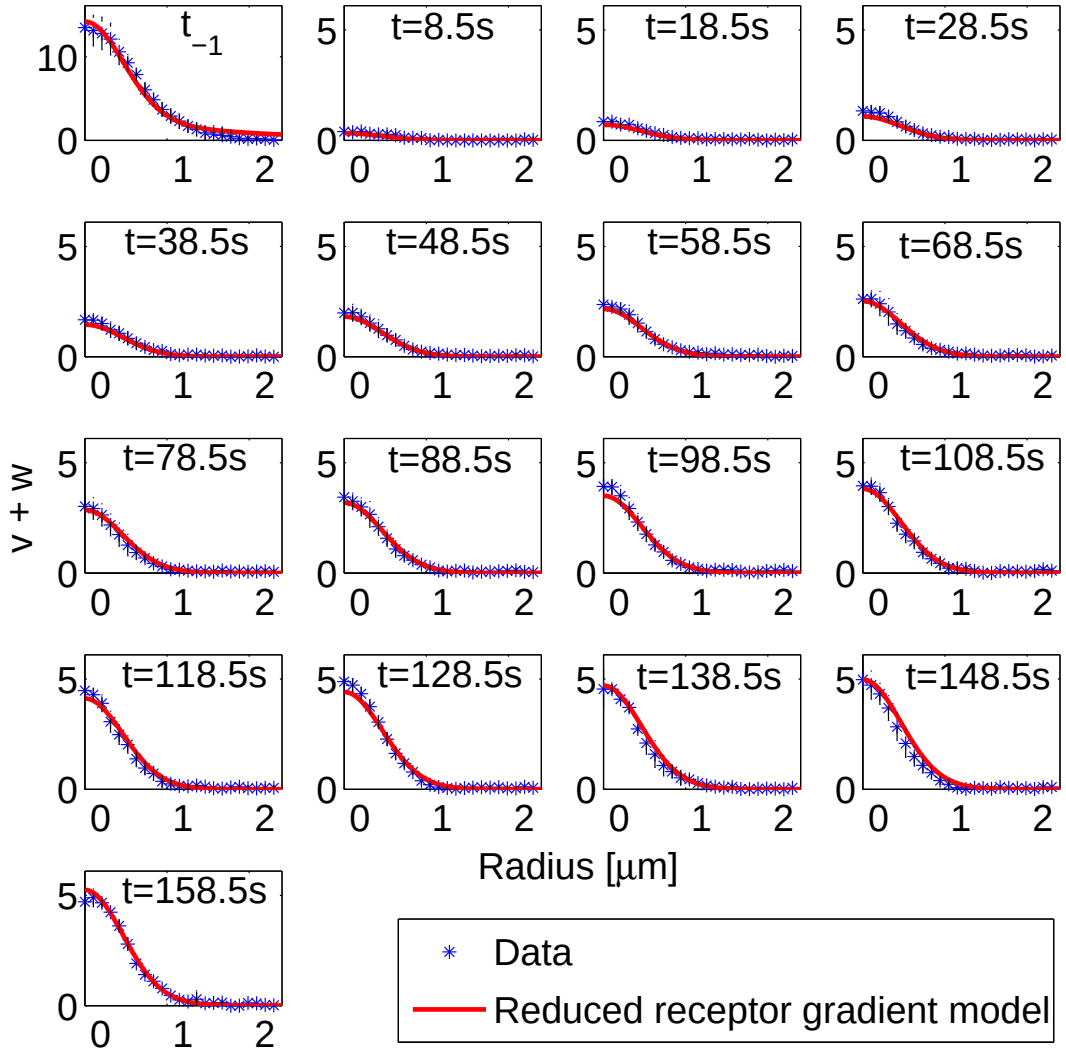

Figure 4.14: *Average FRAP data for Cnn (blue asterisks) (cytoplasm side) is shown with the best-fitting reduced receptor gradient model solution of* $v+w$ *given by equation* (4.10.2) *(red solid lines). t -1 denotes the pre-bleach time point and* $t = 8.5$ *s to* $t = 158.5$ *s denote the post-bleach recovery time points.*

degrees of freedom and for a p-value of 0.05 we find that the null hypothesis can be rejected. (The F-test tables list the values of F-statistic for various numerator and denominator degrees of freedom, and for a given p-value). As mentioned in Chapter

Table 4.2: Results of fitting the FRAP kinetics of Cnn with the recovery kinetics of $v + w$ (equation (4.10.2)) given by the reduced receptor gradient model. Parameter estimates obtained from fitting, the RMSE values and the coefficients of determination R^2, are listed. 95% confidence intervals for the parameter estimates are also listed.

Parameters	**Avg data (cytoplasm side)**	**95% Confidence Intervals**	**Units**
$\overline{k_{on}}$	1.84	$-2.9 \times 10^5 - -2.9 \times 10^5$	s^{-1}
k_{turn}	0.0037	0.0034–0.004	s^{-1}
D_N	0.0019	0.0016–0.0021	$\mu m^2\ s^{-1}$
P_{max}/L_{cyt}	10.34	$-3.2 \times 10^3 - -3.2 \times 10^3$	-
p_{grad}	2.40	2.30–2.49	μm^{-2}
RMSE	0.1914	-	-
N	391	-	-
R^2	0.9897	-	-

2, the null hypothesis of the F-test is that both the reduced and full model fit the data equally well. Rejecting the null hypothesis means that the extra parameters in the full (i.e. more complex model) are necessary to explain the data and that the improvement in the fit is not merely due to overfitting.

However, in the case of model fits where $N \gg P$, the larger models are favoured by the F-test. Visual examination of the fit with the reduced model shows that the fit is of acceptable quality, and that there are no trends in the data that are unaccounted for by the model. It can be seen, however, that the fit to steady state, given at the pre-bleach time point, is noticeably worse in the case of the reduced model. This may be expected since small parameters, such as k_{off} and k_{out}, may make a difference to the steady state, which occurs at large times. (We present a discussion about the parameter estimates from the two models in Section 4.11.2). Furthermore, the confidence bounds listed in Table 4.2 are tightly spaced and such that the estimated parameter values lie centrally in the confidence intervals (for the parameters

k_{turn}, D_N and p_{grad}), suggesting that these parameters have been estimated reliably. (We note that the confidence intervals for the parameters $\overline{k_{on}}$ and P_{max}/L_{cyt} are still too broad and we discuss a fix for this problem in Section 4.11.3). Therefore, we accept that the reduced model fits the data well (except for the steady state) and can be used as a useful mechanistic description of the underlying biology.

4.11 Discussion and conclusions

We began this chapter by examining the Cnn FRAP data in different ways so as to gain insights into the Cnn incorporation mechanism. We learned that the visual observation of Cnn fluorescence spreading radially outwards is not supported when the successive FRAP curves are studied. This prompted us to propose that there may be a pre-existing Cnn receptor gradient to which Cnn binds during recovery. We hypothesised that this pre-existing receptor gradient should follow a Gaussian distribution, since the Cnn recovery curve at the first time point after bleaching also shows a Gaussian distribution. We supported this hypothesis by showing that simpler receptor distribution geometries cannot reproduce the observed Gaussian profiles of Cnn fluorescence. We modified our Cnn diffusion model to incorporate the new receptor gradient hypothesis and showed that the resulting model fits the Cnn data well.

Using this model we were able to predict the width of the Cnn receptor gradient. Having found a model that can explain the Cnn FRAP behaviour, we sought experimental verification for the presence of a receptor gradient. Our collaborators had previously postulated Asl and DSpd2 as two putative receptors for Cnn, since blocking either one of these proteins reduces the incorporation of Cnn into the centrosomes (Conduit et al., 2010). However, it was not clear, prior to this analysis, whether it is Asl or DSpd2 or both that recruit Cnn. Our collaborators used *Drosophila* embryos

expressing either Asl-GFP or Asl-DSpd2 to study whether these molecules form a gradient in the centrosomes. In the preliminary experiments both Asl and DSpd2 were found to exist in a Gaussian distribution around the centre of the centrosomes. However, it was the width of the DSpd2 gradient that matched with the Cnn-receptor gradient predicted by our model[3]. Thus, we are able to verify, using preliminary experiments, the existence of a Cnn receptor gradient and the shape of the predicted gradient matched the one found experimentally. This also showed that DSpd2 may be recruiting Cnn by acting as a Cnn receptor, even though we cannot deny a role for Asl at this point.

4.11.1 Parameter estimates from the full model

We were able to use the full receptor gradient model to estimate model parameters (listed in Table 4.1). However, the full model uses eight parameters. There is a danger of overfitting the data when a model uses a large number of parameters. Moreover, there may be multiple minima for the data fitting function, i.e. several different combinations of parameters may be able to give acceptable fits with the data. (We have not found any parameter combination that minimises the sum of squares more than the results presented in this work. We have, however, found various parameter combinations which result in local minima with higher sum of square values). The confidence intervals on several parameter estimates from the full model are too wide (see Appendix D), for the estimates to be reliable. In order to overcome these difficulties, we reduced the full receptor gradient model to reflect: a) that the cytoplasmic Cnn recovers fast as compared to the time scale of the FRAP experiment, such that, during the FRAP recovery, cytoplasmic Cnn concentration

[3]Further experiments are required to ascertain whether the Asl gradient is solely due to optical artifacts. DSpd2, on the other hand, is distributed over a domain larger than the resolution of the microscope. However, the microscope has limited resolution in the Z-axis and hence further experimental work is necessary to decide whether the DSpd2 gradient is, in part, attributable to optical artifacts.

could be considered to be homogeneous; and b) that the estimated values of k_{off} and k_{out} are small, which may allow us to set these parameters to zero. Having thus reduced the full receptor gradient model, we used it to fit the FRAP data. Even though the F-test suggested that the full model is needed to explain the data, we accept the reduced model based on visual examination of the fit, and the tighter confidence intervals for the estimated parameters. This is because the F-test may erroneously favour the larger model in the case where the number of data points fitted is significantly greater than the number of model parameters, which is the case with the Cnn data. In accepting the reduced model we accept that the cytoplasmic Cnn diffuses fast as compared to the time scale of the FRAP experiment and the reactions namely, the dissociation of Cnn-receptor complex into cytoplasmic Cnn and free receptors and the decay of heavy Cnn into the light Cnn, play a negligible role in the Cnn recovery dynamics.

4.11.2 Parameter estimates from the reduced model

The parameter estimates of the reduced model show significant differences as compared to the estimates from the full model. Notably, the values of k_{on} and P_{max}/L_{cyt} appear to have increased, whereas the value of k_{turn} appears to have decreased. However, these differences are not alarming in light of the fact that the confidence intervals on the estimates from the full model are too wide (for example, some confidence intervals stretch into the unrealistic, negative region). Having said this, our collaborators favour a higher ($O(1)$ or greater) estimate of the parameter P_{max}/L_{cyt}. Note that this is the ratio of peak receptor concentration to cytoplasmic Cnn concentration. Based on fluorescence observations our collaborators believe that this ratio may not be less than one.

4.11.3 Identifiability

We have noted that, even with the reduced receptor gradient model, the confidence bounds on parameters $\overline{k_{on}}$ and P_{max}/L_{cyt} are too wide. We observe that the model solution for the evolution of fluorescence (equation (4.10.2)) has a parameter group

$$\frac{\overline{k_{on}}\mu}{\overline{k_{on}} + k_{turn}},$$

where $\mu = P_{max}/L_{cyt}$. This is a product of a fraction

$$\frac{\overline{k_{on}}}{\overline{k_{on}} + k_{turn}},$$

with the normalised peak receptor concentration P_{max}/L_{cyt}. Parameters that appear together as products are not identifiable (Bates and Watts, 1988), and hence we replace the above parameter group with a single parameter

$$k^*_{on} = \frac{\overline{k_{on}}\mu}{\overline{k_{on}} + k_{turn}},$$

and rerun the data fitting. We obtain an identical fit with just four parameters and improved confidence intervals. Figure 4.15 shows the result of the fit. Table 4.3 lists the parameter estimates and confidence intervals, along with the RMSE and R^2 coefficient values.

The fluorescence in the centrosome is given by the combination of Cnn-receptor complex and heavy Cnn. The difference between these two species is that one of them is immobile, whereas the other is diffusible. In the absence of this difference (for example, if both the species were immobile) the two species would be indistinguishable. In the absence of diffusion, the fluorescence could be composed entirely of Cnn-receptor complex, or of heavy Cnn, or any intermediate combination of the two. That is, the

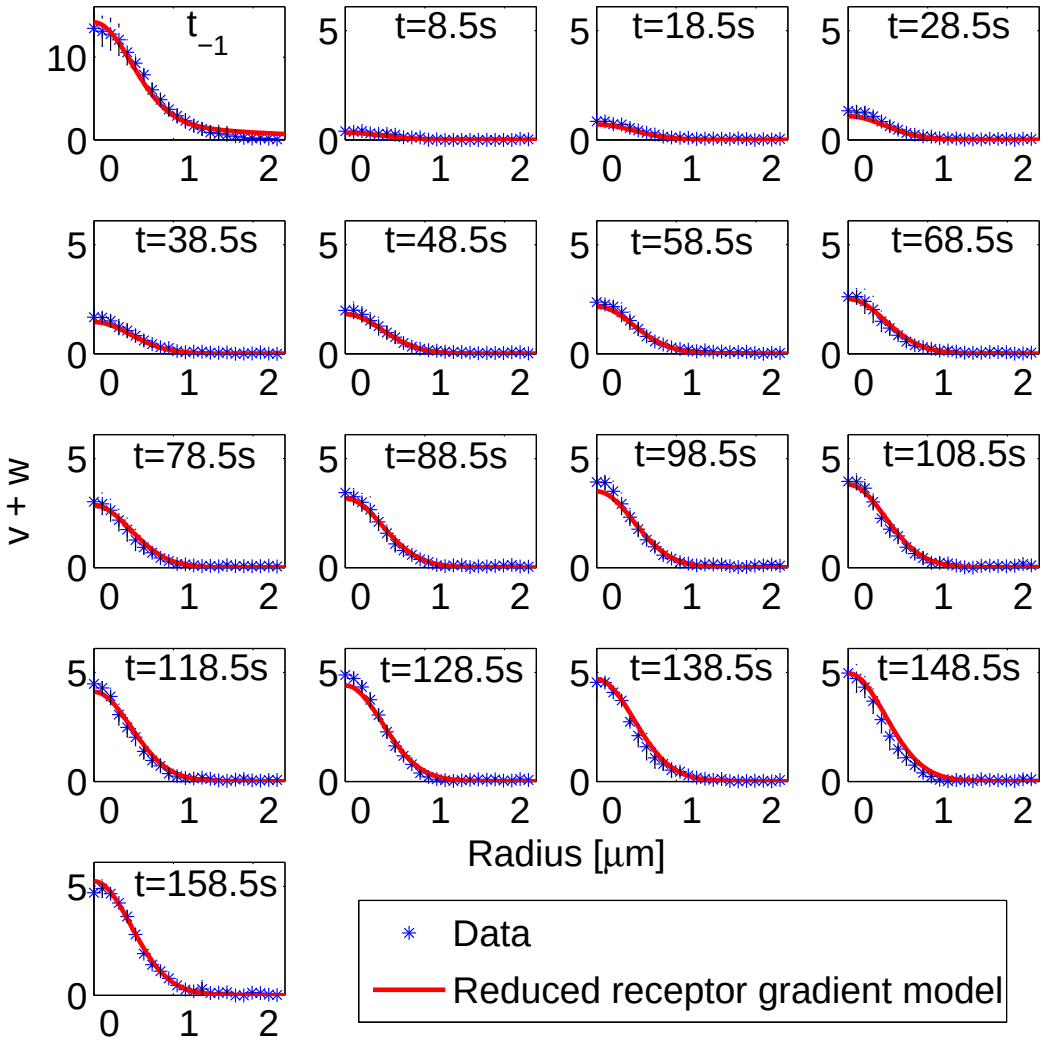

Figure 4.15: *Average cytoplasm side FRAP kinetics data for Cnn (blue asterisks) are shown with the best-fitting reduced receptor gradient model solution of* $v+w$ *(red solid lines) given by equation* (4.10.2)*, with the parameter group substitution as mentioned in Section 4.11.3.* $t = 8.5$ *s to* $t = 158.5$ *s denote the post-bleach recovery time points.*

relative proportions of the two species in the centrosome could not be estimated reliably and would be unidentifiable. In such a situation the very existence of heavy Cnn would be difficult to justify. For example, in the case of Cnn FRAP data, if we ignore

Table 4.3: Results of fitting the FRAP kinetics of Cnn with the recovery kinetics of $v + w$ given by the reduced receptor gradient model, equation (4.10.2), with the parameter group substitution as mentioned in Section 4.11.3. Parameter estimates obtained from fitting, the RMSE values and the coefficients of determination R^2, are listed. 95% confidence intervals for the parameter estimates are also listed.

Parameters	**Avg data (cytoplasm side)**	**95% Confidence Intervals**	**Units**
k^*_{on}	10.5099	10.07-10.94	-
k_{turn}	0.0036	0.0035–0.0038	s^{-1}
D_N	0.0021	0.0018–0.0023	$\mu m^2\ s^{-1}$
p_{grad}	2.38	2.29–2.46	μm^{-2}
RMSE	0.1931	-	-
N	391	-	-
R^2	0.9895	-	-

the pre-bleach state, i.e. if we do not use the pre-bleach state to fit the steady state, we cannot estimate D_N reliably. Figure 4.16 shows the result of fitting the reduced model to average Cnn FRAP data while ignoring the steady state. Table 4.4 shows the parameter estimates from this fit. It can be seen that the 95% confidence interval for D_N is very broad and stretches into an unrealistic negative region. This is because the heavy Cnn diffusion during FRAP evolution is negligible. The pre-bleach state shows a wider Cnn fluorescence gradient than the recovery gradients, and therefore including the pre-bleach gradient in the fitting allows us to estimate D_N more reliably. However, we need to be cautious while fitting the steady state. This is because the small parameters may be important at large times (i.e. when the system reaches steady state).

4.11.4 Mode of transport for incorporated Cnn

One of the questions we began by asking was how the incorporated Cnn is transported

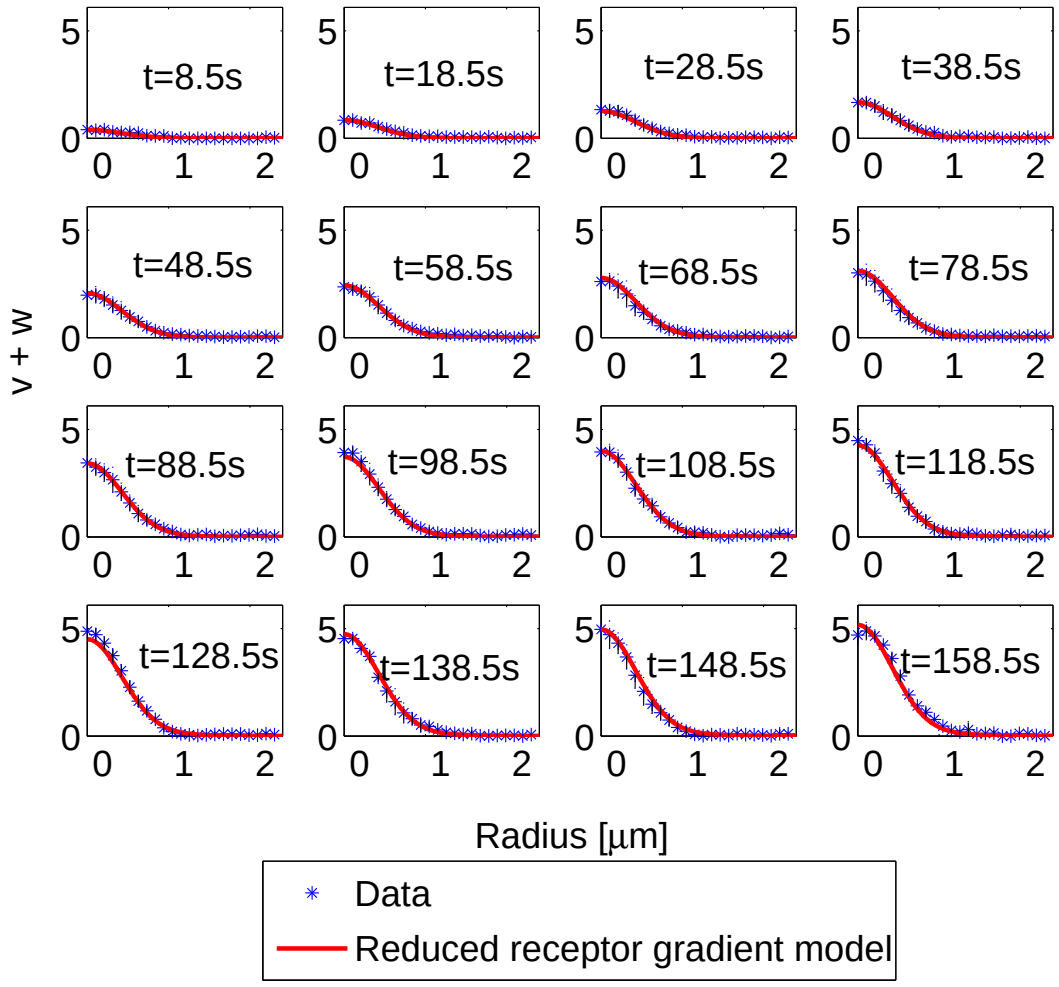

Figure 4.16: *Average FRAP kinetics data for Cnn (except for the pre-bleach state) (blue asterisks) (cytoplasm side) are shown with the best-fitting reduced receptor gradient model solution of* $v + w$ *(red solid lines), equation* (4.10.2)*, with the parameter group substitution as mentioned in Section 4.11.3.* $t = 8.5$ *s to* $t = 158.5$ *s denote the post-bleach recovery time points.*

in the centrosome. Two plausible modes of transport were identified as diffusion and advection. In Chapter 3 we selected the diffusion model over the advection model owing to the slightly worse fit offered by the advection model. However, having now selected the correct receptor geometry, we need to ask this question again. As we

Table 4.4: Results of fitting the FRAP kinetics of Cnn with the recovery kinetics of $v + w$ given by the receptor gradient model, equation (4.10.2), with the parameter group substitution as mentioned in Section 4.11.3. The pre-bleach state (i.e. the steady state) is not used for the fitting. Parameter estimates obtained from fitting, the RMSE values and the coefficients of determination R^2, are listed. 95% confidence intervals for the parameter estimates are also listed.

Parameters	**Avg data (cytoplasm side)**	**95% Confidence Intervals**	**Units**
k^*_{on}	7.79	5.98–9.61	-
k_{turn}	0.006	0.0046–0.0073	s^{-1}
D_N	0.0075	-0.0028–0.0179	$\mu m^2\ s^{-1}$
p_{grad}	2.82	2.69–2.95	μm^{-2}
RMSE	0.0968	-	-
N	368	-	-
R^2	0.9937	-	-

mentioned before, the movement of Cnn during the FRAP recovery process is imperceptibly small, if any. Thus, we do not to use these data to distinguish between the modes of transport. If we could extend the time for which the fluorescence recovery of Cnn is monitored, we may be able to better understand the mode of Cnn transport.

In the next chapter, we use Cnn FRAP data gathered over a longer time period to study the incorporation of Cnn. In this chapter we have assumed that the receptor gradient is invariant. In the next chapter we use the information about the receptor gradient, gathered concurrently with FRAP data, in order to understand whether receptor gradient evolution plays a role in the evolution of the Cnn gradient.

Chapter 5

Using the reduced receptor gradient model to further understand Cnn incorporation

In Chapter 4 we saw that a reduced version of the receptor gradient model can satisfactorily fit the data. However, we noted that the imperceptibly small (if any) change in the width of the recovery gradients prevents us from differentiating between the advective versus diffusive transport of Cnn. In fact, the negligible movement away from the receptor gradient raises a question about the very existence of heavy (or altered) Cnn (i.e. a species of Cnn that transports radially from the centrioles), except for in the flares. In order to resolve these difficulties we need to monitor FRAP recovery experiments for a longer time.

The previous FRAP experiments described in Chapter 2 were carried out during mitosis as we believe that Cnn exhibits a biologically relevant steady state during mitosis. Bleaching a system at steady state has several advantages. Firstly, knowing the steady state allows one to identify from the FRAP recovery kinetics the exis-

tence or otherwise of an immobile fraction of the fluorescent molecules. Observing the recovery of the fluorescent molecules for sufficient time could suggest whether there is an immobile fraction and what the proportion of this immobile fraction is. Without knowledge of the steady state, estimation of the immobile fraction cannot be made. Secondly, the concentration of non-fluorescent species can be considered to be constant during the course of recovery. For example, in the case of our model, we could assume that the free receptor concentration is constant at steady state value throughout recovery. Specifically, in the case of the reduced receptor gradient model, this means that the time scale of recovery of fluorescence is determined solely by the rate at which the free receptors are generated, namely k_{turn} (see equation (4.10.2)).

However, studying FRAP recovery during mitosis in *Drosophila* embryos poses a disadvantage. At the end of mitosis the centriole pair in a centrosome disengages and the separated centriole begins to accumulate its own PCM (Conduit et al., 2010). Thus, the time for which the recovery could be monitored is restricted by the length of mitosis. Previous attempts at prolonging observation times by arresting embryos in mitosis using colchicine have not been useful, as discussed in Section 2.1. This is because arresting mitosis alters the Cnn incorporation dynamics such that the steady state in mitosis is lost after the addition of colchicine. Therefore we decided, together with our collaborators, to perform long time Cnn FRAP experiments during S-phase. As shown in Figure 1.5(a), Cnn incorporation continues to increase throughout S-phase. Thus, we lose the advantage of a steady state in order to obtain longer time FRAP data.

In this chapter we begin by describing briefly the altered experimental protocol our collaborators have used to obtain long time FRAP data for Cnn. We present various characteristics of the new data and the results of fitting the data with the reduced

receptor gradient model. Further, we present the observations of receptor gradient evolution and its effect on the Cnn incorporation process. We then focus on the question of the mode of transport of heavy (or altered) Cnn. We conclude by summarising the insights gained from long time FRAP experiments.

5.1 Experimental protocol

Working closely with our collaborators we devised an experimental protocol which our collaborators have used to generate further Cnn FRAP data. According to the new protocol, the FRAP experiment is performed when the syncytial nuclei are in early S-phase. A bleaching radius of 2.5 μm is selected, as previously, and seven Z-images with 400 nm spacing between the images are recorded. Images are captured every 30 seconds (instead of 10 seconds as in previous experiments), so as to minimise the effect of bleaching during observation. The pixel size of the images in (X, Y) is 0.1111 μm. This generates four-dimensional data. Our collaborators select a Z-image which shows the maximum intensity at each time point. The centrosome that is bleached is identified and a 4.7μm line is drawn through it, such that it passes through the centre and is in the direction perpendicular to the future spindle direction (as opposed to parallel to spindle, as in previous experiments). The line is drawn such that half of the line lies to either side of the centrosome. Figure 2.2(b) shows the process of gathering the two-dimensional data from the maximum intensity Z-images, with the only difference being the line drawn in the case of this experiment is perpendicular to the line indicated in the figure. The reason for choosing this line is that the fluorescence intensities are symmetrically distributed across the centre of the centriole, along the diameter perpendicular to the spindle axis. Fluorescence intensities along this line are noted. The process is repeated at each time point after bleaching, and for several embryos, as before. Note that, because of the choice of the diameter along which the

fluorescence is measured, the data are symmetric across the origin (as opposed to the cytoplasmic and spindle side data in the previous case). The rest of the experimental protocol remains identical to the previous protocol given in Chapter 2.

In the previous chapter we showed that the fluorescence intensity profile of DSpd2 matches the predicted profile of Cnn receptor gradient and we assumed the receptor distribution to be constant throughout time. In the new experimental protocol, our collaborators monitor the fluorescence of GFP-DSpd2 in embryos expressing this gene. The time for which DSpd2 fluorescence is monitored is chosen to match the time for which Cnn fluorescence recovery is observed in the GFP-Cnn embryos. These preliminary DSpd2 data are gathered in an identical manner to the Cnn data, except for the bleaching step.

5.2 Insights from the data

Having thus obtained two-dimensional data, our collaborators send the data to us for further analysis. We process the data as described in Section 2.2. The Cnn recovery data are gathered from ten different centrosomes. Figure 5.1 shows the mean Cnn fluorescence data along with the standard deviation at each time point. It can be seen that the fluorescence at later times during recovery increases beyond the fluorescence exhibited at the pre-bleach time point. This is because when the centrosomes were bleached the Cnn fluorescence had yet to reach its maximum intensity at steady state. One of the reasons for performing a long time FRAP experiment is to check whether Cnn shows appreciable radial movement with time. Cnn fluorescence at selected time points is normalised with the peak Cnn fluorescence at that time point in order to compare changes in the widths of the Cnn gradients with time. Figure 5.2(a) shows that the Cnn gradient indeed widens appreciably with time, thus proving

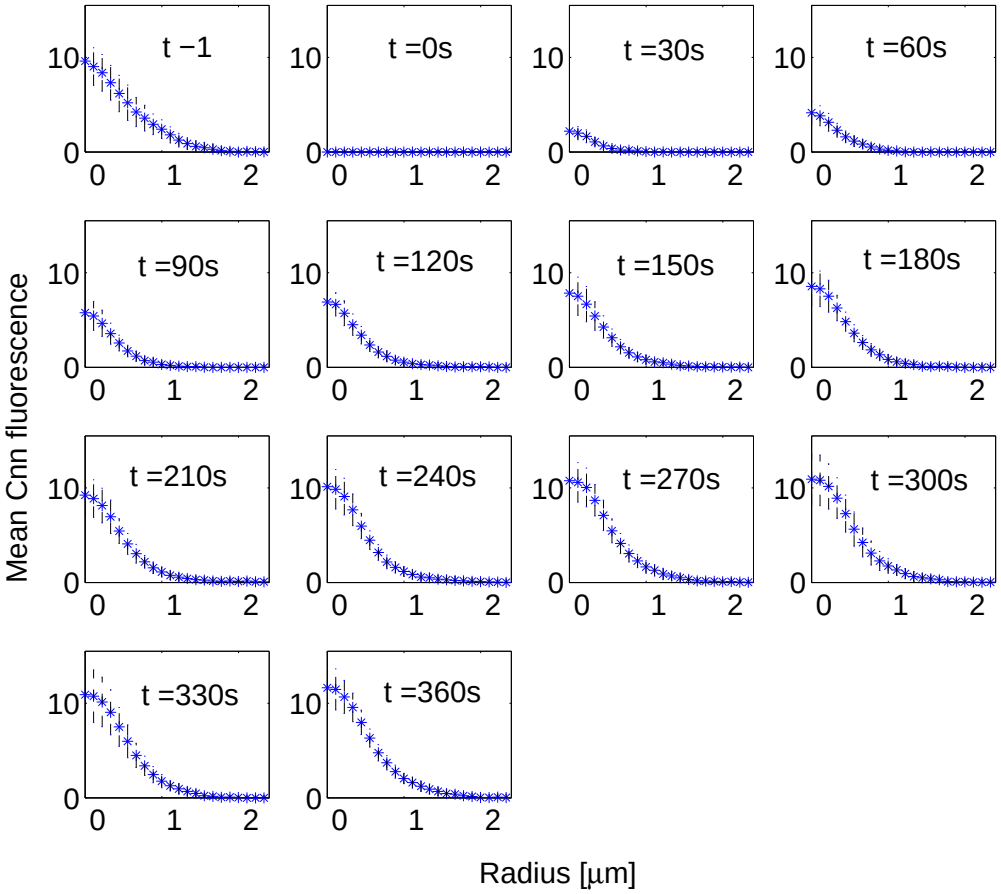

Figure 5.1: *Mean Cnn fluorescence (normalised in the same manner as described in Section 2.2) (blue asterisks) is shown for the pre-bleach time point* (t_{-1})*, just after bleaching at* t = 0 s *and at subsequent time points for which recovery is monitored. The Cnn recovery data is gathered from ten different embryos. Error bars denote the standard deviation.*

that in the case of the S-phase data Cnn moves radially outwards. For this reason we expect that fitting these data with the reduced receptor gradient model may provide a reliable estimate of the heavy Cnn diffusion coefficient (if heavy Cnn indeed undergoes diffusion, rather than advection). Figure 5.2(b) shows the FRAP curve for Cnn. We note that even after 360 seconds, the Cnn recovery curve does not begin to plateau.

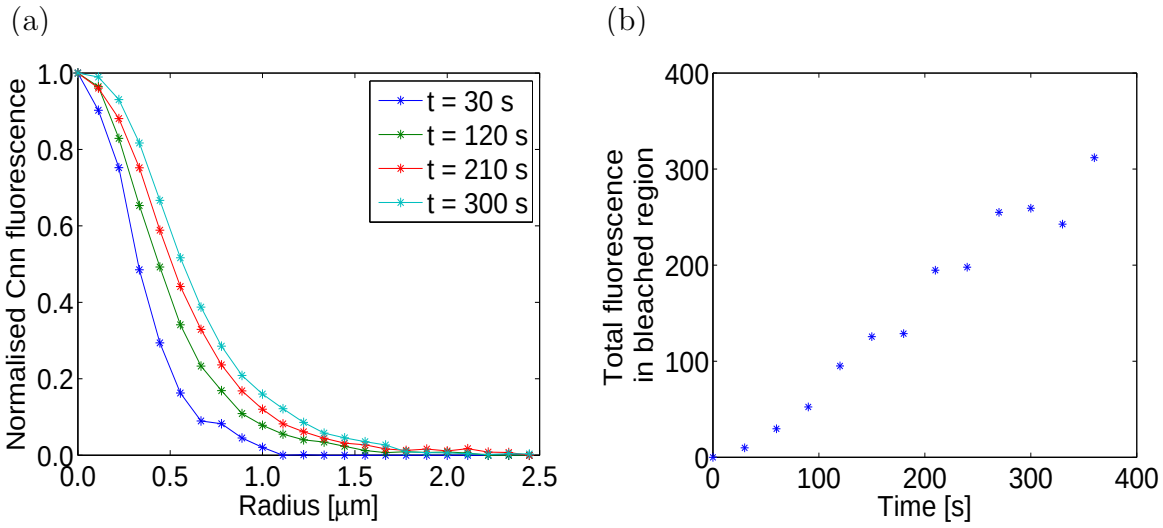

Figure 5.2: (a) *Mean Cnn recovery curves at selected time points, each normalised with the peak Cnn intensity at that time. It can be seen that the width of the Cnn gradient increases steadily with time.* (b) *Total Cnn fluorescence in the bleached region is plotted as a function of time. It can be seen that the recovery does not begin to plateau.*

5.2.1 DSpd2 data

Assuming that the preliminary DSpd2 data collected by our collaborators are not significantly compromised by the optical artifacts arising from the diffraction of light, we process them in a manner similar to the Cnn data. The DSpd2 data are gathered from 15 different centrosomes. Figure 5.3 shows the mean DSpd2 fluorescence and standard deviation for the time points corresponding to Cnn recovery time points. We fit the successive mean DSpd2 gradients using a separate Gaussian distribution, $P_{max}\exp(-p_{grad}r^2)$, at each time point. Figure 5.4 shows the best-fitting Gaussian distributions overlaid on the mean DSpd2 data. We find that the fitted parameters p_{grad} and P_{max} are not constant with respect to time, as would be expected if the DSpd2 distribution (and concentration) was constant throughout time.

Moreover, the fitted p_{grad} values (plotted in Figure 5.5(a)) describe a decreasing linear profile with respect to time. Thus, the width of the DSpd2 distribution continues in-

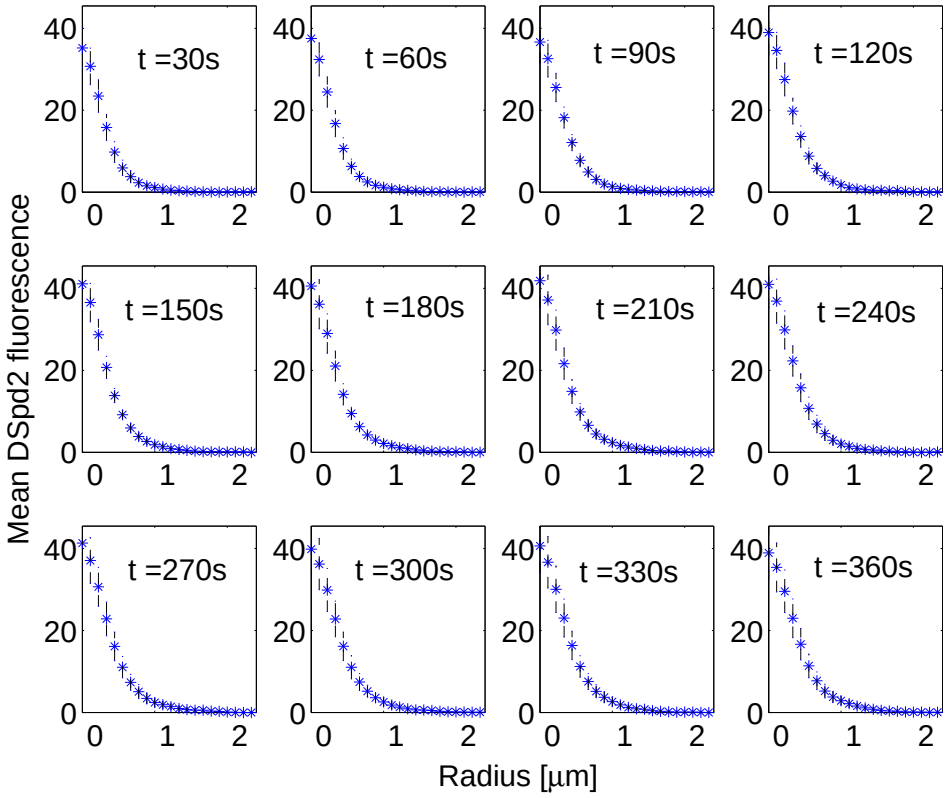

Figure 5.3: *Mean DSpd2 fluorescence (normalised in a similar manner to the Cnn data) (blue asterisks) for time points corresponding to recovery time points for which Cnn fluorescence is also measured. The DSpd2 data are gathered from 15 different embryos. Error bars denote the standard deviation.*

creasing with time. (Note that the width of the distribution is inversely proportional to the parameter p_{grad}). This phenomenon may occur if, for example, the DSpd2 in the centrosomes showed radially outward movement. The evolution of p_{grad} can be fitted with a linear dependence on time and is given as

$$p_{grad}(t) = 6.1 - 0.0071t. \tag{5.2.1}$$

Note that the relationship given by equation (5.2.1) predicts that p_{grad} will have negative values at very large time ($t > 860$ s). However, the DSpd2 (or Cnn) data are not gathered for such long time and it is not immediately obvious whether p_{grad} will

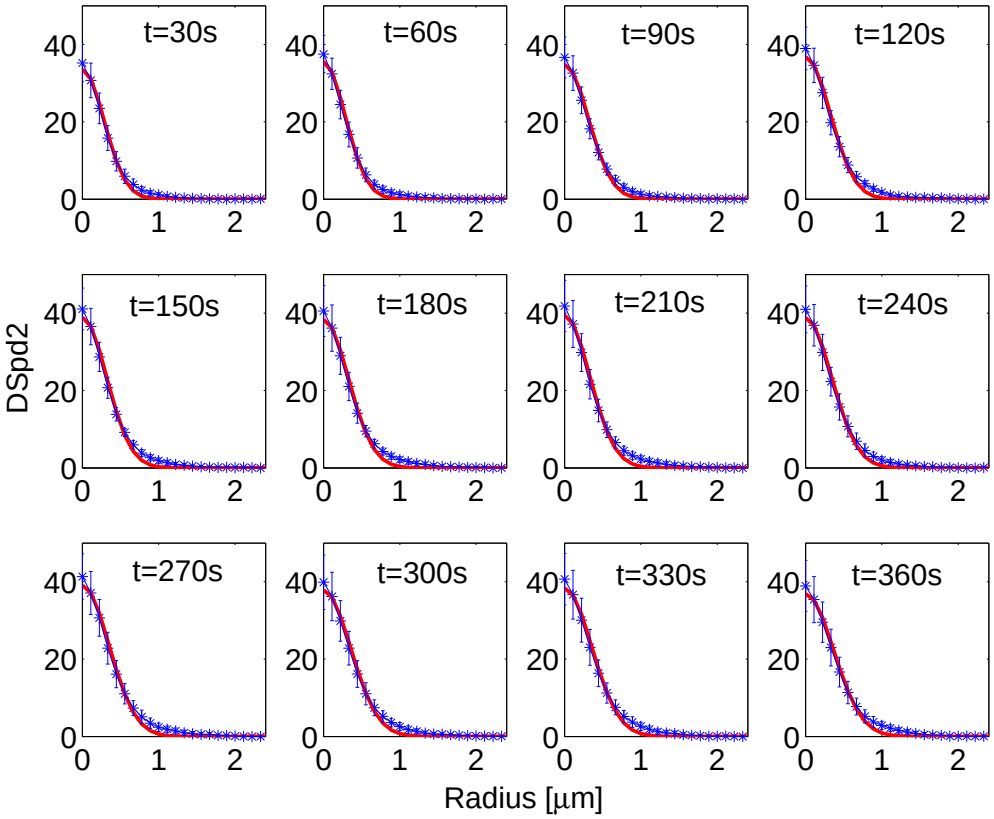

Figure 5.4: *The successive mean DSpd2 distribution profiles (blue asterisks) are each fitted with a separate Gaussian curve,* $P_{max}\exp(-p_{grad}r^2)$ *(red curves).*

continue to vary linearly with time at large times. Therefore, we do not worry about the negative values of p_{grad} for the purpose of our analysis. Also note that the peak DSpd2 concentration given by the parameter P_{max} exhibits a nonlinear dependence on time. We discuss the significance of these trends in subsequent sections. We acknowledge that the fit with the DSpd2 distributions is poor in the region close to $r = 1$ μm. Constructing a mechanistic model of how the DSpd2 profile is established and how it evolves may allow for a better fit. However, for the time being, we accept the fitted Gaussian profiles.

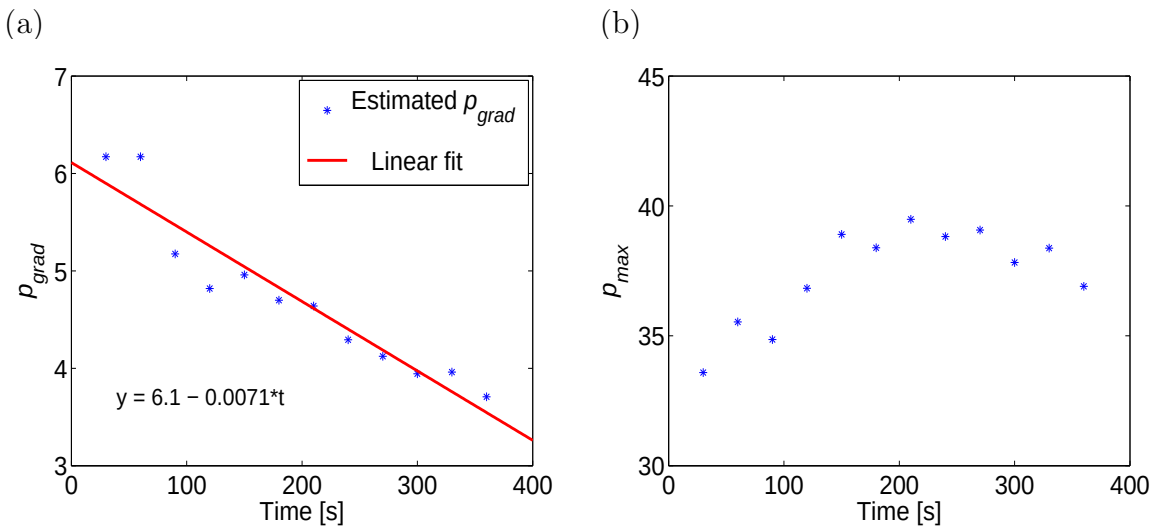

Figure 5.5: (a) *The best fitting p_{grad} values (blue asterisks) obtained from fitting the successive mean DSpd2 distribution profiles are plotted as a function of time. The evolution of p_{grad} shows a linear dependence on time, as the fitted line (red) shows. The equation for the best-fitting line is given.* (b) *The best fitting estimates of P_{max} describe a nonlinear relationship with respect to time.*

5.3 Fitting the receptor gradient model to S-phase Cnn FRAP data

Bleaching does not affect the concentration of nonfluorescent species, such as the free receptors. Therefore, in the case of the steady state FRAP data (used in previous chapters) the free receptor concentration is assumed to remain constant at steady state throughout the recovery process. This simplification allowed us to disregard the decay of bleached Cnn-receptor complex, leading to the regeneration of free receptors, as the free receptor concentration could be obtained from the steady state concentration of the free receptors. Since the Cnn incorporation process is not at steady state during the course of the S-phase FRAP experiment, this simplification cannot be used. Therefore, in the case of these data, we need to consider the decay of the bleached Cnn-receptor complex in order to simulate the recovery process. We present the relevant analytical solution for constant receptor concentration in Appendix E.

5.4 Results and discussion

Figure 5.6 shows the results of fitting the receptor gradient model to the S-phase FRAP data. Table 5.1 lists the parameter values estimated from the best fit. The goodness of fit estimators, namely RMSE and R^2 coefficients, are also listed. In this fit the parameter p_{grad}, which is a tuneable parameter, is assumed to be constant with respect to time. It can be seen that the fit is worse in the case of the initial recovery curves. This is because the predicted value of p_{grad} is such that the receptor gradient is wider as compared to the initial recovery curves, resulting in the prediction of slightly wider recovery curves for the initial time points. Also notice that the parameters $\overline{k_{on}}$ and P_{max}/L_{cyt} can be separately identified, as suggested by the confidence intervals for these parameters (Table 5.1). This is because the functional form of the time evolution of fluorescence in the case of non-steady FRAP involves the parameter $\overline{k_{on}}$ (equation (E.2.7)) (as compared to only k_{turn} in the steady state FRAP). Before commenting further on the parameter estimates, we present a fit using the receptor gradient information obtained from the DSpd2 data fit.

5.4.1 Fit using the evolution of receptor gradient

Figures 5.4 and 5.5 show that, in contrast to our previous assumption, the receptor gradient is not constant with respect to time. Both the width as well as the peak height of the receptor distribution change throughout the course of the experiment. Thus, it may be important that part of the Cnn gradient evolution during the recovery be attributed to the receptor gradient evolution.

We have shown in Figure 5.5(a) that the distribution of DSpd2, which is the Cnn receptor, widens with time (as indicated by the fitted p_{grad} parameter decreasing with time). This observation suggests that, like Cnn, DSpd2 also undergoes radial trans-

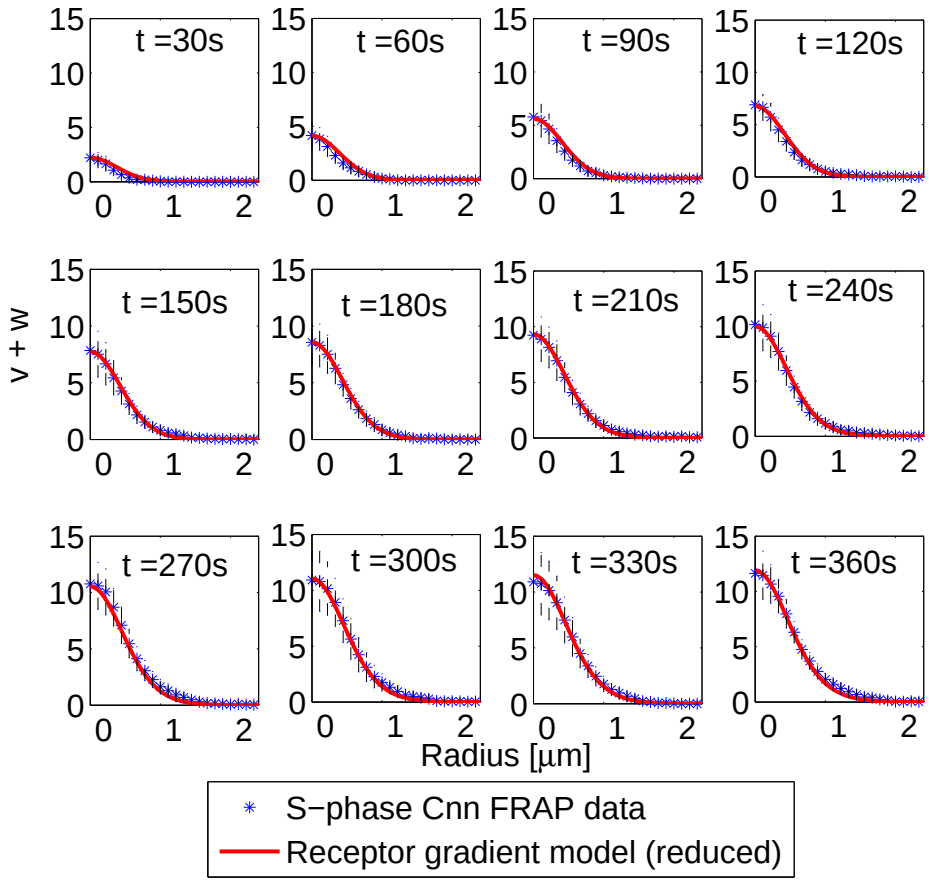

Figure 5.6: *Mean S-phase Cnn FRAP data (blue asterisks) are fitted with the reduced receptor gradient model* (E.1.1)-(E.1.6) *(red curves). The parameter p_{grad}, which parameterises the width of the receptor gradient, is a tuneable parameter. The evolution of p_{grad} in time is not considered. The error bars denote the standard deviation.*

port (either by diffusion or by advection). We could model the transport of DSpd2 in a similar manner to that of Cnn, obtain the diffusion coefficient (or advection velocity) for DSpd2 and use this mechanistic description for the evolution of the receptor gradient in modelling Cnn incorporation dynamics. However, for the time being, we restrict the mechanism of receptor gradient evolution to a phenomenological description. We know that p_{grad} evolves linearly with respect to time, as given by equation (5.2.1). We use this functional form for the evolution of the receptor gradient for the data fitting. Numerical solution of the FRAP evolution obtained using the Comsol

Table 5.1: Results of fitting the S-phase FRAP kinetics of Cnn with the recovery kinetics of $v + w$ given by the reduced receptor gradient model (E.1.1)-(E.1.6). Parameter estimates obtained from fitting, the RMSE values and the coefficients of determination R^2, are listed. 95% confidence intervals for the parameter estimates are also listed. Notice that p_{grad} is used as a tuneable parameter. The evolution of p_{grad} in time is not considered.

Parameters	**Avg data**	**95% Confidence Intervals**	**Units**
$\overline{k_{on}}$	0.0176	0.0003–0.035	s^{-1}
k_{turn}	0.1856	0.037–0.34	s^{-1}
D_N	0.0005	0.0005–0.0006	$\mu m^2\ s^{-1}$
P_{max}/L_{cyt}	5.7	0.76–10.64	-
p_{grad}	3.6673	3.6672–3.6675	μm^{-2}
RMSE	0.209	-	-
N	276	-	-
R^2	0.9955	-	-

Multiphysics software is used for the data fitting. Figure 5.7 shows the results of fitting the receptor gradient model (with evolution of p_{grad}) to the S-phase FRAP data. It can be seen that the fit is still worse in the case of the initial recovery curves, albeit in a different manner to the earlier fit (Figure 5.6). This may be because we have not considered the evolution of P_{max} for the fitting. Table 5.2 lists the parameter values estimated from the best fit. The goodness of fit estimators, namely RMSE and R^2 coefficients, are also listed. Note that we have only fitted four parameters in this instance, as the estimate for the fifth parameter, p_{grad}, has been obtained from the DSpd2 fits.

One may argue that the increase in the width of the Cnn distribution is solely due to the increase in the width of the DSpd2 gradient. If that were the case, it would be difficult to justify the very existence of the 'heavy Cnn' species, since the radial

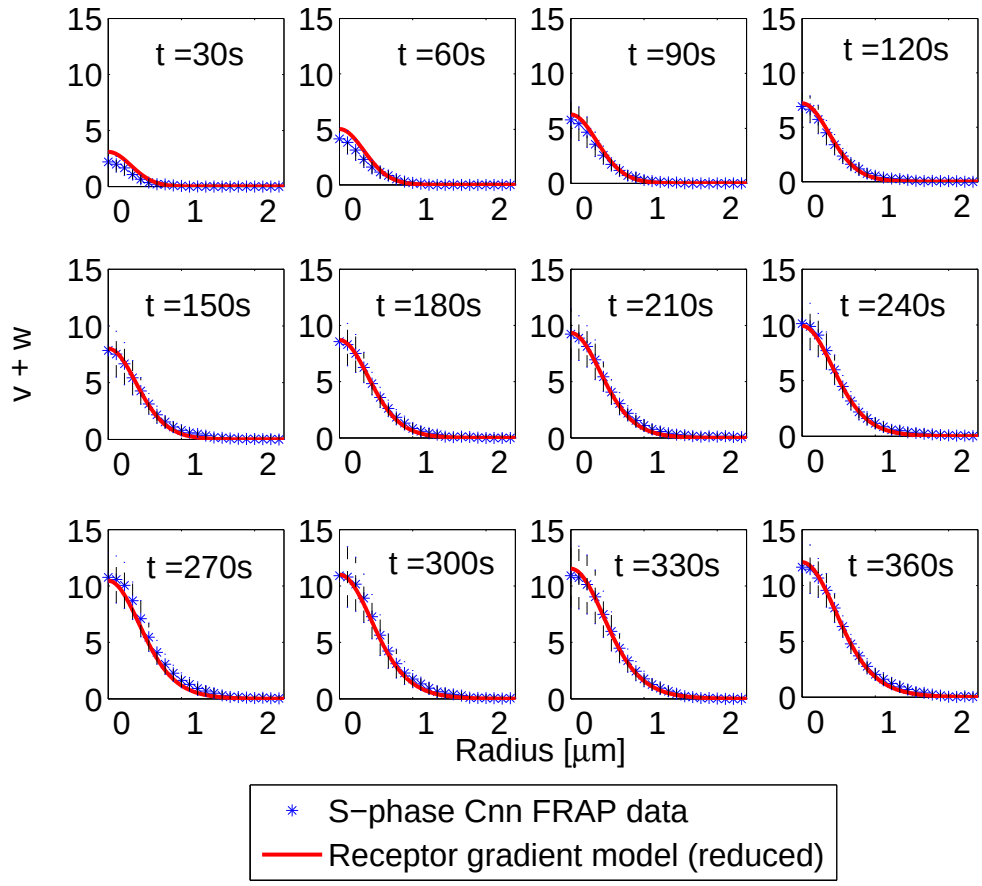

Figure 5.7: *Mean S-phase Cnn FRAP data (blue asterisks) are fitted with the reduced receptor gradient model* (E.1.1)-(E.1.6) *(red curves). The evolution of the parameter* $p_{grad}(t)$*, as given by equation* (5.2.1)*, is used. The error bars denote the standard deviation.*

movement of Cnn fluorescence could be explained by the radial movement of the Cnn-receptor complex. In Figure 5.8 we have overlaid the profiles of Cnn at the first and the last time point after bleaching and the corresponding profiles of DSpd2. Each of these profiles are normalised with their peak intensities so as to allow the comparison of only the widths of the distributions. The figure shows that the width of the first post-bleach Cnn distribution matches with that of the corresponding DSpd2 distribution, whereas the Cnn profile at the last post-bleach time point has a wider distribution as compared to the corresponding DSpd2 profile. Thus, we conclude that

Table 5.2: Results of fitting the S-phase FRAP kinetics of Cnn with the recovery kinetics of $v + w$ given by the reduced receptor gradient model (E.1.1)-(E.1.6). The evolution of the parameter $p_{grad}(t)$ as given by equation (5.2.1) is used. Parameter estimates obtained from fitting, the RMSE values and the coefficients of determination R^2, are listed. 95% confidence intervals for the parameter estimates are also listed.

Parameters	**Avg data**	**95% Confidence Intervals**	**Units**
$\overline{k_{on}}$	0.029	0.0272–0.0309	s^{-1}
k_{turn}	0.2133	0.1321–0.2946	s^{-1}
D_N	0.0009	0.0008–0.0009	$\mu m^2\ s^{-1}$
P_{max}/L_{cyt}	5.69	5.227–6.15	-
RMSE	0.2608	-	-
N	276	-	-
R^2	0.993	-	-

the radial movement of Cnn receptors is not sufficient to explain the radial movement of the Cnn fluorescence, and that a 'heavy Cnn' species is required to explain the movement.

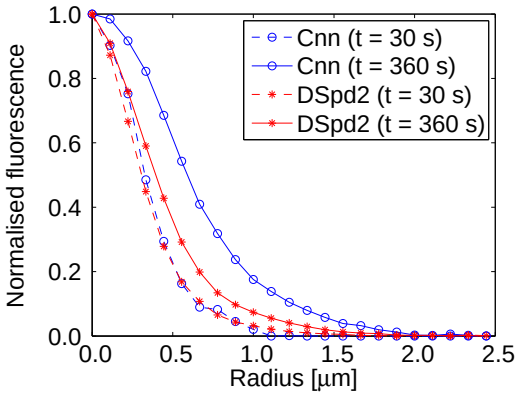

Figure 5.8: *The first and the last mean Cnn and mean DSpd2 profiles are plotted, each normalised with respect to the peak intensity of the respective species at the time. It can be seen that the initial Cnn distribution closely approximates the DSpd2 distribution. However, with increasing time, the Cnn distribution becomes wider than the DSpd2 distribution at the corresponding time.*

5.4.2 Comments on parameter estimates

We have already mentioned that the non-steady state FRAP experiment allows the parameters k_{on} and P_{max}/L_{cyt} to be separately identified. This was not possible using the steady state FRAP experiment. The estimated value of D_N is slightly higher in the case of the fit with p_{grad} obtained from the DSpd2 gradient (Table 5.2), as opposed to the fit with p_{grad} as a tuneable parameter (Table 5.1). This occurs for the following reason. We have allowed p_{grad} to be obtained directly by fitting the Cnn data in a model assuming that the receptor gradient is constant with respect to time (Table 5.1). This predicted value of p_{grad} is smaller than that obtained from fitting the DSpd2 distribution at the initial times, i.e. the predicted receptor distribution is wider than the actual receptor distribution at initial times. Thus, Cnn must diffuse to a lesser extent in order to explain the width of the Cnn distribution in this case. Whether we accept one diffusion coefficient or the other (or neither) depends upon whether Cnn is solely diffusively transported. We attempt to answer this question in Section 5.6. We also note that the value of k_{turn} predicted in the case of the S-phase data is much higher as compared to that predicted for the steady state FRAP (Table 4.3). We argue that the value of k_{turn} may be modified by the cells (or nuclei) as they progress from S-phase to mitosis because of the associated change in microtubular dynamics. We justify this argument after we have established whether Cnn is transported by advection (along microtubules) or pure diffusion or both.

5.5 The colchicine experiment

Colchicine is a drug commonly used in cell biology for studying the cell cycle. The drug works by blocking microtubule polymerisation by binding to tubulin monomers. Traditionally this drug has been used to study cells/chromosomes by arresting cells in mitosis. We utilise the drug to assess the role of microtubules in the movement of

Cnn around the centrioles. The hypothesis is that if the incorporated Cnn undergoes pure diffusion, altering microtubule dynamics should not alter the radial movement of Cnn. It is clear that if blocking microtubules reduces the radial movement of Cnn, then diffusion is not the only method of Cnn transport, and that Cnn may undergo advection along microtubule tracks (see Figure 1.2 for a schematic representation of microtubule distribution in the centrosomes, and Figure 3.11 for a hypothesised advection mechanism of Cnn along microtubules).

Our collaborators inject colchicine into the growing syncytial embryos expressing GFP-Cnn at the end of a nuclear division cycle (i.e., at the beginning of the S-phase of the next cycle). Even though colchicine arrests the nuclei in mitosis, it allows progression through S-phase to the mitotic stage. As the nuclei progress through S-phase, data are captured in exactly the same manner as described in Section 5.1. Embryos expressing GFP-DSpd2 are similarly treated with colchicine and the profiles of DSpd2 are captured at time points corresponding to the Cnn recovery time points. We process these data as mentioned in Section 2.2. The various aspects of the processed data are presented in Appendix F. It can be seen that, in the case of this experiment as well, the estimated values of p_{grad} vary linearly with time (Figure F.3) as given by

$$p_{grad}(t) = 6 - 0.006t. \tag{5.5.1}$$

Note that the evolution of $p_{grad}(t)$ in the case of the colchicine experiment (5.5.1) is slightly different to that obtained from the experiment without colchicine (5.2.1). (We reiterate that more experiments may be required to determine whether the optical artifacts are exaggerating the DSpd2 gradients). Also note that as in the case of the experiment without colchicine, the equation (5.5.1) predicts negative values of p_{grad} for large times ($t > 1000$ s). However, we are not concerned with the large time values of p_{grad} since we do not have data for the corresponding time points, and we

cannot establish whether the linear relationship of p_{grad} with respect to time will hold for large times. We use the functional form of $p_{grad}(t)$ given by equation (5.5.1) for fitting the data from the colchicine experiment.

5.6 Results and discussion

The S-phase FRAP experiment without colchicine presented earlier in this chapter provides the control data set for the colchicine experiment. In Figure 5.9(a) we overlay the Cnn profiles from this control experiment (no colchicine) and the colchicine experiment, each normalised with the respective peak heights. The figure shows that Cnn distributions increase in width even in the presence of colchicine. It also shows that the radial movement of Cnn is less in the presence of colchicine than in the absence of it. This shows that microtubules play a role in the radial movement of Cnn, and diffusive processes may not be sufficient to explain the Cnn movement in the presence of microtubules. Figure 5.9(b) shows that even though the DSpd2 distributions also increase in width in the colchicine experiment, the Cnn distribution cannot be completely explained by the DSpd2 gradients and a component of Cnn movement (other than the DSpd2 movement) is necessary to explain Cnn movement in the absence of microtubules.

The radial movement of Cnn fluorescence in the absence of microtubules may be attributed to a diffusive process. Thus, we use the reduced receptor gradient model, which incorporates the heavy Cnn diffusion process, to fit the Cnn FRAP data from the colchicine experiment. We expect that since these data only contain a diffusible Cnn species (and not an advecting Cnn species in addition) the estimate of the parameter D_N may be different as compared to the previous estimate in Table 5.2. As before, we use the functional form of the parameter $p_{grad}(t)$ obtained from fitting

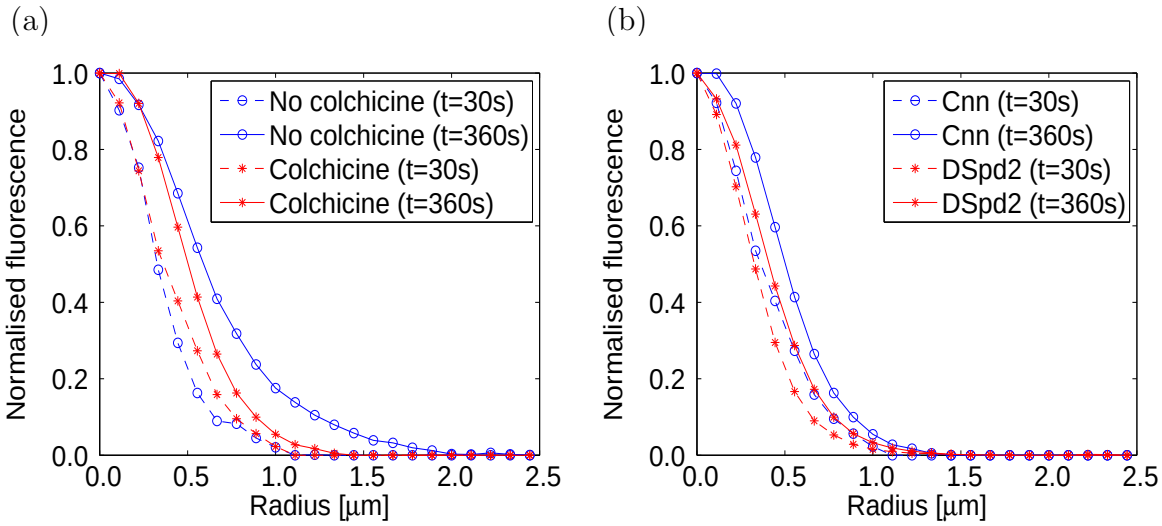

Figure 5.9: (a) *Mean Cnn fluorescence immediately post-bleaching (dashed lines) and at a later time point post-bleaching (solid lines) for the control (no colchicine) experiment (circles) and with colchicine experiment (asterisks), each normalised with the respective peak intensity. It can be seen that the Cnn profiles widen less in the presence of colchicine.* (b) *Mean Cnn profiles (circles) and mean DSpd2 profiles (asterisks) at the first post-bleach time point (dashed lines) and the last one (solid lines), each normalised with the respective peak intensities. It can be seen that even in the presence of colchicine Cnn profiles grow wider than the DSpd2 profiles, thus, microtubular transport is not a complete explanation of Cnn movement.*

the DSpd2 gradients obtained in the colchicine experiment (equation (5.5.1)). Figure 5.10 shows the results of the fitting. The best-fitting parameter estimates obtained from the fit are listed in Table 5.3, along with the goodness of fit estimators, namely the RMSE value and R^2 coefficient. 95% confidence intervals for the parameter estimates are also listed. It can be seen that the estimate for D_N is only slightly lower in this case as compared to the control data (Table 5.2). Thus, the diffusion coefficient estimated from the purely diffusive process (i.e. from the colchicine experiment) is similar to that estimated from the control experiment, where both diffusive and advective processes operated. However, we accept the diffusion coefficient D_N estimated using the colchicine experiment since colchicine is expected to have inhibited the advective transport. The estimate for P_{max}/L_{cyt} is higher in the case of the colchicine

data. This is expected, considering that the peak intensities of DSpd2 in the case of the colchicine data are higher than those in the case of control data (see Figures 5.5(b) and F.3(b)). It is also noted that the value of the parameter k_{turn} is lower than in the control case (Table 5.2). We present the argument for the variability of the k_{turn} estimates from the mitosis data (Chapter 4) to S-phase control data (i.e. the experiment without colchicine) to the colchicine experiment data in Section 5.6.3.

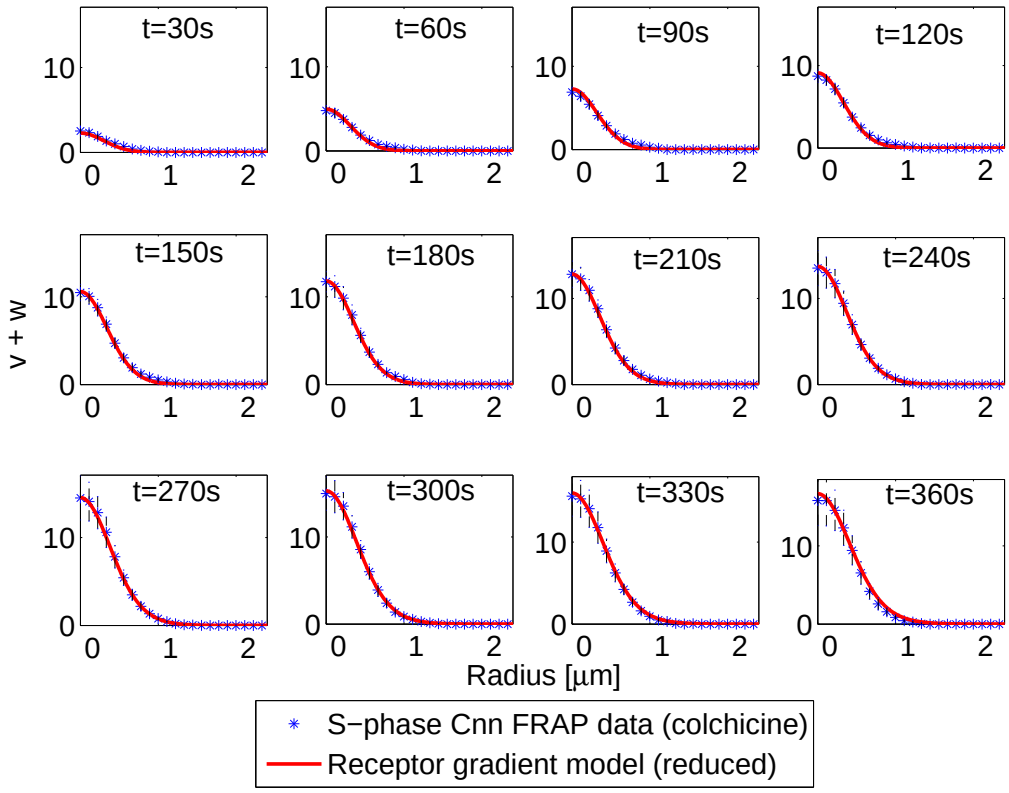

Figure 5.10: *Mean S-phase Cnn FRAP data from the colchicine experiment (blue asterisks) are fitted with the reduced receptor gradient model* (E.1.1)-(E.1.6) *(red curves). The evolution of the parameter* $p_{grad}(t)$ *as given by equation* (5.5.1) *is used. The error bars denote the standard deviation.*

5.6.1 Flaring

The peri-centriolar matrix, PCM, has previously been shown to eject chunks of proteinaceous matrix, called flares. Cnn is known to be a chief component of these flare

Table 5.3: Results of fitting the S-phase FRAP kinetics of Cnn from the colchicine experiment with the recovery kinetics of $v+w$ given by the reduced receptor gradient model (E.1.1)-(E.1.6). The evolution of the parameter $p_{grad}(t)$ as given by equation (5.5.1) is used. Parameter estimates obtained from fitting, the RMSE values and the coefficients of determination R^2, are listed. 95% confidence intervals for the parameter estimates are also listed.

Parameters	**Avg data**	**95% Confidence Intervals**	**Units**
$\overline{k_{on}}$	0.0171	0.011–0.0231	s^{-1}
k_{turn}	0.029	0.0235–0.0345	s^{-1}
D_N	0.0005	0.0004–0.0005	$\mu m^2\ s^{-1}$
P_{max}/L_{cyt}	10.98	8.117–13.85	-
RMSE	0.1807	-	-
N	276	-	-
R^2	0.9981	-	-

particles. As mentioned in Chapter 1, the flare particles are believed to travel along the astral microtubules (Megraw et al., 2002). Thus, it is known that microtubules play a role in the movement of large chunks of the PCM material containing Cnn. However, while gathering the data we have excluded any obvious flare particles. Thus, the microtubule-dependent movement of Cnn observed in the data is not the same as flaring. However, it is likely that flaring is initiated by this initial movement of Cnn along the microtubules.

5.6.2 Sensitivity analysis

Drosophila neuroblasts actively control the incorporation of Cnn into the two daughter centrosomes, such that one of the centrosomes accumulates more Cnn than the other, thereby resulting in the division of neuroblasts into two unequal daughters (Conduit and Raff, 2010). We are interested in understanding how a change in the parameter values of the model may affect the predictions of the model. This infor-

mation may be useful in understanding the best mechanism for changing the amount of Cnn incorporation in the centrosomes.

Sensitivity analysis is used to determine how sensitive a model is to changes in the values of the parameters of the model and to changes in the structure of the model. Parametric sensitivity is usually performed as a series of tests in which parameter values are varied, one at a time, to see how the model output changes. Several methods have been proposed for sensitivity analysis of mathematical models (Saltelli et al., 2006). For this analysis we use the normalised gradient method, which is a slight modification of the original method of Morris (1991). We calculate the sensitivity index, S_{ij}, for parameter j and output i as

$$S_{ij} = \frac{P_j}{X_i} \frac{\partial X_i}{\partial P_j}, \tag{5.6.1}$$

where P_j is the value of the j^{th} parameter, X_i is the value of i^{th} output and $\partial X_i/\partial P_j$ represents the change in X_i with respect to a small change in P_j when all other parameters except for P_j are kept constant at their original value in the model. Table 5.4 lists the sensitivity of the total fluorescence $(v + w)$ predicted by the reduced receptor gradient model with respect to the parameters of the model. It can be seen that the model is most sensitive to the change in parameter P_{max}/L_{cyt}, whereas it is least sensitive to changes in the parameter k_{turn}.

5.6.3 The parameter k_{turn}

The reduced receptor gradient model, which does not take into account the advection of heavy (or altered) Cnn is given by the reactions (4.10.1). However, now that we have established that a component of the Cnn fluorescence advects (apart from the

Table 5.4: Sensitivity indices with respect to each fitted parameter value in the reduced receptor gradient model (E.1.1)-(E.1.6).

Parameters	**Sensitivity index**
$\overline{k_{on}}$	0.87
k_{turn}	0.19
D_N	0.48
P_{max}/L_{cyt}	0.99

diffusing component), we need to modify these reactions as follows:

$$P \xrightarrow{\overline{k_{on}}} C, \qquad C \xrightarrow{k_{turn1}} P + N_1, \qquad C \xrightarrow{k_{turn2}} P + N_2, \tag{5.6.2}$$

where $\overline{k_{on}} = k_{on}L_{cyt}$, N_1 denotes the slow diffusing heavy Cnn species, N_2 denotes the advecting altered Cnn species and k_{turn1} and k_{turn2} denote the respective rate constants for generation of these two species from the Cnn-receptor complex. It is conceivable that, since advection is dependent on microtubules, the value of the parameter k_{turn2} depends upon the presence of intact microtubular structure. Thus, $k_{turn2} = k^*_{turn2}M$, where M is the concentration of functional microtubules. (Note that the term 'functional' here signifies that microtubular structure which is capable of advecting Cnn). $M \to 0$ in the presence of colchicine and therefore the value of $k_{turn2} \to 0$. (Note that we cannot be certain that colchicine destroys all of microtubular structure). The parameter k_{turn} in the case of the reduced receptor gradient model (which does not take into account a separate advecting Cnn species) is such that $k_{turn} = k_{turn1} + k_{turn2}$. This may be the reason for the different estimates of the parameter k_{turn} in the presence and absence of colchicine. Another piece of evidence comes from fitting of the mitosis data. At mitosis, the microtubules are far less functional as compared to during S-phase, as evidenced by a significant reduction in flaring activity. The value of the parameter k_{turn} estimated from the fit to the

mitosis data (Table 4.3) is lower than that estimated from the S-phase data (Table 5.2), which appears consistent with the hypothesis that active microtubules may play a role in the conversion of the Cnn-receptor complex into altered Cnn (via the parameter k_{turn2}). Also note that the model is least sensitive to the parameter k_{turn} (Table 5.4), which means that a large change in the value of the parameter k_{turn} may be necessary to observe an appreciable change in the behaviour of the model.

5.7 Summary

In this chapter we have used the reduced receptor gradient model to fit the non-steady FRAP data gathered during S-phase of the cell cycle. Using non-steady FRAP has allowed us to estimate the parameters $\overline{k_{on}}$ and P_{max}/L_{cyt} separately, which was not possible with the steady state data (Chapter 4). Simultaneous observation of DSpd2 gradients has enabled us to use the receptor gradient information for the data fitting. (Note that further experiments are necessary to establish whether the DSpd2 gradients observed in the preliminary experiments are true gradients or whether they are exaggerated by optical artifacts. Should we discover the latter to be true, further data fitting with the corrected DSpd2 gradients will be necessary). We have learned that the Cnn fluorescence moves radially outwards during S-phase. Through the colchicine experiment we have learned that part of the Cnn movement is microtubule-dependent, while a noticeable proportion is microtubule-independent. Since the microtubule-independent component of movement may occur through diffusion, we have used the data from the colchicine experiment to gauge the diffusion coefficient of the heavy Cnn. We have found that the estimated diffusion coefficient from the colchicine data is not widely different to that estimated from the control data.

We have also hypothesised that the reaction denoted by the parameter k_{turn} may,

in reality, be a combination of two reactions (one in which a diffusible, heavy Cnn species is generated and one in which an advecting Cnn species is generated from the Cnn-receptor complex). We have argued that the component of k_{turn} responsible for generating the advecting Cnn species may be dependent on the presence of functional microtubules. We have not constructed a full model of Cnn incorporation that includes diffusion as well as advection. Considering the dynamic nature and distribution of microtubules, modelling the advection process appropriately is challenging. Moreover, we have shown that advection does not play a major role in Cnn transport. Therefore, we continue to use the description of Cnn incorporation that contains only diffusive transport, with the knowledge that advection also plays a role.

Sensitivity analysis has shown that the model is most sensitive to the parameters P_{max}/L_{cyt} and $\overline{k_{on}}$. Thus, if the reduced receptor gradient model can be shown to be valid for Cnn incorporation in the *Drosophila* neuroblasts, we could argue that the neuroblasts could be altering either (or both) of these parameters in order to control the amount of Cnn incorporation in the two centrosomes. Whether the alterations in P_{max}/L_{cyt} are used for this control can be easily tested experimentally through the use of GFP-DSpd2 in the neuroblasts. Testing whether any other parameters are altered may require collection of FRAP data and fitting to the appropriate model.

We have established that the reduced receptor gradient model is a valid model for describing the Cnn incorporation process during mitosis, as well as S-phase, in *Drosophila* syncytial embryos. This model can now be used, along with various FRAP data, to assess how the various mutants of the Cnn gene (or the DSpd2 gene) affect the Cnn incorporation dynamics. The analysis of this can be useful in building a molecular level understanding of the various players in the centrosome maturation dynamics.

Chapter 6

Conclusions and future work

We mentioned in Chapter 1 that Cnn is an integral component of centrosomes. This protein is conserved across various species. The human orthologue of Cnn protein (CDK5RAP2) is believed to function in enlargement of the human brain during development, since a mutation in this gene leads to microcephaly (Megraw et al., 2011). *Drosophila* embryos without functional Cnn fail to develop (Megraw et al., 1999; Vaizel-Ohayon and Schejter, 1999) and adult *Drosophila* without functional Cnn show defects in the asymmetric stem cell divisions in neuroblasts and mGSCs (Yamashita et al., 2007; Castellanos et al., 2008; Gonzalez, 2008). It has been hypothesised that this asymmetric division function of Cnn may be crucial for human brain development as well (Gonzalez, 2008). *Drosophila* neuroblasts control the asymmetric division by controlling the size of the PCM organised by each centriole pair. Conduit et al. (2010) have shown that the amount of Cnn incorporated in the centrosomes determines the size of the centrosomes. Thus, control of the Cnn incorporation process may lie at the heart of the control of asymmetric stem cell division in *Drosophila* neuroblasts.

Our collaborators have used the FRAP technique to study the incorporation of Cnn into the centrosomes (Conduit et al., 2010). They have shown that Cnn displays

peculiar fluorescence recovery dynamics that hint at a possible Cnn incorporation mechanism. It was believed that Cnn may only be incorporated closest to the mother centriole and spread radially to form a gradient in the centrosome. In this work we set out to construct Cnn incorporation models and, thereby, determine the mechanism of Cnn incorporation in the centrosomes of *Drosophila* syncytial embryos. In particular, we wished to establish whether the model of Cnn incorporating only closest to the centriole and spreading outwards is a valid description and whether this spread of Cnn in the centrosome occurs by diffusion or by advection or both.

6.1 Data collection

Traditionally, FRAP experiments are conducted on systems at steady state. We wished to do the same for the case of Cnn. As such, we performed FRAP experiments during mitosis in syncytial embryos, since Cnn fluorescence had been observed to remain steady during mitosis. With our collaborators we devised an experimental strategy for gathering fluorescence data useful for data fitting.

6.2 Preliminary models

One of the crucial unknowns in the modelling effort was the distribution of Cnn receptors. Working with the hypothesis that Cnn only incorporates closest to the centrioles, we began by constructing two different models, namely the diffusion model and the advection model. In both these models we assumed the existence of an impermeable, spherical, infinitesimally thick receptor shell around the mother centriole. The cytoplasmic (or free) Cnn is assumed to diffuse into the centrosomes and bind to the receptor shell, forming the Cnn-receptor complex. We then postulated that the Cnn-receptor complex may dissociate to produce a new Cnn species, called heavy (or altered) Cnn. The existence of this third Cnn species has been postulated by our

collaborators (Conduit et al., 2010), although isolating and characterising this species to prove its existence may not be trivial. The diffusion and advection models differed in the mechanism of transport of this new Cnn species, with the former model using the diffusion process, while the latter model uses advective transport. After fitting both these models to Cnn FRAP data we found that the diffusion model fits the data slightly better than the advection model. However, neither of the fits were adequate. Not only were we unable to fit the data at radii smaller than the radius of the binding shell (because of the model geometry) but the fit with the remaining data showed systematic errors. These preliminary models thus showed that one or more assumptions may be wrong and the 'infinitesimally thick binding shell' may not be an appropriate description of the receptor geometry.

6.2.1 The detailed geometry diffusion model

It had been postulated that the protein Asl may act as a receptor for Cnn (Conduit et al., 2010). Prof. Jordan Raff's laboratory had shown that Asl is distributed as a hollow cylinder around the mother centriole, and the cylinder walls have finite thickness (Figure 3.20). We believed that this may be a more accurate description of Cnn receptor distribution and used this detailed receptor geometry to model Cnn incorporation. The dimensions of the receptor cylinder were extracted from experimental observation of the Asl distribution. This model, however, showed a worse fit with the data than the previous two models.

This would appear as a backward step, except that the manner in which the detailed geometry model behaved provided clues about improving the model. It became apparent that the binding region and the region where Cnn merely diffuses (or advects) are not easily separable, and may show a larger overlap than had previously been thought. This prompted us to consider that the receptors may be distributed over a

larger domain, rather than being present only closest to the centrioles. This suggestion was counterintuitive considering the visual observations of Cnn FRAP recovery images, as well as being contrary to the initial ideas of our collaborators.

6.3 Lessons from the data

Further support for the possibility of a wider receptor distribution was afforded by the data (gathered during mitosis). We developed a plotting technique whereby we could separate the increase in the peak fluorescence intensity from the increase in the width of the fluorescence distribution of Cnn. This was achieved by normalising the peak intensity of the fluorescence curves at each time point to one. Overlaying the normalised curves thus obtained allowed us to compare only the widths of the curves (separate from their peak heights). When this technique was applied to mitosis FRAP data we learned that the increase in the widths of successive recovery curves is imperceptibly small, if any. Thus, we established that the radial movement of Cnn, if any, is minimal. (The visual observation of radial movement of Cnn from the FRAP movies may be an illusion created by Cnn concentrations at larger radii being initially too low to be visible, and the increase of these concentrations to visible levels creating the illusion of radial movement). This led to the hypothesis that the recovery distribution at the initial time points may arise due to binding of Cnn to a pre-existing receptor distribution. We further learned that the Cnn distribution at each time point could be well-described by a Gaussian distribution. Thus, we hypothesised that the Cnn receptors may also show a Gaussian distribution.

6.4 Simpler receptor geometries are inadequate

We had considered two receptor geometries in Chapter 3, namely the infinitesimally thick receptor shell and the thick-walled hollow cylinder. In Chapter 4 we showed

that several conceivable simple receptor geometry models were unable to reproduce the Gaussian distribution of Cnn. This exercise underscored the need for a Gaussian distributed receptor gradient.

6.5 The receptor gradient model

With the Cnn receptors in a Gaussian distribution, we were able to fit the Cnn mitosis FRAP data well. Not only did we eliminate the systematic errors in the fits with the previous models, but we also used all the available data for fitting (rather than excluding the data near the origin). The fitting exercise also allowed us to estimate the parameters describing the width of the receptor distribution.

6.5.1 Experimental validation

Our collaborators had previously shown that Asl or DSpd2 or both can act as Cnn receptors (Conduit et al., 2010). They made preliminary observations of the GFP-Asl distribution as well as the GFP-DSpd2 distribution in the centrosomes at mitosis. We found that the receptor distribution predicted by our mathematical model exactly matched with the experimentally observed DSpd2 distribution in the preliminary experiments. Not only did this provide experimental support for our receptor gradient model, but, together with previous biochemical analyses (Conduit et al., 2010) we were also able to provide further support for the role of DSpd2 as the Cnn receptor.

Reducing the receptor gradient model allowed us to reduce the number of parameters in the model, which then allowed us to obtain parameter estimates with greater confidence. Using the reduced model we showed that we can reliably estimate four parameters from the mitosis data fitting. The estimation of D_N, however, is suspect since we do not observe any perceptible Cnn movement in the recovery curves. The

estimation of D_N depends only upon the pre-bleach state (which is the steady state), which is wider than the recovery curves (Figure 4.1). The lack of movement during recovery meant that distinguishing between Cnn transport mechanisms was not possible using these data. Moreover, one could even question the existence of the third Cnn species (the first two being the cytoplasmic Cnn and the Cnn-receptor complex) that is proposed to undergo radial transport. We answered these questions through the use of S-phase data.

6.6 S-phase data

As in the case of mitosis, our collaborators collected Cnn FRAP data during S-phase in *Drosophila* syncytial embryos. The aim of this experiment was to observe Cnn recovery for longer times so as to allow the correct estimation of the radial movement of Cnn, if any. Using the plotting technique mentioned above we established that Cnn shows appreciable movement during S-phase and that this movement is greater than the movement shown in mitosis during the same time period. This already suggests that different mechanisms may govern Cnn movement during S-phase and mitosis.

Using the knowledge that DSpd2 is the receptor for Cnn, our collaborators monitored the fluorescence of GFP-DSpd2 in *Drosophila* embryos at times corresponding to the S-phase Cnn FRAP time points. These data showed that the receptor gradient also evolves during S-phase. We were able to use the information about the evolution of the receptor gradient to fit the FRAP data and obtain parameter values. If further experiments demonstrate that the DSpd2 gradient is, in part, attributable to the optical artifacts then more data-fitting work using the corrected DSpd2 gradient will be necessary.

Moreover, we conducted experiments with colchicine to establish whether microtubules have a role in the transport of Cnn. These experiments showed that Cnn movement during S-phase depends partially upon the existence of functional microtubules. Thus, a proportion of Cnn does undergo advection via the microtubules. This experiment also showed that a significant proportion of Cnn movement could still be attributed to diffusion (or non-microtubule-dependent transport mechanisms). The different estimates of the parameter k_{turn} showed that the functional microtubules may affect the rate of the reaction converting Cnn-receptor complex into the altered Cnn. Sensitivity analysis showed that the model is most sensitive to the concentration of the Cnn-receptor DSpd2.

6.7 Cnn incorporation model

Determining the mechanism of Cnn incorporation was one of the major aims of this work. Using data from S-phase as well as mitosis, and going through several rounds of model refinements, we have arrived at a mechanistic description of Cnn incorporation. The complete Cnn incorporation model can be described as below.

1. Cytoplasmic Cnn is a fast diffusing species and is uniformly distributed in the syncytium. This species diffuses into the centrosome and leads to concentration profiles of Cnn in the centrosomes via the following reactions:

   (a) DSpd2 is the receptor for Cnn and is distributed in the form of a Gaussian distribution around the mother centriole. (The mechanism of how DSpd2 distribution evolves is as yet undetermined and is briefly considered in Section 6.8.2);

   (b) binding of Cnn to DSpd2, thereby creating the Cnn-receptor complex, generates the initial Cnn distribution profiles.

2. The Cnn-receptor complex may dissociate to produce heavy Cnn, a species that diffuses more slowly as compared to cytoplasmic Cnn, and altered Cnn, a species that advects along the microtubules. The rate of formation of altered Cnn depends upon the existence of functional (or active) microtubules. These dissociation processes are greately slowed during mitosis, which may explain the lack of Cnn movement observed during mitosis.

Thus, we now have a mechanistic understanding of the Cnn incorporation process. In theory we could construct a mathematical model of Cnn incorporation that includes both the advective as well as the diffusive transport terms. However, modelling the advective process is complicated for the following reasons. Firstly, we do not yet know exactly how the microtubules assist the advection of Cnn. It is possible that Cnn is transported by microtubular motors, which can carry cargo towards the microtubule plus-ends (radially outwards) as well as minus-ends (radially inwards). It is also possible that Cnn associates with the plus-ends of microtubules and the transport results from the polymerisation of microtubules. Flaring has been shown to occur in this manner (Megraw et al., 2002). Secondly, the distribution and lengths of microtubules around the centrioles (let alone the distribution of plus-ends) cannot be easily determined. This introduces several unknowns in the advection process and makes the exercise unhelpful. Even though we have not modelled the advective process explicitly we have been able to determine the existence and the extent of it, which suffices for our purpose. We have summarised this Cnn incorporation model in a co-authored paper (Conduit et al., submitted).

6.8 Future work

We believe that this is the first application of spatially resolved FRAP in model selection and parameter estimation, as well as being the first mechanistic description

of the Cnn incorporation process. In this section we discuss the future research opportunities for this problem, with respect to the dissemination of the results, as well as further research.

6.8.1 Publication plan

The results from this work are relevant to the field of centrosome biology. We have submitted a manuscript with the experimental results (Conduit et al., submitted). In future we will submit a manuscript with mathematical results from this work, including the necessity for the Gaussian distribution of receptors, as well as the preliminary experimental validation for the same (Bakshi et al., in preparation). We have secured a grant for three months from the Platform grant fund (Engineering and Physical Sciences Research Council [grant number EP/I01893X/1]) for the preparation of manuscripts as well as for further research work on this project (outlined in the next section).

6.8.2 Future research

As mentioned in Chapter 1, newly formed centrioles begin to accumulate PCM in a process known as centrosome maturation. Maturation is crucial for centrosome function. Little is known about the pathway of centrosome maturation or PCM assembly. Having elucidated the mechanism of Cnn incorporation, we can now use the same strategy of FRAP experiments combined with mathematical modelling to uncover further centrosome maturation mechanisms.

6.8.2.1 Proposed model of DSpd2 incorporation

One of the first questions that arises from the Cnn incorporation model is how the Cnn receptors are incorporated into the centrosomes in the first place. Similar to Cnn in S-phase, DSpd2 also shows peculiar behaviour of fluorescence recovery beginning

at the centre of the centrosomes, followed by radially outward transport in FRAP experiments. Data gathered by our collaborators (not presented here) show that the Asl distribution around the centrioles does not vary appreciably during the cell cycle. FRAP experiments on GFP-DSpd2 embryos show that the initial recovery curve of fluorescent DSpd2 matches the Asl distribution, suggesting that Asl may be the receptor for DSpd2 (Conduit et al., submitted). We believe that DSpd2 is incorporated in the centrosomes in a similar manner to Cnn. Our collaborators gathered the DSpd2 fluorescence data in the colchicine experiment. The data show that microtubules may not play a role in the outward spread of DSpd2. Thus, it is possible that DSpd2 incorporation may be explained by the reduced receptor gradient model for Cnn, with no advection, and with Asl providing the receptor gradient. Once further experiments establish whether Asl indeed exists in a gradient, or whether it forms some other distribution in the centrosomes, we would like to use this information and test the DSpd2 incorporation model by fitting it with the DSpd2 FRAP data.

6.8.2.2 Proposed pathway of centrosome maturation

Our collaborators have discovered that PCM assembly depends upon a relatively small number of proteins, with Cnn, DSpd2 and Asl playing particularly important roles. With our work we have shown that the Cnn distribution is established with the help of DSpd2. We propose a possible mechanism for DSpd2 incorporation in Conduit et al. (submitted). We believe that Asl may act as a receptor for DSpd2. Figure 4.11 shows, based on preliminary experiments, that Asl also forms a gradient in the centrosome. (Note that when further experiments correct the Asl distribution by removing the optical artifacts, it can be used in the proposed centrosome maturation pathway). The centriolar protein, Sas-4, is known to associate with Asl (Dzhindzhev et al., 2010). Thus, Asl may be recruited directly by the mother centriole. Asl may then recruit DSpd2 in the centrosome. Diffusion of DSpd2 may create a DSpd2 distribution

that is wider than the Asl distribution. DSpd2 in the centrosomes then recruits Cnn, and establishes the Cnn gradient, which is wider than the DSpd2 gradient. This sequential incorporation of Asl to DSpd2 to Cnn is a possible model for centrosome maturation. Figure 6.1 shows the experimentally observed Asl, DSpd2 and Cnn profiles overlaid with their peak intensities normalised to one, so as to compare the widths of their distributions. In future, we would like to provide mathematical support for the sequential incorporation model by using FRAP data for DSpd2 and Asl.

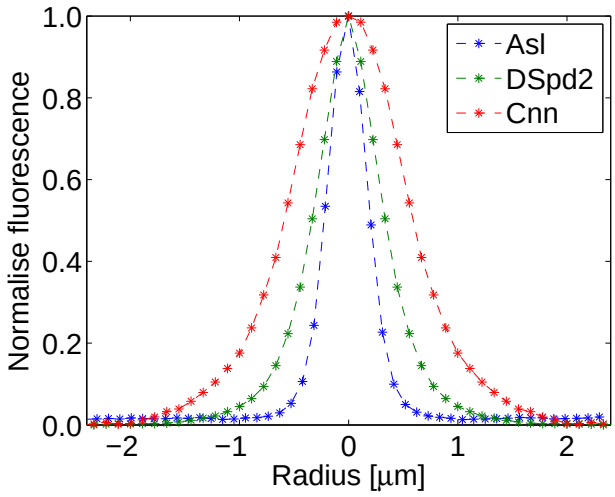

Figure 6.1: *Mean experimentally observed profiles of Asl, Dspd-2 and Cnn, each normalised with their respective peak intensities in order to compare the widths of the successive distributions.*

6.8.2.3 Role in asymmetric stem cell division

It has previously been shown that in *Drosophila* with dysfunctional centrosomes, the polarity of asymmetric division in neuroblasts is lost, leading to reduced fidelity of asymmetric divisions (Gonzalez, 2008). The relative sizes of the two centrosomes in the neuroblasts appear to be important for ensuring the polarity of division. Our collaborators have shown that differential incorporation of Cnn is at the heart of maintaining centrosome-size asymmetry (Conduit and Raff, 2010). The Cnn incorporation model we have developed will allow us to probe the *Drosophila* neuroblast

system in order to understand how Cnn incorporation may be controlled, thereby providing clues about the regulation of asymmetric division of neural stem cells.

6.8.2.4 Using the various models to uncover networks of protein interactions in the centrosome

Having a model of Cnn incorporation that explains the trends observed in S-phase, as well as in mitosis, opens up a number of future possibilities. One can now perturb the system in several ways and understand how the behaviour changes in response to those perturbations. For example, one could use the existing mutants of Cnn protein that accumulate in the centrosome to a lower (or greater) extent and use data fitting to determine which of the model parameters may be affected by this mutation. Once we have established the DSpd2 incorporation mechanism as well as the sequential incorporation model, this exercise of perturbing the various model parameters can also be extended to Asl and DSpd2.

Even though we have focussed on Asl, DSpd2 and Cnn in the above discussion, other centrosomal proteins such as γ-tubulin, D-TACC, Msps, Polo and Aurora A, among others, are all important. All these proteins can be studied using FRAP. Studying these proteins and how they interact with the key centrosome scaffolding proteins (Asl, DSpd2 and Cnn) may help construct a network of protein interactions required for building a functional centrosomal machinery. Building a detailed protein-interaction map of centrosome maturation may aid in understanding how the defects in centrosomes may affect various cell processes and how these defects may be corrected.

Appendix A

Normalisation of various models for data fitting

A.1 Simple geometry diffusion model

Equations (3.3.1)-(3.3.4) denote the dimensional form of the simple geometry diffusion model. Since the data used for data fitting are normalised with the cytoplasmic concentration of Cnn, i.e. L_{cyt}, we normalise the model variables L, N, C, and P with L_{cyt} as well. Thus,

$$\frac{\partial u}{\partial t} = \frac{D_L}{r^2}\frac{\partial}{\partial r}\left(r^2\frac{\partial u}{\partial r}\right) + k_{out}v, \tag{A.1.1}$$

$$\frac{\partial v}{\partial t} = \frac{D_N}{r^2}\frac{\partial}{\partial r}\left(r^2\frac{\partial v}{\partial r}\right) - k_{out}v, \tag{A.1.2}$$

$$\frac{dp}{dt} = k_{turn}w + k_{off}w - \overline{k_{on}}u(r_b,t)p, \tag{A.1.3}$$

$$\frac{dc}{dt} = \overline{k_{on}}u(r_b,t)p - k_{off}w - k_{turn}w, \tag{A.1.4}$$

where $u,\ v,\ w$, and p denote $L,\ N,\ C$, and P, each normalised with L_{cyt}, respectively, and $\overline{k_{on}} = k_{on}L_{cyt}$. The total receptor conservation equation gives

$$p + w = P_{tot}/L_{cyt}.$$

The normalised boundary conditions are given by

$$\begin{aligned}
\left.\frac{\partial u}{\partial r}\right|_{r=r_b} &= \frac{\overline{k_{on}}u(r_b,t)p(t) - k_{off}w(t)}{D_L}, \\
\left.\frac{\partial v}{\partial r}\right|_{r=r_b} &= -\frac{k_{turn}}{D_N}w(t), \\
v(\infty,t) = 0 \ \text{ and } \ u(\infty,t) &= 1.
\end{aligned} \tag{A.1.5}$$

A.2 Simple geometry advection model

The advection model differs from the diffusion model only in the means by which altered Cnn is transported. The PDE for altered Cnn in the case of the advection model is given by equation (3.7.1). The normalised form of equation (3.7.1) is given by

$$\frac{\partial v}{\partial t} = -\nabla.(\bar{a}v) - k_{out}v, \tag{A.2.1}$$

where $v = N/L_{cyt}$. The normalised boundary conditions for altered Cnn are given by

$$v|_{r=r_b} = \frac{k_{turn}}{a}w(t), \qquad v(\infty,t) = 0, \tag{A.2.2}$$

where $w = C/L_{cyt}$.

A.3 Complex geometry diffusion model

Equations (3.12.1)-(3.12.4) denote the dimensional equations in region 1 of the detailed geometry diffusion model. We normalise the model variables $L,\ N,\ C$, and P, with L_{cyt}, so as to mimic the treatment of the data. Thus,

$$\frac{\partial u}{\partial t} = \frac{D_L}{r^2}\frac{\partial}{\partial r}\left(r^2\frac{\partial u}{\partial r}\right) + k_{out}v - \overline{k_{on}}up + k_{off}w, \tag{A.3.1}$$

$$\frac{\partial v}{\partial t} = \frac{D_N}{r^2}\frac{\partial}{\partial r}\left(r^2\frac{\partial v}{\partial r}\right) - k_{out}v + k_{turn}w, \tag{A.3.2}$$

$$\frac{dp}{dt} = k_{turn}w + k_{off}w - \overline{k_{on}}up, \tag{A.3.3}$$

$$\frac{dw}{dt} = \overline{k_{on}}up - k_{off}w - k_{turn}w, \tag{A.3.4}$$

where $u,\ v,\ w$, and p denote $L,\ N,\ C$, and P, each normalised with L_{cyt}, respectively, and $\overline{k_{on}} = k_{on}L_{cyt}$. The total receptor conservation equation gives

$$p(r,t) + w(r,t) = P_{tot}/L_{cyt}.$$

The normalised left boundary conditions are given by

$$D_L\frac{\partial u}{\partial r}\bigg|_{r=r_c} = 0, \qquad D_N\frac{\partial v}{\partial r}\bigg|_{r=r_c} = 0. \tag{A.3.5}$$

Equations (3.12.6)-(3.12.7) denote the dimensional equations in region 1 of the detailed geometry diffusion model. These equations in normalised form are

$$\frac{\partial u}{\partial t} = \frac{D_L}{r^2}\frac{\partial}{\partial r}\left(r^2\frac{\partial u}{\partial r}\right) + k_{out}v, \tag{A.3.6}$$

$$\frac{\partial v}{\partial t} = \frac{D_N}{r^2}\frac{\partial}{\partial r}\left(r^2\frac{\partial v}{\partial r}\right) - k_{out}v. \tag{A.3.7}$$

The right boundary conditions are given by

$$v(\infty, t) = 0 \quad \text{and} \quad u(\infty, t) = 1. \tag{A.3.8}$$

A.4 Receptor gradient model

The variables L, N, P and C in the receptor gradient model given by equations (4.5.1)-(4.5.4) are each normalised with cytoplasmic Cnn concentration L_{cyt}, to obtain the normalised variables u, v, p and w, respectively. The resulting equations are

$$\frac{\partial u}{\partial t} = \frac{D_L}{r^2}\frac{\partial}{\partial r}\left(r^2\frac{\partial u}{\partial r}\right) + k_{out}v - \overline{k_{on}}up + k_{off}w, \tag{A.4.1}$$

$$\frac{\partial v}{\partial t} = \frac{D_N}{r^2}\frac{\partial}{\partial r}\left(r^2\frac{\partial v}{\partial r}\right) - k_{out}v + k_{turn}w, \tag{A.4.2}$$

$$\frac{dp}{dt} = k_{turn}w + k_{off}w - \overline{k_{on}}up, \tag{A.4.3}$$

$$\frac{dw}{dt} = \overline{k_{on}}up - k_{off}w - k_{turn}w. \tag{A.4.4}$$

Conservation of total receptor concentration gives

$$p(r,t) + w(r,t) = \frac{P_{max}}{L_{cyt}}\exp(-p_{grad}r^2) = \mu\exp(-p_{grad}r^2).$$

The normalised boundary conditions are

$$\begin{aligned} D_L\frac{\partial u}{\partial r}\bigg|_{r=0} &= 0, \qquad D_N\frac{\partial v}{\partial r}\bigg|_{r=0} = 0, \\ u(r\to\infty) &= 1, \qquad v(r\to\infty) = 0. \end{aligned} \tag{A.4.5}$$

Appendix B

Numerical simulations of various Cnn incorporation models

B.1 Detailed geometry diffusion model - steady state solution

We use the Comsol Multiphysics software package to simulate the detailed geometry diffusion model, equations (A.3.1)-(A.3.7). Comsol uses the FEM to solve systems of PDEs. This approach is particularly suited for systems involving nontrivial geometries. The model is solved over a three-dimensional cylindrical domain with $r \in (0.1, 6)$ μm and $h \in (-6, 6)$ μm. The binding region is a hollow cylinder with inner radius of 0.1 μm, an outer radius of 0.3 μm and a height of 0.2 μm. The parameter values used are listed in Table B.1. These parameter values are chosen arbitrarily. A stationary solver is used for obtaining the steady state solution. A free tetrahedral mesh with minimum mesh size of 0.05 μm is selected. Refining the mesh further makes the computation prohibitively costly without improving the accuracy of the solution. Figure B.1 shows the steady state solution of the detailed geometry diffusion model.

Table B.1: Parameter values used for simulation of the detailed geometry diffusion model (equations (A.3.1)-(A.3.7)).

Parameters	**Values**	Units
$\overline{k_{on}}$	2	s^{-1}
k_{off}	0.00001	s^{-1}
k_{turn}	0.5	s^{-1}
k_{out}	0.00001	s^{-1}
D_L	1	$\mu m^2 s^{-1}$
D_N	0.0001	$\mu m^2 s^{-1}$
P_{tot}/L_{cyt}	0.1	-

B.2 Detailed geometry diffusion model - FRAP solution

For the FRAP simulations only the fluorescent species are considered. Evolution of the bleached and fluorescent species are coupled through interaction with the Cnn receptors. However, since the bleaching is performed on a system that has reached steady state, the free receptor concentration can be obtained from the steady state solution. The radius of bleaching, r_{bl}, is chosen to be 2.5 μm. The bleaching beam is considered to be cylindrical with a radius of $r_{bl} = 2.5\mu$m and a height spanning the height of the domain. Comsol uses a backward difference formula for solving the time-evolution problem. Figure B.2 shows the evolution of u_f and $v_f + w_f$ in a FRAP setting. Since the observed fluorescence evolution is believed to be from two primary sources, namely the heavy Cnn and Cnn-receptor complex (which only exists in the binding region), we have plotted the evolution of the combination of these two species. It can be seen from Figure B.2(a) that initially the bleaching of light Cnn is simulated by a continuous gradient rather than a sharp change in concentration. This is a meshing artifact. A refined mesh near the bleaching radius can be used to obtain a sharper change in fluorescent light Cnn concentration. We have simulated

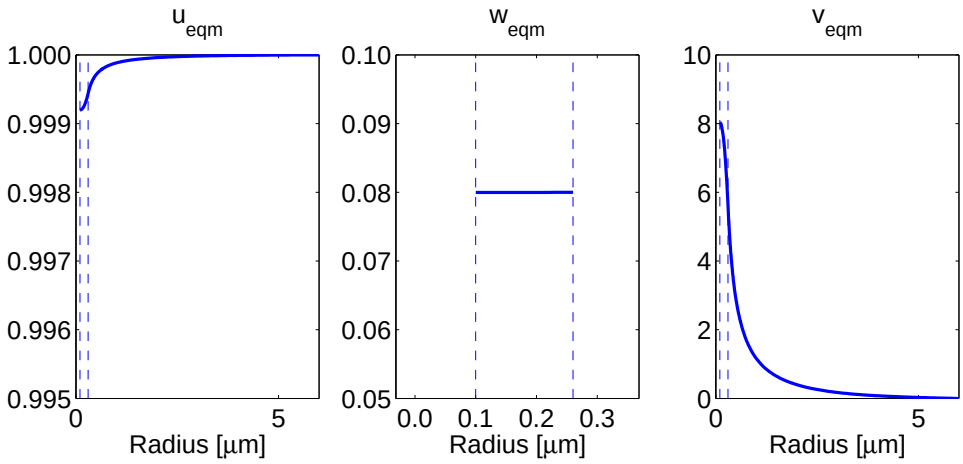

Figure B.1: *Steady state solution of the detailed geometry diffusion model given by equations* (A.3.1)-(A.3.7). *Profiles of* u_{eqm}, w_{eqm} *and* v_{eqm} *are shown. The blue dashed lines identify the boundaries of the binding region.*

systems with such a refined mesh and found that the refining makes little difference to the evolution of $v_f + w_f$, due to the fast diffusion of light Cnn. Therefore, in order to save computational time, when using the numerical solution for data fitting we have not used a refined mesh near the bleaching radius. For this reason we show the numerical solution without the refined mesh.

B.3 Receptor gradient model - steady state solution

We use the Comsol Multiphysics software package to simulate the receptor gradient model, to obtain the steady state solution of the normalised model given by equations (A.4.1)-(A.4.4). The model is solved over a domain $r \in (0, 6\ \mu\text{m})$. As the model is spherically symmetric, we only need to study the radial dependence of concentrations. The parameter values used are listed in Table B.2. These parameter values are chosen arbitrarily. A stationary PDE solver is used with mesh size of 0.005 μm. Figure B.3 shows the steady state solution of the receptor gradient model.

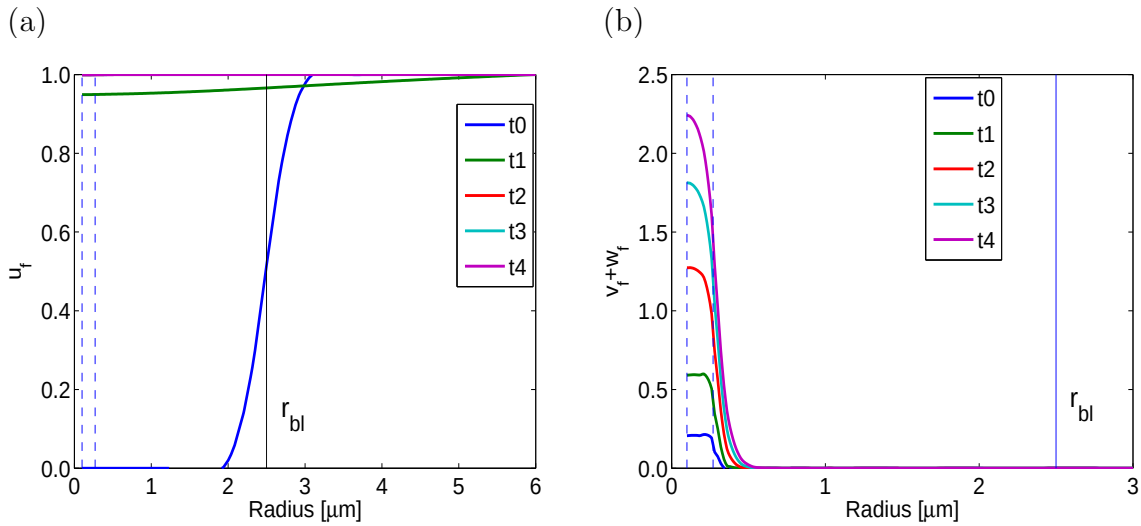

Figure B.2: *Evolution of fluorescent light Cnn,* u_f, (a), *and the combination of fluorescent heavy Cnn and Cnn-receptor complex,* $v_f + w_f$, (b), *as given by the detailed geometry diffusion model* (A.3.1)-(A.3.7). *The blue dashed lines identify the boundaries of the binding region. The solid black line denotes the radius of the bleaching region.*

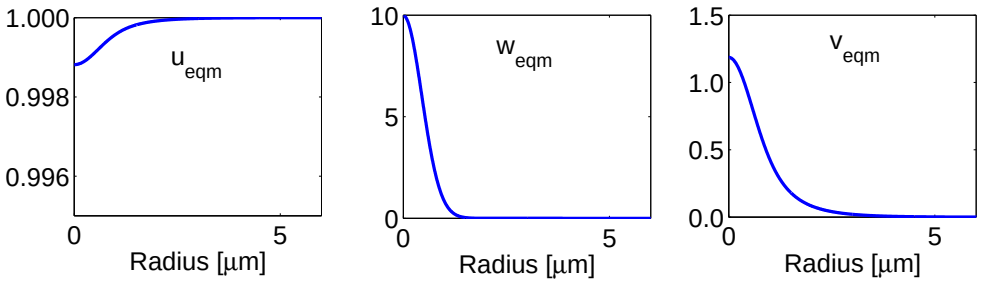

Figure B.3: *Steady state solution of the receptor gradient model given by equations* (A.4.1)-(A.4.4). *Profiles of* u_{eqm}, w_{eqm} *and* v_{eqm} *are shown.*

Table B.2: Parameter values used for simulation of the receptor gradient model (equations (A.4.1)-(A.4.4)).

Parameters	**Values**	Units
$\overline{k_{on}}$	1	s^{-1}
k_{off}	0.001	s^{-1}
k_{turn}	0.001	s^{-1}
k_{out}	0.001	s^{-1}
D_L	1	$\mu m^2 s^{-1}$
D_N	0.001	$\mu m^2 s^{-1}$
P_{tot}/L_{cyt}	10	-

B.4 Receptor gradient model - FRAP solution

The FRAP system is solved as in the previous cases. The free receptor concentration is chosen to be at steady state, since the FRAP experiment is performed when the Cnn incorporation process is at steady state, during mitosis. The radius of bleaching is selected to be $r_{bl} = 2.5$ μm. Figure B.4 shows the evolution of u_f and $v_f + w_f$ in a FRAP setting. Since the experimentally observed fluorescence evolution is from two primary sources, namely the heavy Cnn and Cnn-receptor complex, we have plotted the evolution of the combination of these two species. It can be seen from Figure B.4(a) that, initially, the bleaching of light Cnn is simulated by a continuous gradient rather than a sharp change in concentration. As in the previous case of the detailed geometry model, we allow the bleached profile to be continuous, rather than a step change, as the fast diffusion of u means that this change makes no difference to the evolution of $v_f + w_f$. Also, using a one-dimensional spherically symmetric description of this model means that we cannot allow the bleaching beam to have a cylindrical geometry, which is more physically realistic. However, the following considerations hold. Firstly, the bleaching geometry only affects the unbleached light Cnn population, since the bleaching radius is chosen such that all of the incorporated

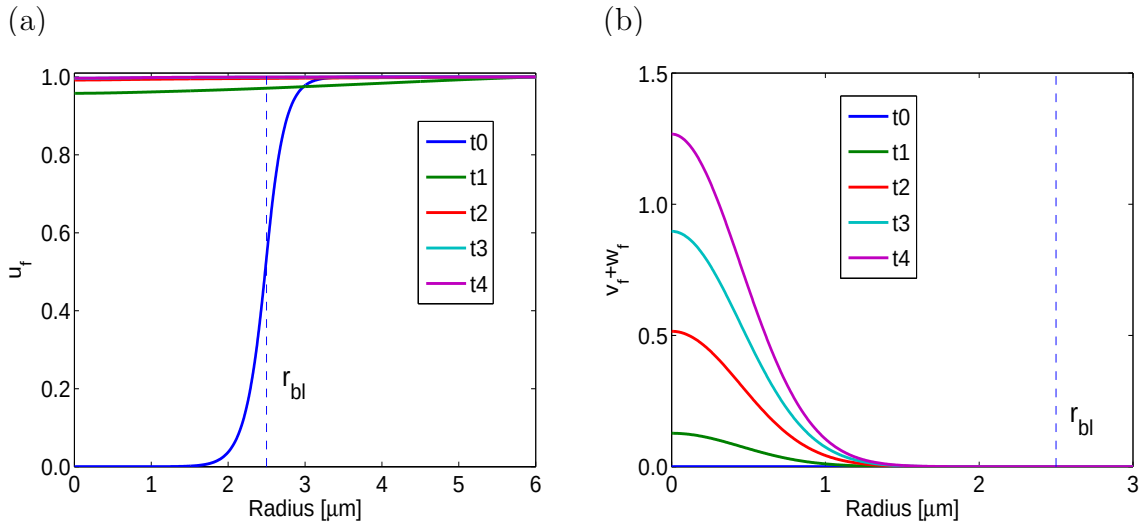

Figure B.4: *Evolution of fluorescent light Cnn,* u_f, (a), *and the combination of fluorescent heavy Cnn and Cnn-receptor complex,* $v_f + w_f$, (b), *as given by the receptor gradient model* (A.4.1)-(A.4.4). *The blue dashed line denotes the radius of the bleaching region.*

Cnn is completely bleached. In other words, the concentration of heavy Cnn or Cnn-receptor complex outside of the bleached radius is essentially zero. Secondly, light Cnn diffuses fast as compared to the FRAP time scale, thereby equilibrating quickly. Thus, using a spherical bleaching geometry in place of a more realistic cylindrical one would essentially not affect the evolution of $v_f + w_f$.

Appendix C

Reduced receptor gradient model and analysis

The reduced model given by reactions (4.10.1) can be formulated mathematically as

$$\frac{\partial N}{\partial t} = \frac{D_N}{r^2}\frac{\partial}{\partial r}\left(r^2\frac{\partial N}{\partial r}\right) + k_{turn}C, \tag{C.0.1}$$

$$\frac{dP}{dt} = k_{turn}C - \overline{k_{on}}P, \tag{C.0.2}$$

$$\frac{dC}{dt} = \overline{k_{on}}P - k_{turn}C, \tag{C.0.3}$$

where $\overline{k_{on}}$ denotes the pseudo-first order binding rate and is given by $k_{on}L_{cyt}$. As in the case of the full receptor gradient model, the total receptor concentration is conserved. Thus,

$$P(r,t) + C(r,t) = P_{max}\exp(-p_{grad}r^2).$$

The boundary conditions for N are given by a homogeneous Neumann condition at the origin and homogeneous Dirichlet condition at the right boundary. Thus,

$$\left.\frac{dN}{dr}\right|_{r=0} = 0, \qquad N|_{r\to\infty} = 0. \tag{C.0.4}$$

C.1 Non-dimensionalisation

In order to non-dimensionalise the model we introduce the following non-dimensional variables and parameters.

$$v = \frac{N}{L_{cyt}}, \qquad w = \frac{C}{L_{cyt}}, \qquad p = \frac{P}{L_{cyt}}, \qquad r^* = \sqrt{\frac{k_{turn}}{D_N}}r,$$
$$t^* = k_{turn}t, \qquad \alpha = \frac{\overline{k_{on}}}{k_{turn}}, \qquad \mu = \frac{P_{max}}{L_{cyt}}, \qquad b = \frac{p_{grad}D_N}{k_{turn}}. \tag{C.1.1}$$

Dropping the asterisks for clarity the non-dimensionalised model is given by

$$\frac{\partial v}{\partial t} = \frac{1}{r^2}\frac{\partial}{\partial r}\left(r^2\frac{\partial v}{\partial r}\right) + w, \tag{C.1.2}$$

$$\frac{dp}{dt} = w - \alpha p, \tag{C.1.3}$$

$$\frac{dw}{dt} = \alpha p - w, \tag{C.1.4}$$

where

$$p(r,t) + w(r,t) = \mu \exp\left(-br^2\right).$$

The initial conditions are given by

$$v(r,0) = 0, \quad p(r,0) = p_{tot}(r) \quad \text{and} \quad w(r,0) = 0.$$

The non-dimensionalised boundary conditions are given by,

$$\left.\frac{dv}{dr}\right|_{r=0} = 0, \qquad v|_{r\to\infty} = 0. \tag{C.1.5}$$

C.2 Analysis

Having made the assumption regarding $L(r,t) = L_{cyt}$ on the time scale of our experiment, the ODE for w becomes linear. The solution for w is given from simplifying equation (4.6.12) to reflect the model reduction. Thus,

$$w = \mu \exp(-br^2)\frac{\alpha}{\alpha+1}\left(1-\exp(-(\alpha+1)t)\right). \tag{C.2.1}$$

We note that this is an explicit solution for w, unlike equation (4.6.12), which gave a solution of w implicit in u. It can be seen from equation (C.2.1) that the solution for w is Gaussian at all times. Having solved for the Cnn-receptor complex, we can explicitly solve for heavy Cnn v. As mentioned in Chapter 4, we use the model in Cartesian coordinates for the purpose of analysis. To solve for v, we rewrite the PDE for v in three-dimensional Cartesian coordinates. Thus

$$\frac{\partial v}{\partial t} = \frac{\partial^2 v}{\partial x^2}+\frac{\partial^2 v}{\partial y^2}+\frac{\partial^2 v}{\partial z^2}+\mu \exp(-b(x^2+y^2+z^2))\frac{\alpha}{\alpha+1}\left(1-\exp(-(\alpha+1)t)\right), \tag{C.2.2}$$

where the source w given by equation (C.2.1) is also expressed in Cartesian coordinates. The corresponding boundary conditions are given by $v \to 0$ as $(x,y,z) \to (\pm\infty, \pm\infty, \pm\infty)$. The Green's function solution for equation (C.2.2) is given by

$$G(x',y',z',t') = \frac{1}{\left(4\pi(t'-t)\right)^{3/2}}\exp(-\left(\frac{(x-x')^2+(y-y')^2+(z-z')^2}{4(t'-t)}\right). \tag{C.2.3}$$

Using the method of Green's functions, the solution for v is obtained by taking the convolution of the source of v with the fundamental solution of the heat equation:

$$\begin{aligned} v(x',y',z',t') =& \frac{\alpha\mu}{\alpha+1}\int_{-\infty}^{\infty}\int_{-\infty}^{\infty}\int_{-\infty}^{\infty}\int_{0}^{t'}\frac{\exp(-b(x^2+y^2+z^2))\left(1-\exp(-(\alpha+1)t)\right)}{(4\pi(t'-t))^{3/2}} \\ & \exp\left(-\frac{((x-x')^2+(y-y')^2+(z-z')^2)}{4(t'-t)}\right)\mathrm{d}t\mathrm{d}x\mathrm{d}y\mathrm{d}z. \end{aligned} \tag{C.2.4}$$

The integral description of v thus involves the convolution of two Gaussian curves in space, which yields a third Gaussian curve, the width of which is given by the combination of the two component Gaussians. Thus,

$$v(x', y', z', t') = \frac{\alpha\mu}{\alpha+1}\int_0^{t'} \frac{(1-\exp(-(\alpha+1)t))}{(4b(t'-t)+1)^{3/2}} \exp\left(-\frac{(x'^2+y'^2+z'^2)}{4(t'-t)+\bar{b}}\right) \mathrm{d}t, \tag{C.2.5}$$

where $\bar{b} = 1/b$. The integral in equation (C.2.5) cannot be written in closed form. However, it can be evaluated numerically to obtain the evolution of v. The evolution of the total fluorescence is thus given by $v+w$, which is obtained by summing equations (C.2.1) and (C.2.5).

C.3 FRAP analysis

In the absence of bleaching, the above solution is for the evolution of w and v from the naive model. However, since bleaching is carried out when the system reaches steady state in the FRAP experiment, the above solution has to be altered slightly to reflect this fact. We note that even though after bleaching the previously fluorescent species are subdivided into two populations, fluorescent and bleached, respectively, the free receptors, on account of being non-fluorescent, exist as a single population. Thus, at steady state, we can estimate what the free receptor concentration should be. This is obtained by solving stationary version of equation (C.1.3) and using the conservation condition for the total receptor concentration, yielding

$$p_{eqm}(r) = \frac{\mu\exp(-b(x^2+y^2+z^2))}{\alpha+1}. \tag{C.3.1}$$

The concentration of free receptors thus remains at p_{eqm} throughout the recovery process, since the FRAP experiment does not alter the equilibrium of the system. The evolution of the fluorescent Cnn-receptor complex, denoted as w_f, is thus given

by

$$\frac{dw_f}{dt} = \alpha p_{eqm} - w_f. \tag{C.3.2}$$

Since bleaching completely destroys the fluorescence in the system, the initial condition for both $w_f(r,0)$ and $v_f(r,0)$ is zero. The solution of w_f is given by

$$w_f = \mu \exp(-b(x^2+y^2+z^2))\frac{\alpha}{\alpha+1}\left(1-\exp(-t)\right), \tag{C.3.3}$$

and the corresponding v_f solution is given by

$$v_f(x',y',z',t') = \frac{\alpha\mu}{\alpha+1}\int_0^{t'} \frac{(1-\exp(-t))}{(4b(t'-t)+1)^{3/2}} \exp\left(-\frac{(x'^2+y'^2+z'^2)}{4(t'-t)+\bar{b}}\right) \mathrm{d}t. \tag{C.3.4}$$

The evolution of fluorescence after bleaching is given, in spherical polar coordinates, by

$$\begin{aligned} v_f(r',t') + w_f(r',t') =& \frac{\alpha\mu}{\alpha+1}\Bigg(\exp(-br'^2)\left(1-\exp(-t')\right) \\ &+ \int_0^{t'} \frac{(1-\exp(-t))}{(4b(t'-t)+1)^{3/2}} \exp\left(-\frac{(r'^2)}{4(t'-t)+\bar{b}}\right) \mathrm{d}t\Bigg). \end{aligned} \tag{C.3.5}$$

For the purpose of data fitting, we need to redimensionalise equation (C.3.5), while allowing heavy Cnn and Cnn-receptor complex to be normalised by L_{cyt}. Thus, the redimensionalised equation is given by

$$\begin{aligned} v_f(r',t') + w_f(r',t') =& \frac{\overline{k_{on}}\mu}{\overline{k_{on}}+k_{turn}}\Bigg(\exp(-p_{grad}r'^2)\left(1-\exp(-k_{turn}t')\right) \\ &+ k_{turn}\int_0^{t'} \frac{(1-\exp(-k_{turn}t))}{(4p_{grad}D_N(t'-t)+1)^{3/2}} \exp\left(\frac{-p_{grad}r'^2}{4D_N p_{grad}(t'-t)+1}\right) \mathrm{d}t\Bigg), \end{aligned} \tag{C.3.6}$$

where space and time are now given in dimensional form.

Appendix D

Confidence intervals for the receptor gradient model fit

Table D.1: 95% confidence intervals for the parameter estimates obtained from fitting the Cnn FRAP data with the receptor gradient model (equations (A.4.1)-(A.4.4)).

Parameters	**Sample estimates**	**95% Confidence intervals**	**Units**
$\overline{k_{on}}$	0.1118	-9.11–9.33	s^{-1}
k_{off}	7.4e-5	-0.39–0.39	s^{-1}
k_{turn}	0.1278	-3.12–3.37	s^{-1}
k_{out}	5.9e-4	4.6e-4–7.3e-4	s^{-1}
D_L	1.35	-11.15–13.86	$\mu m^2 s^{-1}$
D_N	1.9e-4	1.65e-4–2.14e-4	$\mu m\ s^{-1}$
P_{max}/L_{cyt}	0.74	-30.32–31.8	-
p_{grad}	4.1	1.98–6.28	μm^{-2}

Appendix E

Modelling the Cnn FRAP experiment performed during S-phase

E.1 Model equations

The non-dimensionalised receptor gradient model is given by equations (C.1.2)-(C.1.5). As mentioned previously, bleaching creates two subpopulations of the fluorescent species, namely bleached and unbleached. The free receptors, on account of being non-fluorescent, exist as a single species. Thus, the evolution equations after bleaching are given as

$$\frac{\partial v_f}{\partial t} = \frac{1}{r^2}\frac{\partial}{\partial r}\left(r^2\frac{\partial v_f}{\partial r}\right) + w_f, \tag{E.1.1}$$

$$\frac{dw_f}{dt} = \alpha_f p - w_f, \tag{E.1.2}$$

$$\frac{\partial v_b}{\partial t} = \frac{1}{r^2}\frac{\partial}{\partial r}\left(r^2\frac{\partial v_b}{\partial r}\right) + w_b, \tag{E.1.3}$$

$$\frac{dw_b}{dt} = \alpha_b p - w_b, \tag{E.1.4}$$

$$\frac{dp}{dt} = w_f + w_b - \alpha_f p - \alpha_b p, \tag{E.1.5}$$

where the subscripts f and b denote the fluorescent and the bleached species, respectively. Assuming that the total receptor concentration is constant, it can be given by the sum of three species as

$$p(r,t) + w_f(r,t) + w_b(r,t) = \mu \exp(-br^2).$$

The boundary conditions are given by

$$\begin{aligned} \left.\frac{dv_f}{dr}\right|_{r=0} &= 0, \qquad v_f|_{r\to\infty} = 0, \\ \left.\frac{dv_b}{dr}\right|_{r=0} &= 0, \qquad v_b|_{r\to\infty} = 0. \end{aligned} \tag{E.1.6}$$

Notice that the parameter α is also assigned the subscripts b and f. This is because this is a pseudo-first order rate constant for the reaction of the cytoplasmic Cnn with the receptors. Since the cytoplasmic Cnn population is also divided into the fluorescent and bleached subpopulations, we have denoted the parameter α accordingly (see Section 3.4.5 and section E.2 for more details). Note that we need to consider the details of the full model in order to arrive at the correct simplification of it for modelling the FRAP experiment. Thus, if we consider the cytoplasmic Cnn species u_f and u_b, the boundary conditions for these can be given by

$$\begin{aligned} \left.\frac{du_f}{dr}\right|_{r=0} &= 0, \qquad u_f|_{r\to\infty} = 1, \\ \left.\frac{du_b}{dr}\right|_{r=0} &= 0, \qquad u_b|_{r\to\infty} = 0. \end{aligned} \tag{E.1.7}$$

E.2 Analysis

We have argued (in Section 2.2), and subsequently shown (in Chapter 4) that cytoplasmic Cnn diffuses and forms a homogeneous distribution on a much faster time scale than the FRAP experiment. Applying this argument to the bleached form of cytoplasmic Cnn, we argue that the bleached cytoplasmic Cnn diffuses quickly and its concentration diminishes to zero soon after bleaching. Thus, the formation of new bleached Cnn-receptor complex (after the bleaching event) from the bleached cytoplasmic Cnn (given by $\alpha_b p$ in equation (E.1.4)) is negligible on the time scale of the FRAP experiment. We rewrite the evolution equation for w_b as

$$\frac{dw_b}{dt} = -w_b. \tag{E.2.1}$$

The initial conditions for the fluorescent species are given by

$$v_f(r,0) = 0, \quad w_f(r,0) = 0.$$

We are not interested in following the formation and diffusion of bleached heavy Cnn, v_b, over time, as this species does not contribute to the fluorescence and can be decoupled from the remaining system of equations. We do, however, need to monitor the decay of the bleached Cnn-receptor complex, w_b, since this decay leads to the generation of free receptors, via which it contributes to the evolution of fluorescence. The evolution of w_b is given by

$$w_b = w_{b0} \exp(-t), \tag{E.2.2}$$

where w_{b0} is the concentration of Cnn-receptor complex at the time of bleaching. Even though we have a pre-bleach fluorescence profile of Cnn available from the FRAP experiments, it is not possible to deduce what proportion of this fluorescence

is given by the Cnn-receptor complex. We have shown in Appendix C that evolution of the Cnn-receptor complex in the receptor gradient model is given by equation (C.2.1). Thus, we can deduce that the profile of the Cnn-receptor complex at any time point (say, for example, a time point just prior to bleaching) is given by some fraction of the total receptor concentration profile. Thus, for the time being, we use

$$w_{b0} = k\mu \exp(-br^2),$$

where $0 < k < 1$ denotes the fraction of the total receptor population that exists as a Cnn-receptor complex just prior to bleaching.

E.2.1 Solving for w_f

Next we consider equation (E.1.2) for w_f. Using conservation of total receptor concentration we can rewrite this equation as

$$\frac{dw_f}{dt} = \alpha\left(\mu \exp(-br^2) - w_f - w_b\right) - w_f. \tag{E.2.3}$$

We have dropped the subscript f for the parameter α, since the fluorescent cytoplasmic Cnn is expected to quickly equilibrate (and the bleached cytoplasmic Cnn concentration to quickly decay to zero). Thus, the only Cnn-receptor binding reaction (denoted by parameter α) occurring in the centrosome is that between the fluorescent cytoplasmic Cnn and the receptors. Substituting the expression for w_b (E.2.2) in equation (E.2.3) and rearranging gives

$$\frac{dw_f}{dt} + w_f(\alpha + 1) = \alpha\left(\mu \exp(-br^2) - w_{b0}\exp(-t)\right). \tag{E.2.4}$$

Solving equation (E.2.4) using the integrating factor $I_f = \exp((\alpha+1)t)$ gives

$$w_f = \frac{\alpha\mu \exp(-br^2)}{\alpha+1} - w_{b0}\exp(-t) + C\exp(-(\alpha+1)t),$$

where C is a constant of integration, and is given using the initial condition $w_f(r,0) = 0$ as

$$C = w_{b0} - \frac{\alpha\mu \exp(-br^2)}{\alpha+1}.$$

Thus, the solution for w_f in the non-steady FRAP experiment is given as

$$w_f = \frac{\alpha\mu \exp(-br^2)}{\alpha+1}\left(1 - \exp(-(\alpha+1)t)\right) + w_{b0}\exp(-t)\left(\exp(-\alpha t) - 1\right). \quad \text{(E.2.5)}$$

E.2.2 Solving for v_f

Notice that the equation for v_f (E.1.1) is identical to the equation for v in the case of the full model (C.1.2), except that the source function w_f is given by equation (E.2.5). Thus, the solution is obtained using the method of Green's functions as

$$\begin{aligned} v_f(r',t') =& \frac{\alpha\mu}{\alpha+1}\int_0^{t'} \frac{(1-\exp(-t))}{(4b(t'-t)+1)^{3/2}} \exp\left(-\frac{(r'^2)}{4(t'-t)+\bar{b}}\right) \mathrm{d}t \\ &+ k\mu \int_0^{t'} \frac{\exp(-t)\left(\exp(-\alpha t)-1\right)}{(4b(t'-t)+1)^{3/2}} \exp\left(-\frac{(r'^2)}{4(t'-t)+\bar{b}}\right) \mathrm{d}t, \end{aligned} \quad \text{(E.2.6)}$$

where w_{b0} is substituted by $k\mu\exp(-br^2)$ and $\bar{b} = 1/b$. Thus, the evolution of combined (normalised) fluorescence from both the Cnn-receptor complex and the heavy

Cnn is given in dimensional form as

$$
\begin{aligned}
&v_f(r',t') + w_f(r',t') = \frac{\overline{k_{on}}\mu}{\overline{k_{on}} + k_{turn}} \Bigg(\exp(-p_{grad} r'^2) \left(1 - \exp(-k_{turn} t')\right) \\
&+ k_{turn} \int_0^{t'} \frac{(1 - \exp(-k_{turn} t))}{(4 p_{grad} D_N (t' - t) + 1)^{3/2}} \exp\left(- \frac{(r'^2)}{4 D_N (t' - t) + 1/p_{grad}} \right) \mathrm{d}t \Bigg) \\
&k\mu \Bigg(\exp(-p_{grad} r^2) \exp(-k_{turn} t) \left(\exp(-\overline{k_{on}} t) - 1 \right) \\
&+ k_{turn} \int_0^{t'} \frac{\exp(-k_{turn} t) \left(\exp(-\overline{k_{on}} t) - 1 \right)}{(4 p_{grad} D_N (t' - t) + 1)^{3/2}} \exp\left(- \frac{(r'^2)}{4 D_N (t' - t) + 1/p_{grad}} \right) \mathrm{d}t \Bigg).
\end{aligned}
\tag{E.2.7}
$$

Appendix F

Insights gained from the colchicine experiment

S-phase embryos expressing GFP-Cnn were injected with colchicine and the FRAP experiment was performed as described in Section 5.1. The data were obtained from ten different centrosomes. Figure F.1 shows the mean successive normalised Cnn recovery profiles obtained from the FRAP experiment.

The DSpd2 data were gathered from 12 different centrosomes. Figure F.2 shows the successive normalised mean DSpd2 profiles (blue asterisks) for the time points corresponding to the Cnn recovery time points. It is possible that a part of DSpd2 gradient is attributable to optical artifacts. However, for the purpose of our analysis, we assume that the observed DSpd2 gradient is entirely due to the graded distribution of DSpd2 molecules. The DSpd2 gradients at each time point are fitted with a separate Gaussian curve, as described in Section 5.2.1. The resulting fits are also plotted in Figure F.2. The best-fitting values of the parameters p_{grad} and P_{max} obtained from the fits are each plotted in Figure F.3(a) and (b), respectively. It can be

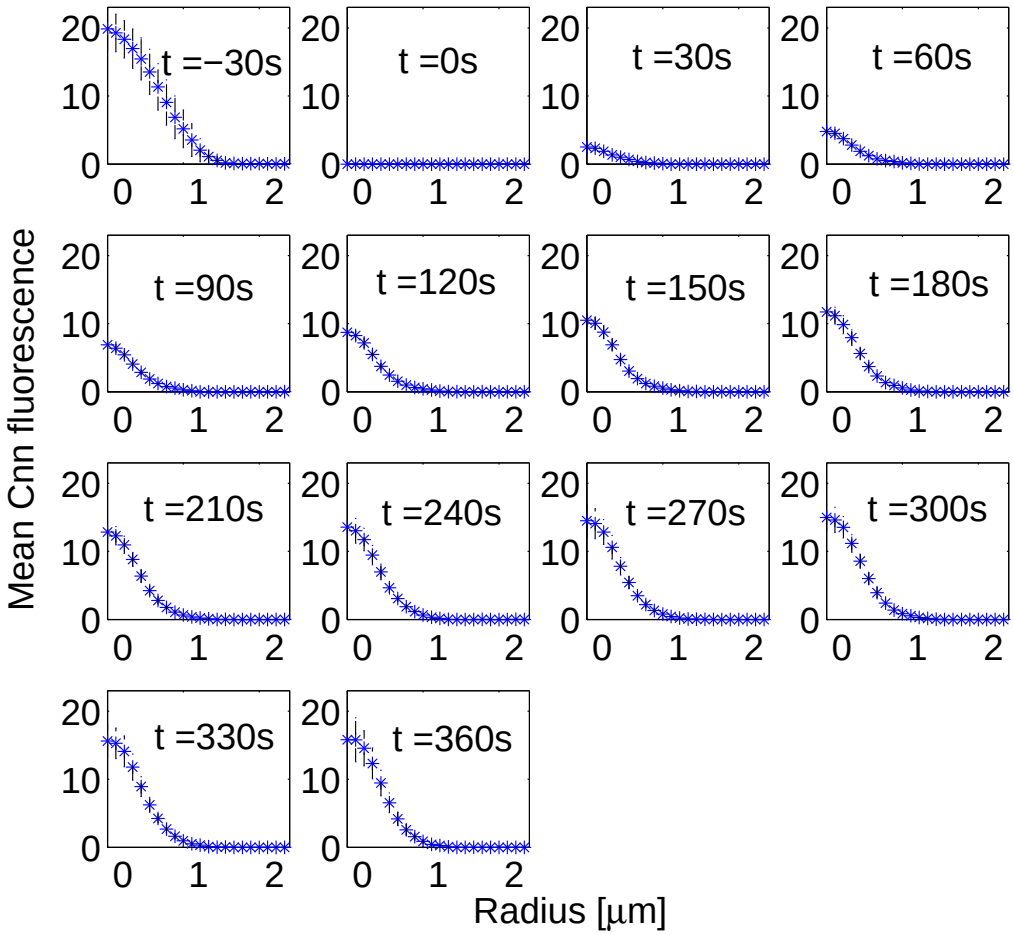

Figure F.1: *Mean Cnn fluorescence (normalised in the same manner as mentioned in Section 2.2) (blue asterisks) is shown for pre-bleach time point* ($t = -30$ s)*, just after bleaching at* $t = 0$ s *and subsequent time points for which recovery is monitored in the colchicine experiment. The data were obtained from 10 different centrosomes. Error bars denote the standard deviation.*

seen that the estimated values of p_{grad} linearly decrease with time and are given by

$$p_{grad}(t) = 6 - 0.006t. \tag{F.0.1}$$

Other noteworthy aspects are that the parameter P_{max} shows a nonlinear dependence on time. The values of P_{max} obtained are consistently higher as compared to those

obtained from the previous experiment without colchicine (Figure 5.5).

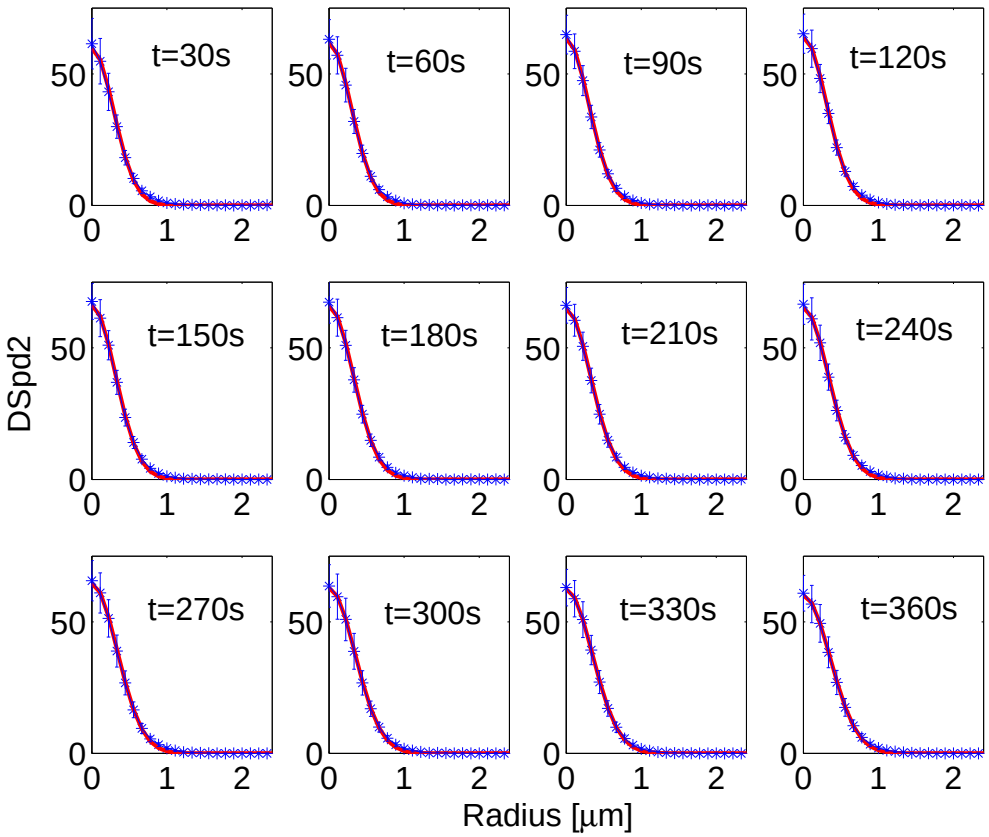

Figure F.2: *Mean DSpd2 fluorescence (normalised in a similar manner to the Cnn data) (blue asterisks) for time points corresponding to recovery time points for which Cnn fluorescence is measured in the colchicine experiment. The DSpd2 data were gathered from 12 different centrosomes. Error bars denote the standard deviation. The successive DSpd2 distribution profiles are each fitted with a separate Gaussian curve,* $P_{max}\exp(-p_{grad}r^2)$*, (red curves).*

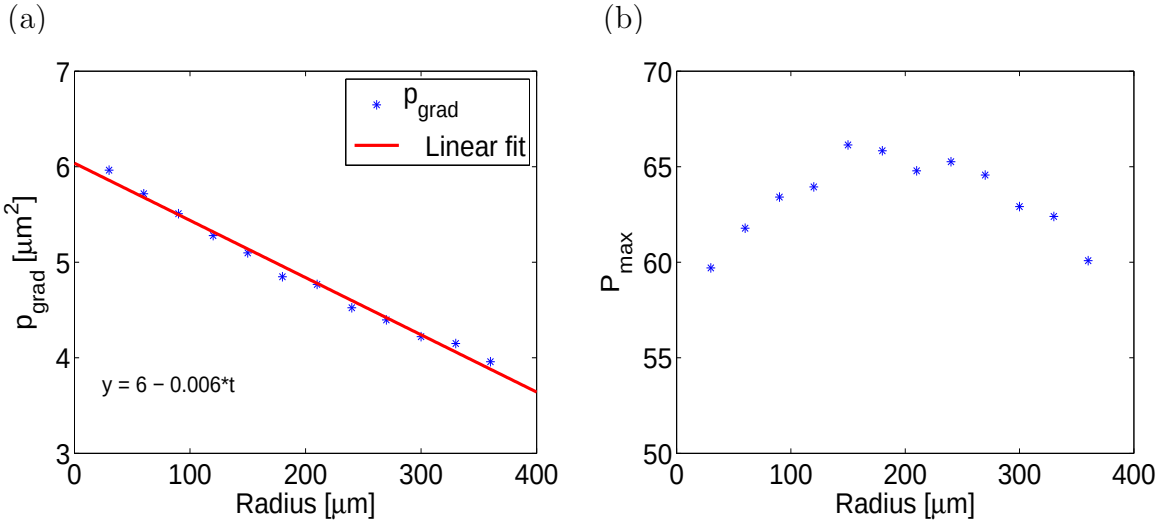

Figure F.3: (a) *The best fitting p_{grad} values (blue asterisks) obtained from fitting the successive DSpd2 distribution profiles from the colchicine experiment are plotted as a function of time. The evolution of p_{grad} shows a linear dependence on time, as the fitted line (red) shows. The equation for the best-fitting line is given.* (b) *The best fitting estimates of P_{max} describe a nonlinear relationship with respect to time.*

Bibliography

B. Alberts, A. Johnson, J. Lewis, M. Raff, K. Roberts, and P. Walter. *Molecular Biology of the Cell*. Garland Science, 2002.

D. Axelrod, D. E. Koppel, J. Schlessinger, E. Elson, and W. W. Webb. Mobility measurement by analysis of fluorescence photobleaching recovery kinetics. *Biophysical Journal*, 16(9):1055–1069, 1976.

J. Azimzadeh and W. F. Marshall. Building the centriole. *Current Biology*, 20(18): R816–R825, 2010.

S. Bakshi, P. Conduit, O. Dushek, J. Raff, R. E. Baker, E. A. Gaffney, and P. K. Maini. A novel mathematical model for the incorporation of centrosomin in *Drosophila* centrosomes. in preparation.

R. Barkus, O. Klyachko, D. Horiuchi, B. J. Dickson, and W. M. Saxton. Identification of an axonal kinesin-3 motor for fast anterograde vesicle transport that facilitates retrograde transport of neuropeptides. *Molecular Biology of the Cell*, 19:274–283, 2008.

R. Basto, J. Lau, T. Vinogradova, A. Gardiol, C. G. Woods, A. Khodjakov, and J. W. Raff. Flies without centrioles. *Cell*, 125(7):1375–86, 2006.

D. M. Bates and D. G. Watts. *Nonlinear Regression Analysis and its Applications*. John Wiley and Sons, 1988.

M. Bettencourt-Dias and D. M. Glover. Centrosome biogenesis and function: centrosomics brings new understanding. *Nature Reviews. Molecular Cell Biology*, 8(6): 451–63, 2007.

J. Bond and C. G. Woods. Cytoskeletal genes regulating brain size. *Current Opinion in Cell Biology*, 18(1):95–101, 2006.

G. Callaini and M. G. Riparbelli. Centriole and centrosome cycle in the early *Drosophila* embryo. *Journal of Cell Science*, 97 (Pt 3):539–43, 1990.

G. Carrero, D. McDonald, E. Crawford, G. de Vries, and M. J. Hendzel. Using FRAP and mathematical modeling to determine the in vivo kinetics of nuclear proteins. *Methods*, 29(1):14–28, 2003.

G. Carrero, E. Crawford, M. J. Hendzel, and G. de Vries. Characterizing fluorescence recovery curves for nuclear proteins undergoing binding events. *Bulletin of Mathematical Biology*, 66(6):1515–45, 2004.

E. Castellanos, P. Dominguez, and C. Gonzalez. Centrosome dysfunction in *Drosophila* neural stem cells causes tumors that are not due to genome instability. *Current Biology*, 18(16):1209–14, 2008.

T. Coleman and Y. Li. On the convergence of interior-reflective Newton methods for nonlinear minimization subject to bounds. *Mathematical Programming*, 67: 189–224, 1994.

T. F. Coleman and Y. Li. An interior trust region approach for nonlinear minimization subject to bounds. *SIAM Journal on Optimization*, 6(2):418–445, 1996.

P. Conduit, J. Richens, C. Vicente, M. Pratt, Z. Novak, S. Bakshi, A. Wainman, and J. Raff. A spatiotemporal analysis of PCM dynamics reveals a mechanism for mitotic PCM assembly in flies. submitted.

P. C. Conduit and J. W. Raff. Cnn dynamics drive centrosome size asymmetry to ensure daughter centriole retention in Drosophila neuroblasts. *Current Biology*, 20: 2187–2192, 2010.

P. C. Conduit, K. Brunk, J. Dobbelaere, C. I. Dix, E. P. Lucas, and J. W. Raff. Centrioles regulate centrosome size by controlling the rate of Cnn incorporation into the PCM. *Current Biology*, 20:2178–2186, 2010.

R. Courant, K. Friedrichs, and H. Lewy. On the partial difference equations of mathematical physics. *IBM Journal of Research*, pages 215–234, 1967.

A. Debec, C. Marcaillou, Y. Bobinnec, and C. Borot. The centrosome cycle in syncytial *Drosophila* embryos analyzed by energy filtering transmission electron microscopy. *Biology of the Cell*, 91:379–91, 1999.

I. Dinov. F distribution tables, 2002. URL `http://www.socr.ucla.edu/applets.dir/f_table.html`.

N. S. Dzhindzhev, Q. D. Yu, K. Weiskopf, G. Tzolovsky, I. Cunha-Ferreira, M. Riparbelli, A. Rodrigues-Martins, M. Bettencourt-Dias, G. Callaini, and D. M. Glover. Asterless is a scaffold for the onset of centriole assembly. *Nature*, 467(7316):714–8, 2010.

M. Elsner, H. Hashimoto, J. C. Simpson, D. Cassel, T. Nilsson, and M. Weiss. Spatiotemporal dynamics of the COPI vesicle machinery. *EMBO Reports*, 4(10):1000–4, 2003.

S. Ghaemmaghami, W.-K. Huh, K. Bower, R. W. Howson, A. Belle, N. Dephoure, E. K. O'Shea, and J. S. Weissman. Global analysis of protein expression in yeast. *Nature*, 425(6959):737–41, 2003.

S. F. Gilbert. *Developmental Biology*. Sinauer Associates, eighth edition, 2000.

M. Gomez-Ferreria and L. Pelletier. Centrosome biogenesis: centrosomin sizes things up! *Current Biology*, 20(24):R1069–71, 2010.

P. Gonczy. Mechanisms of asymmetric cell division: flies and worms pave the way. *Nature Reviews. Molecular Cell Biology*, 9:355 – 366, 2008.

P. Gönczy. Towards a molecular architecture of centriole assembly. *Nature Reviews. Molecular Cell Biology*, 13(7):425–35, 2012.

C. Gonzalez. Centrosome function during stem cell division: the devil is in the details. *Current Opinions in Cell Biology*, 20(6):694–8, 2008.

T. Gregor, W. Bialek, R. R. de Ruyter van Steveninck, D. W. Tank, and E. F. Wieschaus. Diffusion and scaling during early embryonic pattern formation. *Proceedings of the National Academy of Sciences of the United States of America*, 102 (51):18403–7, 2005.

T. Gregor, E. F. Wieschaus, A. P. McGregor, W. Bialek, and D. W. Tank. Stability and nuclear dynamics of the bicoid morphogen gradient. *Cell*, 130(1):141–52, 2007.

M. A. Hallen and A. T. Layton. Expanding the scope of quantitative FRAP analysis. *Journal of Theoretical Biology*, 262:295–305, 2010.

M. K. Harrison, A. M. Adon, and H. I. Saavedra. The G1 phase CDKs regulate the centrosome cycle and mediate oncogene-dependent centrosome amplification. *Cell Division*, 6(1):2, 2011.

J. G. Heuer, K. Li, and T. C. Kaufman. The *Drosophila* homeotic target gene centrosomin (cnn) encodes a novel centrosomal protein with leucine zippers and maps to a genomic region required for midgut morphogenesis. *Development*, 121(11): 3861–76, 1995.

P. Kalab and R. Heald. The RanGTP gradient - a GPS for the mitotic spindle. *Journal of Cell Science*, 121:1577–1586, 2008.

M. Kang, C. A. Day, K. Drake, A. K. Kenworthy, and E. DiBenedetto. A Generalization of Theory for Two-Dimensional Fluorescence Recovery after Photobleaching Applicable to Confocal Laser Scanning Microscopes. *Biophysical Journal*, 97(5): 1501–1511, 2009.

I. H. M. N. Klonis, Melanie Rug. Fluorescence photobleaching analysis for the study of cellular dynamics. *European Biophysics Journal*, 31(1):36–51, 2002.

J. Lagarias, J. Reeds, and M. Wright. Convergence properties of the Nelder-Mead simplex method in low dimensions. *SIAM Journal on Optimization*, 9(1):112–147, 1998.

K. Li and T. C. Kaufman. The homeotic target gene centrosomin encodes an essential centrosomal component. *Cell*, 85(4):585–96, 1996.

K. Li, E. Y. Xu, J. K. Cecil, F. R. Turner, T. L. Megraw, and T. C. Kaufman. *Drosophila* centrosomin protein is required for male meiosis and assembly of the flagellar axoneme. *The Journal of Cell Biology*, 141(2):455–67, 1998.

J. Lippincott-Schwartz, E. Snapp, and a. Kenworthy. Studying protein dynamics in living cells. *Nature Reviews. Molecular Cell Biology*, 2(6):444–56, 2001.

T. A. Markow, S. Beall, and L. M. Matzkin. Egg size, embryonic development time and ovoviviparity in *Drosophila* species. *Journal of Evolutionary Biology*, 22(2): 430–4, 2009.

W. Marshall. Centriole evolution. *Current Opinions in Cell Biology*, 21:14–19, 2009.

A. R. Martins, P. Machado, G. Callaini, and M. Bettencourt-Dias. Microscopy Methods for the Study of Centriole Biogenesis and Function in *Drosophila*. In L. Cas-

simeris and P. Tran, editors, *Microtubules: in vivo*, chapter 13, pages 223–242. Academic Press, 2010.

T. L. Megraw, K. Li, L. R. Kao, and T. C. Kaufman. The centrosomin protein is required for centrosome assembly and function during cleavage in *Drosophila*. *Development*, 126(13):2829–2839, 1999.

T. L. Megraw, S. Kilaru, F. R. Turner, and T. C. Kaufman. The centrosome is a dynamic structure that ejects PCM flares. *Journal of Cell Science*, 115(23):4707–4718, 2002.

T. L. Megraw, J. T. Sharkey, and R. S. Nowakowski. Cdk5rap2 exposes the centrosomal root of microcephaly syndromes. *Trends in Cell Biology*, 21(8):470–80, 2011.

M. D. Morris. Factorial sampling plans for preliminary computational experiments. *Technometrics*, 33(2):161 – 174, 1991.

K. W. Morton and D. F. Mayers. *Numerical Solution of Partial Differential Equations: An Introduction*. Cambridge University Press, 2005. ISBN 0521607930.

F. Mueller, D. Mazza, T. J. Stasevich, and J. G. McNally. FRAP and kinetic modeling in the analysis of nuclear protein dynamics: what do we really know? *Current Opinion in Cell Biology*, 22(3):403–11, 2010.

P. Müller, K. W. Rogers, B. M. Jordan, J. S. Lee, D. Robson, S. Ramanathan, and A. F. Schier. Differential diffusivity of Nodal and Lefty underlies a reaction-riffusion patterning system. *Science*, 336:721–724, 2012.

J. Nelder and R. Mead. A simplex method for function minimization. *The Computer Journal*, 7(4):308–313, 1965.

E. A. Nigg and J. W. Raff. Centrioles, centrosomes, and cilia in health and disease. *Cell*, 139(4):663–678, 2009.

E. A. Nigg and T. Stearns. The centrosome cycle: Centriole biogenesis, duplication and inherent asymmetries. *Nature Cell Biology*, 13(10):1154–60.

G. Pereira and E. Schiebel. Centrosomes-microtubule nucleation. *Journal of Cell Science*, 110:295–300, 1997.

R. Peters, J. Peters, K. H. Tews, and W. Bähr. A microfluorimetric study of translational diffusion in erythrocyte membranes. *Biochimica et Biophysica Acta*, 367(3): 282–94, 1974.

R. D. Phair and T. Misteli. High mobility of proteins in the mammalian cell nucleus. *Nature*, 404(6778):604–9, 2000.

R. D. Phair and T. Misteli. Kinetic modelling approaches to in vivo imaging. *Nature Reviews. Molecular Cell Biology*, 2(12):898–907, 2001.

A. Saltelli, M. Ratto, S. Tarantola, and F. Campolongo. Sensitivity analysis practices: Strategies for model-based inference. *Reliability Engineering & System Safety*, 91 (10-11):1109–1125, 2006.

M. Schlosshauer and D. Baker. Realistic protein-protein association rates from a simple diffusional model neglecting long-range interactions, free energy barriers, and landscape ruggedness. *Protein Science*, 13:1660–1669, 2004.

L. F. Shampine and M. W. Reichelt. The MATLAB ODE Suite. *SIAM Journal on Scientific Computing*, 18(1):1–22, 1997.

E. D. Siggia, J. Lippincott-schwartz, and S. Bekiranov. Diffusion in inhomogeneous media: theory and simulations applied to whole cell photobleach recovery. *Biophysical Journal*, 79:1761–1770, 2000.

R. Skeel and M. Berzins. A method for the spatial discretization of parabolic equations in one space variable. *SIAM Journal on Scientific and Statistical Computing*, 11 (1):1–32, 1990.

B. L. Sprague and J. G. McNally. FRAP analysis of binding: proper and fitting. *Trends in Cell Biology*, 15(2):84–91, 2005.

B. L. Sprague, R. L. Pego, D. A. Stavreva, and J. G. McNally. Analysis of binding reactions by fluorescence recovery after photobleaching. *Biophysical Journal*, 86 (6):3473–3495, 2004.

B. L. Sprague, F. Müller, R. L. Pego, P. M. Bungay, D. a. Stavreva, and J. G. McNally. Analysis of binding at a single spatially localized cluster of binding sites by fluorescence recovery after photobleaching. *Biophysical Journal*, 91:1169–91, 2006.

D. L. Stenoien, S. Sen, M. A. Mancini, and B. R. Brinkley. Dynamic association of a tumor amplified kinase, Aurora-A, with the centrosome and mitotic spindle. *Cell Motility and the Cytoskeleton*, 55:134–146, 2003.

W. Sullivan. *Drosophila* early development, 2002. URL `http://bio.research.ucsc.edu/people/sullivan/drosophila.html`.

H. Thompson, C. Hong, J. Chen, U. Euteneuer, and M. A. McNiven. Dynamin 2 binds gamma-tubulin and participates in centrosome cohesion. *Nature Cell Biology*, 6:335–342, 2008.

D. Vaizel-Ohayon and E. D. Schejter. Mutations in centrosomin reveal requirements for centrosomal function during early *Drosophila* embryogenesis. *Current Biology*, 9(16):889–898, 1999.

F. H. Walters, L. R. Parker, S. L. Morgan, and S. N. Deming. *Sequential Simplex Optimization : A Technique for Improving Quality and Productivity in Research, Development, and Manufacturing*. CRC Press Inc, 1991.

Y. Yamashita, D. Jones, and M. Fuller. Orientation of asymmetric stem cell division by the APC tumor suppressor and centrosome. *Science*, 301:1547–1550, 2003.

Y. M. Yamashita, A. P. Mahowald, J. R. Perlin, and M. T. Fuller. Asymmetric inheritance of mother versus daughter centrosome in stem cell division. *Science*, 315(5811):518–21, 2007.

D. Zyss and F. Gergely. Centrosome function in cancer: guilty or innocent? *Trends in Cell Biology*, 19(7):334–46, 2009.